University of California
Santa Barbara

On the Role of Mn-Ni-Si Precipitation in Irradiated Reactor Pressure Vessel Steels: Implications to Life Extension and Advanced Damage Tolerant Alloys

A dissertation submitted in partial satisfaction of the
requirements for the degree Doctor of Philosophy
in Materials

By
Nathan Taylor Almirall

Committee in Charge:
Professor G. Robert Odette, Chair
Professor Carlos G. Levi
Professor Anton Van der Ven
Professor Baron Peters, University of Illinois Urbana-Champaign

March 2021

The Dissertation of Nathan Taylor Almirall is approved.

Carlos G. Levi

Anton van der Ven

Baron Peters

G. Robert Odette, Committee Chair

March 2021

On the Role of Mn-Ni-Si Precipitation in Irradiated Reactor Pressure Vessel Steels:

Implications to Life Extension and Advanced Damage Tolerant Alloys

By

Nathan Taylor Almirall

Acknowledgements

Before acknowledging the significant contributions of colleagues and support staff, I would like to thank my brilliant family. I'm truly lucky to have my immensely supportive parents, Marilyn and Peter. Every step of the way I counted on their love and support. I sincerely thank my sisters, Katie and Michelle, and my brother Daniel for encouraging me and advising me on how to navigate the stressful times of grad school. All my family and extended family expressed their love in countless ways. I learned from them and I'm forever grateful. I made it here because of them, and love them beyond words can express.

I thank my advisor, Professor Bob Odette for mentoring and guiding me in graduate school. I value and respect his opinion. I am forever grateful for what he taught me and the supreme effort he put into my growth as a scientist. He also gave me the amazing opportunity to work on a vital scientific project. I admire and will forever seek to emulate Bob's commitment to ethics and scientific research. Professor Odette and the Materials Reliability and Performance Group have been working on measuring, modeling and managing irradiation effects, including hardening and embrittlement, for more than 40 years. The work reported in this thesis is built on this broad and deep foundation. As is normally the case for an advisor, Professor Odette has been deeply involved in all aspects of this work, with the exception of conduct of the hands-on experiments and measurements. His involvement includes conceptualization; fund raising; design, construction and implementation of a series of UCSB irradiation experiments; directing the corresponding PIE; analysis of the results; multiscale-multiphysics modeling; writing papers and reports; and, developing predictive models of embrittlement used by regulatory agencies. This involvement applies to the following chapters

and will not be repeated each time. I would also like to sincerely thank my committee Drs. Carlos Levi, Anton van der Ven and Baron Peters for their advice and research guidance.

I would like to especially acknowledge my friend and mentor Peter Wells. Every year of this journey, his patience, intelligence and friendship were beyond legendary. Our relationship made those long winter experiments at beamlines feel like sunny vacations. I'm also grateful to Takuya Yamamoto for always answering my scientific questions and conducting ion irradiation experiments for the group around the world. Among many indispensable contributions, David Gragg provided technical support, materials handling and a wonderful lab partner. May he always don Hawaiian shirts and attend the annual Tiki Oasis. In addition, I'm grateful to Kirk Fields for his ingenious mechanical test skills and robust lab support.

Also, I want to thank all the past and current grad students and post docs of the Materials Reliability and Performance Group (MR&P). Among these are Tiberiu Stan, Kevin Cunningham, MD Alam, Soupitak Pal, Nicholas Cunningham and Yuan Wu. Their kindness, wit and friendship kept me sane and made grad school better than I ever imagined it could be.

I am sincerely grateful for our modeling collaboration with Professor Dane Morgan's group at the University of Wisconsin, and especially the work of Drs. Huibin Ke and Mahmood Mamivand. The Brookhaven National Laboratory beamline work was made possible by Drs. Lynne Ecker's and David Sprouster's support. I thank John Barker's tireless efforts on the neutron scattering experiments at the National Institute of Standards and Technology. The Idaho National Laboratory staff Joanna Taylor, Jatuporn Burns, Megha Dubey, Yaoqiao Wu were an invaluable source of support at Center for Advanced Energy Studies. Drs. Randy Nanstad, Phil Edmondson, Keith Leonard, Mikhail Sokolov, Radiation Safety technicians and

Janet Robertson of Oak Ridge National Laboratory provided essential program support in the post irradiation examination campaign. Keith Wilford, Tim Williams and Nick Riddle of Rolls Royce for their excellent expertise, advice and funding.

Last, I would like to thank the UCSB for access to state of the art facilities and its employees for enthusiastically helping me. Tom Mates, Mark Cornish, Stephan Kramer, Aidan Taylor spent time training me on instruments used in this research. The entire UCSB Materials Department, esteemed Professors and Office Staff, especially Jocelyn Guzman, created a welcoming academic environment. See Appendix D for additional acknowledgements.

Vita of Nathan Taylor Almirall

EDUCATION

University of California, Santa Barbara, **September 2013 - Current**
Materials Science Department PhD Student: NEUP Research Fellow, Advisor Dr. G.R.Odette

North Carolina State University, Raleigh, North Carolina **May 2013**
Bachelor of Science in Engineering: Materials Science and Engineering, GPA: 4.00

RESEARCH

Graduate PhD Researcher, UCSB, Santa Barbara, CA
Advisor: G.R. Odette **August 2013-ongoing**

- Collaborated with academia/industry to author 13 publications in peer-reviewed international scientific journals (See Publications) and 7 Department of Energy grant proposals; each executed at national laboratories under the 50k funded budget
- Spearheaded research to systematically quantify nanoscale microstructural evolution of reactor pressure vessel (RPV) embrittlement in order to develop physically-based predictive models of embrittlement at 80 years operation
- Developed expertise accumulating over +300 user hours on Focused Ion Beam, Atom Probe Tomography, Scanning Electron Microscopy & mechanical polishing to characterize failure/damage resulting from neutron/ion irradiation
- Empirically validated engineering predictive models that incorporated mechanical structure-property relationships to forecast failure and lifetime of steels for light water reactors; these models integrated the nanoscale hardening features and synergistic effects of alloy chemistry not treated by currently underpredicting regulatory models
- Conducted mechanical failure testing (tensile, microhardness, shear punch) and metallurgical analysis of advanced superclean steels for reactors with the targeted properties of high toughness and yield strength

Research Assistant for Integrated Manufacturing Science & Technology, NCSU, Raleigh, NC **2012**

- Led documentation of atmospheric plasma experiments to alter the seed germination under tutelage of Dr. Jerome Cuomo, a distinguished research professor in NC State University
- Co-authored a grant proposal, subsequently submitted to American Seed Research Foundation

WORK EXPERIENCE

Brunswick Nuclear Plant, Progress Energy, Southport, NC **May 2011- August 2012**
Engineering Intern

- Reduced time-critical bi-annual nuclear power plant outage by 2 hours via restructuring automation contained within Reactor Pressure Vessel (RPV) Heatup/Cooldown Evaluation by translating insights from program managers into Visual Basic (VB) and Excel macros for engineers
- Restructured legacy Access queries and VB to streamline automated retrieval of plant documents, including components drawings which generated $10k/year of annual savings

- Screened and verified over 2500 piping component information sheets to aid the FAC program inspection of corrosion, required to ensure safe operation

ADDITIONAL EXPERIENCE

- Student Member of the UC Santa Barbara Radiation Safety Committee (December 2015 – Present)
- Judge at the Santa Barbara County Science and Engineering Fair to Junior High students (2018-2019)
- Student Member of The Minerals, Metals & Materials Society (TMS) (2013 - Present)
- Mentored and taught Materials Science and Engineering to 100+ Cary County Middle School students in a Science Math Interactive Learning Experience (SMILE) camp, 2012-2013
- Game of Thrones Wiki Consultant for IGN Entertainment, 2011-2014

SKILLS

Technical: Focused Ion Beam (FIB), CAMECA 3000 & 4000XHR LEAP Atom Probe Tomography (Laser & Voltage mode), Small Angle Neutron Scattering, X-Ray Diffraction, Mechanical Property Testing (Tensile, Shear, microhardness) Scanning Electron Microscopy, Transmission Electron Microscopy, Visual Basic for Applications (VBA), FORTRAN 2003, Solidworks, MATLAB, MS Excel, Access, Word, PowerPoint

Honors & Activities: Nuclear Energy University Programs Fellow, U.S. DOE (2013-2016), Boy Scouts of America Eagle Scout, NCSU Scholars Program Member, Webmaster of Tau Beta Pi Engineering Honor Society, Member in Pi Tau Sigma International Engineering Honor Society, National Honor Society Member

PUBLICATIONS

G.R. Odette, N. Almirall, P.B. Wells, T. Yamamoto, Dislocation Complexion in Irradiated Multi Constituent Reactor Pressure Vessel Steels, (2021) Under Review in Acta Materialia.

T. Davis, M.A. Auger N. Almirall, P. Hosemann, G.R. Odette, P. Bagot, M.P. Moody, D. Armstrong, Atom probe characterization of segregation driven Cu and Mn-Ni-Si co-precipitation in neutron irradiated T91 tempered-martensitic steel, Materialia, 14 (2020).

B.M. Jenkins, J.O. Douglas, N. Almirall, N. Riddle, P. Bagot, J. Hyde, G.R. Odette, M. Moody, The Effect of composition variations on the response of steels subjected to high fluence neutron irradiation, Materialia 11 (2020) 100717, https://doi.org/10.1016/j.mtla.2020.100717.

N. Almirall, P.B. Wells, T. Yamamoto, K. Yabuuchi, A. Kimura, G.R. Odette, On the Use of Charged Particles to Characterize Precipitation in Irradiated Reactor Pressure Vessel Steels with a Wide Range of Composition, Journal of Nuclear Materials 536 (2020) 152173, https://doi.org/10.1016/j.jnucmat.2020.152173.

N. Almirall, P.B. Wells, S. Pal, P.D. Edmondson, T. Yamamoto, K. Murakami, G.R. Odette, The mechanistic implications of the high temperature, long time thermal stability of nanoscale Mn-Ni-Si precipitates in irradiated reactor pressure vessel steels, Scripta Materialia 181 (2020) 134-139, https://doi.org/10.1016/j.scriptamat.2020.02.027.

N. Almirall, P.B. Wells, T. Yamamoto, K. Wilford, T. Williams, N. Riddle, G. R. Odette, Precipitation and Hardening in Irradiated Low Alloy Steels with a Wide Range of Ni and Mn Compositions, Acta Materialia, 179, (2019), 119-128, https://doi.org/10.1016/j.actamat.2019.08.027.

N. Almirall, P.B. Wells, H. Ke, P. Edmondson, D. Morgan, G. R. Odette, On the Elevated Temperature Thermal Stability of Nanoscale Mn-Ni-Si Precipitates Formed at Lower Temperature in Highly Irradiated Reactor Pressure Vessel Steels, Scientific Reports 9 (2019) 1-12, https://doi.org/10.1038/s41598-019-45944-z.

E. Reese, N. Almirall, T. Yamamoto, S. Tumey, G. R. Odette, E. A. Marquis, Dose rate dependence of Cr precipitation in an ion-irradiated Fe18Cr alloy, Scripta Materialia (2018) 213-217, https://doi.org/10.1016/j.scriptamat.2017.11.040.

S. Shu, P.B. Wells, N. Almirall, G. R. Odette, D. Morgan, Thermodynamics and kinetics of core-shell versus appendage co-precipitation morphologies: An example in the Fe-Cu-Mn-Ni-Si system, Acta Materialia 157 (2018)298-306, https://doi.org/10.1016/j.actamat.2018.07.037.

S. Shu, N. Almirall, P.B. Wells, T. Yamamoto, G. R. Odette, D. Morgan, Precipitation in Fe-Cu and Fe-Cu-Mn model alloys under irradiation: Dose rate effects, Acta Materialia 157 (2018) 72-82, https://doi.org/10.1016/j.actamat.2018.07.017.

D.J. Sprouster, R. Weidner, S.K. Ghose, E. Dooryhee, T.J. Novakowski, T. Stan, P.B. Wells, N. Almirall, G.R. Odette, L.E. Ecker, Infrastructure development for radioactive materials at the NSLS-II, Nuclear Instruments and Methods in Physics Research Section A: Accelerators, Spectrometers, Detectors and Associated Equipment 880 (2018) 40-45, https://doi.org/10.1016/j.nima.2017.10.053.

H. Ke, P. Wells, P. Edmondson, N. Almirall, L. Barnard, G. R. Odette, D. Morgan, Thermodynamic and kinetic modeling of Mn-Ni-Si precipitates in low-Cu reactor pressure vessel steels, Acta Materialia 138 (2017) 10-26, https://doi.org/10.1016/j.actamat.2017.07.021.

E. Aydogan, N. Almirall, G.R. Odette, S.A. Maloy, O. Anderoglu, L. Shao, J.G. Gigax, L. Price, D. Chen, T. Chen, F.A. Garner, Y. Wu, P. Wells, J.J. Lewandowski, D.T. Hoelzer, Stability of nanosized oxides in ferrite under extremely high dose self ion irradiations, Journal of Nuclear Materials 486 (2017) 86-95, https://doi.org/10.1016/j.jnucmat.2017.01.015.

D.J. Sprouster, J. Sinsheimer, E. Dooryhee, S.K. Ghose, P. Wells, T. Stan, N. Almirall, G.R. Odette, L.E. Ecker, Structural characterization of nanoscale intermetallic precipitates in highly neutron irradiated reactor pressure vessel steels, Scripta Materialia 113 (2016) 18-22, https://doi.org/10.1016/j.scriptamat.2015.10.019.

Abstract

On the Role of Mn-Ni-Si Precipitation in Irradiated Reactor Pressure Vessel Steels: Implications to Life Extension and Advanced Damage Tolerant Alloys

by Nathan Taylor Almirall

The overarching goal of this research is to advance understanding of, model and predict embrittlement primarily due to hardening by precipitates in Reactor Pressure Vessel (RPV) steels as it pertains to 80-year life extension of fission reactors. The RPV is responsible for primary radioactive containment and pressurizing water in the nuclear reactor. The most immediate materials safety problem facing the RPV steels is neutron irradiation embrittlement, which is the reduction of fracture toughness. Embrittlement is caused by irradiation hardening ($\Delta\sigma_y$), mainly as a result of precipitation, and manifested as upward ductile-to-brittle transition temperature shifts (ΔT). The excess concentration of defects created under irradiation leads to radiation enhanced diffusion (RED), which greatly accelerates precipitation normally limited by extremely slow kinetics at $\approx 300^{O}C$, or at typical reactor operating temperatures. Concomitantly, the radiation induced segregation (RIS) of solute elements leads to enrichment at microstructural features which likely plays a role in the heterogeneous nucleation of precipitates. At lower fluences (ϕt), or displacements per atom (dpa), the hardening features are nm-scale copper rich precipitates (CRPs) and solute defects vacancy complexes at trace impurity levels of $> \approx 0.06$ wt% Cu. Effective Cu concentrations are less than ≈ 0.25 wt%. However, at higher ϕt much larger quantities of alloying elements precipitate to form Mn, Ni, Si nm-scale intermetallic precipitates known as MNSPs. Large volume fractions (f_v) of MNSPs cause severe hardening and embrittlement. The variables controlling the formation and

character of severely embrittling Mn-Ni-Si precipitates (MNSP) under neutron irradiation are neither fully understood nor explicitly treated in regulatory models.

There are five primary questions addressed by this work.

1) What is the quantitative effect of temperature (T_i), fluence/dose (ϕt), flux/dose rate (ϕ), particle type, product form and alloy composition on precipitate size, number density, volume fraction, composition and magnetic character of CRPs and MNSPs?

2) Are very high Ni alloys, with high strength and toughness, irradiation tolerant at low Mn; and how does precipitation and hardening occur in steels with a much wider range of Mn, Ni and Si that conventional normalized and tempered bainitic steels?

3) How can charged particle irradiations (CPI) compliment neutron data to gain insight into precipitation mechanisms?

4) Are MNSPs enhanced or induced by irradiation (equilibrium versus non-equilibrium) and can this ongoing controversy by establishing their detailed character, long-time thermal stability, and formation mechanisms?

5) How can these insights help build an improved high fluence, low flux predictive embrittlement model for steels used in in 80-year extended power reactor service?

Atom probe tomography (APT), small angle neutron scattering (SANS) and transmission electron microscopy (TEM) show the presence of significant volume fractions of MNSPs in all RPV steels at the high 80-year fluence. Precipitation is reflected in $\Delta\sigma_y$, as characterized by tensile, shear and microhardness tests. Ni generally plays the strongest role in the formation of MNSPs. In the absence of sufficient Cu and CRPs, and at low to intermediate Ni, the MNSPs

homogeneous nucleation rates are negligible in a defect free matrix. Heterogenous precipitation occurs at microstructural features, such as segregated network dislocation and irradiation induced interstitial loop sites. Units of % for compositions refers to atomic percent (%) unless otherwise noted. For typical RPV steel compositions (0.75% to 1.6% Ni with ≥ 0.8% Mn and 0.4 – 1.2% Si) MNSPs compositions are generally similar to G ($Mn_6Ni_{16}Si_7$) and Γ_2 (Mn_2Ni_3Si) phases. The formation of these phases is predicted by Calphad and has been confirmed by synchrotron X-Ray and TEM Diffraction measurements in a number of cases. However, in alloys with very low or very high Ni, coupled with variations in Mn and Si, other phase compositions are selected. For example, Ni-silicide type compositions are found in alloys with very low ≤ 0.24 Mn and high ≈ > 3% Ni. Notably at normal levels of > 0.8% Mn, very large MNSP f_v form in 3.5% Ni steels at high fluence. The MNSP high Ni f_v decreases approximately linearly with the decreasing alloy Mn content. Thus precipitation hardening is much lower in high ≈ 3.5% Ni and ≤ 0.24% Mn steels due to what is described as Mn starvation. For the so-called ATR-2 irradiation condition, which is the focus of this study, the high Ni $f_v \approx 2.44$ and 0.69% at 1.04 and 0.24% Mn, respectively. The resulting $\Delta\sigma_y$, which is well correlated with the $\sqrt{f_v}$ (as predicted by dispersed barrier hardening models), are 472 and 260 MPa.

At high ϕ, a very high N and f_v of MNSPs and CRP-MNSPs are observed in low Cu and Cu bearing alloys, respectively. In the latter case, Cu core Mn-Ni-Si shell CRP structures formed at lower dpa evolve into CRP-MNSP appendage co-precipitate features at high dpa. MNSP compositions formed in in rapid and convenient self-ion charged particle irradiation (CPI) are very similar to those found in neutron irradiations (NI). High dpa CPI produce fewer and larger precipitates than in NI. Further, higher dpa are needed to form the same precipitate

f_v for CPI versus NI conditions. The delayed precipitation is consistent with enhanced recombination of vacancies and SIA defects at the higher CPI dpa rates, which reduces the efficiency of RED. The MNSP grow slowly, but eventually reach large f_v at very high dpa. Notably, f_v correlates well with the G and Γ_2 phase solute product, $(Ni^{16}Mn^{6}Si^{7})^{(1/29)}$ and $(Ni^{3}Mn^{2}Si^{1})^{(1/6)}$ and, at high dpa, is close to the equilibrium values, slightly modified by the Gibbs-Thomson effect. However, in steels with very low Mn and high Ni, $Ni_{2-3}Si$ silicide phase type precipitate compositions are observed; and when Ni is low, the precipitate compositions are close to the MnSi phase field. A comparison of dispersed barrier model predictions with measured hardening data suggests that the Ni-Si dominated precipitates are weaker dislocation obstacles than the G phase type MNSPs. Ultimately, f_v from the CPI can be used to estimate $\Delta\sigma_y$ (and ΔT) at lower service relevant dpa. While not quantitatively precise, this allows scoping studies of the embrittlement sensitivity of new RPV alloys.

Post irradiation annealing (PIA) was used to clarify the irradiation induced versus enhanced controversy regarding dominant nanoscale Mn-Ni-Si precipitate (MNSP) formation mechanisms in pressure vessel steels. Radiation induced, non-equilibrium, MNSPs would dissolve under high temperature PIA, while radiation enhanced precipitates would be stable above a critical radius (r_c). A Cu-free, high Ni steel was irradiated with 2.8MeV Fe^{2+} ions at two temperatures to generate MNSPs with average radii ($\bar{r}$) above and below an estimated r_c for PIA at 425°Cup to 52 weeks. The complementary APT and Energy Dispersive X-ray Spectroscopy studies show MNSPs with $r < r_c$ dissolved, while those with $r > r_c$ slightly coarsened, consistent with thermodynamic predictions. Note, the MNSPs would be even more thermodynamically stable at much lower neutron irradiation RPV service temperatures around 290°C.

Finally, the ultimate goal of this research is to create and analyze the high ϕt, intermediate ϕ ATR-2 database on both $\Delta\sigma_y$ and microstructural changes in a large number of irradiated alloys. In the final section, ATR-2 results are integrated with a variety of other (mostly UCSB and surveillance) databases to develop a new high ϕt-low ϕ predictive embrittlement chemistry factor. Special emphasis is placed on the $\Delta\sigma_y$ contributions of MNSPs, which are observed in a wide range of RPV steels at high ϕt. This directly informs the Odette Research Group's development of an advanced embrittlement model which accurately predicts ΔT for low ϕ high ϕt conditions up to 80 full power years of operation.

Table of Contents

List of Tables

List of Figures

Nomenclature

APT	Atom Probe Tomography
%	Atomic percent
ATR	Advanced Test Reactor
CPI	Charged Particle Irradiations
CRP	Cu-Rich Precipitate
DBTT	Ductile to Brittle Transition Temperature
dpa	displacements per atom - dose
DuET	Dual-ion irradiation experimental facility for energy research
EDS	Energy Dispersive X-ray Spectroscopy
EPMA	Electron Probe Micro-Analyzer
f_v	volume fraction (%)
FIB	Focused Ion Beam
LBP	Late Blooming Phase
LEAP	Local Electrode Atom Probe
LWR	Light Water Reactor
MF	Matrix Features
MNSP	Manganese-Nickel-Silicon Precipitate
M/N	Magnetic to Nuclear Scattering Ratio
N	Number density #/m^3
NI	Neutron Irradiation
ORNL	Oak Ridge National Laboratory

PIA	Post Irradiation Annealing
RED	Radiation Enhanced Diffusion
RIS	Radiation Induced Segregation
RPV	Reactor Pressure Vessel
<r>	average radius (nm)
SANS	Small Angle Neutron Scattering
SD	Standard Deviation
ΔT	increase in the DBTT due to irradiation
TEM	Transmission Electron Microscopy
Ti	irradiation temperature
$\Delta\sigma_y$	increase in yield strength due to irradiation
ϕ	neutron flux ($n/cm^2/s$)
ϕt	neutron fluence (n/cm^2)
ϕt_e	effective neutron fluence (n/cm^2)

Chapter 1: Introduction

Light Water Reactors provide 20% of United States electricity but this will drop to zero by ≈ 2050 without life extension & new builds, as shown in Figure 1.1. [1]. Ensuring operation of over half of 98 US reactors requires further life extension to 80-years within the next three decades [2]. The Nuclear Regulatory Commission (NRC) determines the acceptable set of safety requirements for extended operation based on scientific basis. Thus, the Department of Energy (DOE) funds essential research to understand, measure and predict the evolution of materials under neutron irradiation.

Life extension will require ensuring the integrity of the massive 500-1000 ton thick-walled steel reactor pressure vessels (RPV), as shown in Figure 1.2. The RPV serves a critical role in safety of nuclear reactors, pressurizing the reactor core at operating temperature ≈300^{o}C and serving as the primary radioactive containment. At elevated temperatures and pressures, the RPV safely contains the reactor coolant, fuel assembly and support structures of the core. The most immediate materials problem facing the RPV steels is embrittlement, manifested as upward ductile-to-brittle transition temperature shifts. The challenge in studying embrittlement lies in a complex multiscale-multiphysics phenomenon controlled by a combination of many synergistic variables (flux, fluence, irradiation temperature, composition). There is little in-service data for extended life, thus its necessary to develop robust models and a supporting irradiation database.

The primary mechanism of embrittlement is irradiation hardening under neutron irradiation, characterized by increases in the yield stress ($\Delta\sigma_y$) [3–8]. As described in the cited papers, bombardment of neutrons creates high-energy primary recoil atoms that produce excess vacancies and self-interstitial defects in displacement cascades [9]. The diffusion,

clustering and annihilation of defects lead to: a) formation of defect-solute complexes; and, b) radiation enhanced solute diffusion (RED) precipitation [3–8]. Note, radiation induced segregation also plays a role in MNSP nucleation, especially at lower solute contents [10–14]. The nano-scale precipitates and defect clusters result in hardening ($\Delta\sigma_y$) by acting as dispersed obstacles to dislocation glide. Hardening results in embrittlement by increasing the temperature at which the blunting crack tip field critical reaches the critical stress and volume for cleavage fracture [15–18]. Thus understanding these microstructural evolutions under irradiation as a function of the neutron fluence (ϕt, n/cm^2), flux (ϕ, n/cm^2-s), irradiation temperature (T_i), alloy composition (Cu, Ni, P. in at.%) and start of life microstructure, is required to develop robust, physically-based predictive hardening and embrittlement models, like that proposed by Ke et al.[19]; and the reduced order formulation proposed by Eason, Odette, Nanstad and Yamamoto (EONY) fitted to the surveillance database on embrittlement [20].

The major focus of this dissertation will be on the recently completed intermediate flux UCSB ATR-2 irradiation in the Advanced Test Reactor (ATR) at Idaho National Laboratory (INL). The results reported here are for a small subset of data from the UCSB ATR-2 irradiation experiment, involving a large matrix of 172 alloys irradiated to high fluence over a range of temperatures. The objective of the UCSB ATR-2 study is to evaluate and model: a) the formation of and hardening by CRPs, MNSPs and solute cluster complexes at high fluence, pertinent to the extended nuclear plant life of 80-years, or more; and, b) the effects of dose rate, as a basis to extrapolate the ≈ 290°C, intermediate flux (≈ 3.6x10^{12} n/cm^2-s) ATR-2 irradiation results to low flux, vessel service conditions (≈ 4x10^{10} n/cm^2-s) [29, 39]. To address the key objectives of ATR-2 and the fleet of nuclear reactors, we focus on the following five research objectives.

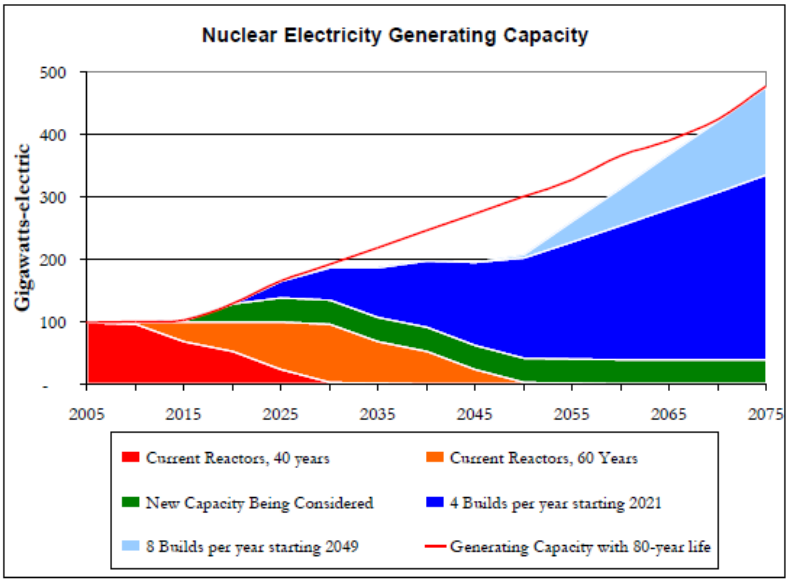

Figure 1.1. Projected nuclear electricity generating capacity for currently operating power plants, construction of new reactors and assuming extended operation to 80-years (red line) [2].

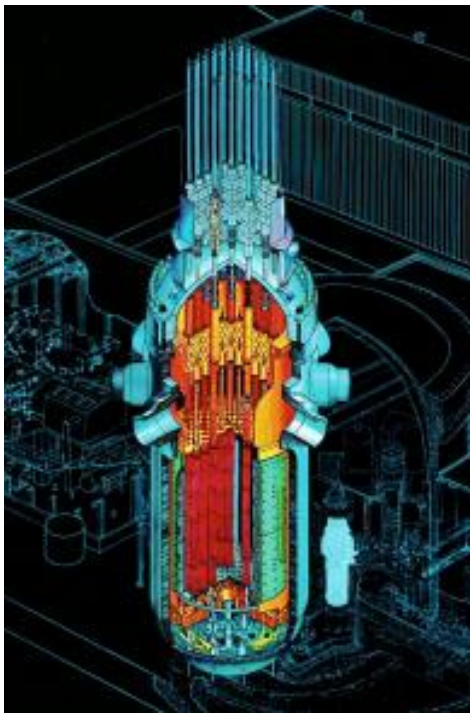

Figure 1.2. Reactor Pressure Vessel (RPV) section view from a light water reactor. The RPV contains the reactor core and serves as primary containment for fissile material [2,23].

1.1 Primary Research Objectives

There are five primary research objectives for this dissertation.

1) Quantify the effect of temperature T_i, ϕt, ϕ, particle type, product form and alloy composition on precipitate size, number density, volume fraction, composition and magnetic character. These relationships establish the conditions for the formation of severely embrittling CRPs and MNSPs LBPs in both high and low Cu steels that are not explicitly treated in current regulatory models.
2) Characterize a new Advanced Steel Matrix (ASM) with varying levels of Cu, Ni, Mn, and Si to expand RPV composition range and explore potential for tougher and higher strength steels in advanced reactors.
3) Compliment neutron data by using charged particle irradiations to gain insight into precipitation mechanisms.
4) Investigate the detailed character, thermal stability and formation mechanisms of the MNSPs to address the ongoing formation mechanism controversy. This controversy primarily centers on the role of thermodynamic driving forces versus radiation induced segregation.
5) Develop an improved high fluence low flux chemistry factor over a wide range of alloys compositions and product form – heat treated conditions. This directly informs the Odette Research Group's development of an advanced embrittlement model which accurately predicts ΔT for low flux high fluence conditions up to 80 full power years of operation.

Chapter 2: Background

2.1 Irradiation Damage Effects

Extending the lifetime of nuclear plants to 80-years is critical to sustaining the world's largest contributor to C-free electricity production [1]. However, embrittlement of reactor pressure vessels may limit the extended lifetimes of light water nuclear reactors [24–26]. Embrittlement is primarily caused by nm-scale precipitates and solute-defect cluster complexes that evolve under irradiation cascade damage production, as shown in Figure 2.1 [3,26,27].

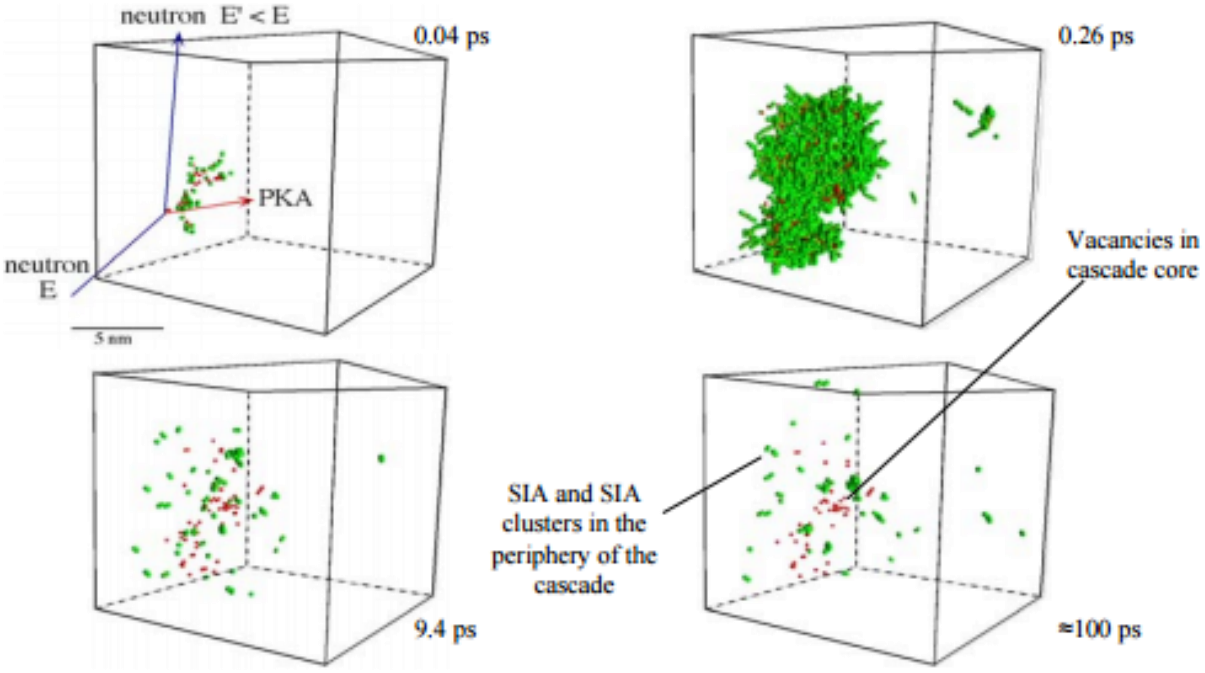

Figure 2.1. A depiction of cascade primary-damage production. Molecular dynamic snapshots illustrate the primary recoil/knock on atom striking the lattice, transferring energy to iron atoms which displace from their original lattice sites. The displacement cascade continues transferring energy until energy dissipates on a ≈100 ps timescale. The resulting SIA and defect-solute complexes can dissolve, cluster, or annihilate at sinks [4,28].

The mechanism of irradiation hardening and embrittlement is shown in Figure 2.2. Neutrons create primary recoil atoms that produce displacement cascades and excess vacancies and self-interstitials [9]. This damage, quantified by units of displacements per atom (dpa), leads to defect-solute clustering and radiation enhanced diffusion (RED), which greatly accelerates precipitation rates normally limited by extremely slow kinetics at ≈ 300^{O}C, or at typical reactor operating temperatures. The resulting nanoscale clusters and precipitates increase yield strength σ_y by pinning dislocations, $\Delta\sigma_y \sim \sqrt{f_v}$. The increased σ_y leads to a corresponding embrittlement manifested as ductile to brittle transition temperature shifts (DBTT). Examination of the Charpy impact energy curves also shows neutron irradiation also causes a reduction of upper shelf energy for reactor pressure vessel steels, as shown in Figure 2.2c [20,29,30].

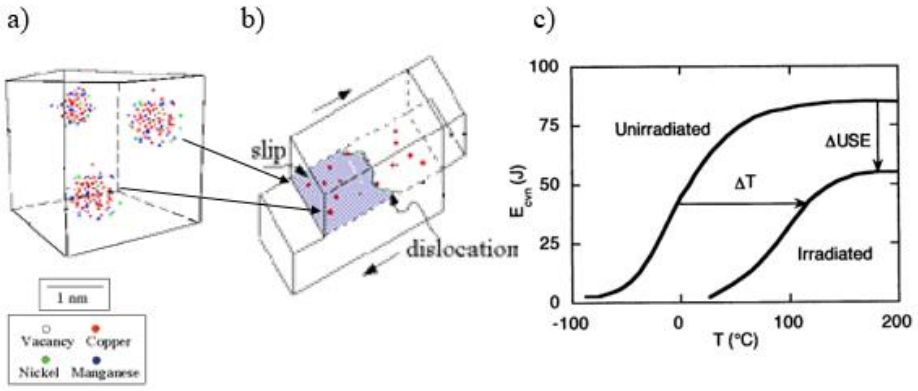

Figure 2.2. Sequence of basic embrittlement mechanisms a) Generation of excess concentrations of defects by high-energy recoil atoms leads to formation of defect-solute complexes and solute complexes. b) Pinning of dislocations by nanoscale clusters and other irradiation features increases yield stress. c) Charpy impact energy curves show the effect of irradiation for a RPV steel. Irradiation hardening leads to corresponding embrittlement. Transition temperature increases and upper shelf energy is reduced [4,28].

RPV steels have a body-centered cubic (BCC), typically bainitic, microstructure with varying additions of alloying elements such as Ni, Mn, Si, C, and Mo along with Cu and P impurities [9,31]. The alloy bulk Cu and Ni contents are the primary thermodynamic driving force behind precipitation [32,33]. Typical ranges for precipitate number densities N and average diameters <d> are $N \approx 7\text{-}20 \times 10^{23}$ #/m^3 and $<d> \approx 2.5\text{-}4$ nm [21]. Four nanoscale irradiation-hardening features have been empirically identified in RPV steels: stable matrix features (SMF); unstable matrix defects (UMD); larger segregated dislocation loops, copper enriched precipitates (CRP); Mn-Ni-Si intermetallic precipitates (MNSPs). [5,17,21,34,35]. Estimates of the net hardening contributions from different features can be obtained with appropriate superposition law, typically in a limit root mean square rule.

SMF include vacancy and interstitial cluster-solute complexes, alloy carbide, phosphide precipitates and pre-precipitation of solutes clusters. The SMF contribution to hardening increases roughly proportionally with the square root of fluence and can be further quantified by post-irradiation annealing recovery experiments [4,33,36].

UMD are smaller defect-solute-cluster complexes which can dissolve during irradiation, especially at low flux. UMDs have two competing roles: 1) directly increasing $\Delta\sigma_y$; 2) acting as point defect sinks, which reduce the efficiency of RED, thus delay formation of SMF and precipitation [4,21,37,38].

The importance of Cu in RPV steels was established by Odette who found the formation Cu-rich precipitates (CRPs) (d <5nm) can be attributed to RED caused by the excess vacancies introduced by irradiation [7]. CRPs, which form at low fluence where they are the dominant hardening features in steels containing > 0.07% Cu, have been extensively studied

for about 3 decades [4,31,39,40]. The CRP hardening contribution saturates with the depletion of matrix copper, as shown in Figure 4.

CRPs are enriched with Mn, Ni and Si, typically with a core-shell structure, however, in both Cu-depleted and Cu-free steels higher extended life fluence leads to formation of Mn-Ni-Si precipitate (MNSP) phases. These so-called 'Late Blooming Phases' (LBP) proposed and modeled by Odette in the 1990s, are slow to nucleate and grow, so they are not included in current regulatory models, in spite of the fact that they can lead to very large embrittlement, even in low Cu steels at high fluence [22,33,41]. MNSPs are enhanced by low flux and irradiation temperature (T_{irr}), and high fluence and Ni content. A number of atom probe tomography and small angle neutron scattering studies have demonstrated the existence of MNSPs, particularly in high Ni steels [32,42,43]. Styman et al have shown that MNSPs also form under thermal ageing conditions in high Ni, Cu bearing steels [16, 23–26].

Cu acts as a catalyst for the formation of MNSPs even in small amounts [4,32] and MNSPs grow on CRPs long after Cu depletion, as an appendage to core-shell CRPs at high fluence beyond the existing surveillance database of $\approx 5x10^{19}$ n/cm^2. Figure 5 shows a CRP with an MNSP appendage at a high fluence of $\approx 10^{21}$ n/cm^2 [22].

Post irradiation annealing (PIA) can decrease the volume fraction or dissolve SMFs, UMDs and coarsen CRPs that are less enriched in Mn, Ni and Si. The recovery temperatures of the various features provide signals of their relative hardening contribution [5,33,48,49]. Thus, annealing experiments contribute to better understanding of the role of thermodynamic driving forces versus radiation induced segregation on detailed character, thermal stability and formation mechanisms of the MNSPs. Notably, there is zero empirical data on the long-term (>52 weeks) annealing of MNSPs at lower temperatures.

2.2 Models

Understanding microstructural evolutions as a function of fluence (neutrons/cm^2), flux (neutrons/cm^2-s), T_{irr}, product form and alloy composition forms the basis for developing predictive models of embrittlement. Great strides in developing embrittlement models, which correlate microstructural evolution to mechanical property changes, have been made over the last 3 decades, see this hierarchal workflow in Figure 2.3. For example, the physically motivated, semi-empirical Eason, Odette, Nanstad and Yamamoto (EONY) model was statistically calibrated to the US surveillance database [5,33]. Capsules of surveillance materials stored in operating reactors, located in areas of somewhat higher flux/fluence, serve as early indications of embrittlement in RPVs. These surveillance materials identically match the composition of in-service reactors, and are periodically removed for mechanical testing. Plates and forgings within the US surveillance database have the following ranges in wt% 0.04-1.26Ni, 0.58-1.96Mn, 0.15-0.37Si, 0.01-0.41Cu, 0.003-0.031P [15]. Up to intermediate fluence, the EONY model predictions are also consistent with test reactor irradiations like the UCSB Irradiation Variables (IVAR) program when flux effects are properly accounted for, see Figure 2.4 [31]. The IVAR program was designed to create a hardening and microstructure database based on the effects of irradiation variables. It involved over 30 irradiation conditions and includes characterization from a library of alloys including LV-series and CM-series. These materials are described in Materials and Methods and Appendix A.

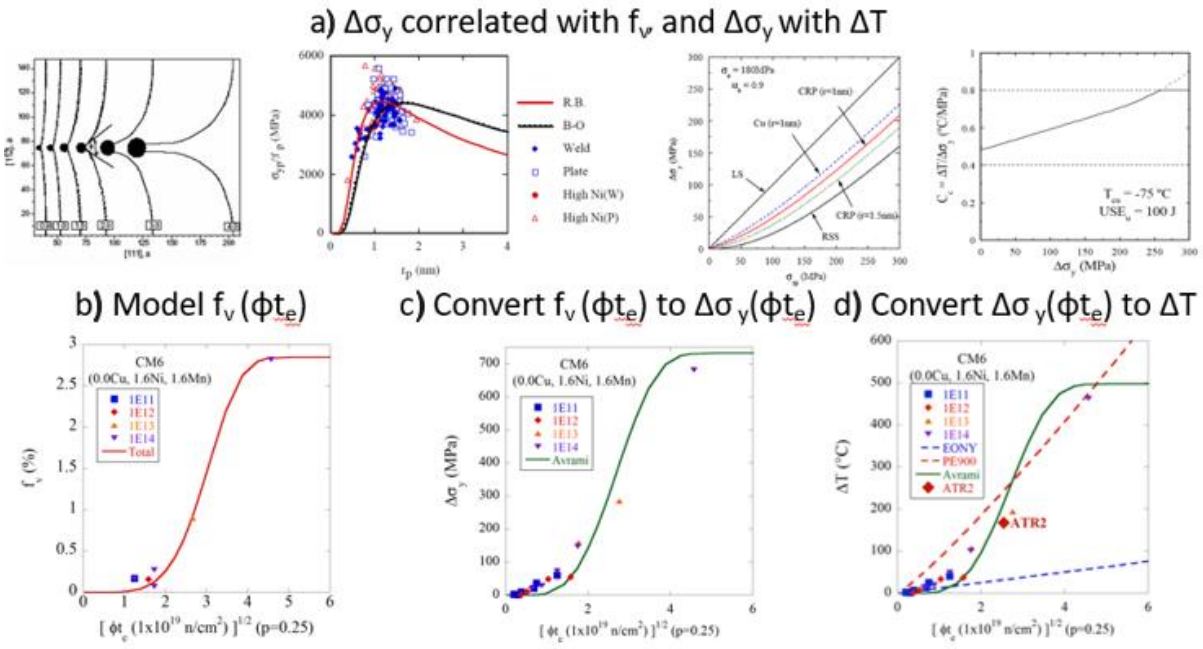

Figure 2.3. Hierarchal modeling allows prediction of embrittlement (ΔT) starting with precipitate volume fraction f_v. a) Dislocation dynamic simulations and Russel Brown hardening model [4,50]. The hardening ($\Delta\sigma_y$) contributions combine from precipitate f_v, unirradiated contributions and other sources using the mixed linear sum (LS) and root sum squared (RSS) superposition rules [51,52]. $\Delta\sigma_y$ correlates with ΔT by a correlation factor. b) Simplified Avrami model of precipitate f_v as a function of effective fluence (ϕt_e). c) $\Delta\sigma_y$ as a function of ϕt_e, converts from f_v using the empirical precipitate hardening relationships [52,53] d) ΔT as a function of ϕt_e converts from $\Delta\sigma_y$ using a well-established correlation factor, see Equation 2.1 [54].

Figure 2.4 empirically shows using hardening data from IVAR that flux effects can be simply accounted for by an effective fluence ϕt_e as shown in Equation 2.1, using a scaling factor, p that depends on flux, T_{irr}, alloy composition and microstructure. Increasing flux typically leads to a decrease in precipitate volume fraction due to enhanced point defect recombination, reducing the efficiency of RED in a way that can be physically modeled [5,20].

$$\phi t_e = \phi t(\phi_r/\phi)^p \quad (2.1)$$

Here, ϕ_r is an arbitrary reference flux, typically assumed to $3x10^{11}$ n/cm^2-s.

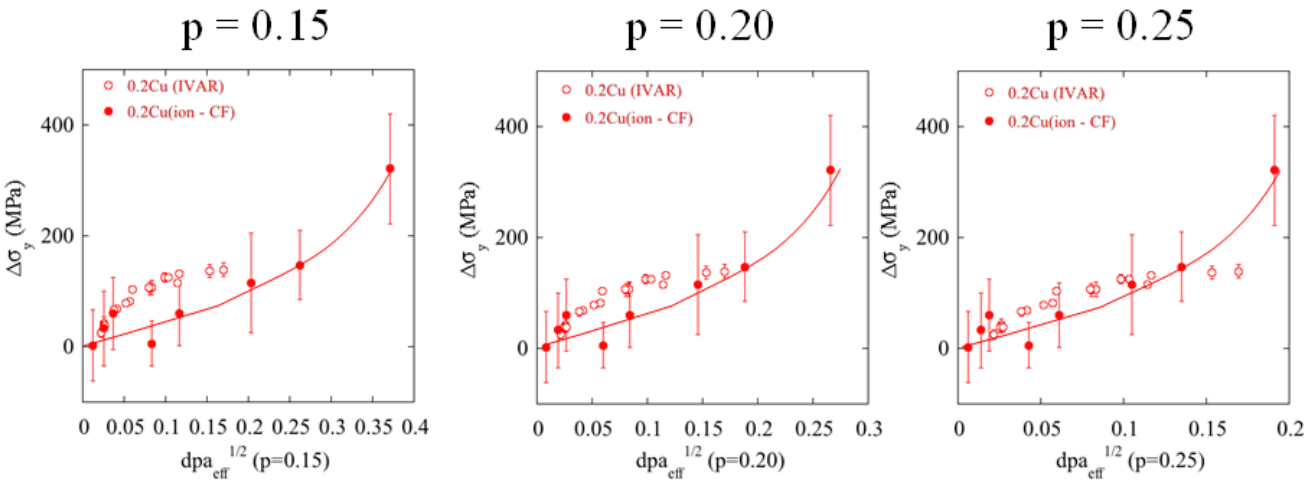

Figure 2.4. Hardening as a function of dose for IVAR and CPI data, showing the effect of dose rate scaling factor p = 0.15-0.25 [23,52].

The EONY model was calibrated by nonlinear least squares fits to the power reactor engineering database (PREDB) which, at that time, was composed of 855 ΔT_c data points. After testing a huge number of trial forms, the EONY model provides good statistical fits, with no significant residual error trends, and with all fit parameters established at a high confidence level [54–56]. The EONY equations can be found in [54–56], and will not be repeated here.

The EONY model, which was adopted by the US Nuclear Regulatory Commission (NRC), provides a robust tool for predicting embrittlement only up to intermediate fluence. Notably, however, observations of embrittlement at higher fluence for accelerated irradiations in test reactors are generally underpredicted by EONY and other surveillance database models. The underprediction trend becomes evident above $\phi t=10^{19}$ n/cm^2, or at approximately 80-years operating life, as illustrated by Figure 2.5 [5]. Figure 2.6 shows a 0.05-0.08 Cu, 1.6 Ni, 1.6 Mn weld, in which the EONY model underpredictions show the strong Ni effect. The EONY

model (dashed blue line) underpredicts the measured hardening while a reduced order Avrami Model (red line) shows reasonable agreement. These under predictions may be caused by a combination of flux effects and high fluence features like MNSPs [4,5,42].

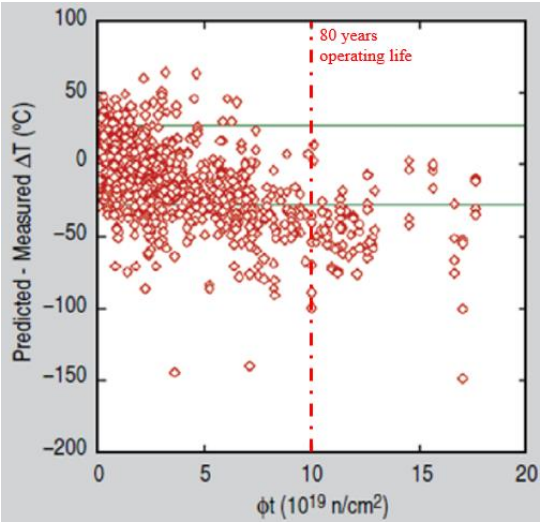

Figure 2.5. Plot of EONY model predicted minus measured test reactor ΔT residuals as a function of fluence. The underprediction trend becomes evident above $\phi t=10^{19}$ n/cm^2 or at approximately 80-years operating life [57].

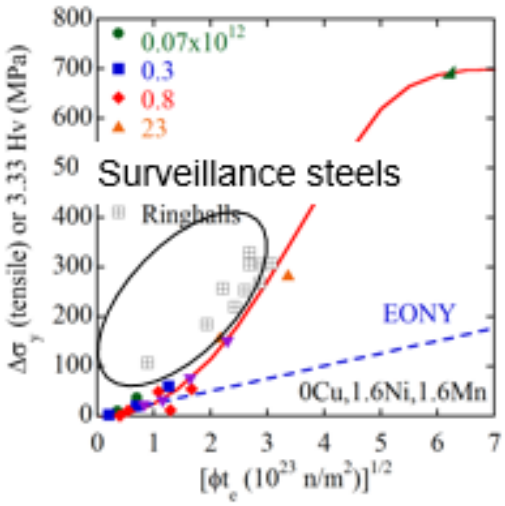

Figure 2.6. The $\Delta\sigma_y$ measured by tensile or hardness testing for the Ringhals 0.05-0.08 Cu, 1.6 Ni, 1.6 Mn weld as a function of effective fluence. The EONY model (dashed blue line) underpredict the measured hardening while a reduced order Avrami Model (red line) shows reasonable agreement [23].

2.3 Irradiation Hardening

A classical dispersed barrier-hardening (DBH) model is used to calculate the hardening contribution of precipitates, σ_p. Since the model has been described in many publications, this will not be repeated here [50–52]. Briefly, combining various terms in the DBH model yields $\sigma_p \approx 6.9x10^4\sqrt{f_v}\alpha_p(d)/d$, where $\alpha_p(d)$ is the precipitate obstacle strength factor. Figure 2.7 shows a plot of CRP and MF hardening contributions as a function of flux and fluence at low fluence. In comparison to low flux (dashed red line), high flux (dotted red line) delays precipitation due to enhanced point defect recombination, reducing the efficiency of RED.

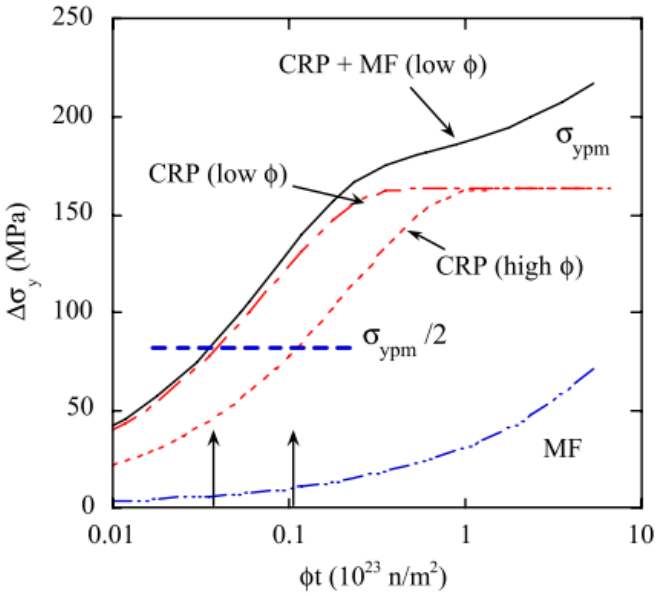

Figure 2.7. Plot of CRP (red line) and MF (blue line) hardening contributions as a function of fluence (ϕt). Also shown is the effect of flux (ϕ) on the CRP hardening contribution at low ϕt. The CRP hardness contribution saturates with the depletion of matrix Cu [23].

2.4 Avrami Curve

The precipitate f_v (ϕt) can be modeled with simple Johnson-Mehl-Avrami-*Kolmogorov* (JMAK) equations, which we simply refer to here as Avrami models [58–60]. Basically, Avrami models account for the solutes that have already precipitated, thus are no longer available for further CRP or MNSP growth, as shown in Figure 2.8 and in the general form

$$df_v/dt \approx C(1-f_v) \tag{2.2}$$

Eq. 2.2 is integrated up to the maximum f_{vmax}. The Avrami equation can be expressed as

$$f_v/f_{vmax} = 1 - \exp[(-\phi t/\phi t_o)^{\beta}] \tag{2.3}$$

Here ϕt_o is the indexing ϕt at $f_v/f_{vmax} = 0.632$. The Avrami model also can be related to the physics of precipitation. For diffusion controlled growth of N pre-existing precipitates $\beta = 3/2$ and for nucleation controlled growth $\beta = 5/2$.

$$f_v/f_{vmax} \approx 1 - \exp[-4.19\psi_s(X_{so}/X_{sp})^{1/2}N(D^*t)^{3/2}] \tag{2.4a}$$

$$f_v/f_{vmax} \approx 1 - \exp[-4.19\psi_s(X_{so}/X_{sp})^{1/2}N(K\phi t)^{3/2}] \tag{2.4b}$$

Here X_{so} is the initial concentration of the controlling solute (e.g., Cu), $\psi_s \approx \ln(X/X_{se})$ is a thermodynamic term to account for the solute activity coefficient in terms of its equilibrium solubility (X_{se}), and X_{sp} is the amount of rate controlling solute in the precipitate. Note Eq. 2.4 ignores the Gibbs-Thomson effect, and ψ_s at the precipitate interface is taken as being negligible; and the RED K is assumed to be constant. Thus the physical factors governing ϕ_{to} are

$$\phi t_o = [4.19\psi_s X_{so}/X_{sp})^{1/2} N K^{3/2}]^{-1} \quad (2.5)$$

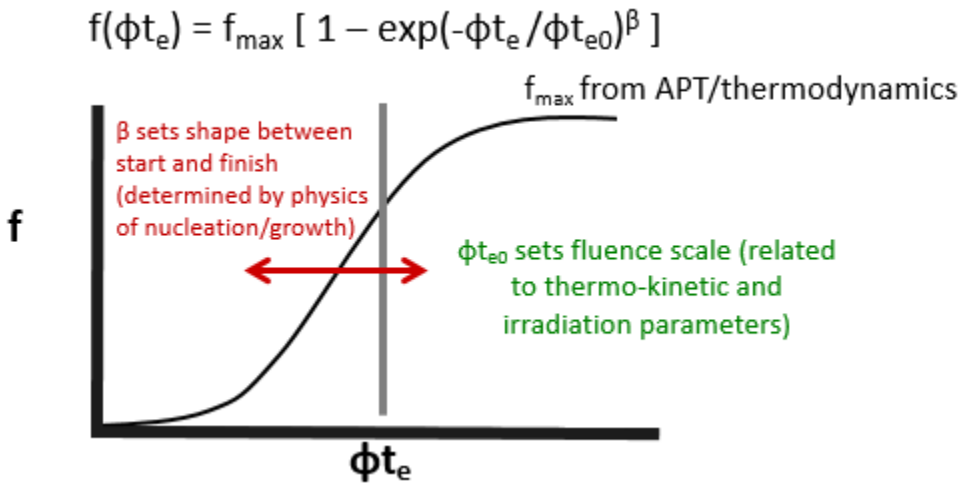

Figure 2.8. Simplest form of the Avrami model as a function of flux-adjusted effective fluence (ϕt_e).

The Avrami model in Figure 2.8 can be generalized for other types of precipitation kinetics. The exponent β controls the shape of the Avrami curve, as mediated by the underlying physics. As earlier stated, β = 5/2 for a constant continuous nucleation rate, rather than the 3/2 for diffusional growth of pre-existing precipitates. Other Avrami model complications are that the Gibbs-Thomson effect is important at small sizes <d>, the RED K decreases with ϕt due to the buildup of defect sinks, and precipitation of solute vacancy traps. Thus, in practice β, ϕt_o and f_{vmax} are fitting parameters that give some indication of the underlying precipitation mechanisms. Further, as an alternative to simple analytical Avrami model forms, the precipitate f_v/f_{vmax} growth equations can be numerically integrated to include all of the physics noted above, including ϕt-dependent processes. The precipitate f_{vmax} and β depend on the alloy composition, and can be measured or computed from Calphad thermodynamic data, modified for the Gibbs Thomson effect.

A single Avrami equation is needed to model the evolution of the MNSP f_v in low Cu steels. Two Avrami equations are needed to model the precipitate CRP + MNSP evolutions in Cu bearing steels, since the β, f_{vmax} and ϕt_o are different for CRPs and MNSPs. For example, Figure 2.9 shows Avrami model fits to CRP and MNSP f_v in a 0.4 Cu 1.3 Ni 1.4 Mn steel (LD). Since the data are for a wide range of ϕ and ϕt the results are plotted on an $\sqrt{\phi t_e}$ scale, using p = 0.25. The f_v can be used to calculate the corresponding $\Delta\sigma_y$ and ΔT (see Chapter 8).

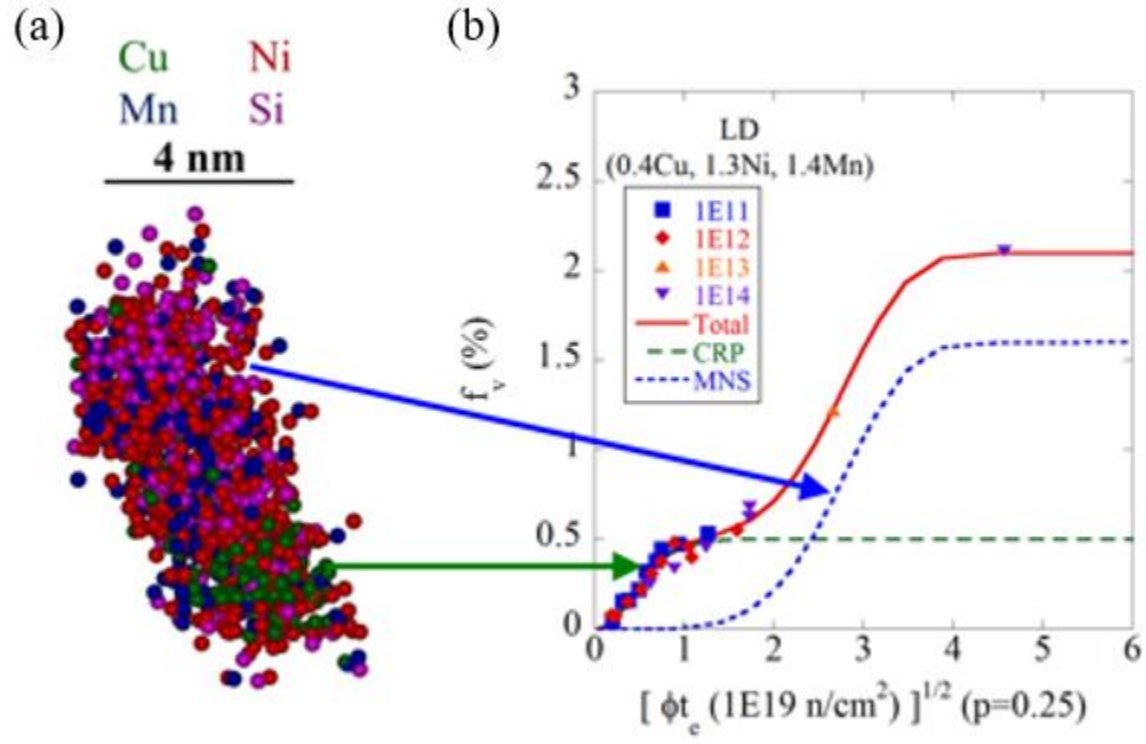

Figure 2.9. a) APT shows solute atoms form a CRP core and a primarily MNSP appendage structure in a 0.4 Cu 1.3 Ni 1.4 Mn steel (LD). b) Two-term Avrami model fits to CRP (green dashed line) and MNSP (blue dashed line) f_v. Since the data are for a wide range of ϕ and ϕt the results are plotted on a $\sqrt{\phi t_e}$ scale, using a scaling factor p = 0.25 [23,26,52].

Chapter 3: Materials and Methods[1]

Introduction

This chapter describes the UCSB ATR-2 irradiation experiment design, the international consortium of participants who provided funding and specimens, and ATR-2 specimen geometries. The benefits and challenges of complementary charged particle irradiations are briefly outlined. Then, the compositions and irradiation conditions of surveillance steels, UCSB split-melt steels and Advanced Steel Matrix studied are detailed in tables and text. Finally the array of mechanical property and microstructural characterization techniques required to characterize radiation damage in RPV steels are presented. The microhardness, tensile, and shear punch testing test methods were used to measure the baseline and irradiated mechanical properties. These values were correlated to microstructure through various microstructural characterization techniques. This chapter concludes on a condensed description of Atom Probe Tomography (APT), Energy Dispersive X-Ray Spectroscopy (EDS) and Small Angle Neutron Scattering (SANS) followed by their respective test procedures and reconstruction methods.

3.1 The UCSB ATR-2 Irradiation and Post Irradiation Examination (PIE) Program

The main challenge associated with the development of an extended life embrittlement prediction model is that there is very little surveillance data at high fluence. To address this

[1] This chapter includes slightly modified text and figures published in G.R. Odette, P.B. Wells, N. Almirall, T. Yamamoto, K. Fields, D. Gragg, R. K. Nanstad, M. A. Sokolov, J. P. Robertson, Update on the Advanced Test Reactor 2 Reactor Pressure Vessel Steel High Fluence Irradiation Project, Light Water React. Sustain. Program (2016).

issue, a large-scale irradiation designed to reach a peak fluence of > $1x10^{20}$ n/cm^2 at an intermediate flux of ≈ $3.7x10^{12}$ n/cm^2 was carried out in the Advanced Test Reactor (ATR) at the Idaho National Laboratory (INL) [61,62]. The irradiation was proposed by the University of California, Santa Barbara (UCSB) in 2008 and awarded by NSUF in 2009.

The UCSB ATR-2 irradiation began in June of 2011 and was completed in January 2014. Specimens were delivered to Oak Ridge National Laboratory (ORNL) hot cells in August of 2015. The ATR-2 program involves an international consortium of participants including UCSB, ORNL, Rolls Royce (RR) in the United Kingdom, the Electric Power Research Institute (EPRI), the Central Research Institute for the Electric Power Industry (CRIEPI) in Japan and Bechtel Marine Propulsion Corporation (BMPC). A number of US utilities also contributed surveillance steels to the ATR-2 irradiation.

UCSB and INL collaborated in the conceptual design of the irradiation test train. INL carried out the corresponding detailed engineering design and safety analysis, ultimately constructing and assembling a test train composed of the 13 thin-walled cups loaded at UCSB. INL conducted the subsequent ATR irradiation. Preparatory work at UCSB was funded by DOE NEUP, NSUF and LWRSP (via ORNL) programs. The PIE was funded by a residual NEUP grant, some remaining NSUF bridging funds, and primarily by the LWRSP via ORNL. RR and EPRI are providing funding for a new alloy matrix and some surveillance steels, respectively. BMPC and CRIEPI funded the PIE on steels that they contributed to the irradiation.

The test assembly included a thermal neutron shield and active temperature control in three zones for irradiations at nominal temperatures of ≈ 270, 290, and 310°C, plus one smaller zone at ≈ 250°C. The majority of the 172 RPV alloys in the experiment were provided by

UCSB. ORNL and their subcontractor ATI Consulting acquired some surveillance steels. Other alloys were contributed by BMPC and CRIEPI. Notably, RR, who was a founding participant in the ATR-2 program, also provided 50 new alloy compositions, the so-called Advanced Steel Matrix (ASM). The ASM focuses on developing new, advanced high Ni steels and filling critical gaps in the database for existing vessels. A large number of other surveillance steels from various operating nuclear reactors were also included to enable a direct comparison between them and the intermediate flux ATR-2. A complete summary of ATR-2 specimen matrices, irradiation conditions and alloy chemistry can be found in Materials and Methods and Appendix B.

UCSB fabricated and loaded 1,625 small specimens into the 13 thin walled-cups. The specimens included ≈ 400 sub-sized tensile specimens (SSJ-2 type), 1150 disc multipurpose coupons (DMC), and 50 disc compact tension (DCT) fracture specimens. The ATR-2 fluence ranged from $\approx 5 \times 10^{19}$ to 1.4×10^{20} n/cm^2. Note, not all the irradiation temperatures covered this entire fluence range, and the overall emphasis was on the 290°C condition. In this case, the target fluence ranged from approximately 60 to 120 years of LWR operation and bridges a flux-fluence gap in the UCSB databases, as shown in Figure 3.1, which is needed to better understand extended life embrittlement.

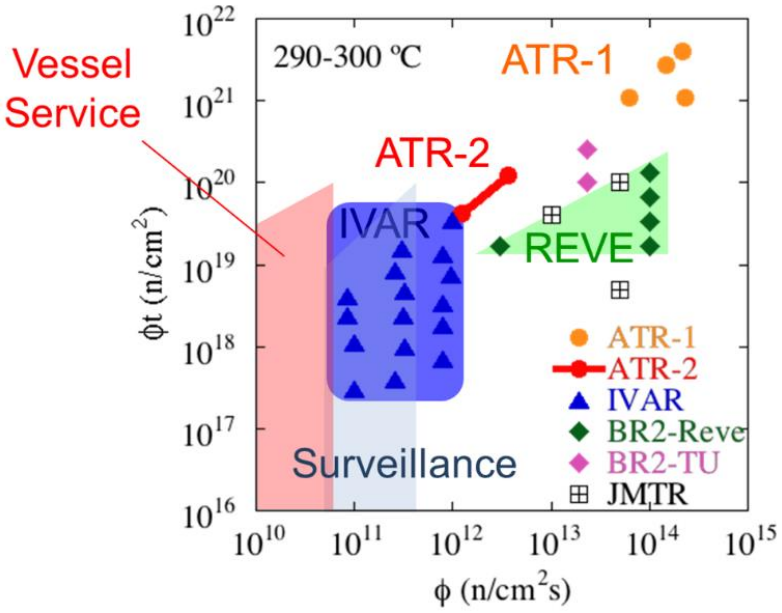

Figure 3.1. A ϕ - ϕ t map showing various UCSB databases.

The sub size tensile (SST), microhardness (μH), shear punch test (SPT) were carried out on all the ATR-2 alloys. A wide variety of microstructural characterization studies included: (a) small angle neutron scattering (SANS); (b) small angle x-ray scattering (SAXS) and x-ray diffraction (XRD); (c) atom probe tomography (APT); and (f) transmission electron microscopy (TEM). This suite of advanced characterization tools was used to identify the detailed nature of various irradiation induced hardening features, especially late blooming phases. The UCSB ATR-2 irradiation test assembly was completed in late spring of 2011 and was successfully installed in the ATR on May 26, 2011. The entire test assembly was shipped to ORNL in August 2015 and post irradiation examination (PIE) of the specimens began shortly thereafter.

In summary, a variety of relatively small specimens of many different RPV steels were irradiated in UCSB ATR-2 over a range of conditions. The specimens will be used to characterize both irradiation hardening and the underlying hardening microstructure. Most of

these steels have been irradiated and tested in previous test reactor and surveillance programs over a wide range of ϕ, ϕ t and T_i conditions. The combined databases will support the continued development of reduced order Avrami-type fitting models linked to detailed, physical thermo-kinetic models which treat CRP and MNSP evolution as a function of flux, fluence, T_{irr}, and alloy composition [29, 39].

The average ϕ, ϕt and T_i (target and as run) for each cup are given in Table 3.1. Except for the two bottom and two top cups, the as-run temperatures were very close to their target values. Details regarding determining the flux and temperature profiles in ATR-2 can be found in the INL as-run reports and Appendix B [61,62].

Table 3.1. Neutron ϕ, ϕ t (E > 1 MeV) and T_i for the cups in the ATR-2 irradiation. Bold text indicates the primary focus in this research are the highest fluence Cups 7&8.

Cup	ϕ (10^{12} n/cm^2-s)	ϕ t (10^{19} n/cm^2)	Target T_i (°C)	Actual T_i (°C)
1	1.34	5.11	290	247
2	1.94	7.43	290	268
3	2.54	10.35	290	280
4	3.13	11.90	270	268
5	3.36	12.80	250	255
6	3.58	13.70	290	285
7	**3.64**	**13.90**	**290**	**291**
8	**3.60**	**13.70**	**290**	**293**
9	3.47	13.20	290	293
10	3.21	12.30	310	319
11	2.89	11.05	290	292
12	2.17	9.08	290	264
13	1.52	5.79	290	238

3.2 Charged Particle Irradiations (CPI)

NI of RPV steels to study embrittlement at high, extended life ϕt are costly and time-consuming. In contrast, charged particle irradiations (CPI) can be used to rapidly explore the effects of embrittlement variables and mechanisms, typically taking tens of hours to produce 80-year NI damage doses, in units of dpa [63–65]. The charged particle is typically a medium weight ion like Fe^{++}. Heavy ion CPI do not produce radioactive byproducts, thus samples can be handled without any special safety procedures. While they do not simulate neutron embrittlement, CPI provide a rapid and cost effective way to gain insight into precipitation mechanisms. Further, CPI can help to determine which new RPV steel compositions are most likely to be susceptible to the formation of large f_v of MNSPs, thus helping to guide future advanced RPV steel development. The CPI were carried out at the Dual Beam Facility for Energy Science and Technology (DuET) at Kyoto University and the High Fluence Irradiation Facility (HIT), at the University of Tokyo facility in Japan.

3.3 Materials

A total of 172 alloys were included in the ATR-2 irradiation. These can broadly be split into 7 groups: UCSB split-melt steels, UCSB simple model alloys, program alloys that have been included in other irradiations acquired by UCSB, UCSB and EPRI acquired surveillance steels, and the RR, CRIEPI and BMPC matrices. Each alloy matrix has a particular set of goals. The UCSB split melt steel matrix contains alloys with systematic variations in the main solute elements that dictate a material's sensitivity to irradiation embrittlement: Cu, Ni, Mn and P. The surveillance alloys enable direct comparison of irradiation hardening at the intermediate test reactor ATR-2 flux with that for irradiations at much lower flux surveillance conditions. The RR matrix includes alloys that contain a much wider range of Ni and Mn contents than

has previously been studied to develop better alloys for future RPV applications. The CREIPI and BMPC irradiations involve a smaller set of steels, but share generally similar objectives. The focus here is on the UCSB split-melt steels and surveillance alloys.

3.3.1 UCSB Split Melt and Model Alloys

The UCSB matrix includes 34 split-melt steels (SMS) with systematic variations in Cu, Ni and Mn contents to investigate the individual and combined effects of these solutes. The SMS were processed and have microstructures and properties that are typical of A-533B steels used in RPVs. The heat treatments can be found in Table 3.2. The SMS include the L and CM series, based on their supplier. The L and CM series are similar, but the CMs have a slightly larger base Mn content and a wider range of Ni. The compositions of a subset of the SMS, that was included as tensile specimens are given in Table 3.2. In addition to the SMS, 11 simple model ferritic alloys variously containing only Cu, Ni, Mn, Si and Mo were also included in the experiment, though have not been tested yet.

3.3.2 Surveillance and Program Alloy Matrix

Early recognition of the potential importance of RPV embrittlement led to including vessel wall-mounted surveillance capsules in most US and international reactor vessels, nominally containing the most sensitive plant specific steels. Sets of surveillance steel CVN specimens, irradiated at a somewhat higher neutron flux than the vessel itself, are periodically removed and tested, to provide an estimate of the ΔT that the RPV will experience at a later time. Nine surveillance materials were procured specifically for ATR-2. In addition, eleven other archival surveillance alloys, which had been previously studied by UCSB in the Irradiation Variables Program (IVAR), were also included for a total of twenty-two surveillance alloys. While flux effects have been extensively studied for many years, they are

still not fully understood. Thus, the surveillance alloys will allow for direct comparison of results from this high-flux test irradiation with those from the much lower flux surveillance irradiations. The compositions of the surveillance alloys are given in Table 3.3. Finally, a number of program plates and welds that have been in a number of other irradiations were also included. The composition of the program alloys is given in Table 3.4.

3.3.3 Advanced Steel Matrix (ASM)

RPV steels in US light water reactors (LWR) have typical alloy compositions (wt.%) ranging from ≈ .02 to 0.4Cu, 0.2 to 1.0Ni, 1.0 to 1.8 Mn, and 0.1 to 0.5 Si. Rolls Royce (RR) supplied a new advanced steel matrix (ASM) to the ATR-2 experiment with a much wider range of solute contents than in typical US RPV steels. The purpose of this matrix is twofold. First, the wide range of compositions in these alloys will improve the understanding of the synergistic relationships among the various solutes. Second, this matrix will assist in the development of new alloys for future light water reactors. High Ni steels have a number of attractive attributes, like higher unirradiated strength and toughness than conventional RPV steels, but are potentially more susceptible to irradiation embrittlement due to the strong correlation between alloy Ni content and MNSP formation. Figure 3.2 shows the ranges of compositions explored in previous UCSB irradiations (blue box) and the ATR-2 irradiation (red box) due to the addition of the ASM (blue points).

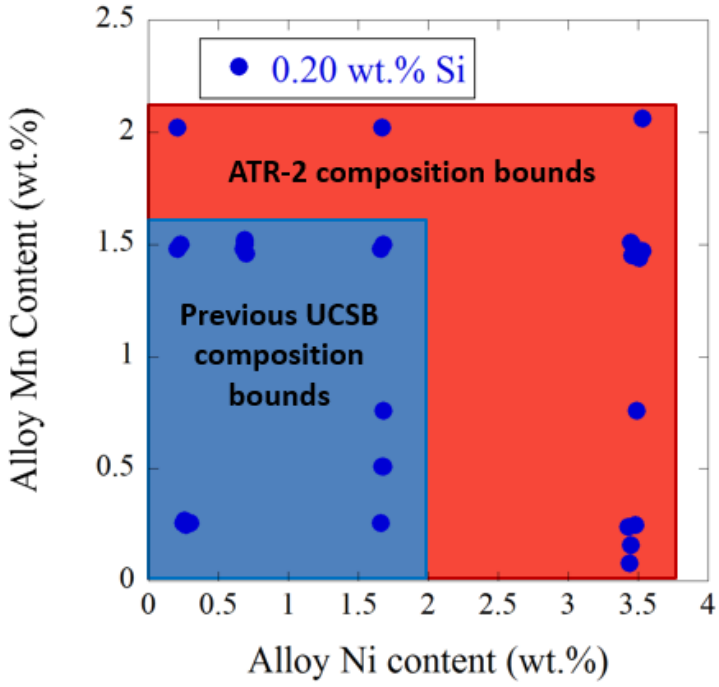

Figure 3.2. Range of Mn and Ni contents for all ASM alloys with 0.20 wt.% Si (blue dots), along with boxes showing the range of compositions explored in previous UCSB irradiation experiments (blue box) and the in ATR-2 irradiation (red box).

Table 3.2. The composition (wt.%) of the steels in the UCSB split melt matrix.

Alloy Code	Cu	N	Mn	Cr	Mo	P	C	S	Si	Fe
LB	0.40	0.18	1.35	0.06	0.53	0.005	0.16	0.005	0.22	97.10
LC	0.41	0.86	1.44	0.06	0.55	0.005	0.14	0.008	0.23	96.30
LD	0.38	1.25	1.38	0.06	0.53	0.005	0.19	0.015	0.23	96.02
LG	0.01	0.74	1.37	0.05	0.55	0.005	0.16	0.005	0.22	96.90
LH	0.11	0.74	1.39	0.09	0.55	0.005	0.16	0.005	0.24	96.72
LI	0.20	0.74	1.37	0.09	0.55	0.005	0.16	0.005	0.24	96.65
LJ	0.42	0.81	1.34	0.05	0.56	0.005	0.13	0.005	0.13	96.56
CM3	0.02	0.85	1.60	0.00	0.49	0.006	0.13	0.000	0.16	96.74
CM5	0.02	0.86	1.61	0.04	0.53	0.050	0.15	0.000	0.16	96.58
CM6	0.02	1.68	1.50	0.05	0.54	0.007	0.15	0.003	0.17	95.88
CM7	0.00	1.70	1.55	0.05	0.56	0.047	0.16	0.003	0.17	95.76
CM9	0.01	0.86	0.85	0.04	0.55	0.003	0.15	0.003	0.15	97.38
CM10	0.02	0.88	1.66	0.05	0.53	0.008	0.16	0.004	0.17	96.52
CM11	0.34	0.85	1.64	0.02	0.53	0.006	0.15	0.003	0.18	96.28
CM16	0.22	0.82	1.58	0.00	0.51	0.004	0.16	0.000	0.25	96.46
CM17	0.22	1.59	1.54	0.00	0.50	0.004	0.16	0.000	0.25	95.74
CM19	0.42	0.85	1.63	0.01	0.51	0.005	0.16	0.003	0.16	96.25
CM20	0.43	1.69	1.63	0.02	0.50	0.006	0.16	0.003	0.16	95.40
CM22	0.42	0.84	0.84	0.02	0.56	0.002	0.14	0.003	0.14	97.04
CM31	0.01	0.80	1.65	0.05	0.51	0.006	0.16	0.003	0.17	96.64

*L heat treatment: 900°C/1hr austenitize, air cool, 664°C/4hr temper, air cool, 600°C/40hr stress relief, air cool. CM heat treatment: 900°C/30min austenitize, salt quench to 450°C/hold for 10min, 660°C/4hr temper, air cool, 607°C/24hr stress relief, cool at 8°C/hr to 300°C, air cool.

Table 3.3. The composition (wt.%) of the steels in the surveillance matrix.

Alloy	Cu	Ni	Mn	Cr	Mo	P	C	S	Si	Fe
SB1*	0.20	0.60	1.33	0.11	0.49	0.005	0.22	0.016	0.23	96.82
SB2*	0.06	0.75	0.79	0.35	0.58	0.010	0.20	0.009	0.28	96.97
SB3*	0.05	0.56	1.32	0.08	0.59	0.010	0.24	0.016	0.24	96.89
SW1*	0.14	0.19	1.06	0.06	0.50	0.016	0.13	0.009	0.27	95.90
SW2*	0.36	0.78	1.42	0.04	0.49	0.013	0.18	0.011	0.18	96.54
SW3*	0.22	0.72	1.37	0.09	0.48	0.016	0.12	0.011	0.20	96.77
SW4*	0.03	0.90	0.94	0.03	0.23	0.004	0.14	0.014	0.32	97.39
SW5*	0.04	0.95	1.41	0.13	0.48	0.009	0.09	0.009	0.45	96.44
SW6*	0.29	0.60	1.44	0.14	0.36	0.014	0.10	0.011	0.50	96.55
SW7*	0.24	0.54	1.70	0.06	0.43	0.014	0.09	0.016	0.56	96.35
SW8*	0.24	0.56	1.68	0.07	0.40	0.014	0.09	0.016	0.55	96.38
SW9*	0.28	0.63	1.59	0.08	0.43	0.011	0.09	0.015	0.51	96.36
SW10*	0.22	0.07	1.37	0.16	0.46	0.014	0.13	0.016	0.29	97.27
SW11*	0.19	1.02	1.30	0.05	0.51	0.017	0.11	0.015	0.18	96.61
SW12*	0.20	1.20	1.31	0.04	0.54	0.010	0.11	0.017	0.18	98.64
WA	0.21	0.63	1.69	0.14	0.40	0.014	0.08	0.013	0.45	96.37
WB	0.28	0.69	1.63	0.10	0.40	0.018	0.09	0.009	0.54	96.52
WC	0.06	0.62	1.30	0.08	0.31	0.009	0.08	0.010	0.37	97.22
W62	0.23	0.60	1.61	0.12	0.39	0.016	0.08	0.007	0.59	96.59
W63	0.3	0.69	1.65	0.10	0.43	0.016	0.10	0.011	0.63	96.37
W65	0.22	0.60	1.45	0.09	0.39	0.015	0.08	0.015	0.48	96.88
W67	0.18	0.61	1.27	0.14	0.43	0.009	0.10	0.009	0.50	97.99

*Procured by ORNL and ATI Consulting

Table 3.4. The composition (wt.%) of other program steels.

Alloy	Cu%	Ni%	Mn%	Cr%	Mo%	P%	C%	S%	Si%	Fe%
EA	0.20	0.11	1.47	0.05	0.52	0.013	0.23	0.024	0.26	97.12
EC	0.35	0.60	1.30	0.04	0.44	0.005	0.16	0.009	0.17	96.93
ED	0.40	0.60	1.36	0.04	0.44	0.006	0.12	0.013	0.51	96.51
FE	0.01	1.69	1.30	0.02	0.51	0.009	0.21	0.006	0.20	96.05
W73	0.31	0.60	1.56	0.25	0.58	0.017	0.10	0.005	0.45	96.44
WM	0.27	0.57	1.61	0.10	0.41	0.017	0.08	0.007	0.62	96.59
HSST02	0.14	0.67	1.55	0.04	0.53	0.009	0.23	0.014	0.20	96.62
A302B	0.14	0.20	1.20	0.24	0.60	0.02	0.20	0.017	0.28	97.39
A508	0.03	0.8	0.74	0.36	0.59	0.015	0.20	0.005	0.026	97.47
JRQ	0.14	0.82	1.40	0.12	0.50	0.019	0.18	0.004	0.25	98.61

Table 3.5. The composition (wt.%) of Advanced Steel Matrix alloys.

Alloy	Cu%	Ni%	Mn%	Cr%	Mo%	P%	C%	Si%	Fe%
A1	0.06	0.30	0.26	0.10	0.49	0.005	0.21	0.21	98.37
A2	0.06	0.27	0.25	0.11	0.49	0.006	0.15	0.20	98.46
A3	0.06	0.27	0.25	0.10	0.52	0.004	0.07	0.20	98.53
A4	0.06	0.26	0.26	0.11	0.53	0.006	0.20	0.62	97.95
A5	0.06	0.27	0.25	0.10	0.52	0.005	0.20	0.05	98.55
A6	0.20	0.25	0.26	0.10	0.52	0.006	0.20	0.22	98.24
A7	0.58	0.25	0.25	0.10	0.53	0.005	0.23	0.20	97.86
A8	0.06	0.25	0.26	0.10	0.52	0.035	0.21	0.20	98.37
A9	0.58	0.25	0.26	0.10	0.52	0.033	0.21	0.21	97.84
A10	0.06	3.53	1.47	0.10	0.48	0.008	0.27	0.22	93.86
A11	0.06	3.49	1.46	0.10	0.52	0.005	0.16	0.20	94.01
A12	0.06	3.51	1.44	0.10	0.52	0.005	0.05	0.20	94.12
A13	0.07	3.49	1.48	0.10	0.52	0.005	0.23	0.63	93.48
A14	0.06	3.44	1.48	0.10	0.52	0.006	0.22	0.03	94.14
A15	0.31	3.47	1.48	0.10	0.52	0.008	0.21	0.20	93.70
A16	0.60	3.46	1.50	0.10	0.52	0.004	0.22	0.20	93.40
A17	0.06	3.45	1.51	0.10	0.50	0.029	0.23	0.20	93.92
A18	0.59	3.44	1.50	0.10	0.50	0.029	0.21	0.20	93.43
A19	0.06	1.66	0.26	0.13	0.52	0.008	0.23	0.20	96.93
A20	0.06	1.66	0.26	0.10	0.52	0.005	0.07	0.20	97.13
A21	0.06	1.66	0.26	0.10	0.52	0.005	0.23	0.05	97.12
A22	0.06	1.68	1.50	0.10	0.52	0.006	0.29	0.21	95.63
A23	0.06	1.66	1.48	0.10	0.50	0.006	0.06	0.21	95.92
A24	0.06	1.71	1.51	0.10	0.50	0.005	0.26	0.59	95.27
A25	0.06	1.68	1.50	0.10	0.50	0.004	0.05	0.63	95.48
A26	0.05	3.48	0.25	0.10	0.52	0.009	0.26	0.19	95.14
A27	0.06	3.43	0.24	0.10	0.52	0.003	0.06	0.20	95.39
A28	0.06	3.47	0.25	0.10	0.52	0.006	0.27	0.62	94.70
A29	0.06	3.48	0.26	0.10	0.52	0.004	0.05	0.62	94.91
A30	0.06	0.21	2.02	0.10	0.52	0.004	0.19	0.20	96.70
A31	0.06	1.67	2.02	0.10	0.53	0.005	0.21	0.20	95.21
A32	0.06	3.53	2.06	0.13	0.53	0.010	0.22	0.23	93.23
A33	0.06	3.45	0.16	0.10	0.52	0.005	0.22	0.20	95.29
A34	0.07	3.44	0.08	0.09	0.52	0.006	0.22	0.19	95.38
A35	0.06	0.23	1.50	0.11	0.49	0.007	0.27	0.21	97.12
A36	0.06	0.23	1.50	0.11	0.49	0.007	0.27	0.21	97.12
A37	0.06	0.21	1.48	0.10	0.52	0.005	0.06	0.21	97.36
A38	0.06	0.21	1.49	0.10	0.52	0.007	0.27	0.62	96.72
A39	0.06	0.21	1.48	0.10	0.52	0.003	0.05	0.59	96.99
A40	0.04	0.70	1.46	0.11	0.49	0.004	0.21	0.21	96.78
A41	0.12	0.69	1.52	0.10	0.52	0.005	0.20	0.20	96.65
A42	0.04	0.69	1.50	0.10	0.52	0.015	0.20	0.21	96.73
A43	0.08	0.68	1.48	0.10	0.52	0.017	0.23	0.19	96.70
A44	0.13	0.69	1.51	0.10	0.52	0.021	0.21	0.21	96.61
A45	0.06	0.26	0.27	2.28	0.52	0.003	0.21	0.20	96.20
A46	0.06	3.46	1.45	2.34	0.52	0.006	0.21	0.20	91.75
A47	0.06	1.68	0.76	0.10	0.50	0.005	0.28	0.21	96.41
A48	0.07	3.49	0.76	0.10	0.50	0.003	0.28	0.21	94.59
A49	0.06	1.67	0.51	1.21	0.50	0.005	0.22	0.20	95.63
A50	0.06	1.68	0.51	2.32	0.51	0.003	0.23	0.20	94.49

3.4 Methods

3.4.1 Mechanical Property Testing

Vickers Microhardness Testing (μHv)

Vickers microhardness (μH) testing was carried out in the Low Activation Materials Development and Analysis Laboratory (LAMDA) at Oak Ridge National Laboratory and at UCSB. A LECO 400 series microhardness tester with digitized image analysis was used to make 5 indents per specimen, see Figure 3.3. A square-base diamond-pyramid indenter was used with a 500g load and a 10 second dwell time. Both diagonal lengths of the indents were measured and the average value of the two was used to determine the microhardness. Prior to each test series the system is recalibrated/validated by measuring five indents on a certified hardness calibration block.

The mean and standard deviation microhardness were determined for the unirradiated baseline and irradiated condition. The difference, or ΔHv (kg/mm2), was determined by subtracting the baseline from the irradiated value. The standard deviation in ΔHv was determined by a root sum square of the standard deviations of the baseline and irradiated microhardness measurements. Changes in μH_v were used to estimate the corresponding

changes in yield stress ($\Delta\sigma_y$) based on a nominal relation, $\Delta\sigma_y$ (MPa) = 3.33*$\Delta\mu H_v$ (kg/mm^2) [66].

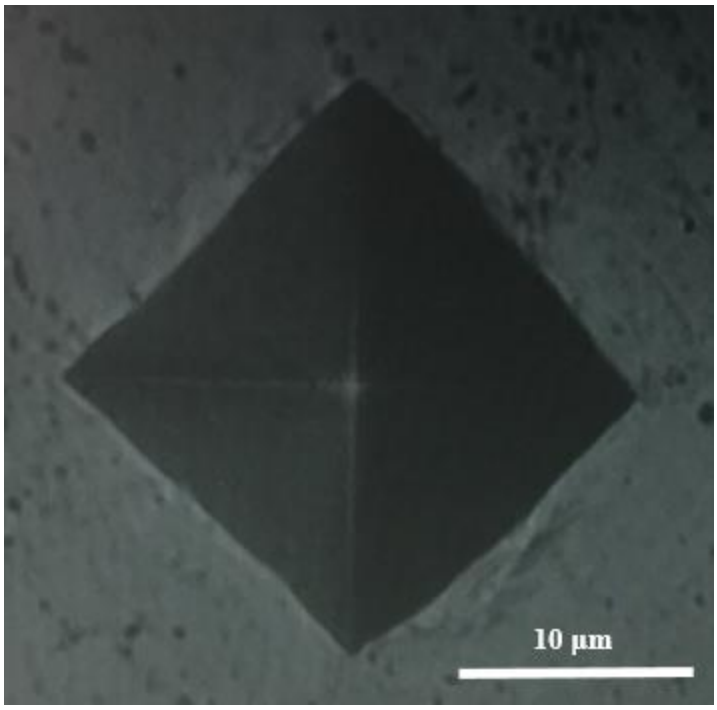

Figure 3.3. Vickers pyramid impression on an RPV steel as viewed through an optical microscope.

Tensile Testing

SSJ-2 type tensile specimens, shown in Figure 3.4, are nominally 16 mm long with a gauge section width of 1.2 mm and thickness of 0.5 mm. It should be noted that approximately half of the specimens have a nominal gauge length of 5.0 mm, while the others have a 2.2 mm gauge length. No significant differences in the tensile properties have been observed between the two gauge lengths. Groups of ≈ 18 specimens were loaded in boxes designed to maximize heat transfer.

The dog-bone tensile specimens are clamped by grips in an alignment fixture prior to placement in on an MTS 810 load frame. The specimens were loaded at a rate of 0.008 mm/s at strain rates of 0.002 to 0.003/min. Standard engineering stress-strain curves are recorded

based on precise measurements of the width and thickness of the gauge section of individual specimens. A best fit to the elastic loading region is used to establish the 0.2% offset yield stress ($\sigma_y \approx s_y$). The ultimate engineering stress (s_u) at maximum load is also recorded. The tensile tests on irradiated specimens are generally stopped at a load that is ≈ 70% of the maximum to keep the specimen intact. An example stress-strain curve, with a 0.2% offset line is shown in Figure 3.5.

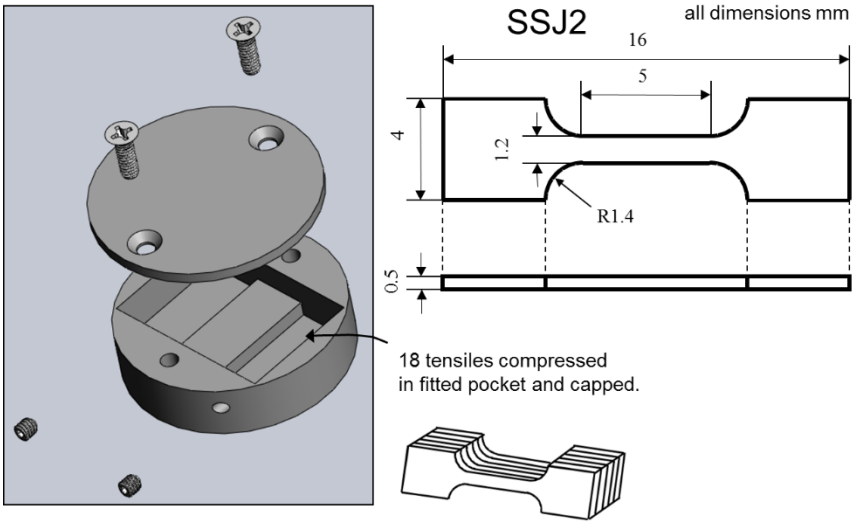

Figure 3.4. Schematic of the tensile loading box (left) and SSJ-2 tensile specimens (right). Note that half of the specimens have a gauge length of 5.00 mm (showed), while the others have a 2.2 mm gauge length.

The focus of tensile testing thus far has been on the two highest ϕt ($\approx 1.38 \times 10^{20}$ n/cm^2) conditions at 290°C, cups 7 and 8. Three or more unirradiated (control) specimens were tested to establish the baseline yield stress (σ_{yu}) and ultimate engineering tensile stress (s_{uu}), and used to determine the corresponding irradiation hardening ($\Delta\sigma_y$ and Δs_u).

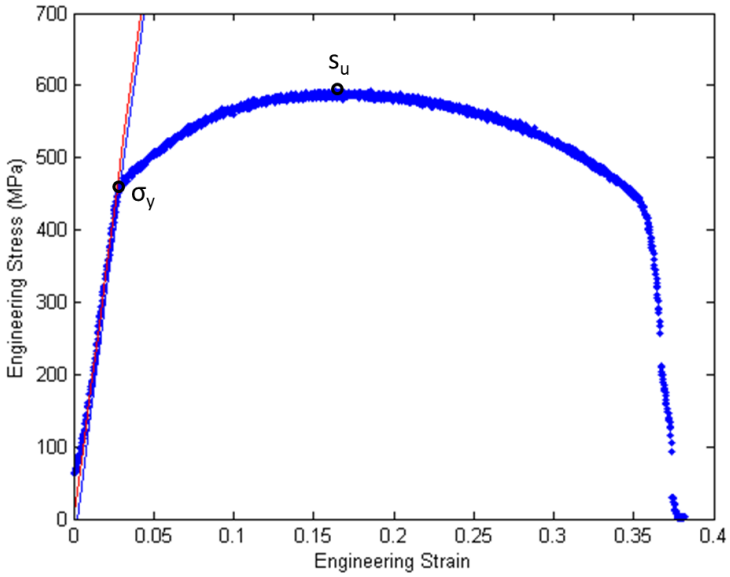

Figure 3.5. Example stress-strain curve with 0.2% offset line.

Shear Punch Testing

The majority of specimens (≈ 1000 out of 1625) in ATR-2 are 20 mm diameter x 0.5 mm thick discs DMCs. The DMCs were included for all the alloys because they permit a wide range of PIE studies on a single specimen based on a sequence of tests, such as shear punch tests, μH and a host of microstructural characterization methods. The effects of irradiation on constitutive properties was obtained from shear punch tests (SPT) on the DMCs with minimal specimen preparation. The load-displacement data from SPT has been used to derive true-stress, true-strain (σ-ε) data. However, here SPT is used to measure the shear yield stress (τ_y) and its relation to σ_y. A previously established relation, of $\sigma y \approx 1.77 \tau y$, is close to the theoretical Von Mises value of $\sqrt{3}$. To facilitate DMC testing, we have developed an automated SPT apparatus that is briefly described in the next section. However, in this thesis, SPT were conducted using a simpler single specimen punch fixture. The SPTs were carried out on 10

unirradiated surveillance steels and four unirradiated RR alloys that span a wide range of σy. The test fixture is shown in Figure 3.6. These tests were carried out as part of qualification and calibration of the automated SPT apparatus. The basic premise of a shear punch test is very similar to a tensile test. A specimen is clamped tightly in a fixture with a punch above it and a die below. The punch and die are precision machined and aligned to have optimal diametrical clearance. A measured load is applied to the top of the punch, while the backside displacement of the extruded disc blank being sheared is measured with a lever arm displacement meter. The displacement increases until the punched disc is injected into the die.

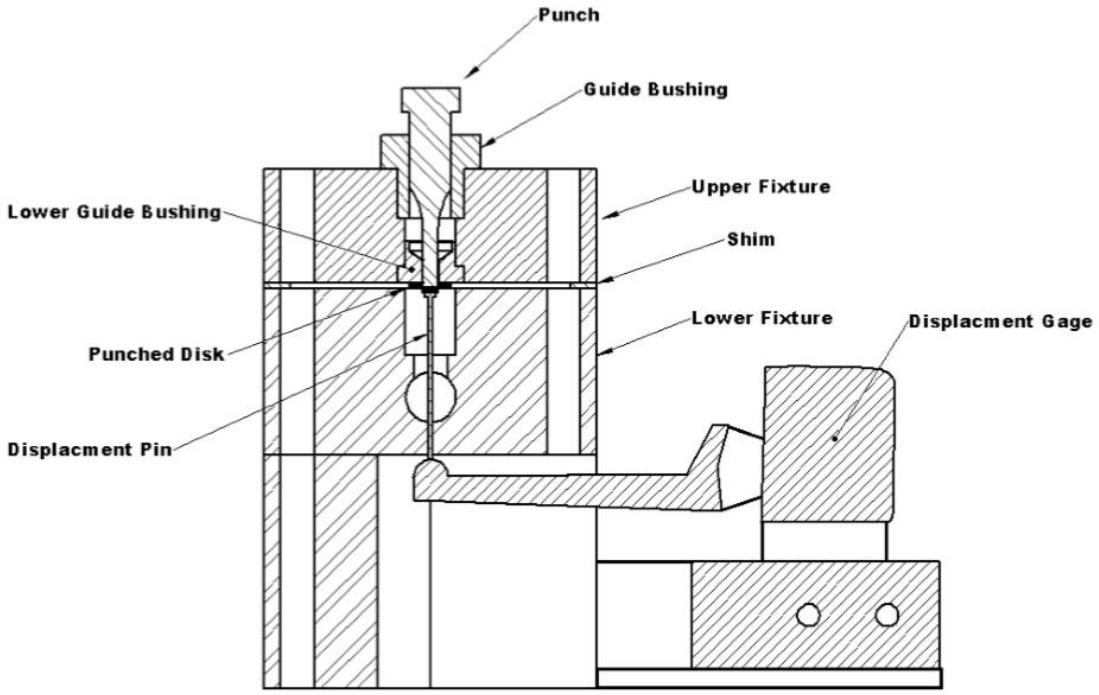

Figure 3.6. Schematic of the single specimen punch shear punch tester. The shear stress is calculated based on punch load (P), the average of the punch and die diameter (D), and specimen thickness (t) as $\tau = P/(\pi Dt)$.The shear strain (es) is defined by dividing the measured backside displacement by the DMC thickness. Thus, the measured load and displacement can be converted to shear stress and strain. A typical shear punch curve is shown in Figure 3.7 [9].

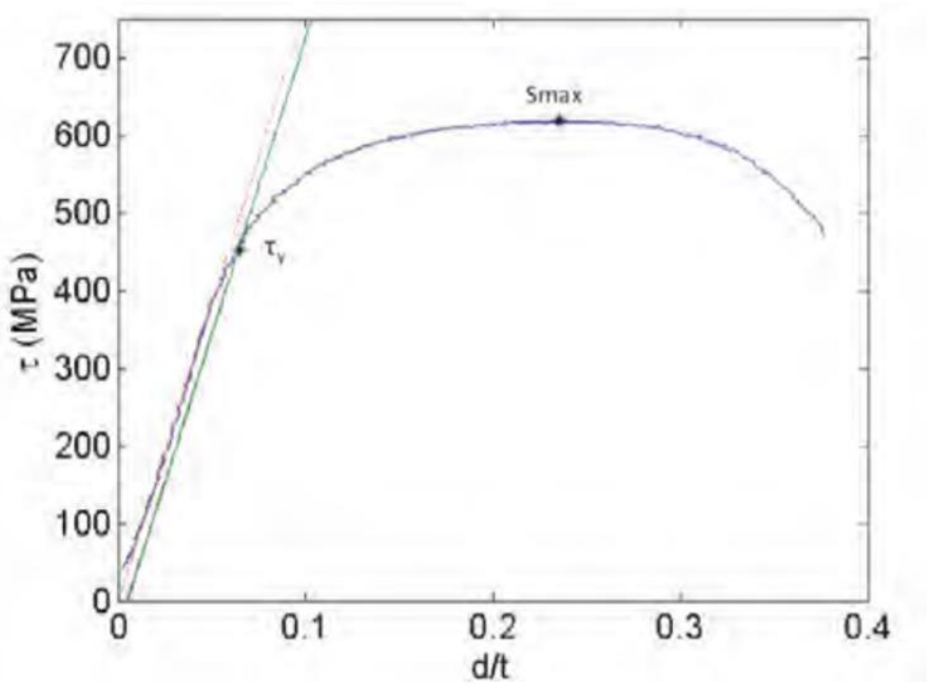

Figure 3.7. A typical shear punch curve [9].

As in a tensile test, the quasi-linear elastic region is fit and a 0.2% offset parallel line is used to index the shear yield stress (τ_y). For ideal shear dominated conditions, the theoretical relation between τ_y and the uniaxial yield stress (σy) is given by the von Mises yield criterion as $\sigma_y = \tau_y\sqrt{3}$. A best fit empirical correlation developed by UCSB on the Rolls Royce steels found $\sigma_y \approx 1.78\tau y$, within ≈ 2.5% of the theoretical relation [9]. A plot of σ_y versus τ_y for these RPV steels with a wide range of yield stress is shown in Figure 3.8.

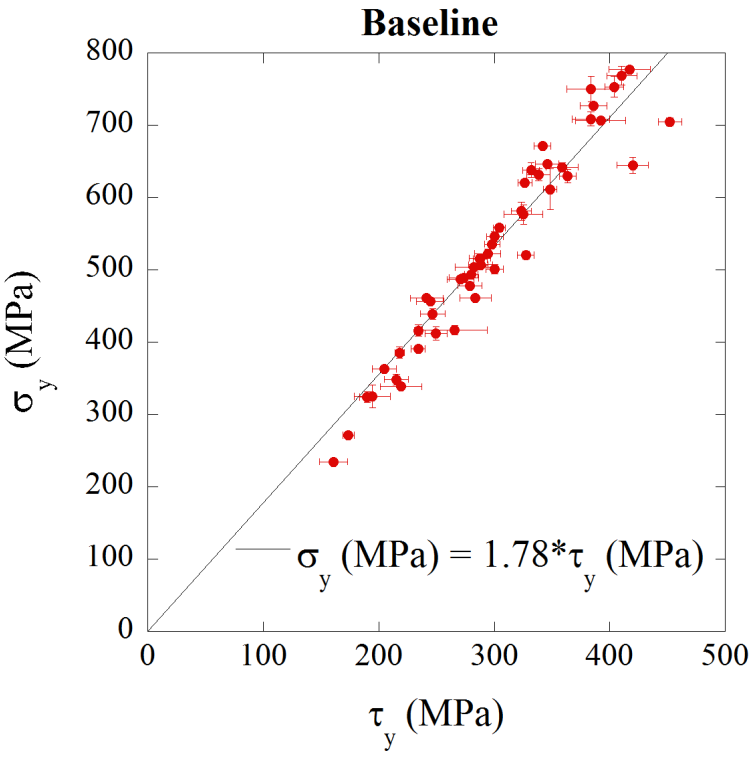

Figure 3.8. σ_y versus τ_y for steels with a wide range of yield strengths showing the empirical relation $\sigma_y \approx 1.78\tau_y$ [9].

Automated Shear Punch Testing

The single punch used initially for the SPT results requires a standard load frame to apply forces to the punch. Single punch tests are time consuming and potentially subject to variability due to factors such as clamping loads. Further, such tests result in higher radiation exposures to the test personnel from the activated steel samples due to the increased time and handling required for testing. To address these issues, we have developed an automated shear punch tester. The instrument consists of a pneumatically clamped upper assembly, with a hydraulic actuator and a load sensor. A precision punch is coupled to the load sensor through a hardened guide for accurate alignment. Both the guide and punch are interchangeable so different SPT diameters can be used. The lower assembly consists of an indexing loading table

that supports and positions the DMC for testing. The loading table can be removed and exchanged to support varying diameter test coupons, though the focus to date has been on designing the instrument to test the 20 mm DMCs. The current design allows four 3.0 mm punch diameter SPTs per 20 mm coupon; however the SPT can easily be modified to obtain a larger number of tests per DMC. A precision die is placed under the test specimen that is exactly matched to the punch for optimal clearance. A spring-loaded follower contacts the bottom face of the test specimens and tracks the bottom-face deflection throughout the punching process. The load cell and deflection sensor provide the load-displacement data necessary to compute shear stress and strain. The SPT tool is computer-controlled (clamping, load actuation, blank ejection, and digital data acquisition). The main benefit of the automated instrument, shown in Figure 3.9 and Appendix B, is a much higher testing throughput relative to the single punch fixture. Another advantage is that the automated SPT instrument is self-contained, occupying a relatively small footprint, and does not require a load frame, facilitating installation in the LAMDA facility. Further, automated SPT will involve reduced personal radiation exposures.

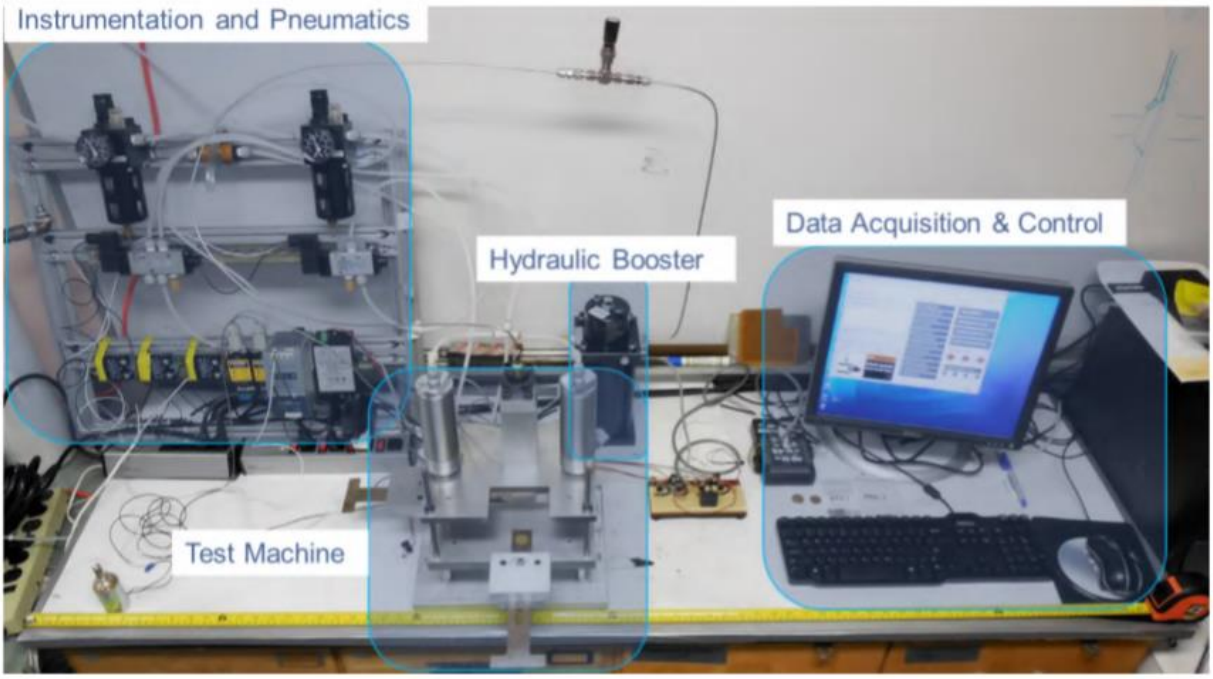

Figure 3.9. Automated shear punch instrument showing necessary components on a lab bench.

3.4.2 Microstructural Characterization

The nanoscale precipitates that form under irradiation in RPV steels are characterized by radii from ≈ 1-3 nm and number densities from ≈ 10^{23}-10^{24} m^{-3}. The precipitate sizes and character make imaging them by standard TEM techniques very difficult. Thus, the primary methods used here to characterize the precipitates are atom probe tomography (APT) and small angle neutron scattering (SANS). All techniques have their own inherent strengths and weaknesses, but can be highly complementary in combination. For example, both APT and SANS measure precipitate size distributions, average size (<r>), number density (N) and volume fraction (f_p), while APT can also measure the precipitate compositions and morphologies. SANS samples precipitates in large volumes of material, while APT typically samples volumes that are ≈ 13 orders of magnitude smaller. SANS requires beam time at user nuclear reactor facilities, with limited access. APT requires hot Focused Ion Beam (FIB)

micromachining that is possible only at a very limited number of facilities. A brief description of these techniques follows.

Atom Probe Tomography

Atom probe tomography (APT) is a destructive microscopy technique that measures compositional distributions on the nano-scale, including precipitates and solute segregation. An APT specimen is fabricated, by electropolishing or FIB milling (FIBing), a needle typically ≈ 100 nm in diameter with a smoothly rounded tip. The needle is then mounted on a stage in an atom probe, in this case a Local Electrode Atom Probe (LEAP), in ultrahigh vacuum ($< 10^{-10}$ torr) and cooled to cryogenic temperatures (20-60K). In LEAPs, a high voltage electrode is located close to the needle tip to create a very high local electric field at the needle tip. A standing voltage is applied that is just below that needed to electrostatically evaporate the atoms from the tip surface, where the field is highly concentrated. High frequency voltage pulses (100-200 kHz) are then used to increase the field to the point that there is a significant probability that a tip atom will be ionized and evaporated, typically at a steady rate of 0.2-0.5% per pulse, that can be controlled by modifying the standing voltage. The tip is sequentially evaporated along the needle axis until a sufficient number of ions are collected or the tip breaks, which is often the case.

The evaporated ions are accelerated by the electric field and pass through an aperture in the local electrode prior to being individually counted by a position sensitive detector. The position of the on the detector is determined by the x-y timing of a voltage pulse in the cross wire detector after charge amplification by a microchannel plate. A schematic of a LEAP is tip-electrode configuration is shown in Figure 3.10.

The time-of-flight between the voltage pulse causing evaporation and detection is used to determine the field emitted ion's mass-to-charge ratio, which is specific, with some overlaps, to a particular element and isotope. The detector position is used to determine the ion's location on the tip surface based on application of simple electrostatic field optics to a perfectly rounded needle tip. If ions evaporate prior to or slightly after the peak of the voltage pulse, then they acquire slightly less energy than those that evaporate at the peak voltage. Thus, there is a spread in the time-of-flight and corresponding mass-to-charge ratio spectrum. The LEAPs used for this thesis are equipped with so-called reflectrons, which alter the flight paths of ions with varying energies, and significantly reduce spread in the time-of-flight, thus improving mass resolution. The drawback to the high mass resolution instruments is that some ions are lost in the reflectron, reducing the collection efficiency from ≈ 65% to 37%.

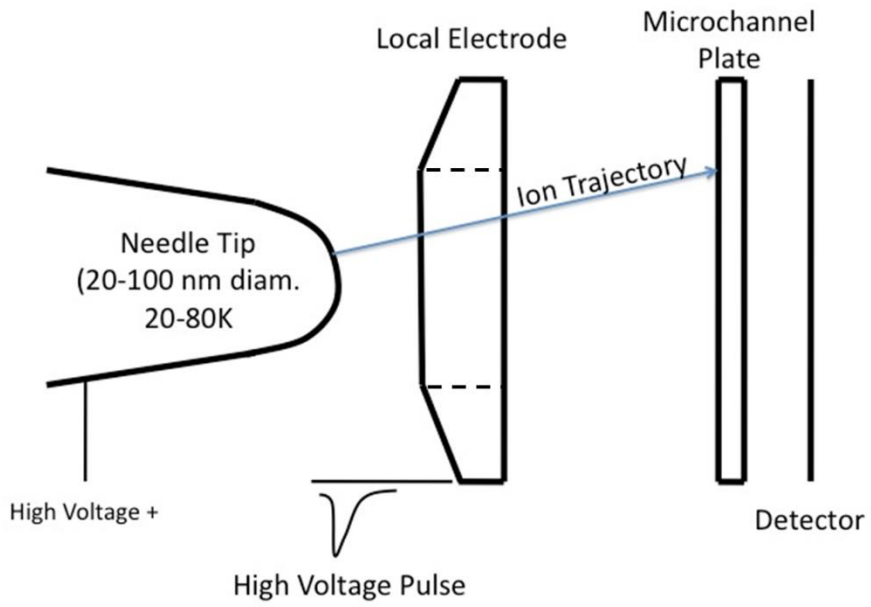

Figure 3.10. Schematic of a Local Electrode Atom Probe. Note that it is not to scale [52].

Three-dimensional (3D) reconstruction of the atomic positions is carried out with a proprietary software package, here the Cameca Integrated Visualization and Analysis Software

(IVAS) by assuming there is a uniform layer-by-layer removal of atoms from the tip. After each ion is evaporated, the associated volume is divided by the area of the evaporating surface within the field of view of the detector, incrementally changing the needle length in the z-direction, hence the position of the reconstructed tip surface. The next ion that evaporates is assumed to come from the repositioned surface. By continuously repeating this process a full 3D map of the element specific map of the atomic positions can be created. Note field emission of multi-atom/element ions is common, as is multiple ion charge to mass ratios for a particular isotope.

The resulting 3-dimensional datasets are then used to measure spatial distribution of the solutes, in this case the precipitates formed under irradiation. Precipitates are characterized by IVAS cluster analysis algorithms. The basic premise is that the atomic density of solute atoms is higher in precipitates than in the matrix. First, the distance (d) between specific solutes, here Cu, Ni, Mn and Si, and their Nth nearest solute neighbor is found, where the Nth atom is defined as the order (K). If d is less than a cutoff distance defined by the user (d_{max}), the solute is considered to be a core atom. After all core has been defined, all atoms within d_{max}, even those that are not solutes, are considered to be in the cluster. Clusters that have fewer than N_{min} atoms are excluded from the analysis. In addition to characterizing the precipitate size distribution, <r>, N and f_p, APT also measures the local bulk, matrix and precipitate compositions. Note the typical maximum volume of a sampled tip is less than 600,000 nm^3, equivalent to ≈ 50 million atoms. Nanoscale precipitation is governed by the local tip composition, which is seldom completely uniform from tip to tip. However, fluctuations in local compositions can be exploited to establish the relation between the alloy composition and the characteristics of the precipitates. For example, in this work the f_p closely tracks the local

alloy Cu, Ni, Mn and Si contents. However, APT may not be practically applicable to highly heterogeneous materials, or when number of feature of interest is low in the sampled tip volume. Of course many tips can be examined, but beyond a point this becomes impractical, especially in the cases of activated materials.

While APT is arguably the best tool for measuring the detailed nature of the precipitates that form under irradiation, the data must be cautiously interpreted in the face of a number of measurement artifacts. The most significant artifact is so-called trajectory aberrations. Trajectory aberrations are due to flattened or dimpled regions that form around a precipitate, deviating from an ideally rounded tip. In the case of RPV steels the deviation in local curvature causes surrounding matrix atoms to be focused onto the detector in the precipitate region. The flattened or dimpled region is caused by the lower potential needed to evaporate the precipitate solutes compared to the surrounding Fe matrix. Non-physically high precipitate atomic densities, which can be as high as 3 to 4 times that of the surrounding bcc matrix, signal trajectory aberrations. The reconstruction algorithm does not have any information on the incoming ion trajectory, only the location they hit the detector. As a result both focused matrix and actual precipitate solutes are reconstructed as if they originated from the same tip region. Although significant progress has been made in understanding trajectory aberrations, and other APT artifacts, this knowledge has not been converted to a standard practice and improving the fidelity of APT reconstructions is still work in progress. In this scientific research, all Fe that is nominally reconstructed in a precipitate is treated as an artifact and excluded from compositional and size measurements.

APT needle preparation was primarily performed at the Center for Advanced Energy Studies (CAES) Microscopy and Characterization Suite (MaCS) and ORNL Lamda, using

their Focused Ion Beam dedicated to working with activated specimens. After liftouts were created, they were welded to posts on a 22 or 36 grid coupon and partially sharpened to minimize the activated material on the coupon. The coupons were then shipped to UCSB where the final tip shaping was completed at the UCSB CNSI. The APT tips were prepared by standard Focused Ion Beam liftout and annular milling methods to form a tip radius of 50-100 nm, see Figure 3.11a. The FIB voltages and beam currents were reduced to 5 kV and 48 pA and 2 kV and 27 pA for final cleanup steps and removal of Ga damage layer [67]. Figure 3.11b shows a finished tip from a CPI steel, in which sharpening targets the dose varying from ≈ 4.0-4.4 dpa over the 150 nm depth sampled. APT was performed in voltage mode with a tip temperature of 44-50K, a pulse fraction of 20%, and a targeted detection rate of 0.5%/pulse, and a 200 kHz pulse repetition rate. The residual Ga-ion damage region was excluded from the analysis. Details of APT reconstruction will be discussed in a Chapter 4.

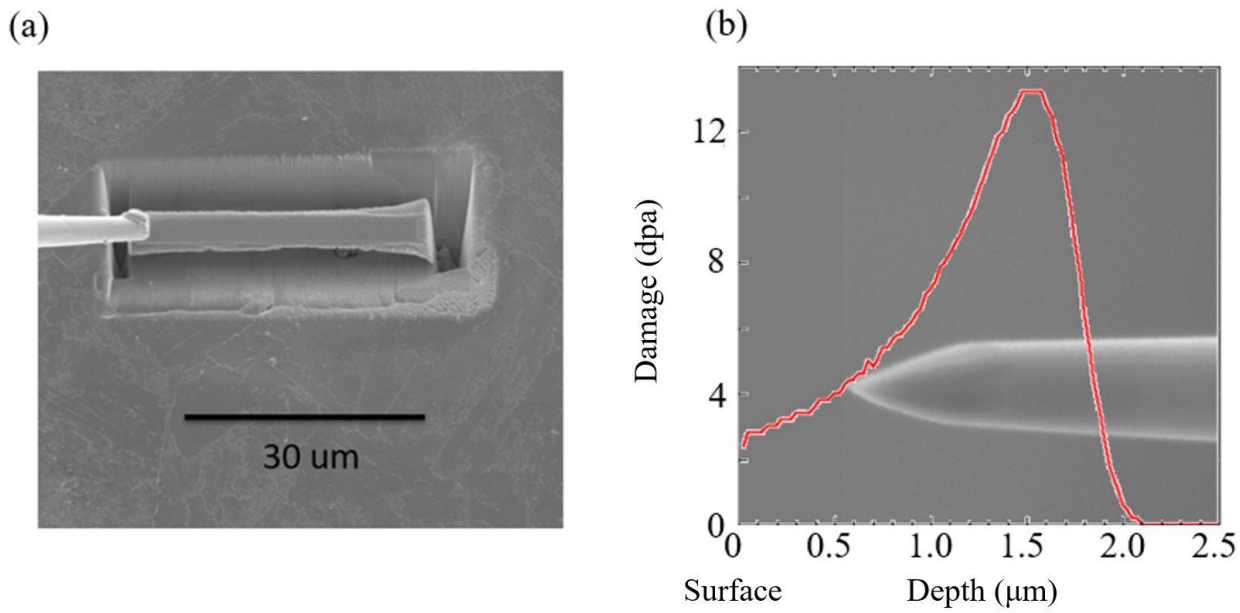

Figure 3.11. a) A scanning electron microscope image showing the FIB liftout from a CPI steel that is subsequently sectioned and mounted onto the micro-tip posts; and, b) annular milling produces a FIB sharpened APT specimen with the SRIM calculated damage (peak of 13 dpa) as a function of depth overlaid [68].

Energy Dispersive X-ray Spectroscopy

Energy Dispersive X-ray Spectroscopy (EDS) is based on an electron striking a sample, causing electron excitation and subsequent ejection. The energy of the characteristic X-ray produced depends on the chemical identity of the sample. Further detail of the technique can be found elsewhere [69].

EDS was performed using an FEI TALOS F200X S/TEM in the Low Activation Materials Development and Analysis Laboratory at Oak Ridge National Laboratory by Dr. Philip Edmondson and Peter Wells. EDS mapping was performed using a probe size of ~1 nm and current of 1.0 nA, respectively. Analysis of the data was performed using the Bruker-Esprit software. While the TALOS is capable of providing high-resolution chemical maps, it was not fully calibrated for quantitative chemical analysis. Thus, to complement these high resolution

maps, additional EDS scans were performed on the FEI Titan 300 kV FEG S/TEM at UCSB. A line scan with 4 nm spacing between points was taken across three grains, one with a high density of very large precipitates and two with a few sparse precipitates present, to measure the local solute contents.

Small Angle Neutron Scattering

Small Angle Neutron Scattering (SANS) is based on coherent scattering of cold neutrons by atomic nuclei around the $\theta = 0$, Bragg peak. In the case of solute rich precipitates embedded in a solvent rich matrix, the coherent scattering cross section, $d\Sigma/d\Omega$, is a function of θ or more precisely the scattering vector, $q = 4\pi\sin\theta/\lambda$ where λ is the neutron (or x-ray) wavelength. As shown in Figure 3.12, 2 λ is the angle between the incident beam and detector x-y position. The magnitude $d\Sigma/d\Omega$ (q) depends on the square of the coherent scattering length density difference between the matrix and precipitate. The coherent nuclear scattering length (b) is a property of a specific nuclear isotope. The coherent magnetic b is a function of the atomic magnetization of in the precipitate or matrix phase. Scattering length density (SLD), ρ, is the product of the atomic density and the scattering length, usually taken as the averages for the matrix and precipitate, respectively. The amplitude of $d\Sigma/d\Omega$ (q) is a function of $\Delta\rho^2$ between the matrix and precipitate, and the corresponding q dependence is a function of the size, or size distribution, of the precipitates. The $d\Sigma/d\Omega$ (q) generally scales with $(1/qr)^2$, hence, smaller precipitates produce scattering at higher q. This makes it relatively easy to characterize nm-scale precipitates formed during irradiation in a matrix phase that is would otherwise be free of features in this size range in the unirradiated condition. The precipitate scattering is reflected in the difference between irradiated (with nano precipitates) versus unirradiated

(without nano precipitates) steels. If $\Delta\rho^2$ is known, SANS can be used to determine the precipitate size distribution, $<r_p>$, N_p and f_p.

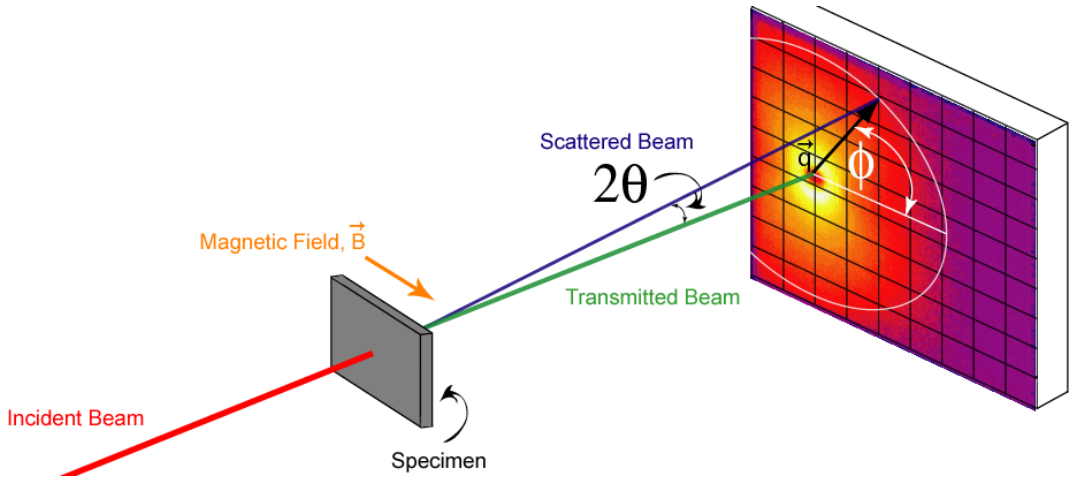

Figure 3.12. A schematic of the experimental setup for SANS.

SANS (and SAXS) measures the number of scattered neutron counts, I, at a detector position at q and ϕ where ϕ is the azimuthal angle around the beam, $I(q, \phi)$, for a specified total beam fluence on the specimen. The total $I(q, \phi)$ for the steel is isolated by appropriate adjustments for background and beam attenuation. The corresponding precipitate $I_p(q, \phi)$ is found by subtracting an unirradiated (nano precipitate free) control. The $I_p(q, \phi)$ is then converted to a $d\Sigma/d\Omega(q, \phi)_p$, using a known isotropic scattering standard, in this case water.

Precipitates in ferromagnetic Fe produce both nuclear (N) and magnetic (M) small angle scattering, depending on their respective SLD. The nuclear SLD depends on the precipitate and matrix compositions that are not known a priori, so $\Delta\rho_n^2$ is also unknown. However, the Cu, Mn, Ni, Si solute rich precipitates are believed to be non-magnetic, or only weakly magnetic. Thus when the Fe matrix is magnetically fully saturated with a known

magnetic SLD, $\Delta\rho_m^2$, the $d\Sigma/d\Omega(\ (q)_m$ is known. The magnitude of the magnetic scattering varies with $\sin(\phi)^2$, ranging from 0 parallel to 1 perpendicular to the magnetic field, respectively. In practice, a fitted magnetic to nuclear scattering ratio (M/N) is used to convert the data at all ϕ to a magnetic scattering cross section, that is then fit to extract the precipitate size distribution $<r_p>$, N_p and f_p.

SANS measurements were carried on out the NG7 beam line at the National Institute of Standards and Technology Center for Neutron Research. Small (dimensions) coupons were mounted in an automated sample changer in a 1.5 T horizontal magnetic field. The average neutron wavelength was 5 Å. A 2D ^{3}He detector measured the scattering intensity, I, as a function of q and ϕ. The I(q, ϕ) are measured for both unirradiated controls, that do not contain nano precipitates, and the irradiated steels. The I(q, ϕ) are corrected and normalized to one another by background subtraction and transmission measurements, as well as adjustments for different sample volumes probed by the neutron beam; the differences are generally minimal. Variations in detector pixel efficiencies are accounted for in converting $I_p(q, \phi)$ the to an absolute $d\Sigma/d\Omega(q)_{n/m}$ differential scattering cross-sections using a isotropic scattering water standard. After conversion of the entire set of detector cross sections to an equivalent $d\Sigma/d\Omega(q)_m$, the data are least square fit using the assumed $\Delta\rho_m^2$ and a spherical q-dependent form factor and log normal size distribution. The fitting parameters are the precipitate size-distribution mode radius (r_m) and width parameter (β) and $d\Sigma/d\Omega(0)_m$. The fitted parameters are then used to calculate the precipitate $<r>$, N_p and f_p. Multiple scattering features can be fit simultaneously. Multiple feature fits are also used to remove scattering artifacts due to experimental uncertainties and bias. Finally, we note that scattering at very high the q is due to an essentially isotropic incoherent background from various sources, but discussion is

beyond the scope of this document. The irradiated and unirradiated $d\Sigma/d\Omega(q)$ are approximately the same at high q which is a useful check on the data. The major difference is due to the removal of solutes from the matrix by precipitation that can be readily accounted for is necessary. Further details regarding SANS theory, experimental details and data analysis can be found elsewhere [38,70–73].

The major assumption in the SANS analysis is that the precipitates are non-magnetic. This assumption has been shown to be valid for Cu rich precipitates that are dominant at lower fluence. However, this assumption may not be valid at high fluences where Mn, Si and most importantly, Ni, are the dominant solutes in the precipitates. Specifically, if the precipitates are partially magnetic, then the magnetic scattering contrast, $\Delta\rho_m^2$, assumed in the analysis is too large, resulting in an underestimate of the precipitate f_p and N_p. Work is ongoing to address this issue, including magnetic property measurements of the bulk precipitate phases, as well as SANS measurements at various temperatures. Further, Small Angle x-ray Scattering (SAXS) will be used to better evaluate the magnetization of the precipitates. The results of this research will be discussed in future work.

Chapter 4: Compositional Analysis: Electron Probe Micro-Analyzer (EPMA) and Atom Probe Tomography (APT)

Introduction

This section reports on a compositional analysis comparison of EPMA to APT for RPV steels. Since the amount and identity of the precipitate phase formed under irradiation varies with the corresponding bulk composition, it is important to quantify the variability between sampling regions for the same alloy. The commonly used EPMA non-destructively acquires the average chemical composition at spatial scales (down to 2um). The APT provides information on the atomic positions and chemical identity in the extremely small volume of a needle shaped tip, with a typical hemispherical radius of ≈ 50 nm and ≈ 500 nm length. Our cross plots of the atomic compositions of key elements, such as Cu, Ni, Mn, Si demonstrate the reliability and difference between sampling techniques in the steels.

This section also explains the nontrivial methods necessary to analyze the collected APT spatial and composition data. The recorded x, y, z isotope positions are reconstructed by custom and proprietary post processing codes like the IVAS (3.6.12), which was used in this work. There are a large number of assumptions in the standard reconstruction algorithms, like the uniform erosion of the tips and the assumed shape evolution of its shape as a perfect hemisphere. Further the results are sensitive to the method and parameterization of analyzing the precipitates in terms of their number densities, sizes, shapes, mole fractions and compositions. Our parameter selection and other contributions to the analysis of APT specimens will be explained. For instance, the $^{58}Ni^{+2}$ and $^{58}Fe^{+2}$ mass spectrum peaks overlap, hence it is necessary to deconvolute the contributions of these two elements. A sensitivity study

conducted will show other methods have neglected the peaks in initial cluster identification, which leads to large underestimates of the cluster size and volume fraction, since it misses a large fraction of the Ni actually present.

4.1 Materials and Methods

APT Experimental Conditions and Reconstruction[i see acknolwedgements)]

Atom probe tomography (APT) is a well-known, high-resolution microscopy technique which provides information on the atomic positions and chemical identity in the extremely small volume of a needle shaped tip, with a typical hemispherical radius of ≈ 50 nm and ≈ 500 nm length. APT is an extremely powerful tool for characterizing the high number density of nm-scale precipitates in irradiated RPV steels. We refer the reader to details of the APT technique described Chapter 3, in several outstanding books [74,75] and numerous journal papers, for example [76–78].

This section covers the nontrivial methods necessary to analyze the collected APT spatial and composition data. For instance, multiple field evaporations of various alloy constituents produce a spectrum of flight times that are directly related to the ion's mass to charge ratio (MCR). Sharp peaks in the MCR spectrum mark a particular isotope and charge state. Note the $^{58}Ni^{+2}$ and $^{58}Fe^{+2}$ peaks overlap, hence it is necessary to deconvolute the contributions of these two elements. Some studies have neglected the $^{58}Ni^{+2}$ and $^{58}Fe^{+2}$ peak in the initial cluster identification [79,80]. However, depending on the algorithm used, this method leads to large underestimates of the cluster size and volume fraction, since it misses a large fraction of the Ni actually present. This is the case for the Integrated Visualization and Analysis Software (IVAS) maximum separation distance algorithm.

Thus a sensitivity analysis on the methods of peak deconvolution was conducted. Since this overlapping peak contains 68.01% of all naturally occurring Ni and 0.28% of all the corresponding Fe, we initially ranged it to be Ni. After the solute clusters had been identified, a correction was made to the number of Fe and Ni atoms using abundance ratios for other Ni and Fe isotopes. This correction resulted in a slightly reduced Ni content in the bulk, matrix and solute clusters in relation to the initial ranging of the mass spectrum. There is sufficient Ni in the bulk (0.19-3.50%) to warrant this correction.

In this work, the recorded x, y, z isotope positions are reconstructed by proprietary post processing codes like the IVAS (3.6.12), which was used in this work. There are a large number of assumptions in the standard reconstruction algorithms, like the uniform erosion of the tips and the assumed shape evolution of its shape as a perfect hemisphere. Further the results are sensitive to the method and parameterization of analyzing the precipitates in terms of their number densities, sizes, shapes, mole fractions and compositions. Note, precipitate compositions typically vary spatially in a complex manner, like core-shell and precipitate appendage structures [81]. The low evaporation field of the precipitates changes the local magnification factor resulting in a focusing of matrix atoms into the precipitate region on the detector and is signaled by higher than physical atom densities in the reconstructed dataset [70,78,82–85]. These artifacts can result in distortions of the composition, shape, and size of precipitates, and most specifically their apparent Fe content, some or all of which actually comes from the adjoining matrix thus contributing to the higher than physical atom density in the precipitate region. The effects of TA increase with decreasing precipitate size and generally lead to a precipitate-matrix mixing zone artifact over a length scale of ≈ 1 to > 2 nm [86]. In this work the precipitate diameters average only ≈ 2.4 nm, thus we assume that the Fe content

indicated by a standard IVAS analysis is a TA and reconstruction artifact. Both STEM-EDS and multi technique characterization studies (small-neutron scattering, temperature dependent small angle magnetic neutron scattering, small-angle X-ray scattering, positron annihilation coincidence Doppler broadening orbital electron momentum spectrum measurements and combined electrical resistivity and Seebeck coefficient measurements) have all clearly shown high concentrations of Fe in the precipitates is an APT artifact [87,88].

IVAS cluster analysis maximum separation algorithms were used to determine the number density (N), size distribution, average diameter (<d>), volume fraction (f) and compositions of the precipitates. Fine-tuning of the image compression factor and k-value was required to reach an accurate planar d spacing, identified by low-index crystallographic poles, such as (110) and (200). The dataset image compression factor ranged between 1.50 and 1.65 and the k-value between 2.7 and 5.2. The maximum separation method was used to distinguish the clustered solutes from those in the surrounding matrix [89,90].

The key cluster analysis parameters are a maximum separation distance to define a solute atom (Ni, Mn, Si, Cu, P) as being part of a cluster (d_{max}) and a minimum number of solute atoms that defines a cluster (N_{min}). Notably, the results of the cluster analysis can be strongly influenced by these parameters [91]. A d_{max} that is too large will include some solutes in the cluster that are actually in the matrix. Using a d_{max} that is too large may also incorrectly merge closely adjacent clusters. Values of d_{max} (and N_{min}) that are too small can result in incorrect classification of random fluctuation as clusters, and underestimate the number of solutes in larger clusters. Thus in all cases, a sensitivity analysis was performed to determine the most suitable values of d_{max} and N_{min}. The optimal $d_{max,}$ based mainly on the solute separation distance distribution deviations from random, was found to be 0.50-0.60nm, with a

corresponding N_{min} of 15-30 atoms. The maximum separation envelope of additional elements (L) and the erosion distance (E) were taken as equal to d_{max}, consistent with the less than or equal to recommendation in [91]. These values have been found to produce self-consistent results for a large RPV steel database. Note, however, lower L and E do not have a significant effect, and there is no absolutely "correct" values of these parameters that can be chosen. More details on the principles and practice of the APT technique, and selecting appropriate reconstruction parameters, can be found elsewhere [74,75,77].

The number of solute atoms associated with each precipitate, corrected for efficiency, was determined and multiplied by the atomic volume of Fe. The precipitate *r* was then defined as the radius of a sphere encompassing the total solute volume. While these precipitates are thought to be intermetallic phases, differences in their corresponding average atomic volume versus Fe results in variations in *r* of less than 2%. The MNSP number density (*N*) was calculated by dividing the number of clusters in the dataset by the total volume in the analyzed tip. Precipitates on the edge of the tip are not included in the determining the size distributions, or average <*r*>, but are counted as one half in the estimating N. The associated error f_v, N and <r> estimates are based on the tip-to-tip variations observed here for conditions with multiple tips, or in the one case with a single tip, the average of the others. The standard IVAS reconstructions, as usual, suggested that there is a significant amount of Fe in all of the MNSPs.

As noted above, the Fe nominally in the precipitates was treated as an artifact and was removed when calculating the precipitate size and compositions [52,87,88,92]. After correction for detector efficiency the sizes and volume fraction of the precipitates was determined from the number of solute atoms they contain, assuming a spherical morphology and an atom density equal to bcc Fe. Note the nominal IVAS Fe content is also provided for

those who wish to interpret differently. The precipitate number density (N) was calculated by dividing total identified clusters by the total APT tip volume. Clusters that intersect the tip surface were counted as half of a precipitate. The volume fraction of precipitates (f) was determined by dividing the number of solute atoms in all clusters by total number of atoms of a dataset.

4.2 Results and Discussion[(ii)]

EPMA determined the average bulk composition in 25 unirradiated RPV steels which were included in ATR-2. Table 4.1 shows the EPM results along with the APT measured bulk compositions. Figure 4.1 shows the plots of APT versus those corrosponding bulk compositions for the various elements. These plots indicate the Ni and Si EPMA and APT compositions fall near a 1:1 line. The Cu saturates at ≈ 0.24 as expected due to precipitation. This occurs when the bulk Cu exceeds the solubility limit. Due to small sampling volume APT seldomly measures the coarse scale Cu precipitates [4,55,93]. However the very high value of the EMPA Cu for one alloy of a medium 0.69% Ni, high 0.16% Cu alloy (SB1, not shown) is suspicous, and may result from contamination.

In contrast to the other solutes, the bulk EPMA Mn is significantly and systematically higher in the APT measurments of dissolved Mn. This difference was expected due Mn sequestring by coarse $Mn_{0.6}Fe_{2.4}C$ carbides [32]. This in important. and emphasizes the importance of using local tip specific composition in in analyzing APT data.

Table 4.1. EPMA and APT bulk compositions for 25 unirradiated RPV alloys which were included in ATR-2.

Alloy	EPMA Bulk (at%.)				APT Bulk (%)			
	Cu	Ni	Mn	Si	Cu	Ni	Mn	Si
SB3	0.05	0.49	1.57	0.49	0.04	0.47	0.88	0.51
C17	0.32	1.60	1.54	0.16	0.14	1.43	1.32	0.33
C22	0.34	0.73	0.93	0.28	0.42	0.84	0.84	0.28
C31	0.01	0.67	1.58	0.22	0.04	0.86	0.98	0.31
C6	0.01	1.41	1.68	0.32	0.01	1.68	1.47	0.40
SW9	0.23	0.62	1.81	0.96	0.18	0.59	1.11	0.90
EC	0.48	0.58	1.54	0.39	0.30	0.61	0.97	0.36
SW1	0.17	0.16	1.28	0.42	0.15	0.13	0.86	0.40
SB1	1.28	0.53	1.48	0.55	0.16	0.59	0.87	0.55
SW4	0.03	0.83	1.11	0.78	0.03	0.92	0.99	0.94
SB2	0.05	0.66	0.85	0.45	0.04	0.61	0.55	0.51
SW3	0.30	0.68	1.37	0.43	0.27	0.70	0.90	0.40
LB	0.35	0.16	1.60	0.42	0.28	0.17	1.30	0.46
LC	0.35	0.77	1.62	0.41	0.20	0.83	0.98	0.44
LD	0.35	1.09	1.67	0.50	0.21	1.19	1.02	0.52
LG	0.01	0.69	1.56	0.42	0.01	0.71	0.74	0.42
LH	0.09	0.70	1.61	0.44	0.09	0.71	1.19	0.44
LI	0.32	0.70	1.37	0.33	0.16	0.75	1.09	0.41
SW7	0.22	0.54	1.94	1.11	0.18	0.52	1.23	0.85
SW6	0.32	0.57	1.73	1.08	0.23	0.58	1.19	0.92
SW5	0.03	0.84	1.61	0.81	0.03	0.79	1.06	0.79
W63	0.33	0.62	1.76	0.30	0.20	0.62	1.40	1.00
W73	0.24	0.56	1.72	0.77	0.23	0.47	1.13	0.75
WA	0.16	0.53	1.87	0.59	0.13	0.50	1.40	0.64
WC	0.02	0.62	1.58	1.07	0.02	0.78	1.35	1.16

\

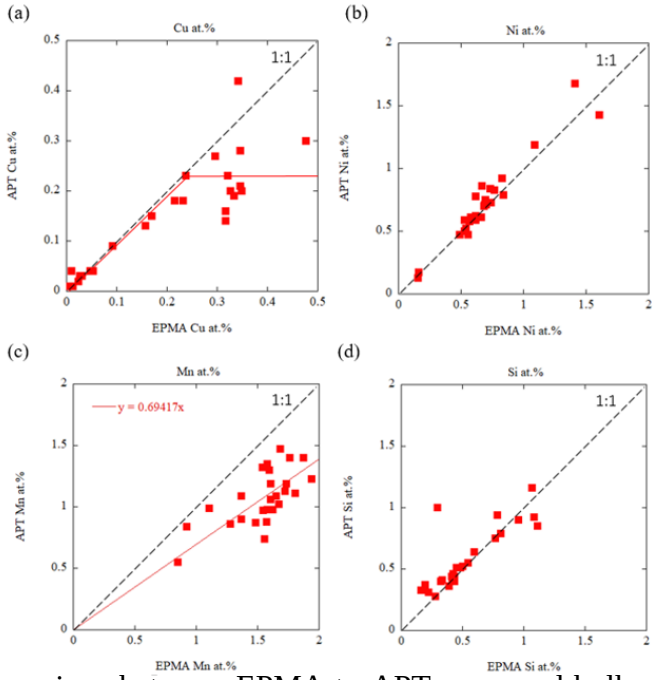

Figure 4.1. The comparison between EPMA to APT measured bulk compositions of solutes for 25 unirradiated RPV steels included in ATR-2. The units are all at.%[(ii)].

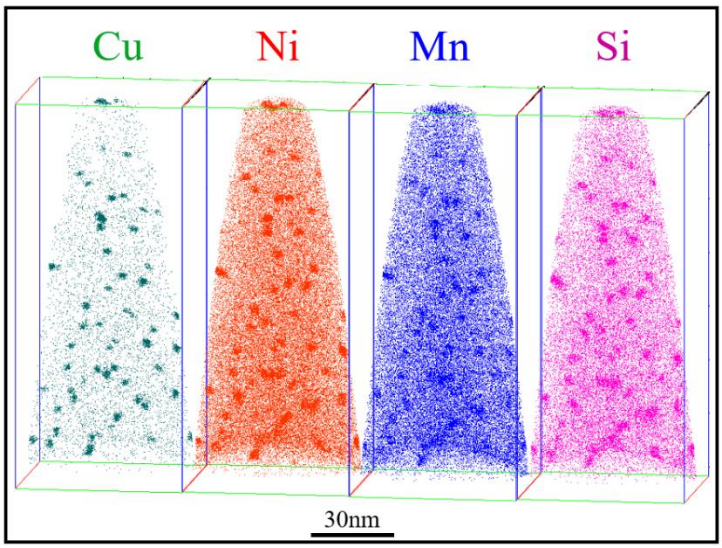

Figure 4.2. APT solute maps for a high Cu medium Ni plate (SB1: 0.16Cu 0.59Ni, 0.87Mn, 0.55Si in at.%). APT found $f_v \approx 0.47\%$ of ≈3 nm Cu-Ni-Mn-Si precipitates.

Acknowledgements

(i) Dr. Peter Wells provided crucial MATLAB coding, mentorship, hands on training in APT data collection and analysis and collected part of the APT data.

(ii) Dr. Soupitak Pal completed the EPMA sample preparation, measurements and data analysis at UCSB.

Chapter 5: Precipitation and Hardening

5.1 Irradiated Low Alloy Steels with a Wide Range of Ni and Mn Compositions

5.1.1 Introduction[2]

Formation of fine scale Mn-Ni-Si precipitates (MNSPs), like the G-phase, is observed in a number of Fe-based alloys, during long-time, intermediate temperature thermal aging, as well as in under irradiation [87,94–96]. Recently, precipitation of an ultrahigh density of Ti-Ni-Si G-phase precipitates, with Ti replacing Mn, was used to create very high strength steels [97]. However, there is little experimental insight on the alloy Mn-Ni-Si dependence of the MNSP number densities, sizes, volume fractions (f), chemistries and crystallographic phases. Here we characterize a matrix of nine compositionally tailored low Cu steels, with systematically varying dissolved Ni (0.19-3.50%) and Mn (0.06-1.34%) contents, at an approximately constant 0.44±0.05% Si. Note the square root of the f_v of MNSPs largely controls hardening and embrittlement [50,98]. Thus the primary research objective of this section is to provide fundamental insight on the Mn-Ni dependence of f_v, and related MNSP characteristics, including their compositions. The second research objective addressed is characterize a new Advanced Steel Matrix (ASM) with varying levels of Cu, Ni, Mn, and Si to expand RPV composition range and explore potential for tougher and higher strength steels in advanced reactors. Specifically, we explore and quantify the hypothesis that large reductions

[2] This chapter includes slightly modified text and figures published in N. Almirall, P.B. Wells, T. Yamamoto, K. Wilford, T. Williams, N. Riddle, G. R. Odette, Precipitation and Hardening in Irradiated Low Alloy Steels with a Wide Range of Ni and Mn Compositions, Acta Materialia, 179 (2019) 119-128.

in the alloy Mn content to 0.3%, or less (typically Mn concentrations are more than 0.8%), can suppress the formation of MNSPs sufficiently to compensate for high ≈ 3.5% Ni [99].

An immediate practical motivation for this work is that such high Ni steels have outstanding unirradiated strength and toughness properties [99–103]. As a specific example, the A508 Gr. 4N steel, with > 3.2% Ni, has a room temperature yield stress that is typically ≈ 25% higher than for A508 Gr. 3 with ≈ 0.6%Ni. The corresponding master curve fracture toughness 100 MPa√m reference temperature, T_o, is lower, with typical values -140°C, compared to -90°C (or higher) for Gr. 3 steels. The improved properties are associated with smaller prior austenitic grains and carbides, and finer martensitic-bainitic lath and packet structures. The corresponding Mn contents are typically ≈ 0.3% versus 1.5% for A508 Gr. 4N and Gr. 3, respectively. The lower Mn in Gr. 4N reduces the irradiation hardening and embrittlement sensitivity, so as to offset the effect of high Ni. To compensate for low Mn, it is important to keep the S and other impurities low. Thus for RPV applications, A508 Gr. 4N is part of an alloy class known as "superclean" steels. Practical issues aside, the fundamental scientific objective of this work was to probe and quantify Ni-Mn interactions in terms of the MNSP characteristic sizes, number densities, volume fractions, compositions and their associations with other microstructural features, as well as their effects on the corresponding irradiation hardening.

5.1.2 Materials and Methods

The primary focus of this section is on the APT characterization of 9 ASM steels neutron irradiated to ≈ 1.4×10^{20} n/cm^2 at ≈ 290°C. The bulk alloy compositions are given in Table 5.1.1, along with the baseline heat treatment.

Table 5.1.1. Nominal steel compositions (%)

Alloy	Bulk at%								
	Cu	Ni	Mn	Si	Cr	Mo	P	C	Fe
A1	0.05	0.28	0.26	0.41	0.11	0.28	0.009	0.97	Bal.
A17	0.05	3.26	1.52	0.39	0.11	0.29	0.005	1.06	Bal.
A19	0.05	1.57	0.26	0.39	0.14	0.30	0.014	1.06	Bal.
A22	0.05	1.58	1.51	0.41	0.11	0.30	0.011	1.34	Bal.
A26	0.04	3.29	0.25	0.37	0.11	0.30	0.016	1.20	Bal.
A34	0.06	3.25	0.08	0.38	0.10	0.30	0.011	1.02	Bal.
A35	0.05	0.22	1.51	0.41	0.12	0.28	0.012	1.24	Bal.
A39	0.03	0.66	1.47	0.41	0.12	0.28	0.007	0.97	Bal.
A48	0.06	3.29	0.77	0.41	0.11	0.29	0.005	1.29	Bal.

Austenitized at 920°C for 1 h followed by an air cool, then tempered at 600°C for 5 h followed by an air cool.

See Chapters 3-4, Table 3.5 and Appendix C for Materials and Methods supplemental information[(i-iv see acknowledgements)].

5.1.3 Results and Discussion

MNSP Characterization

Figure 5.1.1 shows typical solute maps for 4 irradiated alloys with 0.19 to 3.50% Ni, 0.03 to 0.06% Cu, 0.80 to 1.34% Mn, and 0.39 to 0.49% Si. The volume fractions of the MNSPs visibly increase with increasing alloy Ni content. Table 5.1.2 summarizes the average APT bulk, matrix and MNSP compositions for the 9 alloys with systematic variations in bulk Ni and Mn and low <0.06% Cu and typical 0.44±0.05% Si contents. The measured bulk solute values are in reasonably good agreement with the nominal alloy compositions for Cu, Ni, and Si (see Table 5.1.1). However, the dissolved Mn is lower than the nominal value by ≈ 0.02 to 0.67%. The lower concentration. and inhomogeneous distribution of dissolved Mn, are primarily due its sequestering in pre-existing coarse-scale $(Mn_{0.8}Fe_{0.2})_3C$, carbides [32].

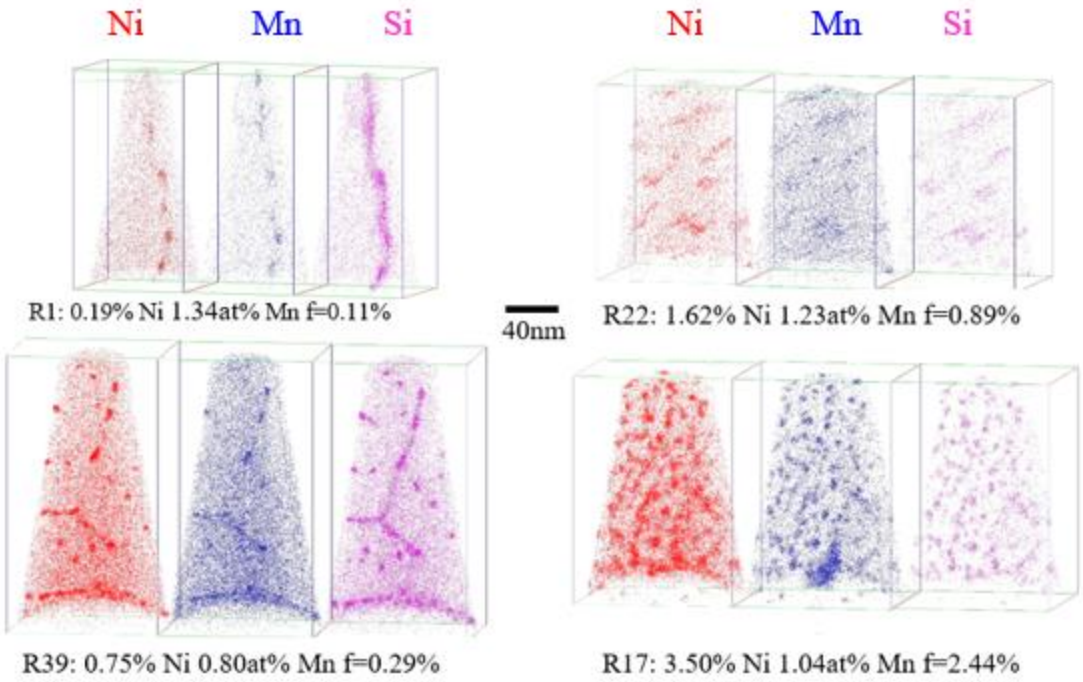

Figure 5.1.1. Solute maps for irradiated ASM alloys with systematically varying Ni from 0.19-3.30% in steels with 0.03 to 0.06% Cu, 0.80 to 1.34% Mn and 0.39 to 0.49% Si. All compositions are in at.%.

MNSPs are found in all cases at the high fluence of ≈ $1.4x10^{20}$ n/cm^2 and 290°C. Note, well-defined CRPs form only at levels more than ≈ 0.07% Cu, thus were not found in these steels [7,8,20]. However, Cu likely still has a catalyzing effect on the formation of MNSPs even at low levels [32], and all the MNSPs contain ≈ 1% Cu, typically involving 8-32 atoms.

Table 5.1.2. Average APT bulk, matrix and precipitate compositions (%) for the 9 ASM alloys

Alloy	Bulk				Matrix				Precipitate				
	Cu	Ni	Mn	Si	Cu	Ni	Mn	Si	Cu	Ni	Mn	Si	Fe*
A1	0.05	0.24	0.24	0.49	0.04	0.21	0.22	0.44	1.5	37.1	14.6	46.8	58.2
A17	0.04	3.50	1.04	0.44	0.02	2.15	0.51	0.15	0.9	62.8	23.9	12.5	57.8
A19	0.05	1.80	0.24	0.47	0.05	1.55	0.22	0.35	1.0	64.4	5.1	29.4	64.3
A22	0.05	1.62	1.23	0.46	0.04	1.25	1.06	0.33	0.8	54.1	26.5	18.6	63.4
A26	0.04	3.40	0.22	0.39	0.04	2.91	0.19	0.25	0.9	73.5	4.7	20.8	58.1
A34	0.06	3.39	0.06	0.40	0.05	3.09	0.06	0.31	0.9	75.9	1.2	22.0	58.2
A35	0.04	0.19	1.34	0.46	0.04	0.17	1.27	0.44	1.3	26.4	42.4	30.0	65.1
A39	0.03	0.75	0.80	0.46	0.03	0.63	0.75	0.37	0.8	46.8	19.7	32.7	65.5
A48	0.05	3.45	0.48	0.42	0.04	2.58	0.32	0.19	1.0	69.2	12.5	17.2	58.6

**The nominal IVAS Fe found in all the MNSPs, that is thought to largely be an artifact.*

Table 5.1.2 summarizes the APT MNSP <d>, N and f_v. The corresponding +/- "uncertainties" reflect the variability between all the tips for the same alloy. Multiple tips were measured and the +/- in Table 5.1.2 refers to the differences between tips. The MNSP f_v increases synergistically with Ni and Mn. At high 3.5% Ni and 1.04% Mn f_v is 2.44%, while f_v is ≈ 0.44% in the high 3.5% Ni, low 0.06% Mn steel. The f_v is very low at ≈ 0.08% in the steel with only ≈ 0.24% Ni and Mn. These results demonstrate the strong synergistic effect of Ni and Mn on MNSPs.

Figure 5.1.1 also shows that the MNSPs in the low-medium Ni steels (0.3-0.8% Ni) are heterogeneously distributed, and are primarily (≈ 70%) located on dislocations (and grain boundaries when present). Note, several of the low ≈ 0.3% Ni alloy tips did not contain any MNSPs, due to their small APT sampling volume. These empty volumes were included in calculating N and f_v. The Mn, Ni, and especially Si, are highly segregated to dislocations. The role of solute segregation to dislocations, and dislocation loops, is important, and has been modeled [11,104], but we will not pursue this mechanism in detail further here. However, we

note the models based on CALPHAD thermodynamics and radiation enhanced diffusion kinetics, reported by Ke et al., strongly support the critical role of heterogeneous MNSP nucleation in low to medium Ni steels [19]. The average MNSP compositions on dislocations are essentially the same as those observed in the matrix. The corresponding MNSP <d> and N are plotted in Figure 5.1.2 as a function of Ni for high and low Mn alloys. The average precipitate diameter, <d>, is ≈ 2.36 ± 0.24 nm, and is insensitive to both Ni and Mn. However, the MNSP N increases by a factor of ≈ 10 between ≈ 0.25 and 1.5% Ni, and by a factor of 2-3 between low and high Mn steels. Between 1.5 and 3.5% the effect of Ni on N is weaker in the high Mn steel.

Table 5.1.3. Bulk Cu, Ni, Mn and Si compositions and APT precipitate <d>, N and f

Alloy	APT Bulk Composition (at%)				<d>	+/-	N	+/-	f	+/-	10^6 atoms
	Cu	Ni	Mn	Si	(nm)	(nm)	(10^{23} m^{-3})	(10^{23} m^{-3})	(%)	(%)	
A1	0.05	0.24	0.24	0.49	2.31	0.02	0.92	0.40	0.08	0.15	9.8
A17	0.04	3.50	1.04	0.44	2.58	0.09	22.2	0.12	2.44	0.17	11.6
A19	0.05	1.80	0.24	0.47	2.47	0.03	5.07	0.09	0.42	0.04	17.8
A22	0.05	1.62	1.23	0.46	2.15	0.08	13.4	0.15	0.89	0.12	10.3
A26	0.04	3.40	0.22	0.39	2.46	0.04	8.37	1.69	0.69	0.11	48.9
A34	0.06	3.39	0.06	0.40	2.17	0.10	6.53	2.05	0.44	0.10	21.9
A35	0.04	0.19	1.34	0.46	2.22	0.03	1.83	0.27	0.11	0.08	20.8
A39	0.03	0.75	0.80	0.46	2.60	0.13	2.42	0.40	0.29	0.04	23.5
A48	0.05	3.45	0.48	0.42	2.29	0.08	21.2	0.60	1.41	0.22	38.9

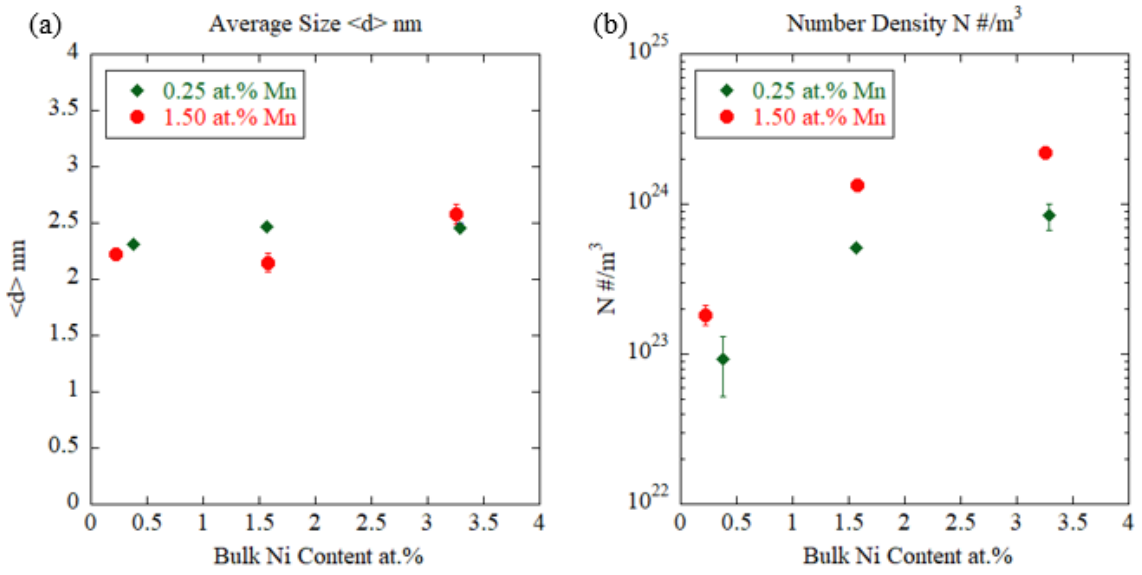

Figure 5.1.2. The effect of Ni at 0.25 and 1.5at%Mn (nominal) on the precipitate: a) average diameter, <d>; and, b) number density, N.

Figure 5.1.3 shows a cross plot of f_v versus Ni at low, intermediate and high Mn. At low Mn (filled red circles), f_v is very low, as is the corresponding N. And at low Ni, the effect of increasing Mn from 0.24% to 1.34% is minimal. In contrast, at high Mn (filled green diamonds), f_v increases approximately linearly with Ni up to ≈ 2.44%. The increase in f_v with Ni at 0.23% Mn is less rapid, but is also approximately linear. The atoms maps in Figure 5.1.4a and b, and the f_v versus Mn cross plot in Figure 5.1.4c, demonstrate the profound and systematic effect of Mn in the 3.5% Ni steels. The increase in f_v with Mn is linear in the high Ni steels. As discussed in the next section, the reason is primarily related to phase composition selection, and corresponding solute balance requirements. That is, at very low Mn the formation of Ni-Mn-Si phase compositions, which can incorporate the largest amount of Ni, is not possible. Indeed at full decomposition Ni ≈ 1-1.2(Mn+Si). Thus the low f_v can be viewed as being due to Mn starvation. In this case Si enriched phase compositions are selected, with Ni/Si ratios of ≈ 2 to 3. At high alloy 3.5% Ni and 1.04% Mn contents, 2.15% Ni remains

dissolved in the matrix, while 3.09% Ni remains dissolved in the high 3.39%Ni, lower 0.06% Mn steel. The Ni-silicide type phase composition f_v is limited by the primary presence of only 2 elements, and a relatively low amount of bulk Si. Note, the increase in f_v from 0.44 to 0.69%, between the 0.06 and 0.25% Mn, is not primarily due to the precipitate Mn fraction; rather this is associated with a higher N in the latter case. This observation suggests that Mn also enhances Ni-silicide type phase composition nucleation rates. Similarly, the increase in f_v of 0.69% to 2.44%, between the 0.25 and 1.50 Mn, as shown in Figure 5.1.4, is associated with a $Ni_2(MnSi)$ type phase composition.

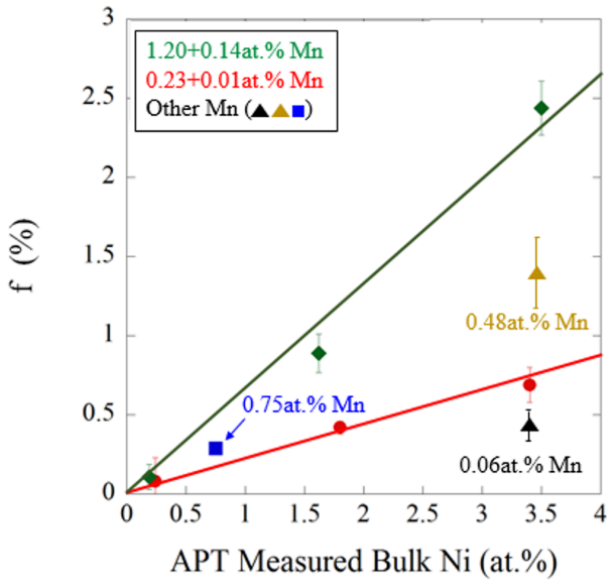

Figure 5.1.3. The effect of Ni on f_v for various Mn contents.

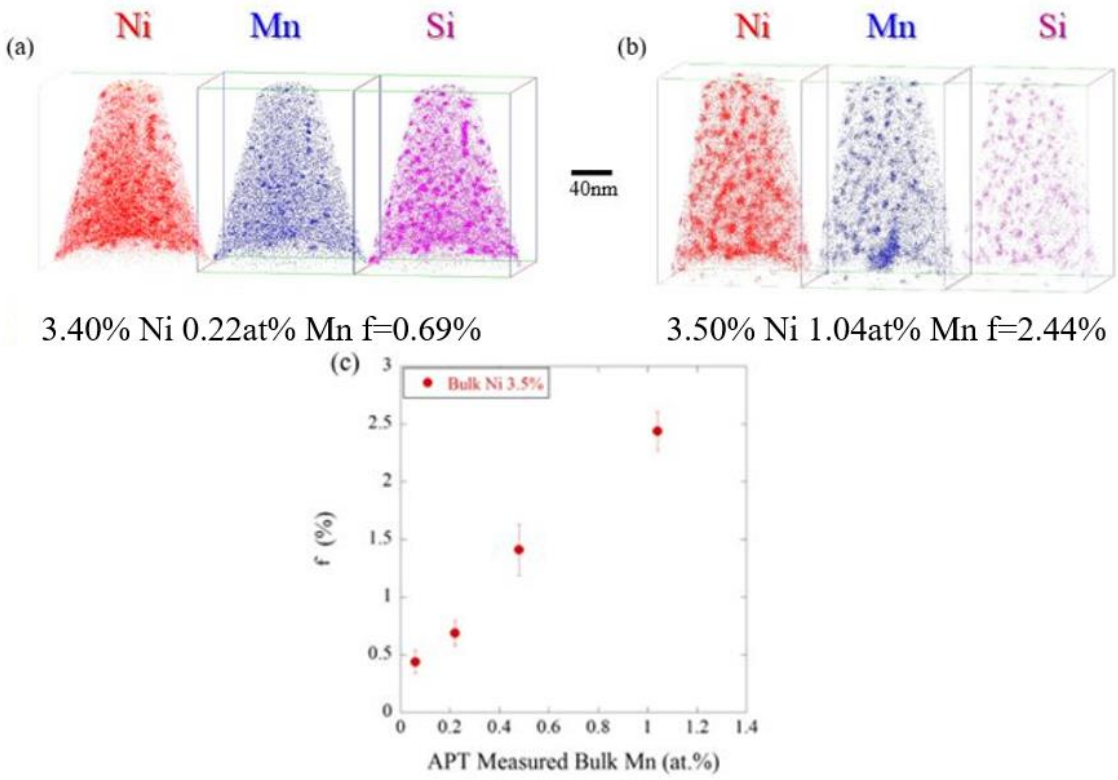

Figure 5.1.4. a) An APT solute map for a high 3.4% Ni, low 0.22% Mn steel; b) an APT solute map for a high 3.5% Ni, high 1.04% Mn steel; and c) a f_v versus bulk Mn cross plot for the high 3.5% Ni steels.

Irradiation Hardening

The isolated contribution of MNSPs to hardening is proportional to $\alpha(d)\sqrt{2f_v}/d$ [98], where $\alpha(d)$ is an obstacle strength factor. Since the precipitates are roughly the same size, it is expected that the dispersed dislocation obstacle hardening will scale with the $\sqrt{f_v}$. Figure 5.1.5 shows the measured irradiation yield stress increase ($\Delta\sigma_y$), summarized in Table 5.1.4, versus the $\sqrt{f_v}$ for the 9 alloys in this study. The filled circles are tensile data, while the unfilled squares are the average of the $\Delta\sigma_y$ estimates from the H_v and SPT. The half-filled squares are the cases where there is no tensile data. The least square fit slope is $\Delta\sigma_y \approx 300$ MPa/$\sqrt{f_v}$ (%). These results are reasonably consistent with previous studies with f_v between 0.2 and 1.25%

based on isolated precipitate strength contributions of $520\sqrt{f_v}$ (MPa) that is root sum square superimposed with ≈ 175 MPa of unirradiated (and unchanged) obstacle strength contributions. However the wide range of unirradiated yield stress values and microstructures for the steels in this study complicate a more detailed analysis.

Table 5.1.4 shows the bulk Ni and Mn compositions, and the precipitate Ni, Mn and Si compositions for the alloys in this study along with the corresponding f_v and $\Delta\sigma_y$. Figure 5.1.5 shows that $\Delta\sigma_y \approx 314\sqrt{f_v}$.

Table 5.1.4. Bulk Ni and Mn compositions and precipitate Ni, Mn and Si compositions (at%), along with f_v and $\Delta\sigma_y$

Alloy	Bulk (%)*		Precipitate (%)				f_v(%)	$\Delta\sigma_y$(MPa)
	Ni	Mn	Cu	Ni	Mn	Si		
A35	0.19	1.34	1.3	26.4	42.4	30.0	0.11	138
A1	0.24	0.24	1.5	37.1	14.6	46.8	0.08	100
A39	0.75	0.80	0.8	46.8	19.7	32.7	0.29	172
A22	1.62	1.23	0.8	54.1	26.5	18.6	0.89	291
A17	3.50	1.04	0.9	62.8	23.9	12.5	2.44	472
A19	1.80	0.24	1.0	64.4	5.1	29.4	0.42	235
A48	3.45	0.48	1.0	69.2	12.5	17.2	1.41	320[+]
A26	3.40	0.22	0.9	73.5	4.7	20.8	0.69	260
A34	3.39	0.06	0.9	75.9	1.2	22.0	0.44	169[+]

**Plus 0.39 – 0.49% Si (%) [+]Shear punch and microhardness $\Delta\sigma_y$ averaged*

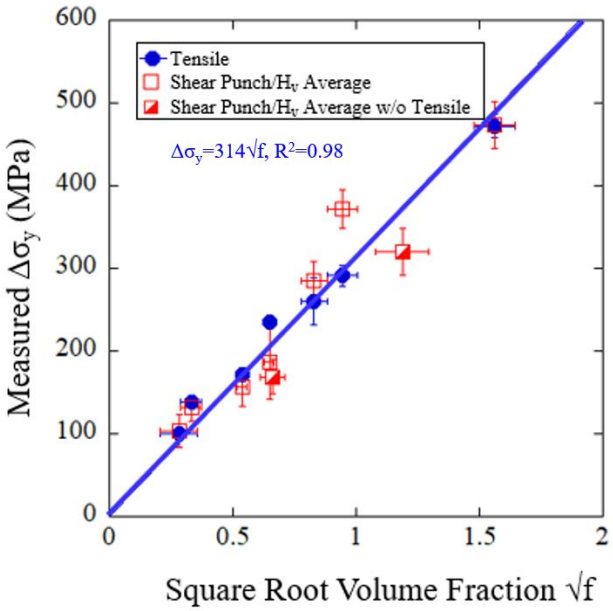

Figure 5.1.5. The measured $\Delta\sigma_y$ plotted as a function of the $\sqrt{f_v}$. Note the half-filled squares are cases where there is no tensile test data.

Table 5.1.5 shows the SANS measured precipitate <d>, N, f_v and M/N for 20 ASM alloys. The ASM alloys show very large ranges of M/N, and a number of them have M/N > 10 or < 1.5. In contrast, the UCSB and surveillance matrices found much lower M/N where most M/N fell between 1.5 and 2.5, see Appendix B. The large variation of M/N ratios for ASM matrix is due to the wide range of compositions in the ASM, hence, corresponding differences in precipitate compositions and phases, see Figure 5.1.6. For example, the precipitates in A34 and A26 have compositions of approximately Ni_3Si, while in SANS they have M/N of 19.3 and > 100, respectively. The scattering length of the Ni_3Si precipitates similar to that of the Fe matrix, so the corresponding scattering contrast is small, leading to very large M/N assuming these features are not magnetic. The two unknowns are the actual phase and corresponding atomic density and the magnetization of the precipitate, if any. The APT composition information allows us to relate these phases to thermodynamic phases in the following section.

Table 5.1.5. Small Angle Neutron Scattering precipitate <d>, N, f_v, and M/N for the measured ASM alloys from cup 8.

Alloy	<d> (nm)	+/-	N (m^{-3})	+/-	f (%)	+/-	M/N
A1	3.84	0.19	1.20E+22	3.00E+21	0.04	0.01	9.96
A4	4.64	0.23	7.58E+21	1.90E+21	0.04	0.01	10.87
A10	2.24	0.11	3.00E+24	7.50E+23	1.77	0.27	1.78
A14	3.86	0.19	4.50E+23	1.13E+23	1.35	0.20	1.17
A17	2.28	0.11	2.90E+24	7.25E+23	1.82	0.27	1.69
A18	2.70	0.14	2.25E+24	5.63E+23	2.31	0.35	1.93
A20	2.28	0.11	3.00E+23	7.50E+22	0.19	0.03	10.68
A21	2.92	0.15	1.10E+23	2.75E+22	0.15	0.02	15.22
A22	2.22	0.11	9.40E+23	2.35E+23	0.54	0.08	1.54
A26	2.26	0.11	6.30E+23	1.58E+23	0.39	0.06	19.3
A28	2.52	0.13	6.30E+23	1.58E+23	0.53	0.08	22.9
A32	1.49	0.07	1.25E+24	3.13E+23	1.72	0.26	1.31
A33	2.20	0.11	5.70E+23	1.43E+23	0.32	0.05	13.6
A34	3.04	0.15	9.10E+22	2.28E+22	0.13	0.02	> 100
A35	2.22	0.11	1.21E+23	3.03E+22	0.09	0.01	0.98
A37	2.50	0.13	7.70E+22	1.93E+22	0.06	0.01	1.36
A39	2.58	0.13	1.39E+23	3.48E+22	0.13	0.02	1.65
A42	1.74	0.09	1.74E+24	4.35E+23	0.49	0.07	3
A47	1.78	0.09	1.10E+24	2.75E+23	0.32	0.05	3.44
A48	2.16	0.11	1.50E+24	3.75E+23	0.81	0.12	2.8

Phase Selection

The ternary Mn-Ni-Si *projection* (see schematic quaternary figure insert) of the Fe-Mn-Ni-Si quaternary CALPHAD based phase diagram at 277°C is shown in Figure 5.1.6 [19,105][(v)]. Note there is no significant difference between the CALPHAD predictions at 277 and 290°C. The filled symbols are the average compositions of the precipitates in the various alloys. With one exception CALPHAD predicts that the precipitates do not contain Fe, consistent with experiment[87,88]. The exception is that at very low Mn, CALPHAD predicts the formation of $L1_2$ Ni_3Fe phase. The open symbols specify the relative dissolved Mn-Ni-Si

compositions in the unirradiated bulk matrix Fe-Mn-Ni-Si ferrite phase, and *they do not represent phases that actually lie in the ternary Mn-Ni-Si projection*. These relative bulk solute compositions are included *only to illustrate how they relate to the precipitate compositions*. Thus the arrows should not be confused with compositions crossing phase boundaries, as the various tie lines are between the matrix (top of the tetrahedron – see insert) and the precipitate phases. Figure 5.1.6 shows that in 8 out of the 9 cases the precipitate Si fraction is higher than the Si solute fraction in the unirradiated bulk. For typical RPV steel compositions (e.g., ≈ 0.7% Ni, > 1.0% Mn, and 0.4%-0.8% Si), CALPHAD predicts the predominant selection of G-phase ($Mn_6Ni_{16}Si_7$) or Γ_2 phase (Mn_2Ni_3Si).

Note the CALPHAD database used in this case effectively either only predicts stoichiometric phases, or in some cases a narrow phase field. However the actual precipitate compositions vary somewhat with the corresponding alloy bulk composition, suggesting that there may be larger G and Γ_2-phase fields, which primarily extend towards higher Mn and lower Ni, over a range of Si. Such composition variations are to be expected, and can be the result of both the higher chemical potentials of the dissolved solutes in a matrix that is still supersaturated (e.g., the system is not fully decomposed in an equilibrium condition), as well as composition dependent interface energy Gibbs-Thomson effects on the precipitates free energies. Thus the free energy of the system is reduced over a range of precipitate compositions, even if the fully decomposed equilibrium phase is stoichiometric. This concept is illustrated in section 5.1.6 using a binary alloy analog. It is important to emphasize that while the structural identities of both these phases have been confirmed by X-ray diffraction measurements for very high fluence irradiations [106], they have not yet been demonstrated for the MNSPs in this study. Thus, in this case, while we note compositional adjacency to

various specific phases, we do not claim the precipitates have the corresponding crystal structures. And we cannot rule out the possibility that the precipitate compositions slightly modified by radiation induced segregation.

As shown in Figure 5.1.7, the precipitate compositions vary in a way such that increases in Mn lead to decreases in Si, at a ratio of ≈ 0.4 to 0.6 lower Si/higher Mn numbers of atoms (that is a 10% increase in Mn lead to a 4 to 6% decrease in Si). These variations mirror the effect of bulk alloy Mn and Si variations. The individual supersaturated solute chemical potentials also explain why the precipitate compositions vary with the alloy bulk chemistry, and the observed tradeoff on the Mn-Si sublattice. The stoichiometric G and Γ_2 phases have (Mn +Si)/Ni ratios of ≈ 0.8 to 1, respectively. Given this rough Mn - Si tradeoff, it is to be expected that f_v would approximately scale with ≈ 1.6 to 2Ni at full decomposition. Indeed, in the nearly fully precipitated case, at very high fluence, $f_v \approx 1.38Ni + 0.49$ in the six core alloys discussed in [32] with G and Γ_2-phases. Again, this relation holds at nearly full decomposition, and only if the Mn alloy content is sufficient to form G and Γ_2 phases. At the lower fluence in this study, $f_v \approx 0.71Ni - 0.16$ for alloys with ≈ 1.2% Mn. Note, that even when nearly fully decomposed, the nm scale precipitate f_v is less than the equilibrium values due to the Gibbs-Thomson effect.

To reiterate, Figure 5.1.6 simply intended to point out the location of the APT data on the ternary projection relative to possible phases. We made no claims they are specific equilibrium phases, since we have not explicitly measured their crystal structures in these particular alloys. Rather we simply attempt to note their compositional adjacencies (or lack thereof). For example the compositions of three 1.7-3.5 Ni low < 0.25 Mn alloys (A19, 24 and 34) are clearly compositionally adjacent to Ni-silicide phases. The low Ni and Mn alloy (A1)

is compositionally adjacent to the MnSi phase field. The low Ni, high Mn alloy (A35) is compositionally adjacent to the T8 phase field. One high Ni and Mn alloy (A22) is compositionally between G and Γ_2 phases. Two others with very high 3.5Ni and intermediate 0.5 to 1Mn alloys (A17, 39) are compositionally further from stoichiometric G or Γ_2 phase compositions, and have higher Ni contents ($\approx$ 12% higher). Finally, the medium 0.7 Ni intermediate 0.8 Mn alloy has Ni similar to the Γ_2 phase field, but lower than the G-phase. All of this seems thermodynamically reasonable. Again note the composition of the nm-scale precipitates may be affected supersaturated solutes and the interface energy that is, in turn, a function of the interface composition. Thus small to modest deviations from nominal stoichiometric compound compositions are to be expected. And even if they have not been modeled, various stoichiometric phases may actually have finite composition fields. Further, as seen in in Figure 5.1.6, and found in LMC studies of the B2 Mn-Ni-Si phase, Mn and Si are relatively interchangeable on their sublattice and thus react to the solutes chemical potential variations in the matrix. However, we have not made claims for this or that specific phase.

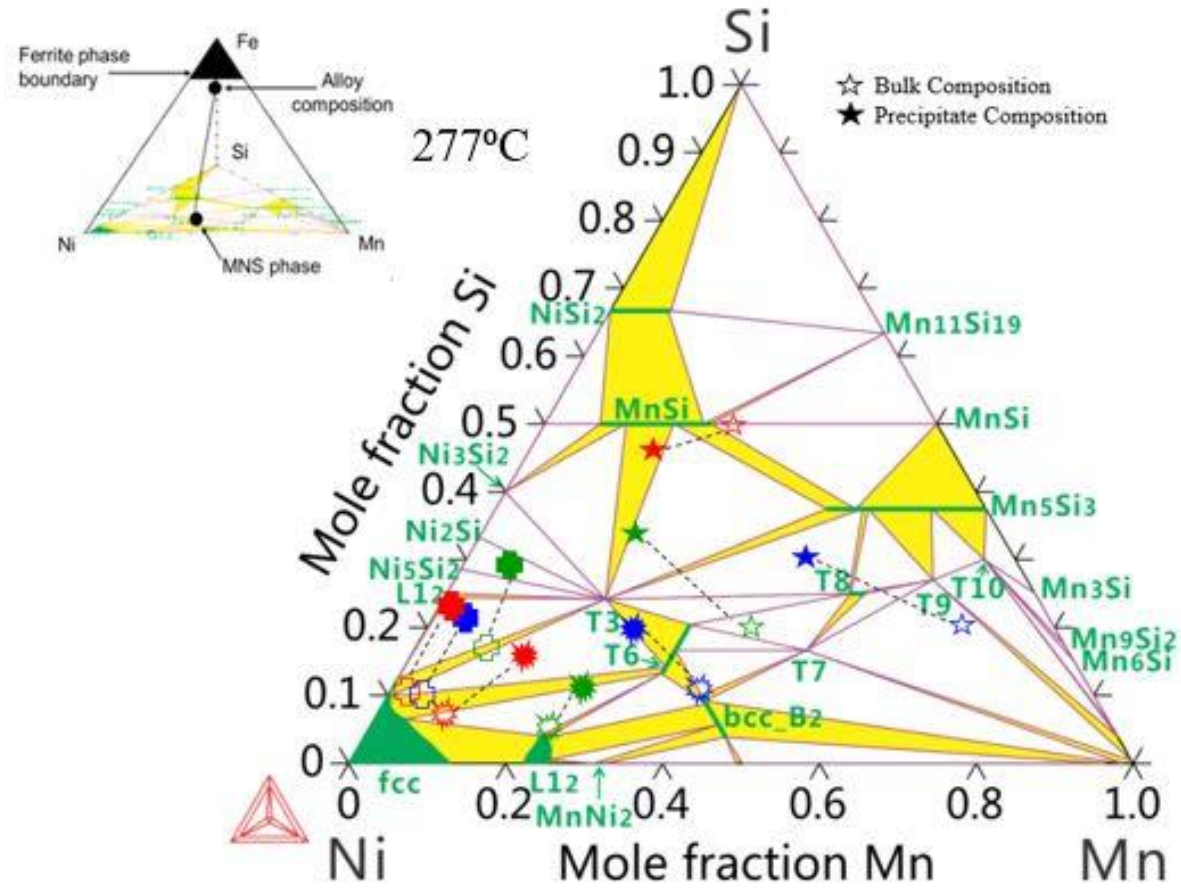

Figure 5.1.6. Bulk matrix and precipitate compositions plotted on the Mn-Ni-Si ternary projection of the Fe-Mn-Ni-Si phase diagram at 277°C. The APT measured precipitate compositions are filled symbols and the corresponding bulk alloy Mn-Ni-Si compositions are unfilled symbols [19,105]. Note, the open symbols are the relative fractions of dissolved solutes in the matrix ferrite phase, at the top of the tetrahedron, and they are not in the Mn-Ni-Si projection. The open symbols are only meant to show how the precipitate compositions relate to the solutes in the bulk. The dashed lines between the open and closed symbols are not tie lines[(v)].

While widely different alloy compositions result in different phase composition selection, it is useful to seek a chemistry (composition) factor that correlates the precipitate f_v data for all 9 of the very diverse steels in this study. A natural choice is Ni^nMn^m (since Si is approximately constant), which reflects the thermodynamic reaction product driving

precipitation (or an effective supersaturation) [19]. For example for the Γ_2 phase the reaction is

$$3Ni(S) + 2Mn(S) + 1Si(S) \leftrightarrows Ni_3Mn_2Si$$

Here S indicates a dissolved solute. The corresponding reaction product is $K_\Gamma(T)[X_{ni}]^3[X_{mn}]^2[X_{si}]$. For the G phase the precipitation reaction

$$16Ni(S) + 6Mn(S) + 7Si(S) \leftrightarrows Ni_{16}Mn_6Si_7$$

The corresponding reaction product is $K_G(T)[X_{ni}]^{16}[X_{mn}]^6[X_{si}]^7$. Here, the K(T) are the temperature dependent reaction constants. Reducing these exponents to the n/m ratios, gives 2.67 for the G-phase and 1.5 for the Γ_2 phase. Figure 5.1.8 shows a least square fit to f_v as a function of Ni^nMn^m, that yields $n \approx 1.6$ and $m \approx 0.8$. Thus the observed n/m ratio of 2, which is close to the average, which is 2.08 for stoichiometric G and Γ_2 phases. Note, this should be considered an empirical observation, and a more detailed thermodynamic analysis will be needed to fully explain the relation, especially for Ni silicide phase compositions, in steels with low Mn contents.

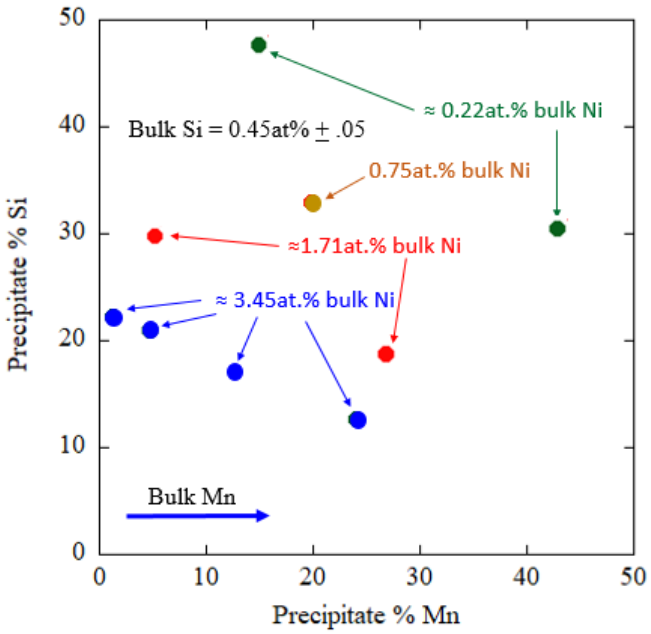

Figure 5.1.7. Precipitate composition Mn-Si variations, for different Ni groupings.

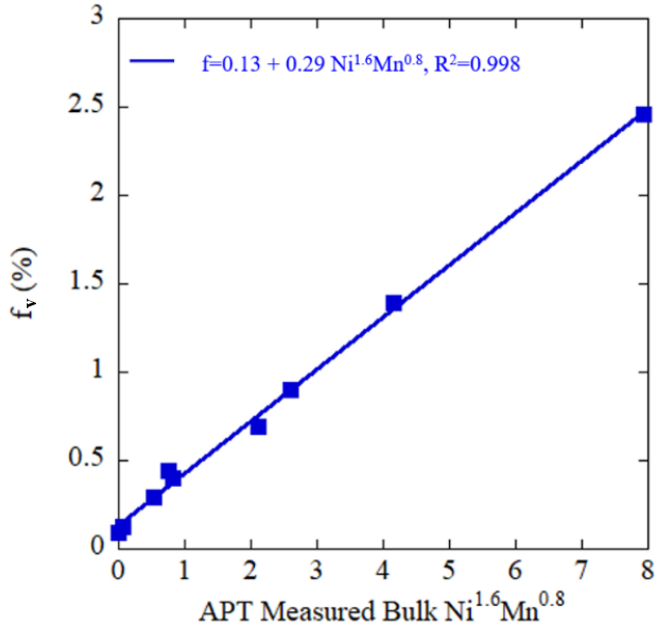

Figure 5.1.8. The Ni^nMn^m reaction product versus average f_v, and a least square fit to the data points for the 9 very compositionally diverse alloys in this study.

Perhaps most importantly, however, the results of this study clearly show that for the very high 3.5% Ni steels, low Mn greatly reduces the amount of precipitation, in a way that can be thermodynamically qualitatively understood. However, even at low Mn, Ni-silicide phases form in lower, but still significant, quantities. For example, f_v is ≈ 0.69% for the 3.4% Ni, 0.22% Mn, 0.39% Si steel. We do not yet have APT data on steels with lower Si, but there is no significant effect of this element on $\Delta\sigma_y$ in the overall ATR-2 database. For example, in the case of 3.5% Ni steels with ≈ 0.25 Mn, the H_v based $\Delta\sigma_y$ actually decreases, but by only 21 MPa, in going from 0.38 to 1.28% Si; and for 3.5% Ni steels with ≈ 0.06 Mn, $\Delta\sigma_y$ decreases 3 MPa in going from 0.38 to 1.28% Si. These differences are insignificant and well within the data scatter.

Non Stoichiometric Phase Compositions

The nm-scale precipitates cannot be expected to have the same composition as bulk equilibrium phases due to the Gibbs-Thomson effect and compositionally dependent interface energies, even if their structure phase is the same as that of the bulk equilibrium phase. Further, in this case the alloys are not fully decomposed; that is they remain supersaturated. Thus the chemical potentials remain higher in solution than at equilibrium. For any reasonable intermetallic free energy curve, this provides thermodynamic access to a wider range of compositions, that still reduce the free energy G. This is schematically illustrated in Figure 5.1.9a for a binary with a terminal phase – AB intermetallic phase. The green line represents the equilibrium condition while the red line is for the partially decomposed state. The Gibbs-Thomson effect shifts the G-curve up in energy and typically to lower X_B due to the composition dependence of the interface energy (red dashed line). Thus a range of compositions is thermodynamically accessible. Further, the precipitate composition would be

expected to vary with the chemical potential of the various dissolved solutes as governed by Henry's law. That is more dissolved/supersaturated matrix Ni would lead to more precipitate Ni (or Mn or Si). Figure 5.1.9b APT shows the range of compositions narrows with increasing precipitate size as would be expected from the considerations outlined above. Note that in this case the composition of the precipitates are 10% lower in Ni and 10% higher in Mn + Si (that trade-off), which does not seem that large a deviation.

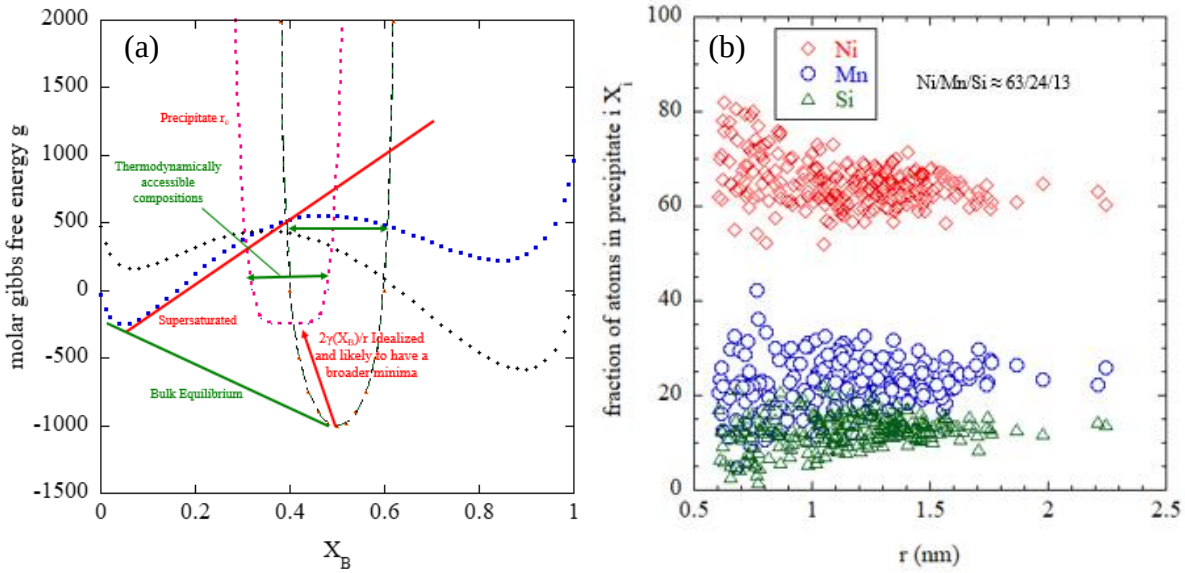

Figure 5.1.9. (a) Molar gibbs free energy curves for a binary with an AB intermetallic phase (b) APT spread in 3.5% Ni 1.0at% Mn alloy of precipitate composition plotted against precipitate radius

5.1.4 Summary and Conclusions

This section reports on the results of characterization of MNS precipitates by APT and irradiation hardening ($\Delta\sigma_y$) by tensile, shear punch and microhardness tests in specially prepared heats of compositionally tailored RPV-type steels, with a wide range of systematically varying Ni and Mn compositions and an approximately constant Si content, that were irradiated to a high fluence $1.4x10^{20}n/cm^2$ at 290°C in the Advanced Test Reactor. Analysis of the data leads to the following conclusions.

- Significant volume fractions (f) of MNSPs form in all of the steels at the high ATR fluence
- While Ni generally plays the strongest role in the formation of MNSPs, f_v and $\Delta\sigma_y$ increase synergistically and systematically with Mn, especially at higher Ni.
- In the absence of sufficient Cu and low to intermediate Ni, the MNS precipitates have difficulty nucleating homogeneously in a defect free matrix, and microstructural features such as network dislocations and irradiation induced interstitial loops act as heterogeneous nucleation sites.
- The wide range of compositions in the 9 alloys results in very different precipitate compositions - for example, near G ($Mn_6Ni_{16}Si_7$) or Γ_2 (Mn_2Ni_3Si) phases in alloys with 0.75% to 1.62% Ni with $\geq$ 0.8% Mn, versus Ni-silicide type compositions in alloys with very low $\leq$ 0.24 Mn and high $\approx$ 1.6 to 3.4% Ni. Note that the G and Γ_2 phases have been identified at high fluence at typical RPV compositions, the specific phase structures not yet confirmed identified in this work.
- The Mn and Si in the precipitates roughly trade off depending on the alloy Mn content.

- At normal levels of > 1% Mn, very large MNS precipitate f_v form in 3.5% Ni advanced steels at high fluence.
- However, f_v decreases approximately linearly with the alloy Mn content, and is found to vary as $f_v \approx 0.13 + 0.3Ni^{1.6}Mn^{0.8}$.
- Thus precipitation hardening is much lower in high ≈ 3.5% Ni < 0.3% Mn steels due to Mn starvation.
- The $\Delta\sigma_y$ is well correlated with the $\sqrt{f_v}$ and can be understood based on dispersed barrier hardening models.

5.2: Surveillance Steel Microstructural Characterization

5.2.1 Introduction

This section reports on the results of characterization of CRP and MNS precipitates by APT in specially procured heats of RPV surveillance and program steels, with a wide range of systematically varying Cu, Ni, Mn and Si that were irradiated to a high fluence $1.4x10^{20}n/cm^2$ at 290°C in the ATR-2. Nine surveillance materials were procured specifically for this experiment. In addition, eleven other archival surveillance alloys, which had been previously studied by UCSB in IVAR, were also included for a total of twenty-two surveillance alloys. While flux effects have been extensively studied for many years, they are still not fully understood. Thus, the surveillance alloys will allow for direct comparison of results from this high-flux test irradiation with those from the much lower flux surveillance irradiations.

5.2.2 Materials and Methods

See Chapters 3-4, Tables 3.3-4 and Appendix C for Materials and Methods supplemental information.

5.2.3 Results and Discussion

Figure 5.2.1 shows an example of APT solute maps for the high Cu, medium Ni weld SW6 (0.30% Cu, 0.60Ni, 1.30Mn, 0.50Si in at%). APT found $f_v \approx 0.67\%$ of 2-3 nm Cu-Ni-Mn-Si precipitates. CRP-MNSPs are well defined at high number densities. Figure 5.2.2 shows solute maps and f_v for the program alloy FE with 0.01% Cu, 1.70% Ni, 1.30% Mn, 0.20% Si demonstrating that MNSPs form even in the absence of a significant amount of Cu at high fluence, especially at high Ni. Table 5.2.2 summarizes the average APT bulk, matrix and MNSP compositions for the 9 new surveillance and 3 program alloys. The measured bulk

solute values are in reasonably good agreement with the nominal alloy compositions for Cu, Ni, and Si (see Table 3.3).

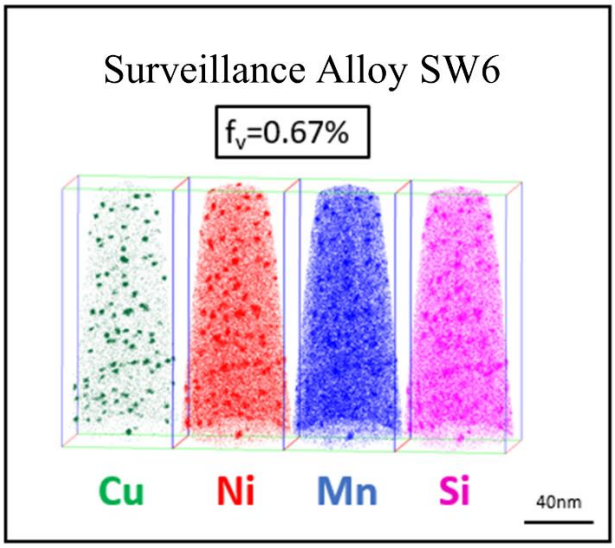

Figure 5.2.1. APT solute maps for a high Cu, medium Ni weld SW6 (0.30% Cu, 0.60Ni, 1.30Mn, 0.50Si in at.%). APT found $f_v \approx 0.67\%$ of 2-3 nm Cu-Ni-Mn-Si precipitates.

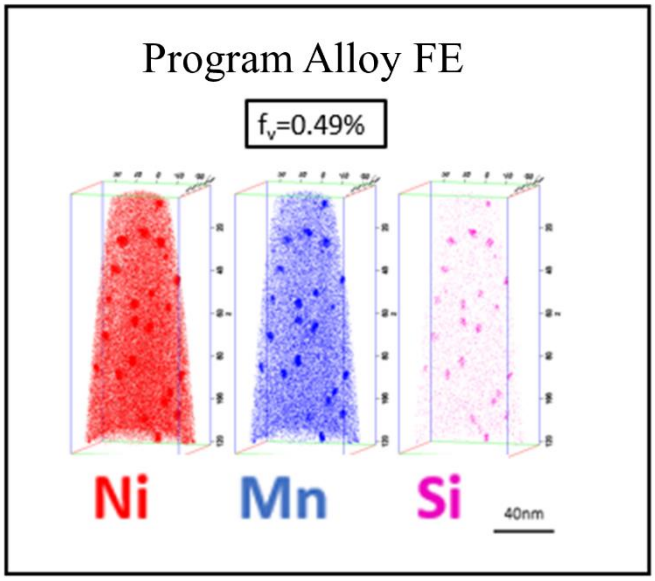

Figure 5.2.2. APT solute maps for an irradiated low 0.01Cu, high 1.70Ni, 1.30Mn, 0.20Si program plate (FE) with $f_v \approx 0.49\%$.

Comprehensive APT analysis includes the mapping of precipitate size distributions, quantifying segregation of Cu-Ni-Mn-Si-P and examining precipitate nucleation on dislocations and loops that are made visible by their solute atmospheres. For example, Figure 5.2.3 shows APT solute maps of Mn-Ni-Si in a low (0.04% Cu), medium-high (0.95% Ni) surveillance weld, SW5. Segregation of the solutes, especially Si, to what appears to be a helical dislocation and perhaps another dislocation segment are obvious. Precipitates form in the segregated regions. These associations are more clearly shown by the 4% Si isoconcentration surfaces. The compositions of the precipitates on dislocations are similar to those in the matrix. A general observation is that MNSPs in low Cu and medium Ni steels predominantly heterogeneously nucleate on dislocations, loops and grain boundaries. Indeed, matrix MNSP may nucleate on small loops and envelope them during growth. Future work includes S/TEM mapping of precipitate-dislocation interactions, as well as measuring dislocation loop densities and quantifying solute segregation at various microstructural features. These results will inform the advanced thermo-kinetic models of MNSP precipitation being developed in our collaboration with Professor Dane Morgan's group at the University of Wisconsin.

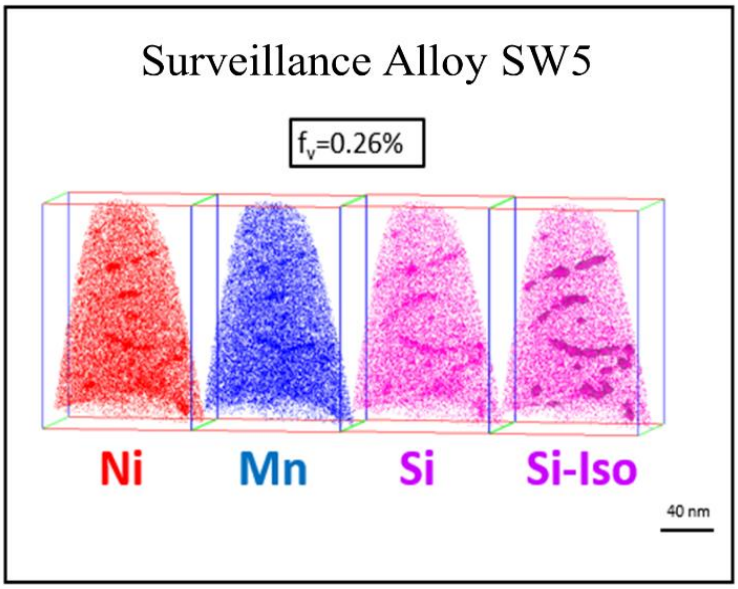

Figure 5.2.3. APT solute maps for an irradiated low 0.04Cu, medium-high 0.95Ni, 1.40Mn, 0.45Si surveillance weld (SW5) showing solute segregation and precipitation on dislocations with $f_v \approx 0.26\%$.

A summary of APT compositions for the 9 new surveillance and 3 program alloys is shown in Table 5.2.1. This table shows that all alloys with bulk Cu > 0.15% form precipitates rich in Cu (15-35% Cu) and deplete the matrix Cu to ≈ 0.06-0.07%. This is consistent with previous studies that show that well defined Cu precipitates (CRPs) will form only at Cu levels ≥ 0.07% [55]. Though CRPs may not form, Cu still has a catalyzing effect for formation of MNSPs even at levels < 0.07%. Table 5.2.2 shows the precipitate <d>, N and f_v for the surveillance alloys. Figure 5.2.4 shows the APT f_v as a function of the alloy bulk Cu content for the surveillance and program alloys. Increased Cu leads to significantly increased precipitate f_v at typical Ni contents of 0.5 – 1.0%, but this effect is decreases at lower Ni contents (0 – 0.49%).

Table 5.2.1. APT bulk, matrix and precipitate compositions for 9 surveillance alloys and 3 program alloys in the cup 7 irradiated condition.

Alloy	Bulk				Matrix				Precipitate			
	Cu	Ni	Mn	Si	Cu	Ni	Mn	Si	Cu	Ni	Mn	Si
SW1	0.15	0.13	0.86	0.40	0.06	0.10	0.82	0.35	35.0	15.4	30.0	19.6
SB1	0.16	0.59	0.87	0.55	0.06	0.42	0.78	0.45	21.4	35.7	20.4	22.4
SB2	0.04	0.61	0.55	0.51	0.04	0.55	0.54	0.46	2.0	46.8	12.3	38.9
SW2	0.19	0.78	1.09	0.37	0.06	0.50	0.94	0.26	20.9	36.7	25.0	17.5
SB3	0.04	0.47	0.88	0.51	0.04	0.39	0.84	0.44	1.4	38.9	22.1	37.7
SW3	0.27	0.70	0.90	0.40	0.06	0.46	0.75	0.28	28.0	33.6	21.4	17.0
SW4	0.03	0.92	0.99	0.94	0.03	0.77	0.93	0.82	0.6	44.0	19.5	35.9
SW5	0.03	0.79	1.06	0.79	0.03	0.68	1.02	0.71	0.4	44.9	18.2	36.5
SW6	0.23	0.58	1.19	0.92	0.07	0.39	1.06	0.77	25.0	29.1	21.7	24.2
EC*	0.25	0.61	0.97	0.36	0.04	0.44	0.85	0.27	23.2	33.5	26.5	16.8
ED*	0.24	0.57	1.05	1.00	0.13	0.44	0.91	0.91	8.7	25.0	28.5	37.9
FE*	0.00	1.70	1.02	0.08	0.00	1.48	0.90	0.06	0.1	60.3	32.0	7.7

**Program Alloy*

Table 5.2.2. APT precipitate <d>, N and f_v for 9 surveillance and 3 program alloys.

Alloy	APT Bulk Composition				<d>	+/-	N	+/-	f	+/-
	Cu	Ni	Mn	Si	(nm)	(nm)	(10^{23} m^{-3})	(10^{23} m^{-3})	(%)	(%)
SW1	0.15	0.13	0.86	0.40	2.94	0.20	1.90	0.51	0.25	0.03
SB1	0.16	0.59	0.87	0.55	2.95	0.02	3.88	1.00	0.49	0.05
SB2	0.04	0.61	0.55	0.51	2.32	0.16	1.95	0.31	0.14	0.07
SW2	0.19	0.78	1.09	0.37	3.32	0.20	3.64	0.86	0.66	0.14
SB3	0.04	0.47	0.88	0.51	2.60	0.52	8.02	0.50	0.21	0.15
SW3	0.27	0.70	0.90	0.40	3.11	0.21	4.11	0.61	0.75	0.05
SW4	0.03	0.92	0.99	0.94	2.50	0.08	3.78	0.40	0.37	0.04
SW5	0.03	0.79	1.06	0.79	2.40	0.07	3.18	0.51	0.25	0.03
SW6	0.23	0.58	1.19	0.92	2.83	0.05	5.73	0.15	0.67	0.01
EC*	0.25	0.61	0.97	0.36	3.02	0.22	3.78	0.18	0.53	0.08
ED*	0.24	.57	1.05	1.00	2.19	0.14	2.99	0.15	0.61	0.03
FE*	0.00	1.70	1.02	0.08	3.26	0.50	2.59	0.60	0.39	0.11

** Program Alloy*

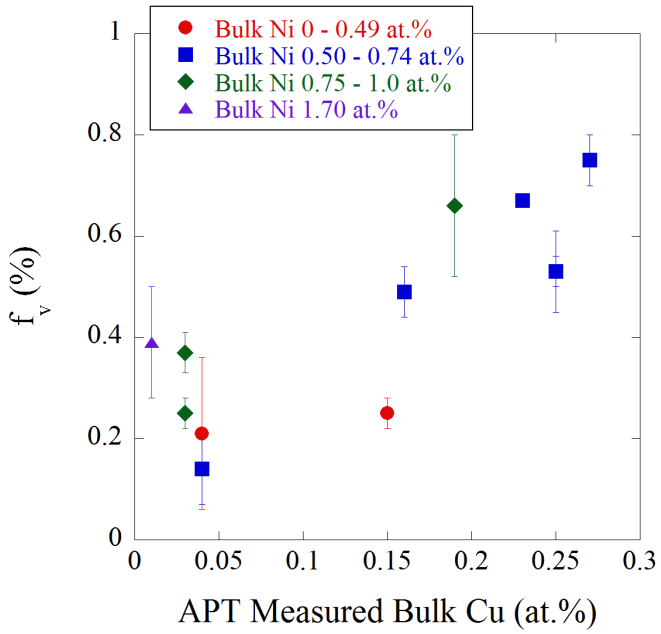

Figure 5.2.4. APT f_v versus the measured bulk Cu content (%) for the surveillance and program alloys showing the strong effect of both Cu and Ni.

Figure 5.2.5 shows precipitation hardening plotted in terms of the square root of precipitate volume fraction ($\sqrt{f_v}$). The increased yield stress were derived from both hardness and tensile tests. Changes in μH_v were used to estimate the corresponding changes in yield stress ($\Delta\sigma_y$) based on a nominal relation, $\Delta\sigma_y$ (MPa) = 3.33*$\Delta\mu H_v$ (kg/mm^2) [66].

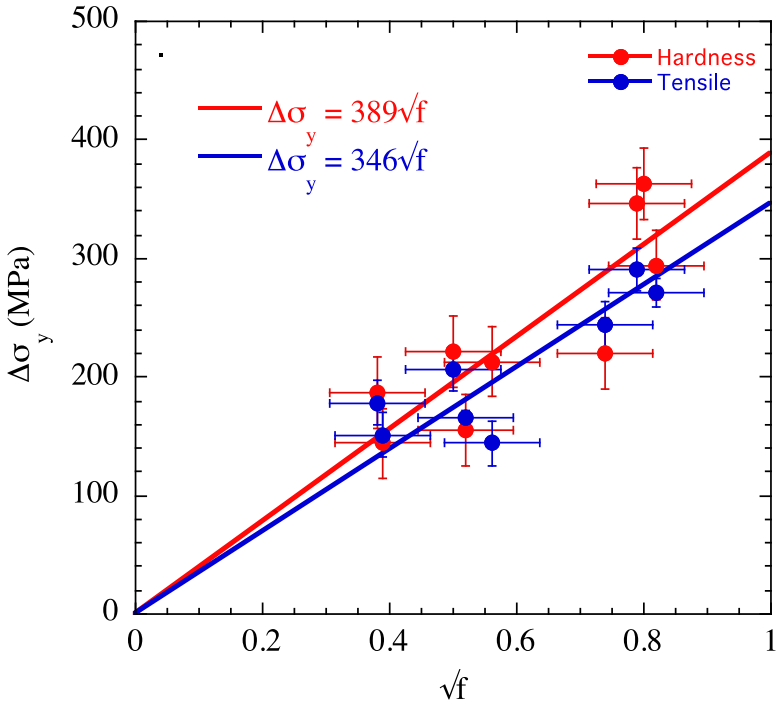

Figure 5.2.5. Precipitation hardening plotted in terms of increase in yield stress derived from both hardness and tensile tests versus the square root of APT precipitate volume fraction ($\sqrt{f_v}$)

Figure 5.2.6 plots the SANS and APT f_v for surveillance steels with representative compositions as in-service reactors. SANS and APT techniques show excellent agreement of the precipitate f_v. The SANS f_v results are approximately 10% lower. The possible sources of error include APT local compositional inhomogeneity and assumptions regarding the magnetic nature of precipitates. The additional SANS results are measuring f_v, <d>, N and M/N and found in Appendix A.

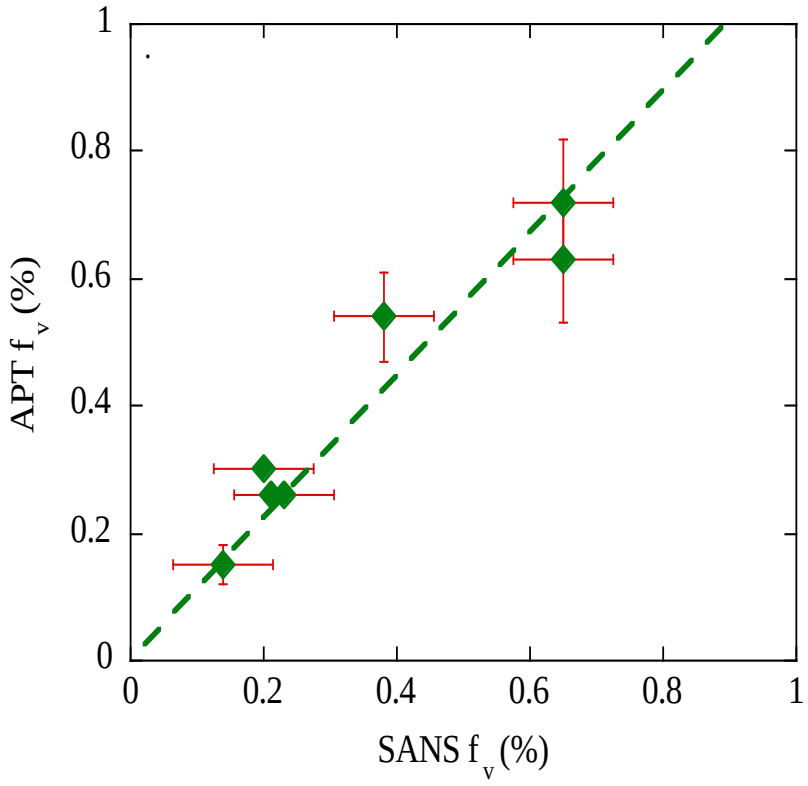

Figure 5.2.6. SANS and APT f_v plotted for surveillance steels.

5.1.4 Summary and Conclusions

Analysis of the data leads to the following conclusions.

- Significant volume fractions (f) of CRPs and MNSPs form in all of the surveillance steels at the high ATR fluence.
- In Cu bearing steels, the CRPs first grow rapidly to a saturated plateau f_v, at dissolved matrix Cu depletion, followed growth of MNSPs at higher fluence.
- The precipitates first grow with a CRP core Mn-Ni-Si shell structure, but the MNSPs later transform to discrete ordered intermetallic appendages at higher fluence.
- In the absence of sufficient Cu and low to intermediate Ni, the MNS precipitates have difficulty nucleating homogeneously in a defect free matrix, and microstructural

features such as network dislocations and irradiation induced interstitial loops act as heterogeneous nucleation sites.

- At typical Mn and Si levels and low <0.07%Cu steels, both N and f_v increase roughly linearly with increasing Ni. For the high >0.2%Cu steels <d> and f_v linearly increases with Cu.
- The total f_v is relatively insensitive to variations in Si and P
- This large database of microstructural observations developed in this work formed the foundation for developing detailed thermo-kinetic models of precipitation in RPV steels under irradiation.

Acknowledgements

(i) Professor Peter Hosemann provided FIB access for active specimens at UC Berkeley.
(ii) Keith Wilford, Tim Williams and Nick Riddle at Rolls Royce provided excellent expertise and advice while Rolls Royce procured the ASM.
(iii) Drs. Randy Nanstad, Philip Edmondson and Keith Leonard, and Janet Robertson at ORNL provided advice, mentorship and technical support.
(iv) Dr. Peter Wells provided crucial MATLAB coding, mentorship, collected part of the APT data (Section 5.2) and hands on training in APT data collection and analysis.
(v) Professor Dane Morgan and Dr. Huibin Ke at the University of Wisconsin provided the thermodynamic phase diagram, phase predictions and modeling insights.

Chapter 6: On the Use of Charged Particles to Characterize Precipitation in Irradiated Reactor Pressure Vessel Steels with a Wide Range of Compositions

6.1.1 Introduction[3]

Here we focus on rapid and convenient charged particle irradiations (CPI) to both: a) compare to precipitates formed in NI; and, b) use CPI to efficiently explore precipitation in steels with a very wide range of compositions. High ϕ material test reactors (MTRs) have been extensively utilized to study RPV embrittlement because they can reach high ϕt in a much shorter time than in a power reactor vessel [5,26]. However, neutron irradiations (NI) of RPV steels to study embrittlement at high, extended life ϕt are costly and time-consuming. In contrast, CPI can be used to rapidly explore the effects of embrittlement variables and mechanisms, typically taking tens of hours to produce 80-year NI damage doses, in units of dpa [63–65]. The charged particle is typically a medium weight ion like Fe^{++}. Heavy ion CPI do not produce radioactive byproducts, thus samples can be handled without any special safety procedures. While they do not simulate neutron embrittlement, CPI provide a rapid and cost effective way to gain insight into precipitation mechanisms. Further, CPI can help to determine which new RPV steel compositions are most likely to be susceptible to the formation of large f_v of MNSPs, thus helping to guide future advanced RPV steel development.

[3] This chapter includes slightly modified text and figures published in N. Almirall, P.B. Wells, T. Yamamoto, K. Yabuuchi, A. Kimura, G.R. Odette, On the Use of Charged Particles to Characterize Precipitation in Irradiated Reactor Pressure Vessel Steels with a Wide Range of Composition, Journal of Nuclear Materials 536 (2020) 152173.

Here we explore the potential of convenient CPI to study microstructural evolutions, with emphasis on the nanoscale precipitates. Limited comparisons show that CPI result in precipitate volume fractions (f) and compositions that are similar to those formed in neutron irradiations (NI). Thus, CPI were leveraged here to characterize precipitation for a matrix of advanced alloys with compositions that extend beyond the typical range the current RPV steels. The focus is on developing so-called super-clean steels, with very high Ni contents (> 3 wt.%), that have superior unirradiated properties [53,99–103]. However, high Ni levels lead to enormous irradiation hardening and embrittlement in RPV steels with typical Mn and Si contents, see Chapter 5.1 [53]. Thus, super-clean steels have much lower Mn (and impurity S) contents, which is aimed at limiting the amount of nanoscale precipitation. The CPI study reported here demonstrates that reductions in Mn do indeed reduce the precipitate f_v, but only to a limited extent. Notably, the CPI can easily reach several dpa resulting in a nearly fully phase separated precipitate volume fractions (f_{vmax}); while such high dpa are well above that experienced by vessels even during extended life, f_{vmax} is a necessary parameter in embrittlement models [4].

However, there are many differences between NI and CPI as noted in the partial list and dpa rates can strongly affect RED accelerated precipitation [3,5,26,27,32,52,65,107–112]. For example, for a fixed set of other variables, far fewer defects escape vacancy-SIA recombination at high dpa rates, thereby reducing the efficiency of RED and defect accumulation. RIS driven precipitation also depends on damage rate, as do the effects of ballistic mixing [109,113]. Further, there are differences between CPI and NI secondary atomic recoil spectra [63]. CPI effects are modified by nearby free surface defect sinks, and experience steep depth gradients in dpa and dpa rates [63,64]. Local dpa rates are also time dependent if

the ion beams are rastered [64]. CPI injects extra interstitials of the bombarding species [63,64]. Finally, accelerator irradiations can also lead to impurity pickup of elements like C [114,115].

Thus one objective of this work was to compare the precipitates formed in RPV steels in both NI and CPI irradiated conditions. This comparison showed that, in general, the differences are moderate. Specifically we directly compare the precipitate average diameters (<d>), number densities (N), f_v and compositions for steels with: a) high 0.24% Cu and 1.03% Ni (LD) and a medium 0.15% Cu and 0.71% Ni (LI) following CPI at ≈ 290°C and NI at ≈ 300°C, both to ≈ 0.2 dpa; b) the same LD alloy NI at 320°C to a high ≈ 1.8 dpa, and CPI irradiated at 290°C to an even higher ≈ 4.0 dpa. While direct comparisons were not possible in the following cases, two other NI low < 0.02% Cu steels, with medium 0.69% Ni (LG) and high 1.71%% Ni (CM6), and 1.15$\pm$0.28 Mn contents, were compared to two other low <0.05% Cu CPI steels with roughly similar respective Ni and Mn compositions (A39 ≈ 0.57% Ni, ≈ 0.91 Mn and A22 ≈ 1.82% Ni, 1.28% Mn). Again, the NI was ≈ 1.8 dpa at 320°C and the CPI was at 290°C to ≈ 4.0 dpa. Note, these A-series steels were also NI in a lower ≈ 0.2 dpa, 290°C irradiation, but comparable dpa CPI data on these alloys is not available. In all cases only a modest differences in composition of the MNSPs was observed. The MNSP f_v was slightly lower in the CPI condition, which is not unexpected due to the high dpa rate, while the corresponding N values are lower and the <d> are somewhat larger.

A second objective of this study was to characterize and analyze the precipitates in new very high Ni (> 3%) alloys formed under CPI as a function of the combined effects of Ni, Mn and Si. The precipitate <d>, N and f_v values generally increase with Mn, Si, Cu and, especially,

Ni. More notably, however, the MNSP f_v increases linearly with the G phase solute product $SP_G = [Ni^{16}Mn^6Si^7]^{1/29}$.

The chapter is structured as follows. The next section reviews the experimental materials and methods. The FIB milling procedures account for the CPI damage depth profile. In the first Results section APT demonstrates the ability of CPI to produce MNSPs with similar f_v and compositions as NI. Supported by these results, the next section summarizes the effects of high dpa CPI on MNSPs in the ASM with a wide range of compositions, including high Ni. Then we carry out a thermodynamic analysis of these results. The final section estimates the irradiation $\Delta\sigma_y$ and ΔT in the CPI at in both nearly fully precipitated and lower dpa NI relevant service conditions. Finally, we summarize the overall results.

6.1.2 Materials and Methods

The compositions and heat treatments of the RPV steels in this section are shown in Table 6.1. The small heat, split-melt steels have microstructures and mechanical properties that are essentially the same as actual RPV steel base metals with similar compositions.

Table 6.1. Nominal steel compositions (%)

Alloy	Bulk at%								
	Cu	Ni	Mn	Si	Cr	Mo	P	C	Fe
LG*	0.00	0.70	1.38	0.43	0.05	0.32	0.01	0.74	Bal.
CM6*	0.02	1.59	1.52	0.34	0.05	0.31	0.01	0.69	Bal.
LD*	0.33	1.18	1.39	0.45	0.07	0.31	0.01	0.88	Bal.
LI*	0.17	0.70	1.38	0.47	0.09	0.32	0.01	0.74	Bal.
A13 †	0.06	3.28	1.49	1.24	0.11	0.30	0.01	1.06	Bal.
A16 †	0.52	3.27	1.52	0.40	0.11	0.30	0.01	1.02	Bal.
A22 †	0.05	1.58	1.51	0.41	0.11	0.30	0.01	1.34	Bal.
A28 †	0.05	3.26	0.25	1.22	0.11	0.31	0.01	1.24	Bal.
A32 †	0.05	3.34	2.08	0.45	0.14	0.30	0.02	1.02	Bal.
A34 †	0.06	3.25	0.08	0.38	0.10	0.28	0.01	1.02	Bal.
A37 †	0.05	0.20	1.49	1.22	0.11	0.30	0.01	1.24	Bal.
A39†	0.03	0.66	1.47	0.41	0.12	0.28	0.01	0.97	Bal.

* Also contains some S and other trace elements. L-series heat treatment: austenized at 900°C for 1 h, air cooled, tempered at 664°C for 4 h, air cooled, stress relieved at 600°C for 40 h, followed by a furnace cooling to 300°C, then air cooled to room temperature. CM heat treatment: tempered at 660°C for 4 h, air cooled, then stress relieved at 607°C for 24 h followed by a slow cool at 8°C/h to 300°C, then air cooled

† A series matrix heat treatment: austenitized at 920°C for 1 h followed by an air cool, then tempered at 600°C for 5 h followed by an air cool.

The NI were carried out in the Belgian Reactor 2 (BR2) at a $\phi \approx 1.0x10^{14}$ n/cm^2-s to a $\phi t \approx 1.3x10^{20}$ n/cm^2 at 300°C [116]; and the Advanced Test Reactor (UCSB ATR-1 experiment) at Idaho National Laboratory at a $\phi \approx 2.3x10^{14}$ n/cm^2-s to a $\phi t \approx 1.1x10^{21}$ n/cm^2 at 320°C [62,117]. This ϕt corresponds to ≈ 0.2 dpa and $1.4x10^{-7}$ dpa/s and ≈ 1.8 dpa and $3.1x10^{-7}$ dpa/s, respectively. These results of these have been partially published previously [32,52]. The target temperature of this irradiation location was 290°C. However, the final INL "as run" irradiation temperature was revised to be ≈ 320°C as reported in [62]. The CPI were carried out at the Dual Beam Facility for Energy Science and Technology (DuET) at Kyoto University in Japan by Dr. Takuya Yamamoto(I see acknowledgements). A rastered beam of 6.4 MeV Fe^{3+} ions produced a peak of 0.6 or 13 dpa at 290°C and a depth of ≈ 1.6 μm in 3.0 mm diameter x 0.5

mm thick disc specimens[4]. The Kinchin-Pease model in the SRIM 2008 code, with a displacement energy of 40 eV, was used for the dpa calculation, as recommended in ASTM E521-96 (2009) [118]. The dpa rate at the APT sampling depth was about ≈ $3.4x10^{-5}$ and ≈ $1.5x10^{-4}$ dpa/s. The sample temperature was controlled using infrared heater on the back of specimen stage and a thermal imaging camera to monitor at the front of the specimens, calibrated with K-type thermocouple measurements on a dummy steel sample. The uncertainty in the irradiation temperature is estimated to be ≈ ± 5°C. The ion beam in the DuET facility is rastered at 300 and 1000 Hz vertically and horizontally, respectively.

Figure 6.1a shows the Focused Ion Beam (FIB) liftouts, which subsequently were sharpened by annular milling to fabricate APT needles with a tip radius of ≈ 50-100 nm. The FIB voltages and beam currents were reduced to 5 kV and 48 pA and 2 kV and 27 pA, respectively, for final cleanup and partial removal of Ga damage layer. Procedures for creating site-specific liftouts and sharpened APT tips by annular milling are described elsewhere [67,119]. The 5 kV cleanup milled the tip to ≈ 500 +/- 50nm depth from the top liftout surface, corresponding to ≈ 0.2 dpa at ≈ $3.4x10^{-5}$ dpa/s and ≈ 4.0 dpa at ≈ $1.5x10^{-4}$ dpa/s. Figure 6.1b shows that at the higher dpa rate the damage profile gradient in this region modest, varying from ≈ 4.0-4.4 dpa over the 150 nm depth sampled. The irradiation conditions are summarized in Table 6.2. We refer to the low and higher dpa rate CPI irradiations as DuET:L and DuET:H, respectively.

[4] Dr. Peter Wells and Nathan Almirall designed a custom sample holder to maximize thermal conductivity during ion irradiation of 36 3 mm diameter disc specimens.

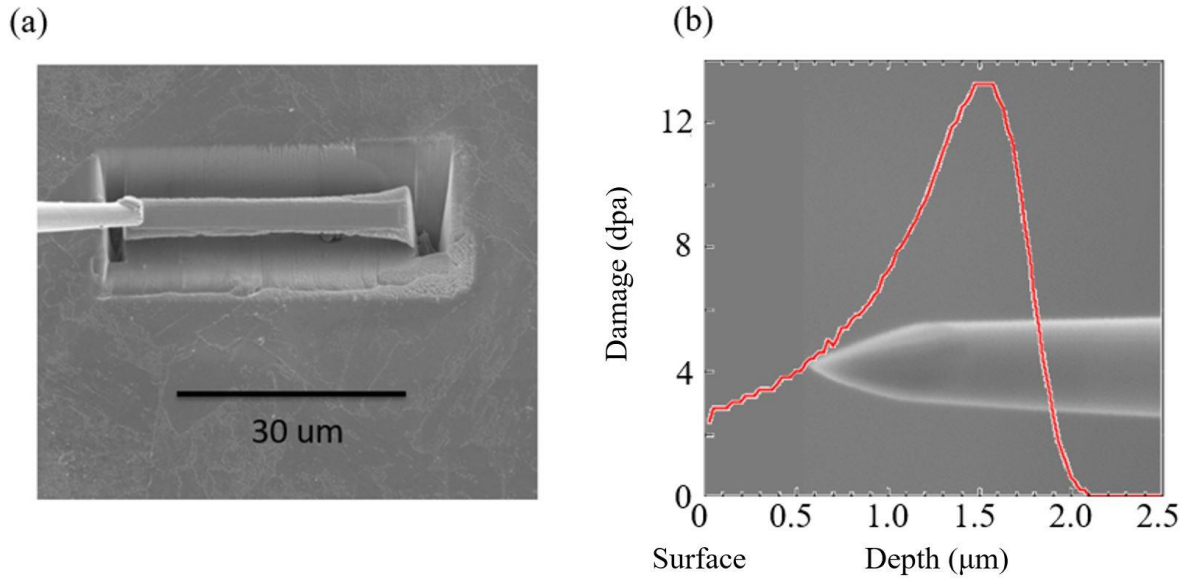

Figure 6.1. a) A scanning electron microscope image showing the FIB liftout from a CPI steel that is subsequently sectioned and mounted onto the micro-tip posts; and, b) annular milling produces a FIB sharpened APT specimen with the SRIM calculated damage (peak of 13 dpa) as a function of depth overlaid [68].

Table 6.2. NI and CPI conditions.

Facility	dpa	Particle	Energy (MeV)	ϕt (n-cm^{-2})	Neutron ϕ (n-cm^{-2}s^{-1})	Dose (dpa)	Dose/dpa Rate (dpa/s)	T_{irr} (°C)
BR2	Low	Neutron	>1	1.3x10^{20}	1.0x10^{14}	0.2	1.4x10^{-07}	300
ATR1	High	Neutron	>1	1.1x10^{21}	2.3x10^{14}	1.8	3.1x10^{-07}	320
DuET:L	Low	Fe^{3+}	6.4	-	-	0.2	3.4x10^{-05}	290
DuET:H	High	Fe^{3+}	6.4	-	-	4.0	1.5x10^{-04}	290

Further information on materials, methods and improvements made to selection of cluster parameters can be found elsewhere, Chapters 3-4 and Appendix C [77].

6.1.3 Results and Discussion

APT Comparisons of the NI and CPI Precipitates

Figure 6.2 shows solute APT maps directly comparing the 0.15% Cu and 0.71% Ni, (LI) and the 0.24% Cu and 1.03% Ni (LD) steels that were NI and CPI at 295±5°C to ≈ 0.2 dpa [52]. We have reported elsewhere [32] that the precipitates track the local composition that varies from tip to tip. Thus the compositions and f_v are the corresponding averages. Unless otherwise noted, the steels in this section contain ≈ 1.04±0.17% Mn and ≈ 0.45±0.1% Si. The relatively homogeneous distribution of quasi-spherical precipitates is qualitatively similar for both irradiation conditions in both alloys. Table 6.3 and Figure 6.3 show the precipitate Mn, Ni and Si compositions in both the CPI and NI conditions are nearly the same for both the LD (25.9±3.8%Cu, 36.9±0.9%Ni, 21.3±3.3%Mn and 15.9±0.4%Si) and LI (23.2±1.0%Cu, 35.2 ±1.0%Ni, 25.3±2.2%Mn and 16.4±2.2%Si) steels. The Si is only slightly higher and Mn slightly lower in the CPI condition. Table 6.4 shows that the main differences are a higher N and f_v in the NI condition, especially for the lower Cu and Ni steel. Figure 6.4 cross plots <d>, N and f_v for both steels in the two-irradiation conditions as a function of the bulk Cu in individual tips (again note, Ni also varies); <d> increases slightly with increasing Cu (and Ni), but is similar for the NI and CPI conditions; N and f_v also increase with Cu (and Ni). These results are qualitatively consistent with trends observed in previous NI studies of Cu bearing RPV steels, showing a large number of CRPs, either with a Mn, Ni and Si shell, or with a MNSP appendage [26,32,53]. The larger f_v in the NI condition is expected due to the much higher CPI dpa rate, which reduces the efficiency of RED. One *seeming* exception to previously observed NI trends, is a lower N for the higher dpa rate CPI case. At lower dpa, the precipitate N generally increases with NI flux, or dpa rate. However, closer analysis of the NI

data shows that this lower dpa trend is not observed at very high dpa and dpa rates (see Figure 6.10 below). Thus the lower CPI N is actually consistent with the high NI dpa trends.

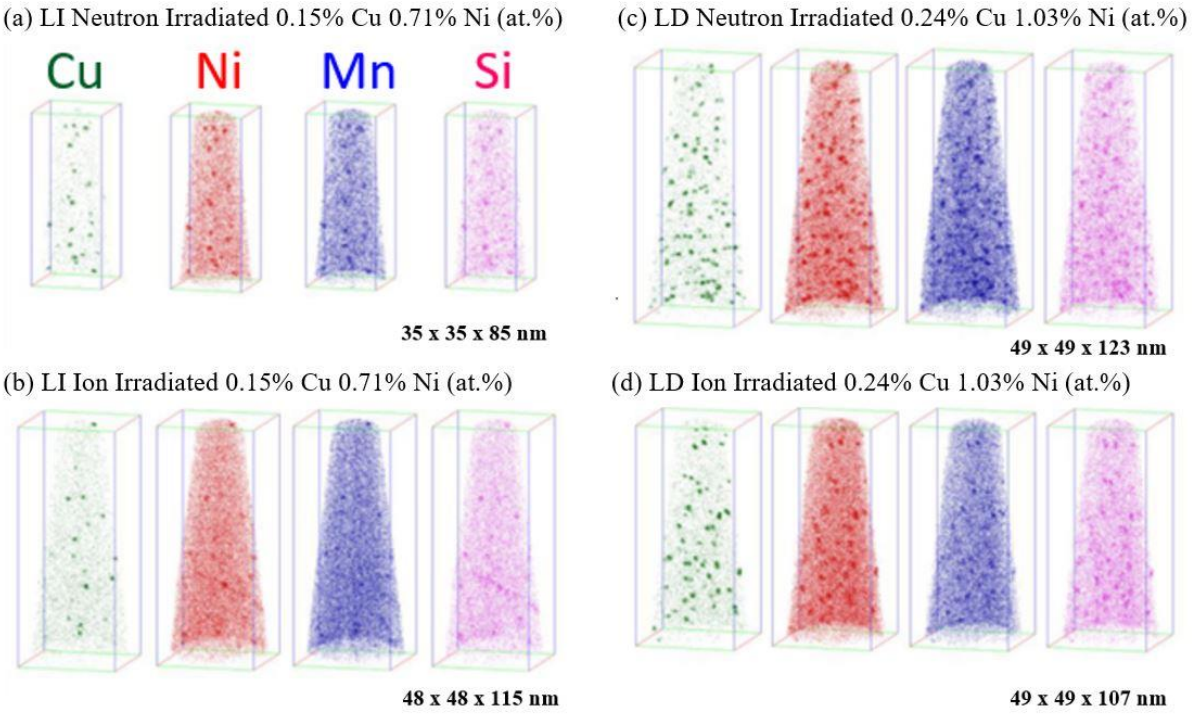

Figure 6.2. Solute maps directly comparing lower dpa ≈ 0.2 dpa CPI (DuET:L) and NI (BR2) conditions at nominally a-b) medium 0.15% Cu and 0.71% Ni (LI); and, c-d) high 0.24% Cu and 1.03% Ni (LD). All compositions are in at.% [52][(ii)].

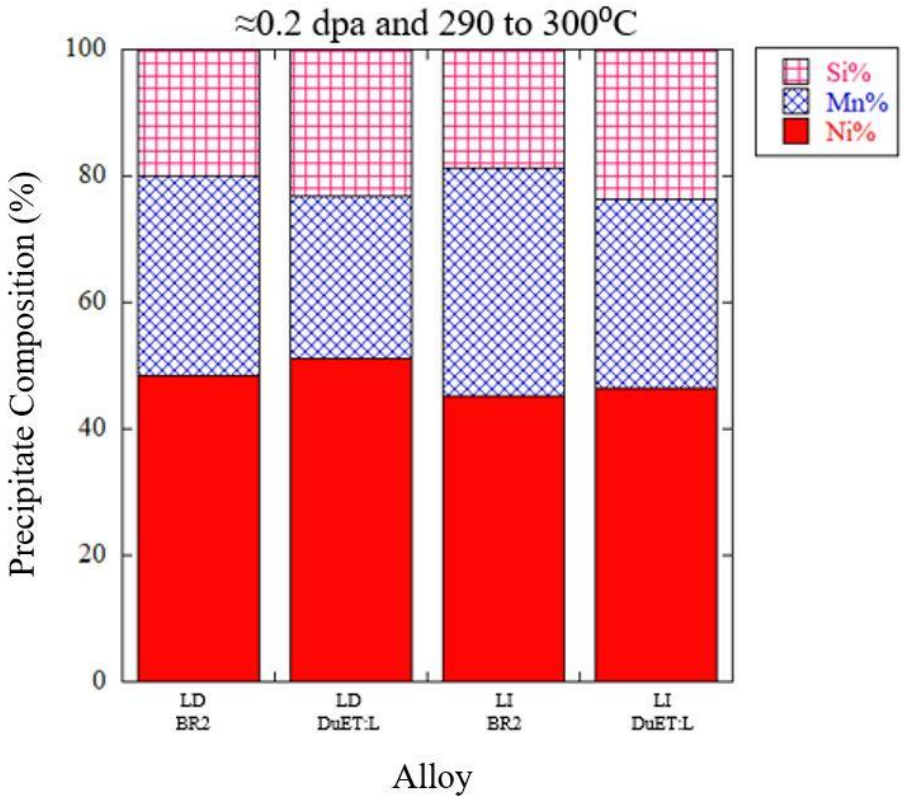

Figure 6.3. Bar graphs comparing the Ni, Mn, and Si precipitate compositions for the lower dpa NI (BR2) and CPI (DuET:L) high 1.03% Ni (LD) and medium 0.71% Ni (LI) steels. All compositions are in at.%.

Table 6.3. Bulk, matrix and precipitate Cu, Ni, Mn and Si compositions at the lower and high dpa in the CPI (DuET:L and DuET:H) and NI (BR2 and ATR1) conditions. The absolute bulk and matrix compositions obtained from APT measurements are in at.%, while those for the precipitates are specified in terms of fractional%.

Alloy	Bulk Comp. (%)				Matrix Comp. (at.%)				Precipitate Composition (fractional%)			
	Cu	Ni	Mn	Si	Cu	Ni	Mn	Si	Cu	Ni	Mn	Si
LD:BR2	0.21	1.00	1.08	0.52	0.06	0.74	0.91	0.41	22.1	37.8	24.6	15.5
LD:DuET:L	0.26	1.06	1.17	0.54	0.11	0.88	1.08	0.46	29.7	36.0	18.0	16.3
LI:BR2	0.15	0.72	1.21	0.43	0.06	0.59	1.11	0.37	24.2	34.2	27.4	14.2
LI:DuET:L	0.15	0.70	1.21	0.44	0.11	0.64	1.19	0.41	22.2	36.2	23.1	18.5
LD:ATR1	0.25	1.18	1.08	0.54	0.04	0.21	0.57	0.08	10.3	46.9	22.5	20.3
LD:DuET:H	0.23	1.22	1.12	0.54	0.10	0.29	1.24	0.17	8.5	50.2	20.9	20.4
LG:ATR1	0.00	0.71	0.87	0.43	0.00	0.11	0.38	0.10	0.2	46.1	31.2	22.5
A39:DuET:H	0.03	0.57	0.91	0.36	0.02	0.19	0.61	0.17	0.8	47.0	29.3	22.9
CM6:ATR1	0.00	1.69	1.42	0.39	0.00	0.21	0.31	0.04	0.1	52.5	35.5	11.9
A22:DuET:H	0.05	1.82	1.28	0.51	0.03	0.46	0.75	0.10	0.9	57.5	23.9	17.7

Table 6.4. Bulk Cu, Ni, Mn and Si compositions and APT precipitate <d>, N and f_v at the low and high dpa in the CPI (DuET:L and DuET:H) and NI (BR2 and ATR1) conditions.

Alloy	Bulk Composition (%)				<d>	+/-	N	+/-	f	+/-	10^6 ions
	Cu	Ni	Mn	Si	(nm)	(nm)	(10^{23} m^{-3})	(10^{23} m^{-3})	(%)	(%)	10^6
LD:BR2	0.21	1.00	1.08	0.52	2.23	0.12	11.7	1.87	0.68	0.10	78.8
LD:DuET:L	0.26	1.06	1.17	0.54	2.28	0.07	7.49	1.17	0.46	0.06	28.1
LI:BR2	0.15	0.72	1.21	0.43	2.19	0.11	6.89	1.14	0.37	0.08	14.1
LI:DuET:L	0.15	0.70	1.21	0.44	2.02	0.11	3.42	0.87	0.13	0.01	16.0
LD:ATR1	0.25	1.18	1.08	0.54	4.01	0.31	6.98	1.26	2.11	0.23	40.8
LD:DuET:H	0.23	1.22	1.12	0.54	4.65	0.39	3.33	0.32	1.97	0.32	160.0
LG:ATR1	0.00	0.71	0.87	0.43	2.54	0.10	15.5	1.61	1.33	0.03	26.5
A39:DuET:H	0.03	0.57	0.91	0.36	4.05	0.30	3.26	0.13	0.91	0.40	14.9
CM6:ATR1	0.00	1.69	1.42	0.39	3.18	0.09	17.3	1.32	2.82	0.14	30.0
A22:DuET:H	0.05	1.82	1.28	0.51	4.99	0.35	4.85	0.62	2.40	0.39	31.5

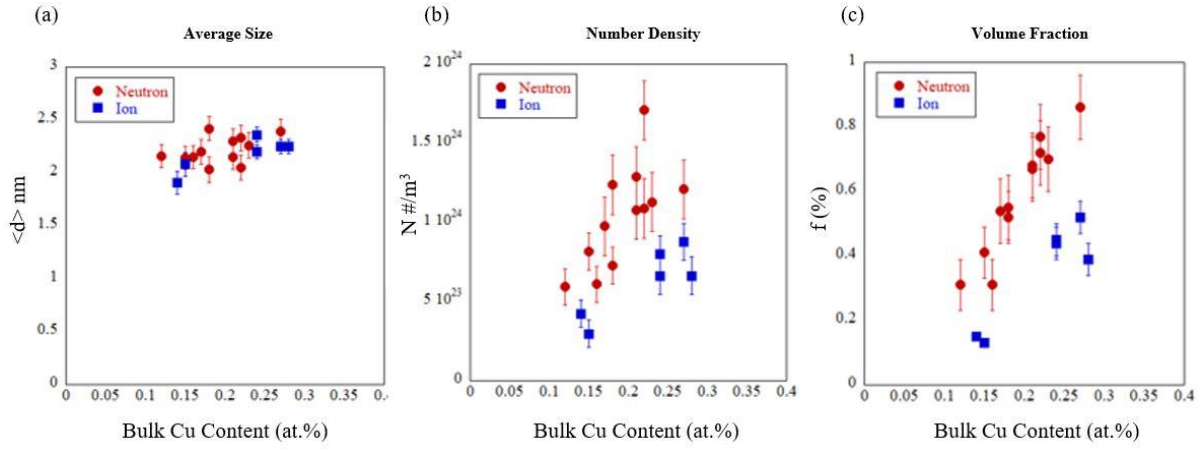

Figure 6.4. The lower dpa CPI (DuET:L) and NI (BR2) individual tip bulk Cu content dependence of the precipitate: a) <d>; b) N; and, c) f_v. Note the higher Cu alloy also contains higher Ni.

Figure 6.5 shows the APT maps for the same high 0.24±0.02% Cu and 1.20±0.02% Ni steel (LD) in the high ≈ 1.8 dpa, 320°C NI and ≈ 4.0 dpa, 290°C CPI conditions. The corresponding MNSP parameters, summarized in Tables 6.3 and 6.4, again show that in the NI condition the N values are larger, while the <d> are slightly smaller. However, the MNSP f_v (1.97-2.11%) and compositions (9.4±0.9%Cu, 48.6±1.7%Ni, 21.7±0.8%Mn and 20.4±0.05%Si) are nearly identical. In both cases the alloy is nearly completely precipitated. Note the small N and <d> differences may partly be due to the higher NI T_i.

Figure 6.6 shows APT maps comparing high dpa NI and CPI conditions for the LG/A32 and CM6/A22) steels with low Cu, and both medium ≈ 0.64±0.07 (LG/A32)) and high ≈1.76±0.06%Ni (CM6/A22). These steels also contain 0.87 to 1.42% Mn and 0.36 to 0.51% Si. The <d>, N and f_v cross plots in Figures 6.7a-c are for individual tips of high Cu and Ni steel (LD). The CPI alloys have distinctly lower N and slightly lower f_v compared to the NI

results. The CPI <d> values are also slightly larger; and the N and f_v increase with Cu in both irradiation conditions. These trends are similar to those in the same steel at lower dpa. Figures 6.7d-f show the corresponding comparison for low Cu and both low and high Ni steels with roughly similar Mn and Si contents. The <d>, N and f_v all increase with Ni, in a way that is similar for both the NI and CPI conditions. If thermodynamic solute product based adjustments (see Section 6.3) are made to account for differences in the Mn, Ni and Si in the medium Ni LG/A32 and high Ni CM6/A22 alloys, the f_v for the NI condition (1.8 dpa at 320°C) are about 13% (medium Ni) to 33% (high Ni) larger than for the CPI condition (4 dpa at 290°C). Again, this observation is consistent with slower precipitation at a higher dpa rate.

Figure 6.8a shows the MNSP fractional compositions are also similar in the paired LG/A39 and CM6/A22 steels, again especially if differences in the bulk alloy compositions are considered. The MNSP compositions in the high Ni alloys average Ni ≈ 55±2.5, while the Mn + Si ≈ 45±.3.0; in the medium Ni steel the MNSP compositions average Ni ≈ 47±0.5, while the Mn + Si ≈ 53±1.0%. As a compliment to Figure 6.8a, the stacked bar graph in Figure 6.8b shows the absolute individual volume fractions of the Mn, Ni and Si solutes in both the bulk steels and precipitates. Here, Cu is excluded since it is a separate attached phase. Figure 6.8b shows that: a) as expected, significant amounts of solutes remain dissolved in the matrix; b) the absolute f_v of the DuET CPI are smaller than for the ATR-1 NI, especially when adjusted for the bulk solute contents; and c) the largest difference in the CPI versus NI relative precipitate compositions is the somewhat lower amount of Mn in A22 versus CM6 (also see Figure 6.8a), but this tracks similar differences in the bulk solute content.

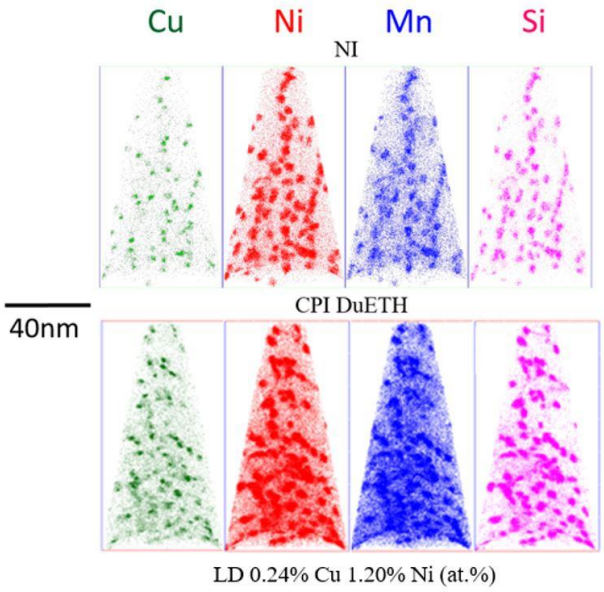

Figure 6.5. Solute maps directly comparing the high dpa ATR1 NI and DuET:H CPI for nominally the 1.20% Ni and 0.24% Cu steel (LD). This steel also contains 1.08 to 1.12% Mn and 0.54% Si. All compositions are in at.%.

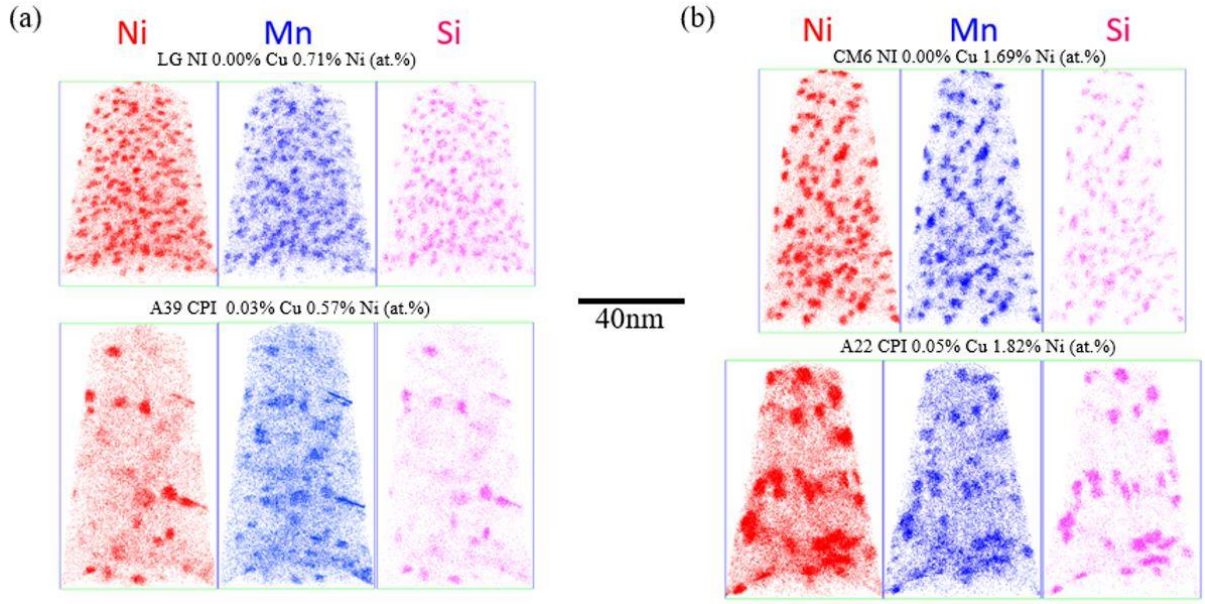

Figure 6.6. Solute maps for DuET:H CPI and ATR1 NI conditions, comparing compositionally similar low ≈ 0.05% Cu steels: a) LG/A39 (0.71 and 0.57% Ni) and b) CM6/A22 (1.69 and 1.82% Ni). These steels contain 0.87-1.42% Mn and 0.36-0.51% Si. All compositions are in at.%.

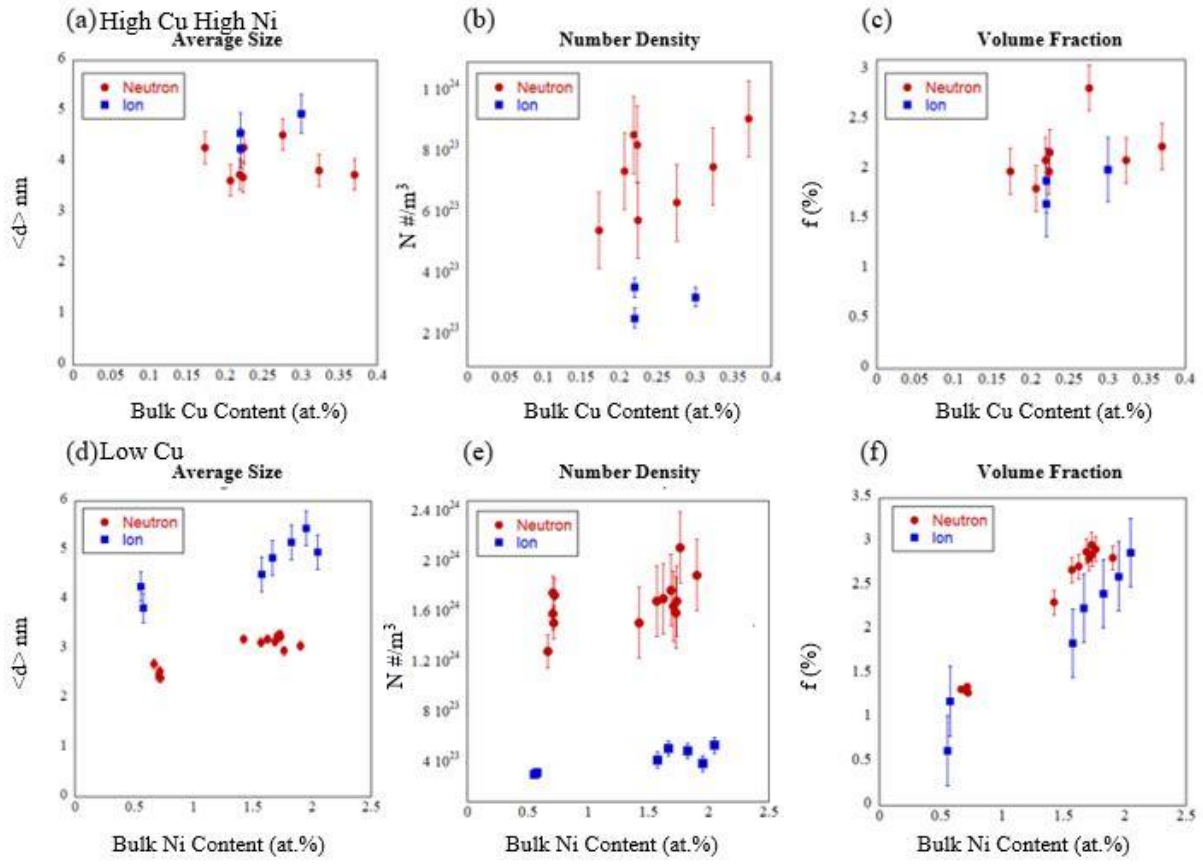

Figure 6.7. The high dpa CPI (DuET:H) and NI (ATR1) individual tip bulk a-c) Cu; and, d-f) Ni alloy content dependence of the precipitate <d>, N and f_v.

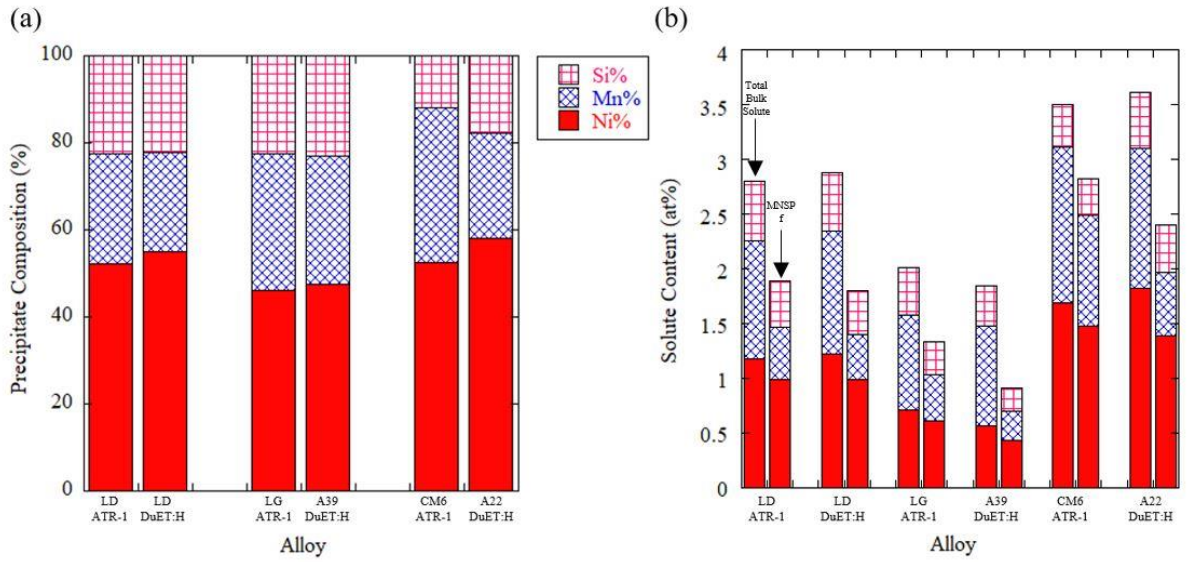

Figure 6.8. Bar graphs comparing the high dpa CPI (DuET:H) and NI (ATR1) LD and paired medium and high Ni steels: a) the relative Mn, Ni and Si compositions; and, b) the total bulk solute content of the steels (first bar), along with the corresponding precipitate f_v for the individual solutes (second bar).

Figure 6.9a-d shows APT map blowups of the CPI and NI precipitates in the high Cu-Ni content steel (LD) for both the low and high dpa conditions. At a lower 0.2 dpa the precipitates exhibit a core-shell structure in both CPI and NI conditions. At high dpa the Cu-rich core grows a MNSP appendage in both cases, consistent with previous high dpa NI observations [32,112,120]. The blown up view Figure 6.9e for the high 3.69 Ni and 1.31 Si alloy with 0.98 Mn (A13) in the high dpa DuET:H CPI condition, suggests that the MNSP is a compact polyhedral intermetallic precipitate.

Clearly, NI and CPI produce similar precipitate microstructures. In a given alloy, the major differences are lower N and f_v and slightly larger <d> (at high dpa) in the CPI condition. While increasing N at higher dpa rate has often been observed in lower dpa NI, Figure 6.10 shows that N actually decreases with dpa for the CPI in a way that is close to the extrapolated trend

for a NI alloy at high $\phi > 10^{13}$n/cm^2-s ($1.6x10^{-8}$ dpa/s) and $\phi t > 10^{20}$ n/cm^2 (0.15 dpa). While this trend is opposite to those observed for NI at lower dpa rates and dpa, it is qualitatively consistent with the effect of ballistic mixing by cascades [113]. Nevertheless, in view of these modest differences, CPI can be used as a convenient tool to assess the relative embrittlement sensitivity to various steel compositions, as well as a way to create RPV steel precipitate microstructures for scientific studies of mechanisms. It should be emphasized that these conclusions are for modest dpa and dpa rate CPI irradiations. This degree of NI and CPI similitude may not be the case for much higher CPI dpa and dpa rates used in studies of phenomena like void swelling and irradiation effects in Fe-Cr steels for advanced reactor applications.

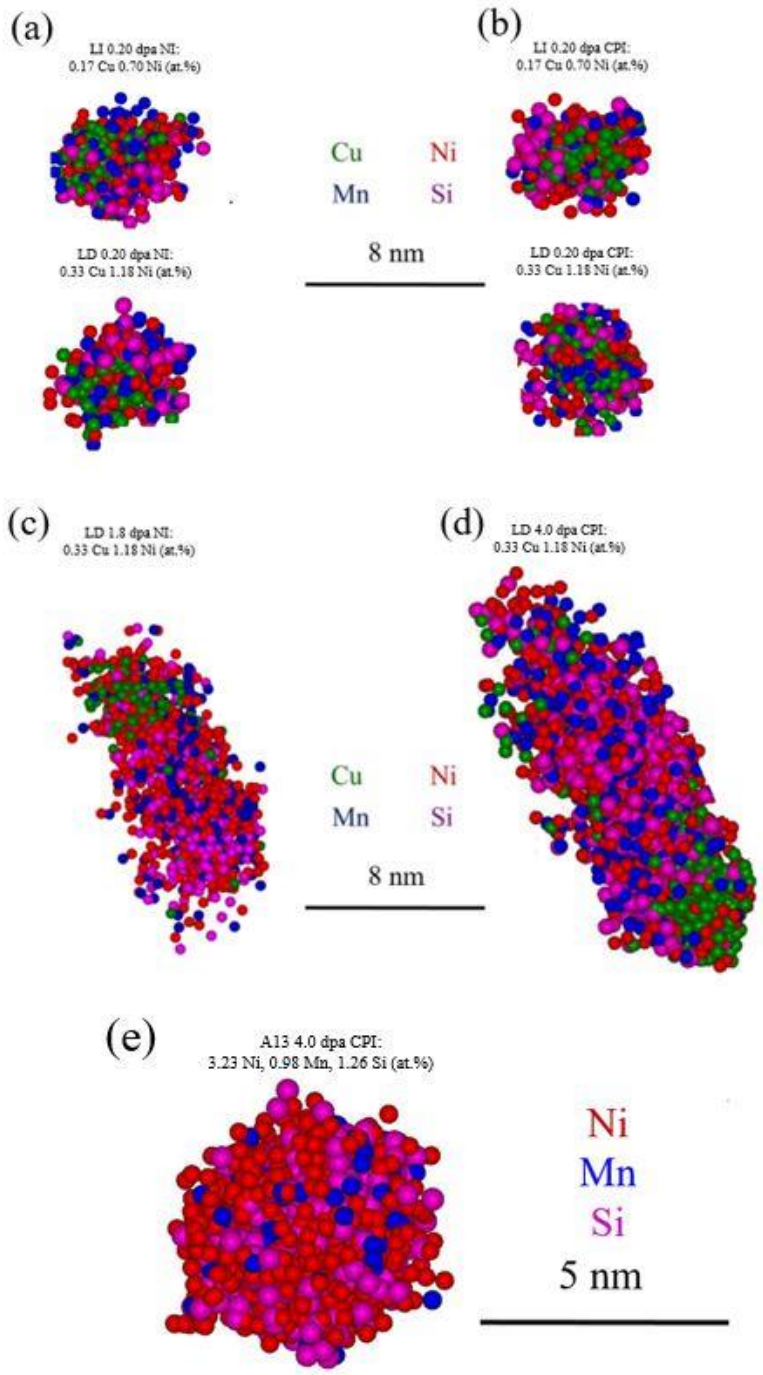

Figure 6.9. APT maps of the typical Cu-Mn-Ni-Si precipitate in high Cu-Ni content steel (LD) and lower Cu-Ni content steel (LI): a and b) lower dpa BR2 NI[(ii)] and DuET:L CPI; c and d) corresponding APT maps for the same steel (LD) from the high dpa ATR1 NI and DuET:H CPI; and, e) an APT map of a typical polyhedral appearing MNSP in highest Mn, Ni, Si steel (A13) in the DuET:H CPI condition[(ii)].

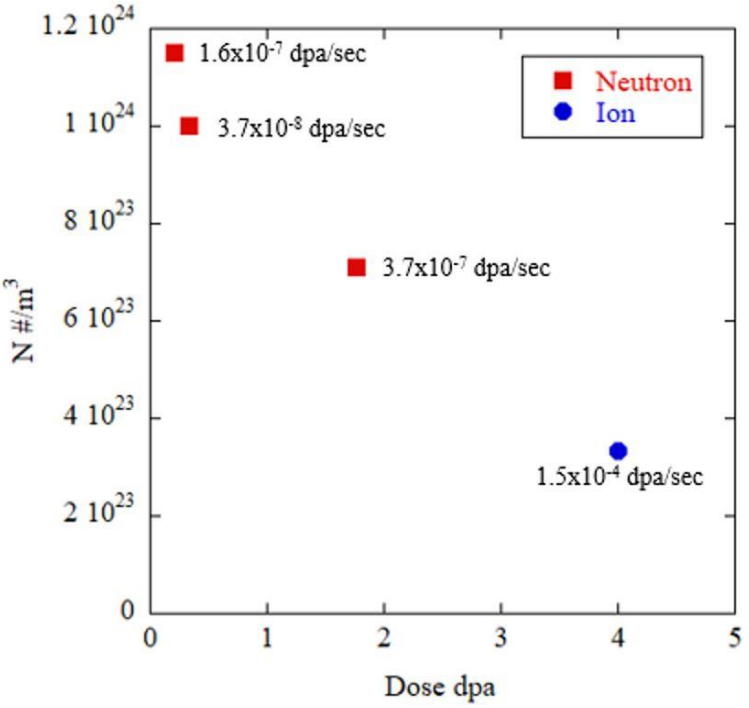

Figure 6.10. A plot showing that N decreases at higher dpa in the high Cu and Ni steel (LD) for both high dpa rate NI and CPI conditions.

Characterization of Precipitation in the DuET CPI Steels

The APT solute maps in Figure 6.11 for the 6 advanced steel series (A-series) CPI at 4 dpa and 290°C (not shown previously) that contain a wide range of 0.19 to 3.69%Ni, 0.03 to 0.25% Cu, 0.08 to 1.21% Mn, and 0.36 to 1.31% Si. The APT maps, precipitate parameters and compositions in Tables 6.5 and 6.6 reveal the effects of systematic variation in bulk solute contents. Figure 6.12a and Table 6.6 shows a very high Ni and Si (3.23 Ni 0.98 Mn 1.26 Si%) A13 steel, with the largest total solute content of ≈ 5.47% in the A-series CPI alloys, contains a very large MNSP $f_v \approx 4.51\%$, even without much Cu. Note the Ni/Mn/Si phase composition, of ≈ 61/14/25, is reasonably close to the stoichiometric G-phase ($Ni_{16}Mn_6Si_7$ - 55/21/24), but with a higher Ni and Si contents, reflecting the larger alloy content of these elements.

Figure 6.11b shows the APT maps for a medium 0.45% Si, high 3.1% Ni (A32). Both alloys contain relatively high 0.98 (A13) and 1.26 (A32)% Mn. As expected that both the Si content and f_v of the MNSPs are lower in A32 compared to the high Si steel (A13). Table 6.6 shows that f_v decreases from 4.51 to 3.83% between A13 and A32, primarily associated with a lower N. The Ni contents of the MNSPs (61.9 and 65.9%) are similar. Thus, in spite of large differences in alloy Si (A32 0.45 and A13 1.26%) the total MNSP percentages of Mn + Si (A13 33.5% and A32 38.6%) are also similar, since they trade off with each other, as observed previously in lower dpa NI study [53].

Figure 6.11c shows the MNSPs in a high 3.69 Ni and 1.31 Si% alloy with low 0.29% Mn (A28). Table 6.6 shows that f_v decreases slightly from ≈ 4.51 to 3.95% between alloy contents of 0.98 (A13) and 0.29% Mn (A28). The lower f_v can be attributed to less Mn (5.00 versus 13.9%) in the A28 MNSPs. In both cases, Ni-Si rich MNSPs have compositions about midway between Ni_2Si and Ni_3Si type phases. Note that some individual tips of A28 steel contain atypically high bulk Ni, producing higher f_v than on average.

Figure 6.11d shows that CRP/MNSP co-precipitates form in the high 0.25% Cu steel with high Ni, Mn and Si (A16). CRPs, with a Cu-rich core and Mn-Ni-Si shell, form rapidly then slowly evolve discrete, what appears to be an ordered intermetallic co-precipitate appendages at higher dpa (see Figure 6.8) [32,120]. CRP/MNSP co-precipitates are observed both in association with dislocations and apparently homogeneously distributed in the matrix. The MNSP appendage accounts for ≈ 95% (3.42%) of the total MNSP f_v ≈ 3.63%. The average A16 MNSP composition is similar to that in the low Cu steel A32, with an otherwise similar composition.

The $f_v \approx 3.42$ and 3.83% in these medium Si and higher Mn A16 and A32 steels, decrease to ≈ 0.73% at very low 0.08% Mn (A34), again mainly due to a lower N. The systematic effect of Mn "starvation" on limiting precipitation and modifying the phase selection was previously reported by Almirall et al. for the A-series steels NI to ≈ 0.2 dpa at 290°C [53]. Figure 6.11e shows that the CPI of a very low Mn, medium Si steel exhibits an enormous amount of Ni, and to a lesser extent Si, segregation to dislocations. In contrast, a limited amount of Mn is located in precipitates on the dislocations, mainly at their intersections.

Figure 6.11f shows an APT solute map for a low Cu and very low 0.2% Ni alloy with medium 1.31 Mn and high 1.21 Si (A37). Table 6.6 shows a small MNSP $f_v \approx 0.58\%$ in this case. All three solutes segregate to dislocations in A37, again forming precipitates at their intersections as well as along them, in string of pearls fashion. The MNSPs in the low Ni, high Si steel contain almost equal amounts of Ni and Si, with compositions of ≈ Ni_2Si_2Mn. These compositions are in the vicinity of the Fe-Mn-Ni-Si quaternary MnSi phase field.

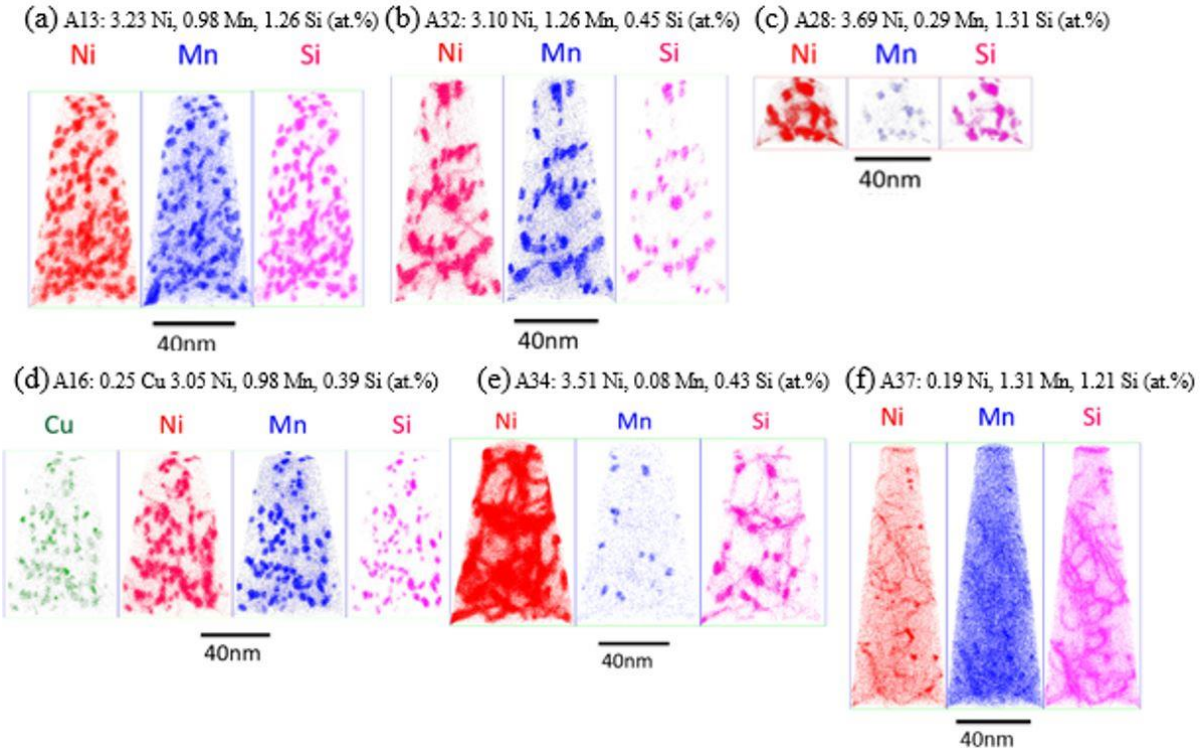

Figure 6.11. The APT solute maps showing the precipitates formed under CPI (DuET:H) in a) very high Ni and Si, medium Mn A13; (b) very high Ni, medium Si and Mn A32; c) low Mn, very high Ni and Si A28; d) high Cu, very high Ni, medium Mn and Si A16; e) very high Ni with very low Mn content A34; f) low Ni, medium Mn and high Si A37. Except for A16, all of the alloys contain low Cu (<0.05%). All compositions are in at.%.

Table 6.5. Bulk, matrix and precipitate Cu, Ni, Mn and Si compositions obtained from APT measurements for the very high fluence ion (DuET:H) and neutron irradiation (ATR-1) conditions.

Alloy	Bulk Comp. (%)				Matrix Comp. (%)				Precipitate Comp. Fraction%			
	Cu	Ni	Mn	Si	Cu	Ni	Mn	Si	Cu	Ni	Mn	Si
LD:ATR-1	0.25	1.18	1.08	0.54	0.04	0.21	0.57	0.08	10.3	46.9	22.5	20.3
LD:DuET:H	0.23	1.22	1.12	0.54	0.10	0.29	1.24	0.17	8.5	50.2	20.9	20.4
LG:ATR-1	0.00	0.71	0.87	0.43	0.00	0.11	0.38	0.10	0.2	46.1	31.2	22.5
CM6:ATR-1	0.00	1.69	1.42	0.39	0.00	0.21	0.31	0.04	0.1	52.5	35.5	11.9
A13:DuET:H	0.05	3.23	0.98	1.26	0.02	0.53	0.39	0.16	0.5	60.9	13.9	24.7
A16:DuET:H	0.25	3.05	0.98	0.39	0.05	0.72	0.40	0.03	5.7	65.1	19.3	9.9
A22:DuET:H	0.05	1.82	1.28	0.51	0.03	0.46	0.75	0.10	0.9	57.5	23.9	17.7
A28:DuET:H	0.05	3.69	0.29	1.31	0.03	1.02	0.09	0.26	0.6	68.0	5.00	26.5
A32:DuET:H	0.04	3.10	1.26	0.45	0.01	0.62	0.43	0.03	0.6	65.9	22.7	10.8
A34:DuET:H	0.05	3.51	0.08	0.43	0.03	0.81	0.04	0.05	0.9	67.7	8.2	23.1
A37:DuET:H	0.04	0.19	1.31	1.21	0.04	0.04	1.21	0.73	1.4	38.4	20.4	39.8
A39:DuET:H	0.03	0.57	0.91	0.36	0.02	0.19	0.61	0.17	0.8	47.0	29.3	22.9

Table 6.6. Bulk Cu, Ni, Mn and Si compositions and APT precipitate <d>, N and f_v for the very high fluence ion (DuET:H) and neutron irradiation (ATR-1) conditions.

Alloy	APT Bulk Comp (%)				<d>	+/-	N	+/-	f	+/-	10^6 ions
	Cu	Ni	Mn	Si	(nm)	(nm)	(10^{23} m^{-3})	(10^{23} m^{-3})	(%)	(%)	
LD:ATR-1	0.25	1.18	1.08	0.54	4.01	0.31	6.98	1.26	2.11	0.23	40.8
LD:DuET:H	0.23	1.22	1.12	0.54	4.65	0.39	3.33	0.32	1.97	0.32	160.0
LG:ATR-1	0.00	0.71	0.87	0.43	2.54	0.10	15.5	1.61	1.33	0.03	26.5
CM6:ATR-1	0.00	1.69	1.42	0.39	3.18	0.09	17.3	1.32	2.82	0.14	30.0
A13:DuET:H	0.05	3.23	0.98	1.26	5.45	0.01	6.62	1.26	4.51	0.18	17.1
A16:DuET:H	0.25	3.05	0.98	0.39	5.82	1.07	2.22	1.44	3.63	0.24	77.0
A22:DuET:H	0.05	1.82	1.28	0.51	4.99	0.35	4.85	0.62	2.40	0.39	31.5
A28:DuET:H	0.05	3.69	0.29	1.31	4.75	0.79	5.90	1.81	3.95	0.08	19.2
A32:DuET:H	0.04	3.10	1.26	0.45	5.74	0.57	4.73	0.47	3.83	0.38	12.0
A34:DuET:H	0.05	3.51	0.08	0.43	5.32	0.53	1.08	0.11	0.73	0.07	21.2
A37:DuET:H	0.04	0.19	1.31	1.21	4.03	1.23	0.56	0.57	0.58	0.25	52.3
A39:DuET:H	0.03	0.57	0.91	0.36	4.05	0.30	3.26	0.13	0.91	0.40	14.9

Visual examination of all of the APT maps in Figure 6.11 shows major to massive amounts of solute segregation to dislocation segments. The role of solute segregated dislocations, and dislocation loops, acting as heterogeneous precipitate nucleation sites, is both widely observed and important [19,26,53,109,112,121]. Models for heterogeneous nucleation of precipitates in irradiated RPV steels have been proposed by both H. Ke et al. and Mamivand et al., based on CALPHAD thermodynamics [105] and RED kinetics [111,112]. JH. Ke et al. also developed a model for MNSP formation in under saturated Fe-9Cr steels, due to RIS at dislocations, even in alloys containing only small amounts of Mn, Ni and Si [109]. It is also visually evident in Figure 6.11 that the CPI A-series alloys have high to very high dislocation densities. A detailed discussion of dislocation structures and the character, as well as the causes and consequences of the corresponding solute segregation, is beyond the scope of this work. However, these key topics are being addressed in detail as part of ongoing work.

To more fully illustrate the previous discussion, Figure 6.12a shows cross plots of the individual effects of variations in Cu, Mn, Ni and Si on <d>, N and f_v of the MNSPs. Note that Cu is not included in the MNSP f; the precipitate Cu is < 2% with the exception of LD and A16 steels. The lines are simply to guide the eye. Except in the case of the Cu bearing steels, N and f_v increase with the solute content. The <d> does not vary much with Mn and Si, but increases slightly with Ni. At very high Ni ≈ 3.2%, the f_v reaches very large values of more than 4%.

The stacked bar graphs in Figure 6.12b show the Mn, Si and Ni contents of both the steels and precipitates for all of the compositions in the high dpa CPI condition. As noted above, the f_v values are lowest for the steels with low Mn and Ni. For steels with more typical Mn contents, f_v increases systematically with Ni. Notably, the data shows that higher Si also

increases f_v. A large effect of Si has not been observed in the case of NI at a lower ≈ 0.20 dpa and 320°C [53]. The solid lines show that the precipitate to alloy solute content ratio ($f_v/[X_{Ni}+X_{Mn}+X_{Si}]$) increases with the steel Mn+Ni+Si. Finally, while the f_v is smaller for low Mn and Ni steels, it is not insignificant. The dominant effect of Ni is also shown in Figure 6.12c, plotting 2Ni + Cu versus the total f_v (including Cu) for both high dpa NI and CPI conditions. Ni dominance is due to the fact that Ni ≈ Mn + Si in both the G and Γ_2 phase type precipitates [32,53,105,111]. As shown in Figure 6.12c, the high dpa NI f_v fall ≈ 37% above those for CPI conditions; again, this is likely a result of the much higher CPI dpa rates.

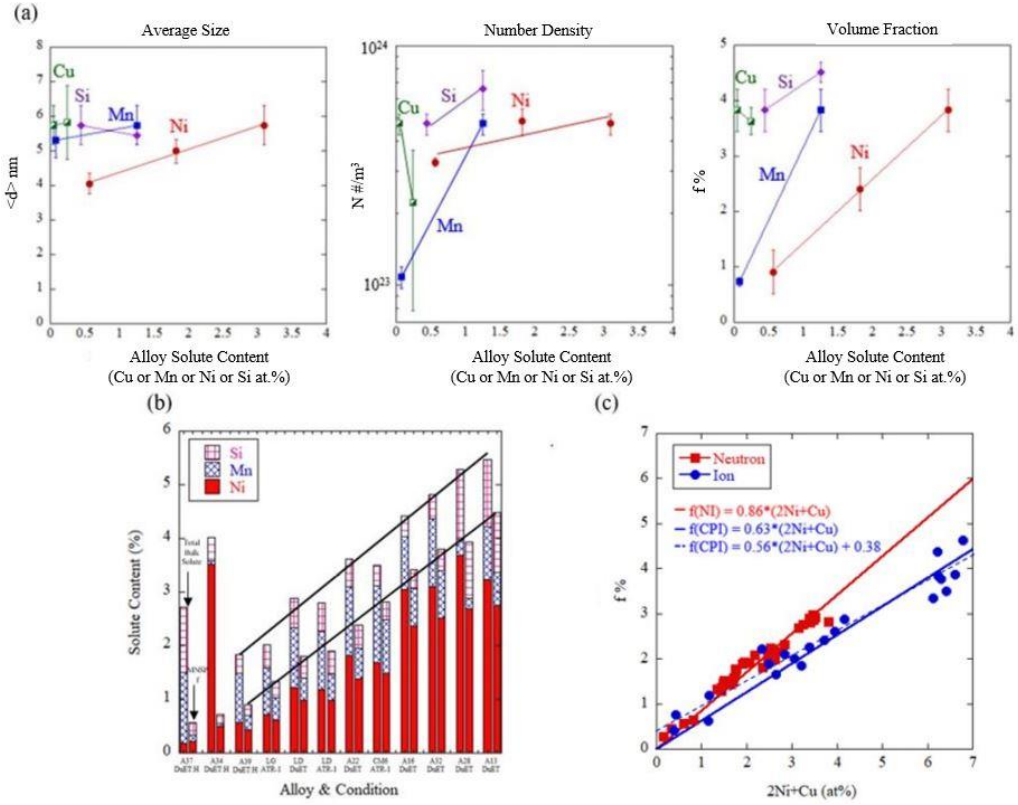

Figure 6.12. a) Cross plots of the individual effects of variations in alloy solute content of Cu, Mn, Ni or Si (%), as shown by the labels in the figure, on <d>, N and f_v of the MNSPs in alloys with otherwise similar (not identical) compositions; b) stacked bar plots of the total bulk solute content (first bar) and precipitate Mn, Ni and Si f_v (second bar). c) 2Ni + Cu versus the total f_v (including Cu) for individual APT tips at high dpa for the NI (red squares) and CPI (blue circles) conditions.

As noted previously, MNSPs are typically G and Γ_2 type phase compositions. However, these phases cannot form at very low Mn, Si and Ni. Thus the lower, but still significant, f_v in in these solute poor alloys suggests the selection of other phases. Figure 6.13 shows the Mn-Ni-Si projection of the Fe-Mn-Ni-Si quaternary at 277°C for the A-series steels in this study. Note, there is not a significant difference between the CALPHAD predictions at 277 and 290°C [111]. For typical RPV steel bulk Mn (≈ 0.8-1.5%), Ni (≈ 0.5-1.6%) and Si (0.2-1.2%) contents, the precipitate compositions are clustered around the G and Γ_2 phases, as expected. However, the compositions of two other alloys with low Mn (A28, A34) are close to the Ni_3Si γ' phase, slightly alloyed with Mn. However, the TEM FFT power spectra shown in Figure E1 of Appendix E suggests that the MNSP structure is consistent with $Ni_2Si^{(v)}$. The MNSPs in the low Ni A37 steel are closer to the phase field labeled MnSi, which actually spans a thermodynamic composition range of ≈ 28 to 38% Ni. The precipitate composition in the A16 and A32 alloys, with the lower Si, high Mn and the highest Ni, fall slightly closer to the Ni_3Mn than to the G phase. This may represent nonstoichiometric enrichment of Ni in the G-phase; or alloying of a Ni_3Mn phase with Si. Note, that even though A16 contains ≈ 0.25% of bulk Cu, the MNSP composition only slightly deviates from the low Cu A32 steel with an otherwise similar composition. This reflects the separate MNSP appendage formation on CRPs (see Figure 6.8). All of these results are highly consistent with trends observed in high dpa NI. A major conclusion is that even with insufficient amounts of any of the Mn, Ni or Si needed to form typical G or Γ_2 type phases, other precipitates still form at very high dpa, albeit at lower f_v.

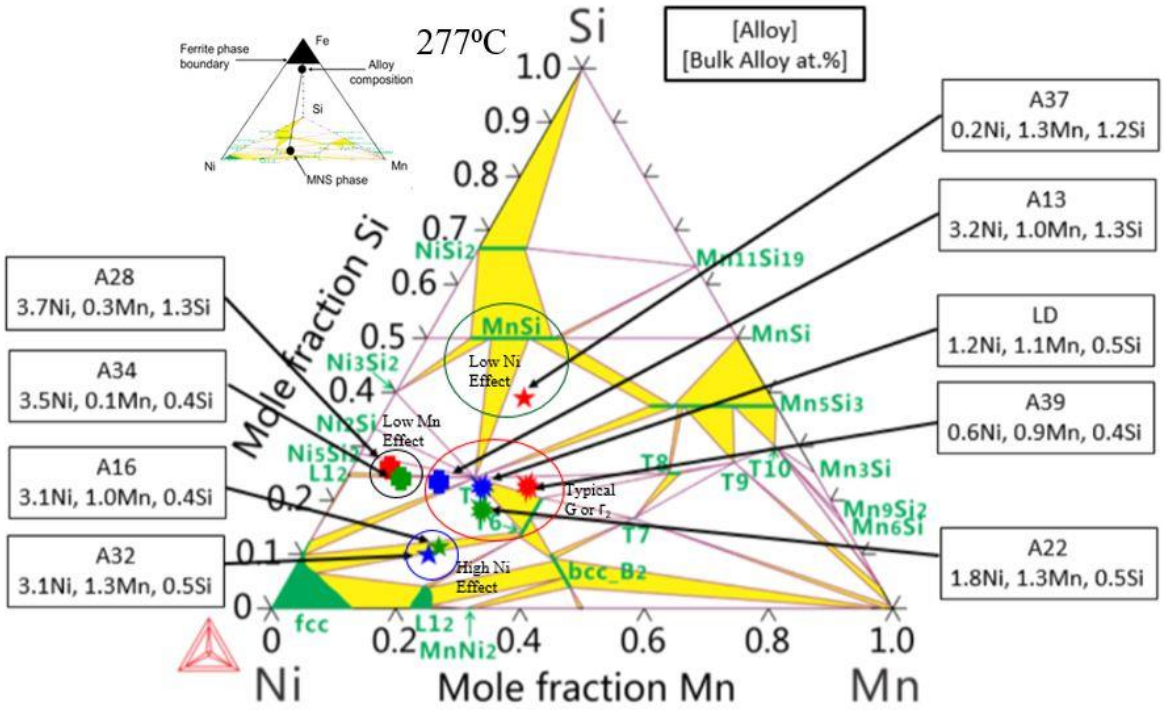

Figure 6.13. The precipitate compositions for the DuET:H condition plotted on the Mn-Ni-Si ternary projection of the Fe-Mn-Ni-Si phase diagram at 277°C. Alloy composition details are shown outside the ternary [105,111](iii).

Thermodynamic analysis and discussion

The MNSP observed in typical RPV steels are the Ni_3Mn_2Si (nominal) Γ_2 phase or the $Ni_{16}Mn_6Si_7$ (nominal) G-phase [105,109,111,112,120]. These phases are formed by the following reactions

$$16Ni(s) + 6Mn(s) + 7Si(s) \Leftrightarrow Ni_{16}Mn_6Si_7 \quad (6.1a)$$

or

$$3Ni(s) + 2Mn(s) + 1Si(s) \Leftrightarrow Ni_3Mn_2Si \quad (6.1b)$$

Here, the (s) indicates dissolved solutes. Taking the precipitate activities as 1, the MNSP solvus is given by

$$\{[X_{Ni}]^{16}[X_{Mn}]^{6}[X_{Si}]^{7}\}^{1/29} = K_G(T) \quad (6.2a)$$

or

$$\{[X_{Ni}]^{3}[X_{Mn}]^{2}[X_{Si}]\}^{1/6} = K_{\Gamma 2}(T) \quad (6.2b)$$

Here, the $\{[X_{Ni}]^{16}[X_{Mn}]^{6}[X_{Si}]^{7}\}^{1/29}$ and $\{[X_{Ni}]^{3}[X_{Mn}]^{2}[X_{Si}]\}^{1/6}$ are solute products ($SP_{G/\Gamma 2}$) for G and Γ_2 phases, the X_i are the dissolved solute mole fractions and $K_{G/\Gamma 2}(T)$ are the temperature dependent equilibrium reaction constant, that incorporates the activity coefficients of the dissolved solutes and the formation free energy of the pertinent G or Γ_2 phase. Ke used CALPHAD to determine the $K_{G/\Gamma 2}(T)$ for a range of typical RPV steel compositions as $K_G(290) \approx 2.56x10^{-3}$ and $K_{\Gamma 2}(290) \approx 2.21x10^{-3}$ [111,112][(iv,v)].

The high dpa ATR-1 NI and DuET:H CPI both produce MNSP full precipitation. The limiting f_v, ignoring the Gibbs-Thomson effect, can be calculated as:

$$f_{vG} \approx \{[X_{Ni} - (K_G/[X_{Mn}{}^{6}X_{Si}{}^{7}])^{(1/29)}\}/0.55 \quad (6.3a)$$

$$f_{v\Gamma 2} \approx \{X_{Ni} - (K_\Gamma/[X_{Mn}{}^{2}X_{Si}])^{(1/6)}]/0.50 \quad (6.3b)$$

These estimates involve several assumptions. First they are for stoichiometric G and Γ_2 phases. Second Equations 3a and b assume that the alloy Ni content controls f_v. The third assumption is there is sufficient Mn and Ni to match the G phase or Γ_2 phase stoichiometric compositions. In reality, even in phases that are stoichiometric at full equilibrium, ranges of compositions are thermodynamically accessible if there are free energy reductions upon solute precipitation from solid solutions, as is the case prior to equilibrium. Further, higher chemical potentials of the individual solutes can alter the MNSP compositions so as to track the overall alloy chemistry. It has also been shown that Mn and Si trade off in MNSPs, again in response to the

steel composition [32,53]. Finally, the nanoscale precipitate compositions are modified their interface energies that also depend on composition. These thermodynamic effects affecting MNSP compositions can be further modified by differences in the solute transport mechanisms and kinetics as a result of RIS.

More detailed thermokinetic models have been reported [111,112] and reduced order fully physical models will be the topic of future publications[(iv)]. Here we simply, assess how well the MNSP f_v correlates with the SPs at high dpa. Least square linear fits of f_v correlate slightly better with SP_G than with $SP_{\Gamma 2}$. Figure 6.14 plots the SP_G fit to the CPI f_v data shown as green squares. The ATR-1 NI data are also shown as blue triangles. Notably, the high dpa CPI and NI $f_v(SP_G)$ follow very similar trends. They extrapolate to $f_v \approx 0$ at $SP_G \approx 0.002$, which is consistent with the calculated CALPHAD K_G(290°C). Since the bulk SP_G does not account for the Gibbs-Thomson effect the actual SP_G is actually may be slightly lower than the CALPHAD prediction. The red circles are lower dose ATR-2 NI to ≈ 0.2 dpa at 320°C. In this case, the f_v values are lower, as expected, indicating the effects of nucleation and initial growth at SP_G less than about 0.01. However, for higher SP_G the f_v trend is very similar that at high dpa.

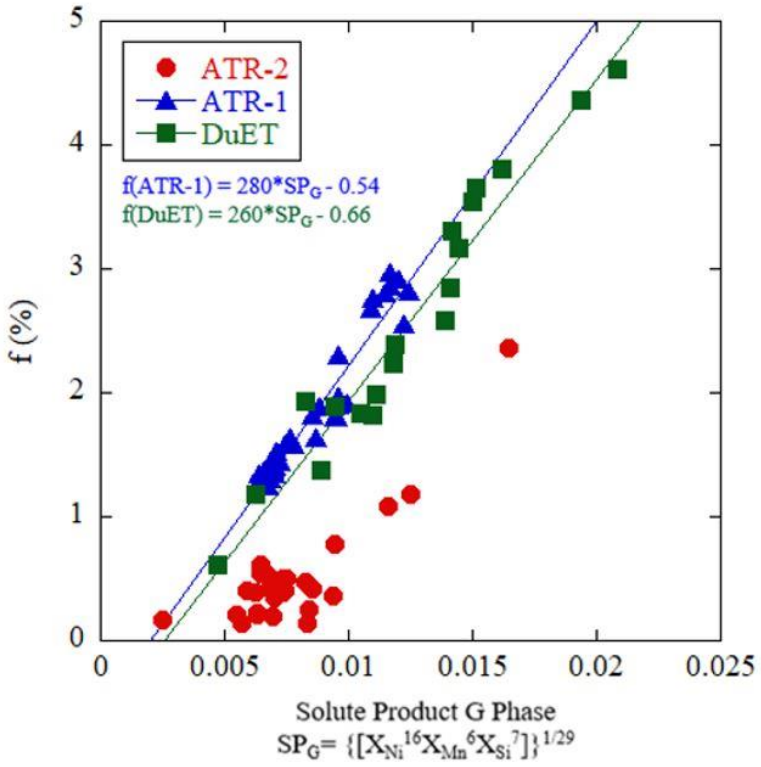

Figure 6.14: SP_G least square fit to the CPI DuET:H and ATR-1 NI individual APT tip f_v data. The high dose ATR-1 NI f_v follow a similar trend, while the lower dose ATR-2 NI f_v are smaller as expected[(iv)].

Figure 6.15 plots the f_v predicted by Equations 3a versus the measured values for CPI that result in G (or Γ_2) phase. The red circles are for alloys that have sufficient Mn and Si to form stoichiometric G phase, while the blue squares do not. In the case of alloys with sufficient Mn and Si to form G-phase, the best-fit line forced though 0 has a slope of 0.90, consistent with a small Gibbs-Thomson effect. The actual best-fit line has an f_v intercept of ≈ 0.004 and a slope of 0.71, consistent with a larger Gibbs-Thomson effect. As expected the high Ni data with insufficient Mn and Si to form stoichiometric G-phase fall below the extrapolated fit lines. Overall, the agreement between the predicted and measured f_v is surprisingly good and highly supportive of the thermodynamic analysis.

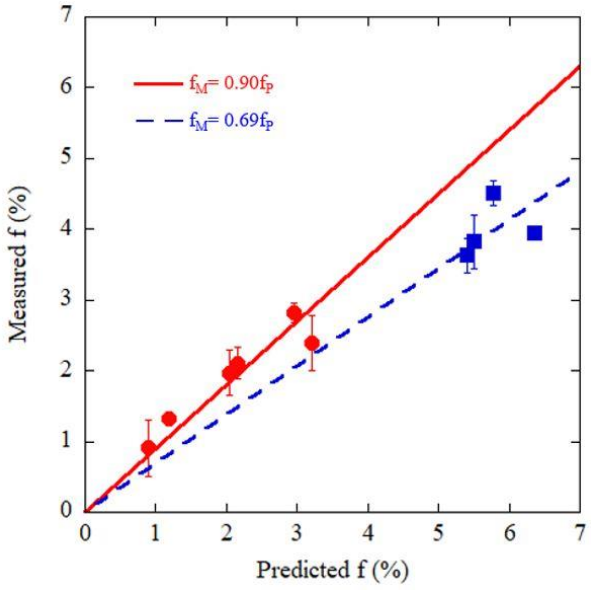

Figure 6.15. Comparison of the equilibrium thermodynamic model predicted to measured f_v. The red circles are alloys with sufficient Mn and Si to form stoichiometric G-phases type precipitates with the equilibrium precipitated Ni. The blue squares have insufficient Mn and Si to form stoichiometric G-phases type precipitates consistent with the large amount potentially precipitated Ni. The slopes of < 1 reflect the Gibbs-Thomson effect on the solubility limit in equilibrium with nanoscale precipitates[iv].

Estimates of $\Delta\sigma_y$ and ΔT

The APT f_v measured in the CPI can be used to estimate the corresponding irradiation hardening ($\Delta\sigma_y$) based on well-established dispersed barrier models [8,26,27,32,51,52,55]. However we use a simpler method using the empirical relation derived in [53].

$$\Delta\sigma_y \approx 314\sqrt{f_v}(\%). \qquad (4)$$

The $\Delta\sigma_y$ for these alloys has been measured for the ATR-2 NI to a lower ≈ 0.20 dpa at 290°C. Thus, in order to compare predicted and measured $\Delta\sigma_y$, the CPI APT f_v must first be adjusted to ATR-2 NI condition, f_{vA2}. Based on the trend in a number of other alloys irradiated in both ATR-1 (A1) and ATR-2 (A2), an empirical adjustment factor was found to be

$$f_{vA2}/f_{vA1} \approx 0.245Ni + 0.65Cu$$

Here Ni and Cu are the bulk alloy compositions. The $\Delta\sigma_y$ predicted f_{vA2} based on assuming the CPI $f_{vcpi} \approx f_{vA1}$ is plotted against the measured ATR-2 hardening in Figure 6.16a. The filled red symbols are for the alloys that form precipitates with G and Γ_2 type compositions. The filled blue squares are for high Ni, low to very low Mn steels that form $Ni_{2\text{-}3}Si$ type precipitate compositions. The lines are least square fits forced through 0,0. It appears that the $Ni_{2\text{-}3}Si$ type precipitates are weaker dislocation obstacles than those with G or Γ_2 phase type compositions. For perspective the estimated $\Delta T \approx 0.7\Delta\sigma_y$ is plotted in Figure 6.16b [55]. In alloys with high Ni and Mn the ΔT are large even at lower service relevant dpa.

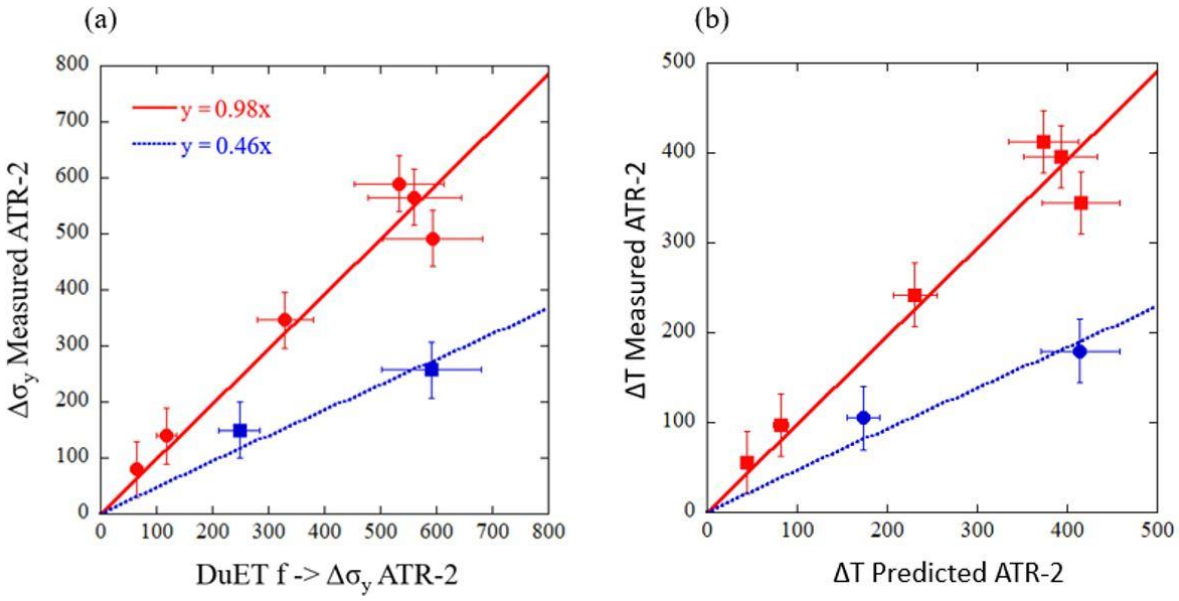

Figure 6.16. The a) $\Delta\sigma_y$ and b) ΔT predictions in NI ATR-2 calculated using an empirical adjustment factor plotted against the measured ATR-2 hardening [55]. The filled red symbols are for the alloys that form precipitates with G and Γ_2 type compositions. The filled blue squares are for high Ni, low to very low Mn steels that form $Ni_{2\text{-}3}Si$ type precipitate compositions[(iv)].

6.1.4 Summary and Conclusions

The results of this study, comparing NI and CPI, can be summarized as follows. The precipitate compositions are similar in both irradiation conditions. At high dpa MNSPs and CRP-MNSPs form in low Cu and Cu bearing alloys, respectively. In the latter case, lower dpa Cu core Mn-Ni-Si shell structures evolve into CRP-MNSP appendage co-precipitate features at high dpa. For a wide range of typical RPV steel compositions, the MNSPs have G and Γ_2 type phase compositions. CPI produces fewer and larger precipitates. Further, higher dpa are needed to form the same precipitate f_v for CPI versus NI conditions. The delayed precipitation is consistent with enhanced recombination of vacancies and SIA defects at higher CPI dpa rates, which reduces the efficiency of RED (and RIS). The MNSP grow slowly, but eventually reach large f_v at high dpa. Notably, f_v correlates well with the G-phase solute product, $(Ni^{16}Mn^{6}Si^{7})$ $^{(1/29)}$, and is close to the equilibrium value, slightly modified by the Gibbs-Thomson effect. However, in steels with very low Mn and high Ni and Si, $Ni_{2\text{-}3}Si$ silicide type compositions are selected rather than those for the G or Γ_2 type phases; and when Ni is low, a MnSi phase field type composition, which still contains ≈ 28-38% Ni, is observed. High Ni and Mn alloys with lower Si form Ni_3Mn type precipitates alloyed with small amounts of Si (10-12%).

Thermodynamic models are able to predict the f_v for alloys with G and Γ_2 type precipitate compositions. Deviations are likely associated with the Gibbs-Thomson effect and/or insufficient Mn and Si to form precipitates with close to stoichiometric compositions. In this case Ni does not fully control f_v. The f_v from the CPI can be used to estimate $\Delta\sigma_y$ and ΔT at lower service relevant dpa. While not quantitatively accurate, this allows scoping studies of

the embrittlement sensitivity of new RPV alloys. The $\Delta\sigma_y$ also suggest that Ni-Si dominated precipitates may be weaker dislocation obstacles than the G and Γ_2 type MNSPs.

Acknowledgements

(i) Dr. Takuya Yamamoto conducted the CPI at the Dual Beam Facility for Energy Science and Technology (DuET) at Kyoto University in Japan with the support of Dr. Kiyohiro Yabuuchi, Akihiko Kimura, and Mr. O. Hashitomi.

(ii) Dr. Peter Wells conducted APT data collection and analysis at the low dpa (0.20 dpa) NI condition.

(iii) Dr. Yuan Wu conducted TEM from alloy A28 at UCSB CNSI.

(iv) Professor Dane Morgan's group at University of Wisconsin provided the thermodynamic phase diagram, phase predictions and modeling insights. Drs. Huibin Ke and Mahmood Mamivand provided the solute products used in the simplified thermodynamic modeling section.

Chapter 7: Nature of MNSPs: RED Enhanced vs RIS Induced

7.1: On the Elevated Temperature Thermal Stability of Nanoscale Mn-Ni-Si Precipitates Formed at Lower Temperature in Highly Irradiated Reactor Pressure Vessel Steels

7.1.1 Introduction[5]

Some have argued that MNSPs are not thermodynamic phases, but are rather non-equilibrium solute clusters primarily formed and sustained up to sizes of a few nm by radiation induced segregation (RIS) primarily at dislocation loops that form in displacement cascades [13,104,122,123]. Specifically these models suggest either that Mn-Ni clusters are not thermally stable in Fe [13,122], or that they are only stable at combinations of very low temperatures and high solute concentrations, hence, require RIS to grow and persist [104,123]. In contrast, equilibrium thermodynamic models predict that RED results in large MNSP mole fractions (*f*) at the low RPV operating temperatures of ≈ 300°C [105]. Notably, the predicted equilibrium precipitate f_v and compositions are in agreement with atom probe tomography (APT) data from steels irradiated to very high fluence [124]. In addition, recent X-ray diffraction and scattering experiments [106] have Γ_2 or G-phase intermetallic crystal structures, consistent with CALPHAD based thermodynamic predictions [19].

[5] This chapter includes slightly modified text and figures published in N. Almirall, P.B. Wells, H. Ke, P. Edmondson, D. Morgan, G. R. Odette, On the Elevated Temperature Thermal Stability of Nanoscale Mn-Ni-Si Precipitates Formed at Lower Temperature in Highly Irradiated Reactor Pressure Vessel Steels, Scientific Reports, 9 (2019) 1-12 and N. Almirall, P.B. Wells, S. Pal, P.D. Edmondson, T. Yamamoto, K. Murakami, G.R. Odette, The mechanistic implications of the high temperature, long time thermal stability of nanoscale Mn-Ni-Si precipitates in irradiated reactor pressure vessel steels, Scripta Materialia 181 (2020) 134-139.

Atom probe tomography (APT) and scanning transmission electron microscopy (STEM) techniques were used to probe the long-time thermal stability of nm-scale Mn-Ni-Si precipitates (MNSPs) formed in intermediate and high Ni reactor pressure vessel steels under high fluence neutron irradiation at ≈ 320°C. Post irradiation annealing (PIA) at 425°C for up to 57 weeks was used to determine if the MNSPs are: a) non-equilibrium solute clusters formed and sustained by RIS; or, b) equilibrium G or Γ_2 phases, that precipitate at accelerated rates due to RED. PIA can provide significant additional insight into the nature of the MNSPs. For example, clusters that form through a RIS mechanism should not be stable during PIA, even at $T_i \approx 290$°C. However, very slow thermal diffusion kinetics precludes conducting meaningful experiments at such low annealing temperatures (T_a). While diffusion rates increase with higher T_a, the equilibrium MNSP phase fractions are also reduced. Thus, dissolution of what are argued to be RIS formed Mn-Ni-(Si) clusters following short term anneals at T_a from 450-500°C [125,126], or in low solute content model alloys at T_a = 400°C [10], does not prove that they are thermodynamically unstable at much lower service $T_i \approx 290$°C. Further, due to their small radii (r) of ≈ 0.50-2.5 nm, even if MNSPs are bulk equilibrium phases, they will dissolve at a higher T_a, due to the Gibbs-Thomson effect, if they are below the critical radius in a post-annealing, solute-depleted matrix. The effect of precipitate size is discussed further in Results. Note this approach can also be used to estimate the phase boundary at elevated temperature.

Because of the slow diffusion rates below ≈ 450°C, very long time (t_a) PIA is required to distinguish kinetic from thermodynamic effects, and to explore MNSP phase boundaries for comparison to thermodynamic models, it is absolutely critical to compare the PIA data to predictions of models that properly account for both thermodynamics and dissolution mechanisms and kinetics. Achieving these fundamental objectives also supports refining the

predictive Mn-Ni-Si precipitation [19] and PIA models, including for application to guiding embrittlement predictions and annealing remediation treatments.

7.1.2 Materials and Methods

The compositions of the two essentially Cu-free split-melt bainitic RPV steels studied here, designated LG and CM6, are shown in Table 7.1.1. The split-melt alloy microstructures and properties are fully representative of actual in-service RPV steels. The two steels have similar compositions, with the exception of Ni, that nominally ranges from ≈ 0.69% (LG, medium) to ≈ 1.57% (CM6, high). These alloys (among many others) were irradiated in the Advanced Test Reactor (ATR) to a very high fluence, $\phi t \approx 1.1 \pm 0.2 \times 10^{21}$ n/cm^2 at a high $\phi \approx 2.3 \pm 0.4 \times 10^{14}$ n/cm^2-s (E > 1 MeV) at ≈ 320 ± 15°C [62]. This ϕt is ≈ 11 times higher than that expected for RPVs at extended life, while the corresponding ϕ is ≈ 4600 times higher than typical RPV $\phi \approx 5 \times 10^{10}$ n/cm^2-s. It is well established that higher ϕ delays precipitation to higher ϕt, with a ϕ-adjusted effective fluence (ϕt_e) roughly scaling as $\phi t_e \approx \phi t(\phi_r/\phi)^p$, where ϕ_r is a specified reference flux and p ranges from ≈ 0.15 to 0.25 [8,31,55,127,128]. Thus the effective ATR ϕt_e is estimated to be only ≈ 2-4x10^{20}, which is 2 to 4 times the maximum $\phi t_e \approx 1 \times 10^{20}$ that an RPV would be expected to experience at an 80-year extended life.

Table 7.1.1. Nominal steel compositions (%)

Alloy	Cu	Ni	Mn	Mo	P	C	Si	Fe
LG	0.01	0.69	1.36	0.31	0.009	0.73	0.43	bal.
CM6	0.02	1.57	1.50	0.31	0.012	0.68	0.33	bal.

Note, the exact relationship between the effective fluence of the ATR irradiation condition and that experienced under extended life is not critical to the main purpose of this experiment, which was to generate significant quantities of MNSPs that could be readily characterized and modeled under long-time, high-temperature PIA [(i see acknowledgements)]. Atom probe tomography (APT) studies show that in the as-irradiated (AI) condition the alloys are nearly fully decomposed, at an approximately saturated MNSP f_v [124]. The two steels were annealed in vacuum for times of 1, 7, 17, 29 and 57 weeks[(ii)]. The MNSPs were characterized by APT up to 29 weeks, and by Scanning Transmission Electron Microscopy (STEM)-Energy Dispersive X-ray Spectroscopy (EDS) at 57 weeks[(i,iii)]. The annealing times were selected to ensure that any changes, or lack thereof, in the MNSPs would not be limited by slow solute thermal diffusion kinetics. Due to the very limited amount of irradiated material, the PIA was performed on 1.5 mm punched discs, precluding a sequence of standard microhardness measurements. See Chapters 3-4 and Appendix C for Materials and Methods supplemental information.

Energy Dispersive X-ray Spectroscopy

At longer annealing times, a significant reduction in the precipitate number density was observed. While APT has very high spatial resolution and measures the detailed chemical nature of the precipitates, it has a very small sampling volume, making it difficult to characterize them when they are present at a very low number density ($< \approx 10^{22}$ m^{-3}). Thus, at the longest annealing time (57 weeks), Energy Dispersive X-ray Spectroscopy (EDS) was performed using an FEI TALOS F200X S/TEM in the Low Activation Materials Development and Analysis Laboratory at Oak Ridge National Laboratory by Drs. Philip Edmondson and Peter Wells[(iii)]. EDS mapping was performed using a probe size of ~1 nm and current of 1.0

nA, respectively. Analysis of the data was performed using the Bruker-Esprit software. While the TALOS provided high-resolution chemical maps, it was not fully calibrated for quantitative chemical analysis. Thus to complement these high resolution maps, additional EDS scans were performed on the FEI Titan 300 kV FEG S/TEM at UCSB. A line scan with 4 nm spacing between points was taken across three grains, one with a high density of very large precipitates and two with a few sparse precipitates present, to measure the local solute contents, see Appendix E[(iv)].

Thermodynamic and Cluster Dynamics Modeling

A cluster dynamics (CD) model, using CALPHAD thermodynamics, thermal diffusion coefficients from literature and fitted precipitate interface energies, was used to guide the experimental design and to help analyze the annealing results [21] [(v)]. The model predictions of the equilibrium f_v have been reported previously and qualitatively favorably compare to the high ϕt ATR data [124]. The corresponding CALPHAD predicted equilibrium f_v for the two low Cu steels as a function of T_a are shown in Figure 7.1.1 for the nominal alloy compositions [105]. Again, the data from all models presented here gives precipitate mole fraction for comparison with APT data. CALPHAD predicts that only the Γ_2 phase ($Mn(Ni,Si)_2$) is stable in the high Ni (CM6) steel, with composition about 33%Mn-52%Ni-15%Si, exists up to 500°C, while the G phase ($Mn_6Ni_{16}Si_7$) persists only up to ≈ 390°C in the medium Ni (LG) steel [105]. Note that this bulk phase CALPHAD thermodynamic calculation leading to Figure 7.1.1 does not include effects of the interface energies of the small precipitates, although they are included in the CD model discussed below. Again a recent XRD study for the as-irradiated condition found G phase precipitates in the medium Ni steel, while the high Ni steel contains the Γ_2 phase, both as predicted by CALPHAD at 320°C [106].

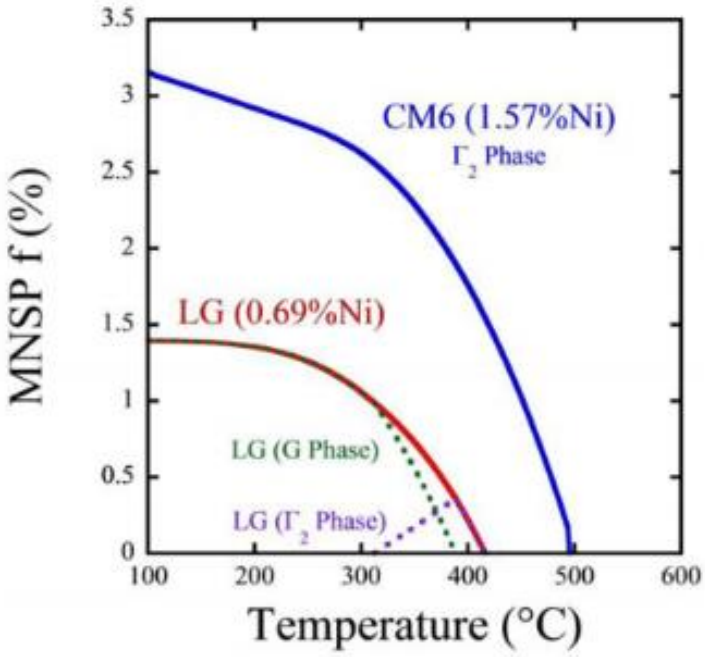

Figure 7.1.1. CALPHAD predictions of Mn-Ni-Si precipitate fv as a function of annealing temperature for two Cu-free steels with varying Ni content[v].

Figure 7.1.1 shows that CALPHAD predicts that the MNSPs in the medium Ni steel (LG) should completely dissolve above ≈ 415°C, while the Γ_2 phase in high Ni steel (CM6) is predicted to fully dissolve at ≈ 500°C. Because lower T_a results in slower solute diffusion, the isothermal annealing was carried out at an intermediate temperature of 425°C, with the intention of testing the thermodynamic model predicting full dissolution in LG (medium Ni) and that some MNSPs would remain in CM6 (high Ni). The complete MNSP dissolution of the phase in the medium Ni steel also acts as a kinetic marker to help estimate the effective diffusion distances at various annealing times that are pertinent to both alloys.

CD modeling was also carried out to help interpret the very complex MNSP dissolution and coarsening processes. Briefly, CD models the evolution of the MNSPs in discrete n-1, n and n+1 cluster sizes, where n is the number of atoms. The n ranges from 2 to n_{max} in a coupled set of n_{max} - 1 ordinary differential equations, which incorporate n-dependent effective solute

impingement and emission transition rate coefficients. In this case the solutes are treated as stoichiometric molecules of the pertinent phase. The CD method applied to modeling G and Γ_2 phase precipitation under irradiation is described elsewhere [19]. The CD model for annealing used here assumes thermal-diffusion controlled kinetics, and requires only 4 key experimental input parameters: a) the effective thermal solute diffusion coefficient (D), derived from the literature; b) the solute equilibrium solubility (X_e), determined by the free energy difference between the dissolved and precipitated solute states (that is the equilibrium phase diagram), evaluated from the Thermo-Calc [129] TCAL2 database [130]; c) the MNSP-Fe interface energy (γ), which differ slightly for the G and Γ_2 phases; and d) the as-irradiated MNSP size distribution, taken directly from the APT measurements. The γ were derived independently as fit parameters in the CD precipitation model, and were not adjusted in this PIA study [19]. Thus, the PIA CD model has no independently adjusted fit parameters.

7.1.3 Results and Discussion

STEM Observations

The APT data on the 29-week annealed high Ni alloy showed a very large reduction in the number densities (N) of the MNSPs, with few, if any, precipitates in a given tip. The tips without MNSPs coincided with lower local Ni and Mn contents. Hence, we first focus on the STEM-EDS characterization the 57-week PIA condition, in order to significantly increase the sampling volume relative to the APT observations. This directly confronts the question of the thermodynamic stability of the MNSPs, given a sufficient alloy Ni and Mn content. The STEM-EDS observations generally show regions with no precipitates and other regions with coarsened precipitates still remaining. A typical region with Mn-Ni-Si precipitates, with $\langle r \rangle \approx$ 2.7 nm versus $\approx$ 1.53 nm in the AI condition, is shown in 2a-e. The main conclusion of the

STEM-EDS study is that sufficiently coarsened MNSP are stable at near nominal amounts of Ni and Mn, even at a very long t_a that is ≈ 8 times that required for full dissolution of the MNSPs in the medium Ni alloy.

Figure 7.1.2d is a dark field (DF) STEM image showing a number of dislocation lines. Figure 7.1.2e is the same DF image overlaid with a partially transparent image of the Ni EDS signal, clearly showing a strong association between the dislocations and the remaining precipitates. This association is not unexpected, since the energy of Mn-Ni solute clusters are lower on dislocations than in the matrix [109,123] and, as a corollary, dislocations are attracted to MNSPs.

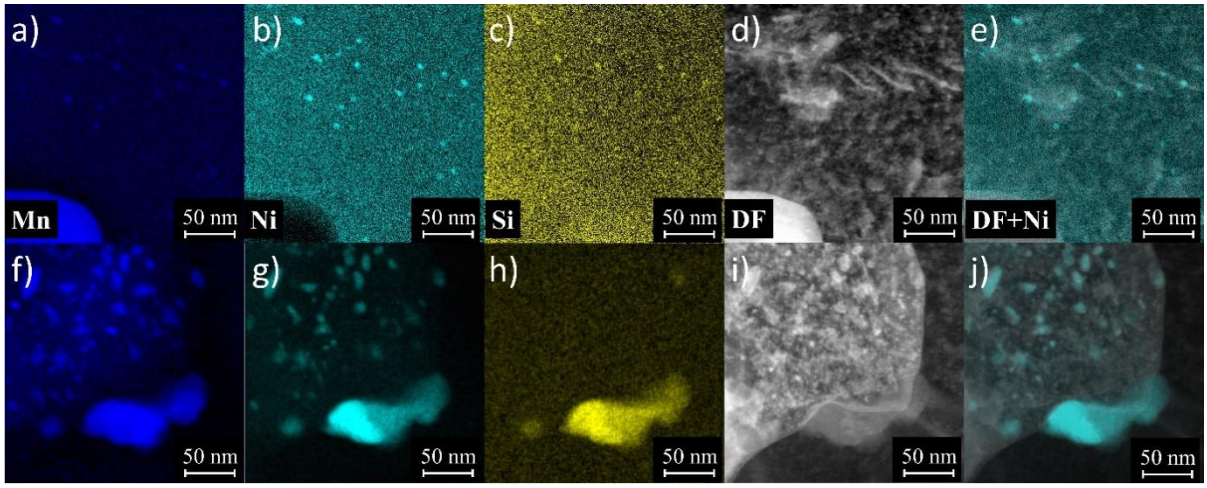

Figure 7.1.2. EDS maps showing Mn-Ni-Si precipitates remaining in the high Ni steel after annealing for 57 weeks at 425°C from: a-e) a region with relatively small precipitates, many of which are located on dislocations and f-j) a region with very large Mn-Ni precipitates[(iii)].

Figures 7.1.2f-j shows one grain that contained very large Mn-Ni enriched features, on the order of 20-30 nm long. These large precipitates were not significantly enriched in Si, except for one even larger MNSP on a grain boundary. The Mn-Ni enriched features are much larger than any previously reported precipitates in a neutron irradiated RPV steel. It is likely

that they are a MnNi B_2 phase [131]. Note, such large features have also been reported following proton irradiation [107]. A FEI Titan STEM EDS line scan was performed to determine the local solute composition of the grain with large precipitates, as well as the two nearby grains which had only a few, sparsely-spaced MNSPs[(v)]. This scan showed the local composition of the grain with large features was ≈ 3.36% Ni, 1.23% Mn and 0.34% Si, while both neighboring grains had compositions of ≈ 1.66-1.70% Ni, 0.60-0.72% Mn and 0.36-0.48% Si. The composition of the very high Ni grain is consistent with the formation of the MnNi B_2 phase with lower Si [131]. Additional details regarding the line scan can be found in Appendix E[(v)].

The most important result from the STEM-EDS study is that, given sufficient Ni, sufficiently large MNSPs are thermodynamically a stable equilibrium phases at 425°C, which is 105°C higher than T_i, and 135°C higher than for normal RPV service conditions. Figure 7.1.2 shows that the MNSPs are much more stable, and unambiguously thermodynamic equilibrium phases, at these lower T_i.

Atom Probe Tomography

Atom maps from the medium Ni steel (LG) for the AI and 425°C PIA conditions are shown in Figure 7.1.3 [(i)]. The MNSPs are very clearly dissolving following the one-week anneal; and the Mn and Si appear to have diffused further than the Ni, hence are the most dilute. The solutes in the medium Ni steel are nearly entirely dissolved after the 7-week anneal, as predicted by the thermodynamic model (see Figure 7.1.1), with only weak indications of residual solute clustering. The solutes are expected to be fully dissolved in the medium Ni steel after the 29 week anneal, since they have presumably diffused approximately twice as far compared to the 7 weeks condition [132].

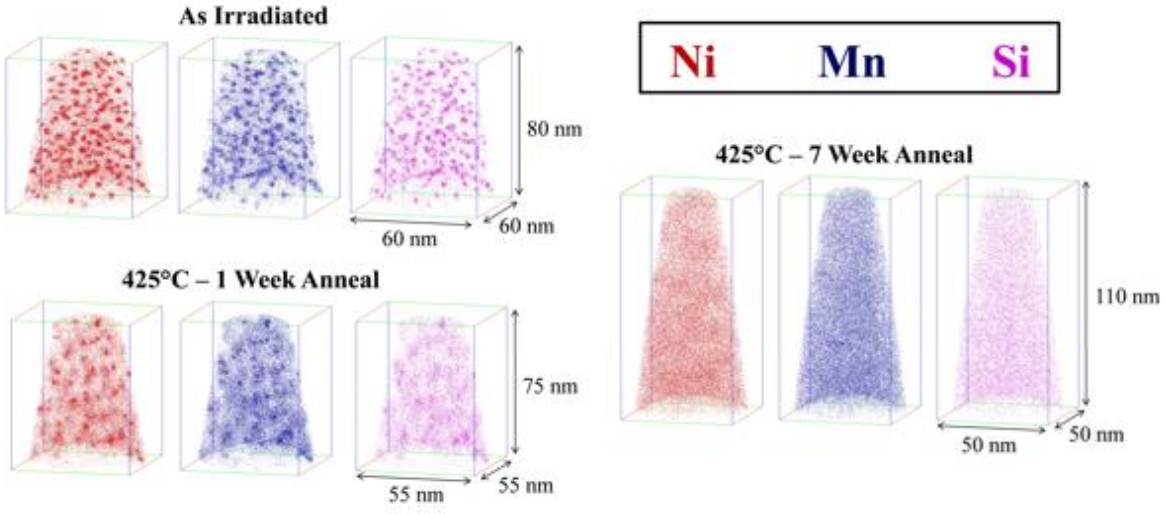

Figure 7.1.3. Atom maps for the Cu-free, medium Ni steel (LG) in the (a) AI condition, (b) 425°C - 1 week annealed condition, and (c) 425°C annealed - 7 week condition[(i)].

Atom maps in Figure 7.1.4 for the high 1.6% Ni steel (CM6) show that the MNSPs are much more stable, with well-defined precipitates still remaining after PIA for 29 weeks. The corresponding APT $<r>$, N and f_v data are summarized in Table 7.1.2 and Figure 7.1.5. Note that Table 7.1.2 gives the average values and uncertainty estimates for a given condition, while Figure 7.1.5 shows a data point for each measured APT tip, demonstrating that N and f_v vary significantly from region to region. As will be discussed below, this variability is dictated by the local bulk composition of an individual APT tip. The solid lines in Figure 7.1.5 are the CD model predictions for the nominal composition. Both N and f_v decrease rapidly with the increasing t_a. There is a corresponding small dip in $<r>$, followed by a slight increase up to 7 weeks, which is primarily due to the dissolution of the smallest MNSPs, rather than significant coarsening of the larger ones. However, it is notable that between 7 and 29 weeks <r> closely tracks the kinetics predicted by the CD model. The initial decrease in the MNSP N is also in agreement with model, but the APT data fall below the CD predictions between 17 and 29

weeks, although the rate of decrease in N and f_v slow, as is expected, under mixed dissolution and coarsening kinetics. Clearly, the nominal CD model over predicts N and f_v at long times. However, this is not surprising given the approximate parameterization of the CD model and the complexity of the interacting and competing processes mediating precipitate annealing, as discussed below. Note, the continuing decrease in N during PIA would make MNSPs very unlikely to be found in APT studies at 57 weeks, while they are clearly present in the STEM-EDS observations. Figure 7.1.6 shows the high sensitivity of the model to modest reductions in alloy Ni and Mn contents, of ≈ 6 and 23%, respectively, that lead to complete MNSP dissolution, again consistent with the STEM-EDS observations of lower solute regions.

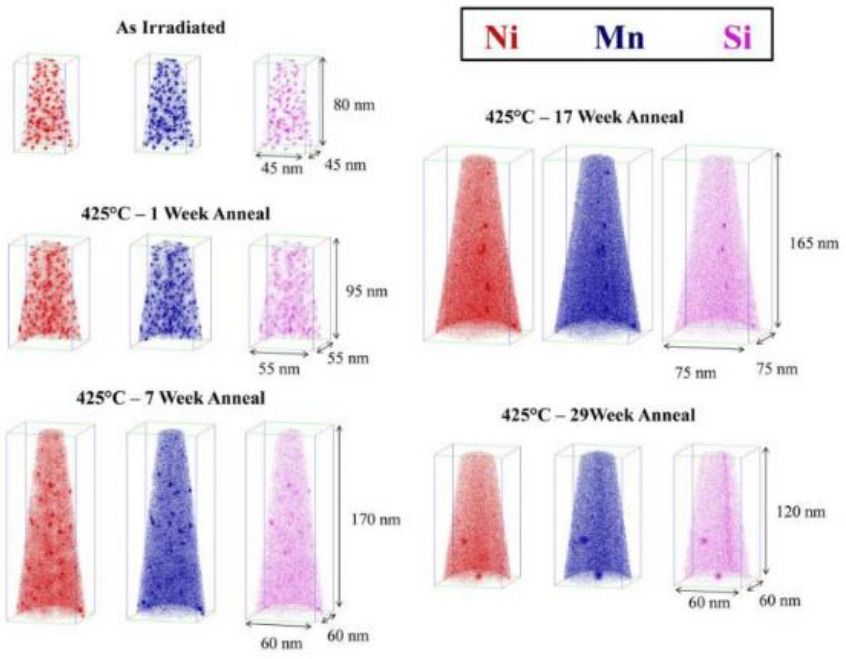

Figure 7.1.4. Atom maps for the low Cu, high Ni steel (CM6) in the AI condition (top left) and 425°C annealed conditions at times of: 1 week (mid left), 7 weeks (bottom left), 17 weeks (top right) and 29 weeks (bottom right)[(i)].

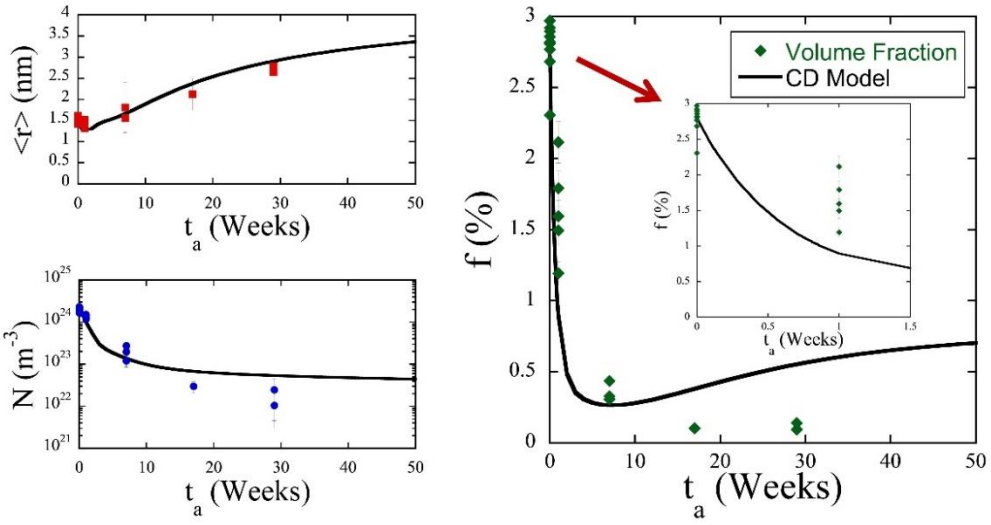

Figure 7.1.5. APT measured precipitate <*r*> (nm), *N* (m^{-3}) and f_v (%) after annealing (points) and CD predictions (lines) for the high Ni steel (CM6) at T_a = 425°C. Note that the plot of f_v vs t_a includes a blowup of the shorter annealing times to more clearly see these values. CD simulation conditions are described in the text[v].

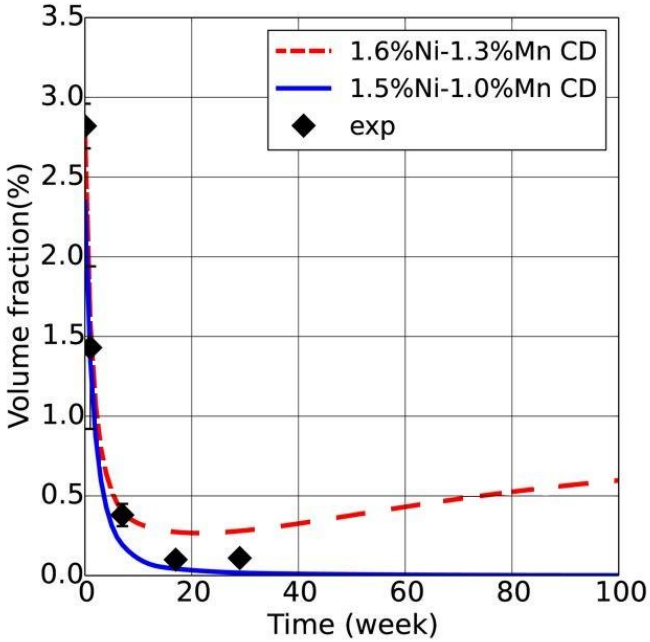

Figure 7.1.6. f_v as a function of annealing time at T_a = 425°C for two CD models with 0.34% Si and either 1.6% Ni and 1.3% Mn or 1.5% Ni and 1.0% Mn[v].

Table 7.1.2. Precipitate summary for the high Ni steel (CM6) from the AI and 425°C annealed conditions.

	Average t_a, $<d>$, N and f[a]			Average Precipitate Composition (%)							Artifact Fe	Relative Comp.
t_a	$<r>$	N	f	Cu	Ni	Mn	Si	Mo	C	P	Fe[b]	Mn/Ni/ Si
0	1.50 ±0.11	19.50 ±1.47	2.82 ±0.14	0.0	52.1	35.2	11.7	0.5	0.5	0.0	58.9	0.35/0.53/ 0.12
1	1.41 ±0.19	11.80 ±2.72	1.43 ±0.53	0.3	53.0	35.4	10.0	0.8	0.3	0.3	62.1	0.36/0.54/ 0.10
7	1.63 ± 0.42	2.19 ±0.70	0.38 ±0.07	0.0	52.8	38.0	7.8	0.9	0.2	0.2	57.6	0.38/0.54/ 0.08
17	2.13 ±0.22	0.30 ±0.08	0.10 ±0.02	0.0	52.6	37.6	7.0	1.6	0.9	0.2	55.8	0.39/0.54/ 0.07
29	2.78 ±0.13	0.14 ±0.07	0.11 ±0.02	0.0	35.8	35.5	14.3	8.7	5.1	0.6	37.5	0.41/0.42/ 0.17

*a) Units: t_a (wks), $<d>$ (nm), N (10^{23} m^{-3}), f_v (%). b) The nominal IVAS Fe found in all the MNSPs, that is thought to largely be an artifact.

The APT observations of MNSP response to PIA at temperatures much higher than they were formed at shows 3 stages: a) initial rapid dissolution of small precipitates between 0 and 7 weeks; b) mixed dissolution and coarsening between 7 and 17 weeks; and, c) coarsening between 17 and 29 weeks at a near minimum f_v. The kinetic order of coarsening beyond 7 weeks, as reflected in the time exponent, is illustrated in Figure 7.1.7, showing plots of $<r(t_a)>^3$ - $<r>(7)>^3$ and $1/N(t_a) - 1/N(7)$, which are both approximately linear in t_a, for classical diffusion controlled coarsening, often called Ostwald Ripening [133]. Notably, the order of coarsening kinetics is insensitive to the various CD model parameters as a combination of interface energy, solubility and diffusion coefficients, which strongly influence the absolute predictions of $<r>$, N and f_v. As discussed further below, the annealing processes in this case are more complex than those that are treated in simple coarsening models. However, the approximately linear t_a-dependence of $<r(t_a)>^3$ and $1/N(t_a)$ kinetics is powerful evidence that coarsening is occurring during the high temperature PIA at longer t_a. The $<r>$ at 17 weeks is a little lower than the mean fit line, likely due to the transition from dissolution to coarsening

dominated kinetics; while $1/N(t_a)$ is almost perfectly linear. In both cases the linear kinetics are within the estimated scatter in the data.

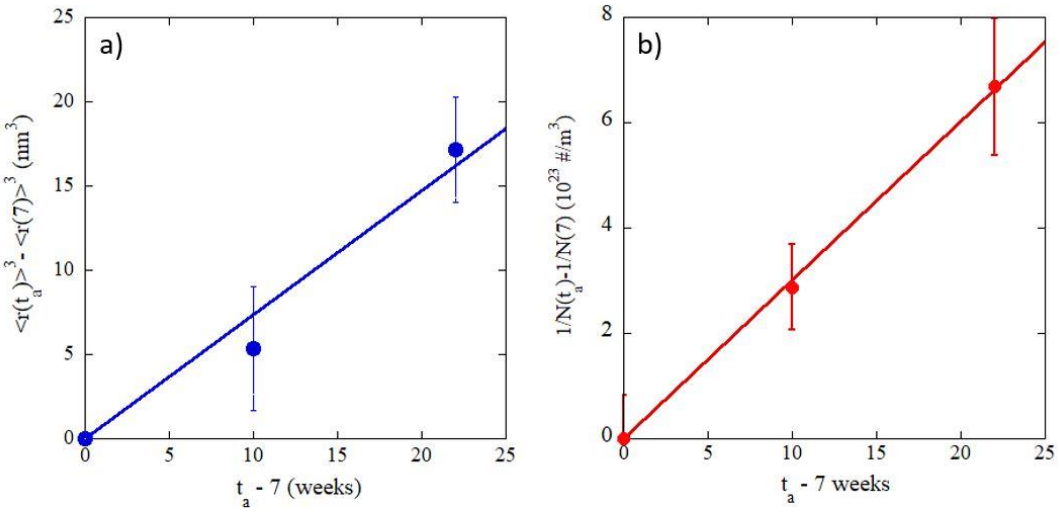

Figure 7.1.7. Plots showing MNSP coarsening kinetics that are consistent with a diffusion controlled mechanism for: a) of $<r(t_a)> - <r(7)>^3$; and, b) $1/N(t_a) – 1/N(7)$.

The average precipitate compositions as a function of t_a are also shown in Table 7.1.2. While Fe is an APT artifact, the nominal IVAS value is included in the table for those that wish to interpret the data differently. Table 7.1.3 summarizes the corresponding matrix compositions, which return to near nominal bulk values, reflecting the small residual f_v of the MNSPs. Table 7.1.4 shows the relative precipitate Mn, Ni and Si compositions compared to the closest known Mn-Ni-Si intermetallic phases. The Γ_2 phase (33%Mn-52%Ni-15%Si) is closest to the composition in the AI condition, but the MNSPs contain less Si for t_a up to 17 weeks, perhaps indicating initial evolution towards the cubic B_2 phase. Assuming the Mo and C are segregated (or co-precipitated) the return to higher Si, at 29 weeks, may signal a partial transition to the lower Ni T_7 phase. Note these phase associations are speculative, since the extent of their composition fields are not known. For example, it is well established that Si and

Mn are relatively interchangeable on their sub lattice in response to changes in the alloy bulk compositions [81,134]. Indeed, while TEM showed extra diffraction spots due to the presence of the precipitates, it was not possible to index them to specific phases, due to their still very small sizes and possible association with dislocations, see Appendix E.

Table 7.1.3. Amount of Mn, Ni and Si in the matrix for the high Ni steel (CM6) from the AI and 425°C annealed conditions.

	Average Matrix Composition (%)					
t_a	Ni	Mn	Si	Mo	C	P
0	0.17	0.32	0.04	0.25	0.16	0.00
1	0.62	0.62	0.18	0.22	0.12	0.00
7	1.43	1.24	0.34	0.25	0.06	0.01
17	1.60	1.08	0.37	0.22	0.08	0.01
29	1.66	1.34	0.38	0.25	0.16	0.00

Table 7.1.4. Relative amount of Mn, Ni and Si in the precipitates and compared with known Mn-Ni-Si phases.

t_a (week)	Mn/Ni/Si	Closest Phase Mn/Ni/Si
0	0.35/0.53/0.12	Γ_2: ≈ 34/47-52/14-20 XRD
1	0.36/0.54/0.10	Γ_2 to B_2 ≈ 41-47/50/3-9
7	0.38/0.54/0.08	Γ_2 to B_2: ≈ 41-47/50/3-9
17	0.39/0.54/0.07	Γ_2 to B_2: ≈ 41-47/50/3-9
29	0.41/0.42/0.17	Γ_2 to T_7: ≈ 50/33/17

Note phase name: $\Gamma_2 = T_6$ and $G = T_3$

It has been previously shown that tip-to-tip variability even in the same steel can be exploited to characterize the effects composition variations on precipitation [19,124]. The local composition also has a strong effect on the precipitate stability during PIA. For example, while MNSPs were still found in all the high Ni steel (CM6) tips in the AI, 1 week and 7 week t_a conditions, they were only found in tips containing more measured ≈ 1.5% Ni and 1.3% Mn

bulk solutes (close to the nominal alloy composition) for longer t_a. Due to the strong and very systematic effect of Ni and Mn, only tips that contained close to nominal alloy composition were included in plots of $<r>$, f_v and N. The full data for all runs taken is provided in Appendix E (Table E1 and Table E2) to more clearly demonstrate the tip-to-tip bulk composition variability and the corresponding impact on precipitate stability. It was also observed that small amounts of Mo and C at a ratio ≈ 1.25 (MoC to Mo_2C), are co-segregated to the MNSPs following the 29 week anneal. Note. other studies have shown these elements are depleted in the MNSPs in the AI condition at lower temperature [16]. Finally, we again note that the TEM-EDS results are qualitatively consistent with the 29 week APT data.

Cluster Dynamics Modeling

Figure 7.1.8 illustrates the complex physics of precipitate annealing at T_a much higher than in their nearly fully decomposed formation condition at lower temperatures in terms of the CD model predictions of critical radius (r_c) versus t_a compared to $<r>^{(v)}$. The critical radius is $r_c = -2\gamma/\Delta G_v$, where γis the MNSP interface energy and ΔG_v is the volumetric dissolved minus precipitate free energy difference for the matrix composition at t_a. Figure 7.1.6 shows that the <r> is initially far below r_c at 425°C in the solute depleted matrix. However, the rapid re-solution of the Mn, Ni and Si, results in a corresponding rapid decrease in r_c, with increasing t_a, while <r> increases following an initial dip. In this case the CD model predicts that the <r> and r_c curves cross at ≈ 5 weeks. At this point f_v begins to increase, initially by growth and subsequently by coarsening with decreasing N. The CD model predicts that the cross over occurs at $<r> = r_c \approx 1.5$ nm. In other cases the intersection could be delayed in t_a and at a larger $<r> = r_c$, while in other cases there would be no intersection at all, leading to full dissolution.

This delicate interaction between <r> and r_c leads to the high sensitivity of f(t_a) shown in Figure 7.1.7. Thus it is useful to try to estimate actual r_c.

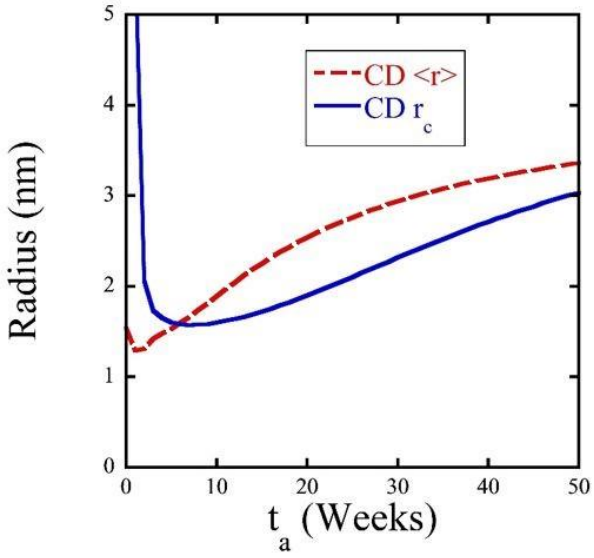

Figure 7.1.8. Cluster dynamics average precipitate radius (<*r*>) and calculated critical radius (r_c) as a function of annealing time. Simulation conditions are the same as in Figure 7.1.5[v].

The histogram plot Figure 7.1.9 shows that the APT *N* continuously decreases with t_a at all MNSP sizes except for r > 2.25 nm. Note, these *N* and corresponding f_v are highly uncertain at the long annealing times, since at most, only a few precipitates are observed in a given APT tip. While precise precipitate size distributions cannot be established, the APT results show that the largest MNSP survive and persist and slightly increase in numbers at longer t_a. Notably, no clusters with r < 2.25 nm were found in the 29 wk. condition. The largest MNSP in the AI condition was r = 2.3 nm, while the 3 precipitates found after the 29 week PIA all had r > 2.6 nm. The largest MNSP in the AI condition had ≈ 4500 solute atoms, the 3 clusters found after the 29-week PIA contained 6500, 7200 and 8100 solute atoms, respectively. Thus the MNSP with r > 2.25 nm are not only stable, but appear to be growing,

supporting the hypothesis that they are equilibrium phases. This interpretation of the APT results is consistent and supported by the EDS observations described previously, which showed a much larger number of coarsened MNSPs persist after annealing for 57 weeks in areas with sufficient Ni and Mn. Based on these results it appears that as parameterized the CD model $r_c \approx 1.5$ nm at the intersection with <r> underestimates the actual r_c which is closer to 2.3 nm. These results along with those in Figure 7.1.8, suggest that at 425°C the solvus boundary is larger than, for example, 1.5% Ni and 1.0% Mn and lower than 1.6% Ni and 1.3% Mn, since these compositions bracket the complete dissolution and overestimation of f_v, respectively.

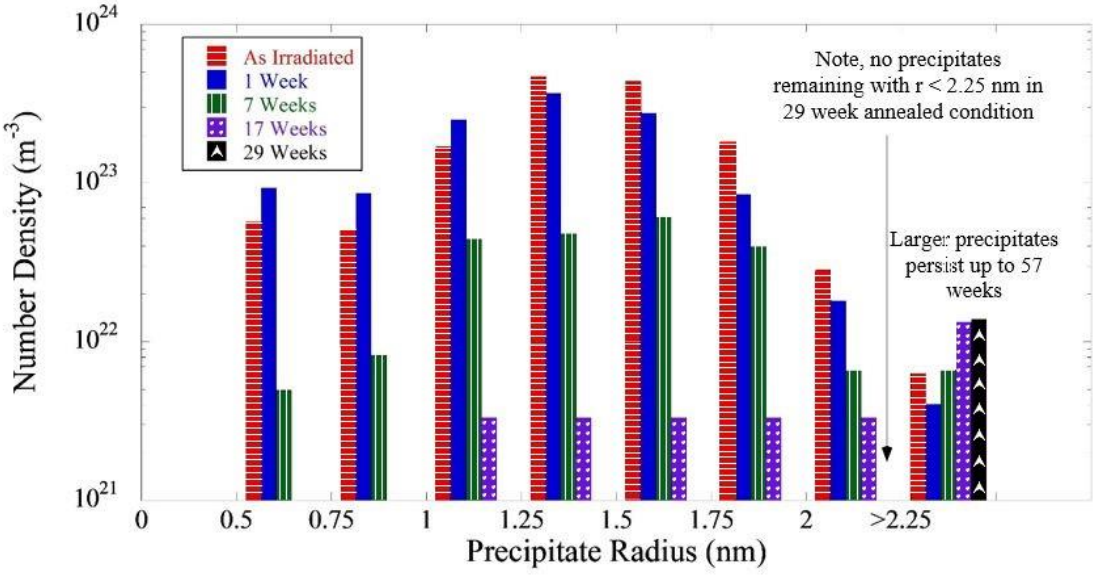

Figure 7.1.9. Size distribution of precipitates in the high Ni steel (CM6) for the AI and annealed conditions. Note that no precipitates with $r < 1$ nm were observed after 17 weeks of annealing and no precipitates with $r < 2.25$ nm were observed after 29 weeks of annealing[(i)].

The full dissolution in the medium Ni steel (LG) at 7 weeks demonstrates that 57 weeks t_a is far more than that needed to dissolve the MNSPs in the high Ni steel (CM6) if they are non-equilibrium solute clusters. The combination of APT results and CD model suggests that

the significant reduction in the precipitate N is consistent with the nano-scale size of the MNSPs, which are predominantly below r_c at 425°C in the initially solute depleted AI matrix. As the small MNSPs dissolve, the corresponding increase in the matrix solute concentration is sufficient to stabilize only the larger precipitates. The fact that MNSPs with r > 2.3 nm are stable in a matrix that is only slightly solute depleted (≈ -0.11%) compared to the total solutes available in the AI condition, suggests that they are not induced by radiation, consistent with thermodynamic predictions, especially for much lower temperatures (see below). Thus, the overall CD predictions are qualitatively consistent with the observations, supporting the thermodynamic basis for the model and the interpretation of the PIA data. However, the CD model over predicts the number of stable precipitates that remain based on an independent (not fitted) γ and ΔG_v, that underpredict r_c at 425°C. Note, the PIA data could be used to fine-tune both precipitation and annealing models. However, such fitting is beyond the scope of this work.

Finally, it is very important to return to the key question: *are the MNSPs stable, thermodynamic phases at a typical RPV service irradiation temperatures that are much lower than 425°C?* This is clearly the case, since the CALPHAD ΔG_v is ≈ 4 times larger at 290°C. Thus the corresponding r_c would be 0.54 nm, consistent, with the lower end of the observed MNSP size distribution in the AI condition.

7.1.4 Summary and Conclusions

PIA was used to investigate the character of MNSPs in neutron irradiated RPV steels. Annealing at 425°C for long times, resulted in complete precipitate dissolution in a medium Ni (0.69%) steel after only 7 weeks, *consistent with thermodynamic predictions*. In contrast, some MNSPs still remained at the longest annealing time of 57 weeks in the high Ni (1.6%)

steel, again qualitatively consistent with the CD model predictions. APT showed that the local regions with the highest precipitate stability contained at least 1.6% Ni and 1.4% Mn, although even in these regions a significant reduction in N and f_v were observed. However, the MNSP N with $r > 2.25$ nm coarsened slightly, while all the smaller precipitates dissolved at long t_a. This suggests that the critical radius r_c at 425°C at the higher Ni and Mn contents is ≈ 2.3 nm. The number of Mn-Ni-Si atoms in the MNSPs found at 29 weeks averaged almost 50% higher than the largest cluster found in the AI condition, again indicating modest coarsening. Notably, the order of the t_a dependence of the increase in <r> and decrease in N is also consistent with classical diffusion controlled coarsening. Finally, TEM-EDS even more clearly showed stable precipitates in grains with sufficient Ni and Mn, even after annealing at 425°C for 57 weeks, again strongly supporting the conclusion that MNSPs are a thermodynamically stable phase.

The <r>, N and f_v predicted by unfitted CD model is only qualitatively consistent with the experimental APT trends. While the model accurately predicts the increases in <r>, it overestimates the corresponding N and f_v. However, the model clearly reveals the basic PIA mechanism mediating the reduction in N and f_v is the large critical radius, r_c, at 425°C in the initially AI solute depleted matrix. The precipitates smaller than r_c dissolve and re-enrich the matrix. Hence, <r> increases with t_a while r_c decreases and after they intersect some of the remaining larger precipitates subsequently continue grow and coarsen even at the higher temperature of 425°C. The CD model over predictions can be traced to its independent parameterization that predicts an r_c that is smaller than that observed.

The key issue that is being addressed in this work is the thermodynamic stability of the MNSPs at much lower irradiation temperatures. Since ΔG_v is of order 4 times larger, and r_c is 4 times smaller, at 290°C compared to 425°C, there can be no question that MNSPs a stable

thermodynamics phase at such service relevant temperatures. Notably, these conclusions are consistent with both CALPHAD thermodynamic predictions and XRD measurements [19,106].

Finally, we note that these results do not mean that solute (Mn-Ni-Si) segregation, including that driven by RIS, does not play a role in MNSP evolution at lower temperatures. Indeed they clearly do especially in the nucleation stage where these solutes segregate to small dislocation loops created in displacement cascades. Depending on the alloy composition, even if bulk MNSP phases (G and Γ_2) are thermodynamically stable, slow homogeneous nucleation rates may greatly limit precipitation. There are many APT observations of heterogeneous nucleation on loops, line dislocations and grain boundaries, especially at lower alloy solute contents and or higher irradiation temperatures. Indeed, RIS is the likely cause of solute cluster formation, widely identified as a generic G-phase, in highly sub saturated alloys [95,97,109,124,135].

Acknowledgements

(i) Dr. Peter Wells designed the annealing experiment, performed the APT and produced comprehensive interpretations of results.
(ii) Dr. Peter Wells and Dave Gragg supported the isothermal PIA experiments.
(iii) Drs. Philip Edmondson and Peter Wells performed the S/TEM-EDS characterization at ORNL.
(iv) Drs. Tiberiu Stan and Soupitak Pal assisted in completing the EDS line scans on the FEI Titan at UCSB CNSI.
(v) Drs. Huibin Ke, Mahmood Mamivand, Shipeng Shu and Professor Dane Morgan at the University of Wisconsin provided all the CD and CALPHAD modeling cited in this paper. They were the source of many helpful discussions and much insight.

7.2: The Mechanistic Implications of the High Temperature, Long Time Thermal Stability of Nanoscale Mn-Ni-Si Precipitates in Irradiated Reactor Pressure Vessel Steels

7.2.1 Introduction

In Chapter 7.1, a recent 425°C PIA study up to 57 weeks, of a nearly fully phase separated highly 320°C neutron irradiated, Cu free, 1.6% Ni RPV steel, APT showed that most MNSPs dissolved, although a very low density of larger MNSPs with r > 2.2 nm, remained and appeared to coarsen at long times [121]. While, the APT MNSP statistics were limited, scanning transmission electron microscopy-energy dispersive X-ray spectroscopy (STEM-EDS) characterization confirmed the stability of the larger MNSPs. These results are consistent with cluster dynamics and kinetic lattice Monte Carlo models [121,136], which predict a large reduction in precipitate number density (N) at small $r < r_c$ at the high PIA temperature of 425°C, in a solute depleted matrix. Thus to further explore the thermal stability of MNSPs, we designed and carried out a special heavy ion irradiation experiment for the same Cu free high Ni steel.

This section details two separate 2.8MeV self Fe^{2+}-ion irradiation sequences to create populations of precipitates that targeted average radii ($\bar{r}$) that were both above and below the estimated r_c, again in the Cu-free 1.6 wt.% Ni steel cited above[(i see acknowledgments)]. One low-high (LH) ion irradiation was split into two temperature increments of 2.5 dpa each: 2.5 dpa at 330°C to nucleate a high N of MNSPs, followed by an increment at 2.5 dpa at 400°C to grow them to a f_v, close to full phase separation, but with $\bar{r} < r_c$. A second high temperature (HH) irradiation to 2.5 dpa at 400°C was aimed at producing a lower N of MNSPs with approximately the same f_v and larger $\bar{r} > r_c$. For thermally stable MNSPs, those larger than r_c

should remain and even grow and ultimately coarsen; while those that are smaller than r_c should fully dissolve. The growth of the larger MNSPs is due to re-precipitation of solutes that initially dissolved during PIA. Note the actual r_c varies with t_a, since the dissolved solute concentrations change with dissolution and re-precipitation [121].

APT maps demonstrate that the LH and HH irradiations were successful in generating a wide range of MNSP sizes, with $\bar{r}$ of 1.74 nm (LH) and 2.67 (HH), respectively[(ii)]. These as-irradiated (AI) alloys were then annealed at 425°C for up to 52 weeks. The main goal was to distinguish between RIS or RED formation mechanisms, associated with the MNSP thermal stability, or lack thereof, in comparison to thermodynamic predictions of r_c.

Note, even if it is shown that the MNSPs are stable, and the driving force for forming MNSPs is largely thermodynamic, RIS may affect the precipitate compositions somewhat [53]. Indeed, it is important to emphasize that RIS and RED work in tandem, and both can and do play a role in MNSP evolution in RPV and other steels. Most notably, MNSPs in low Cu steels are often associated with solute segregation to dislocations (loops and network); for example, see [26]. These associations are partly due to RIS, but are also partly thermodynamic in origin [137]. That is, both RIS and dislocation-modified thermodynamics result in locally enriched microalloy compositions, where MNSP formation rates are much higher than in the matrix. This can be described as dislocations resulting in significant alterations of the local thermodynamics and effective phase boundaries [137]. However, this topic is beyond the scope of this section[6]. Additional general background on embrittlement can be found in Chapter 2

[6] Thermal solute segregation to dislocations, in some cases leading to the formation of precipitates, have been recently described in a growing "linear complexions" literature, which we will not attempt to cite here. Along with RIS, thermal segregation is under investigation in our work. However, while it is an exciting direction of research, this topic is beyond the scope of this work, which focuses on the thermal stability of MNSPs.

and elsewhere [3,8,26].

The nominal composition of the essentially Cu-free high Ni split-melt bainitic RPV steel studied here, designated as CM6, is 0.02 Cu, 1.57 Ni, 1.5 Mn, 0.31 Mo, 0.012 P, 0.68 C, 0.33 Si, bal. Fe in units of%. The standard heat treatment is given in the Section 3.3. The resulting small heat, split-melt alloy microstructure and properties are fully representative of actual RPV steels. Small 1.5x0.5 mm disc specimens were irradiated with 2.8 MeV Fe^{2+} ions in the High Fluence Irradiation Facility (HIT), at the University of Tokyo facility in Japan at ≈ 330°C and 400°C (LH) and 400°C (HH) conditions. The average dpa rate was ≈ $1.5x10^{-4}$ dpa/s, yielding a dose of 5.0 and 2.5 dpa, respectively, at a depth of 500 nm. SRIM 2008 was used to calculate the dpa as a function of depth as shown in the SI Figure S7.2.1. The dpa were based on the Kinchin-Pease model, with a displacement energy of 40 eV, as recommended in ASTM E521-96 (2009) [118,138]. The PIA treatments were in vacuum at 425ºC for 22 and 52 weeks[(iii)]. Other information on the materials, methods and irradiation are included in the SI, Chapters 3-4 and Appendix C.

The previous section's PIA study of neutron irradiated CM6 showed that MNSPs below r_c ≈ 2.2 nm re-dissolved in much shorter times at 425°C, assuring that the 52 week PIA results will not be affected by kinetics [121]. Standard FIB liftouts (see SI) were extracted and fabricated into APT tips and TEM foils at a depth of ≈ 400-600 nm from the surface, where the damage profile is relatively flat. APT and STEM-EDS was used to characterize the MNSPs[(i,iv)]. Other information on the materials, methods and irradiation are included in, Chapters 3-4, Appendix C and Appendix E and elsewhere [74,75,78].

7.2.2 Results and Discussion

Tables 7.2.1 and 7.2.2 summarize the APT and STEM-EDS data, respectively.

Table 7.2.1. An APT precipitate summary for the high low Cu, high Ni steel (CM6) for the AI and 425°C annealed conditions.

		Average t_a, $\bar{r}$, N and f[a]			Average Matrix Composition (%)			Average Precipitate Composition (%)			Artifact Fe	10^6 atoms
	t_a	$\bar{r}$	N	f	Ni	Mn	Si	Ni	Mn	Si	Fe[b]	
330/400	0	1.74 ±0.17	9.50 ±0.53	1.97 ±0.23	0.28	0.74	0.04	57.8	28.4	13.8	57.0	40.8
330/400	22	2.40	0.40	0.20	1.31	1.25	0.30	51.0	33.4	15.6	47.6	13.0
330/400	52	N/A	N/A	N/A				-	-	-		-
400	0	2.61 ±0.03	3.00 ±1.06	1.88 ±0.62	0.65	1.48	0.06	64.0	15.9	20.1	47.1	23.4
400	22	2.30	1.95	0.88	1.16	1.39	0.30	53.4	33.2	13.4	49.4	7.5
400	52	2.82 ±0.05	1.76 ±0.17	1.65 ±0.09	0.68	0.99	0.08	54.0	31.0	15.0	35.9	4.4

*a) Units: t_a (wks), $\bar{r}$ (nm), N (10^{23} m^{-3}), f_v (%). b) The nominal IVAS Fe found in all the MNSPs, that is thought to largely be an artifact.

Table 7.2.2. An EDS precipitate summary for the low Cu, high, high Ni steel (CM6) for the AI and 425°C annealed conditions.

		Average EDS t_a, $\bar{r}$ *and* N[a]	
	t_a	$\bar{r}$	N
330/400	0	4.40±0.80	3.22±.50
330/400	22	4.34±2.20	0.37±0.20
330/400	52	7.12±0.22	0.02±0.01
400	0	6.62±0.82	0.78±0.28
400	52	7.86±1.21	0.51±0.14

*a) Units: t_a (wks), $\bar{r}$ (nm), N (10^{23} m^{-3}).

Figure 7.2.1 summarizes the results of the APT measurements. Figures 7.2.11a and d show the MNSP N(r) for the various conditions. Figures 7.2.11b and e show corresponding examples of the APT reconstructions. Figures 7.2.1c and f_v plot N, $\bar{r}$ and f_v as a function of t_a.

Figure 7.2.2 similarly summarizes the STEM-EDS data. In this case, the Ni MNSPs, which also contain Mn and Si, are shown in Figures 7.2.2b and e. The APT and STEM-EDS results are qualitatively similar. The major difference is that the EDS measurements do not observe smaller MNSPs, while they better quantify the N at larger r. Figure 7.2.2g shows the MNSP composition in the various conditions are similar, except in the case of the HH AI condition, which has higher and lower than average Ni and Mn contents, respectively.

These results show that essentially all of the smaller MNSPs, in the LH AI condition, dissolve by 22 weeks. Note that, in this case, the somewhat lower Ni content in in the LH APT tips also enhanced dissolution. More significantly, however, the initially larger MNSPs in the HH AI condition undergo relatively little change for PIA at 425°C for t_a up to 52 weeks. More specifically, Figure 7.2.1f shows that the HH N systematically decreases up to 52 weeks, while $\bar{r}$ first decreases slightly, and then increases, indicating a small amount of MNSP regrowth and coarsening. The corresponding f_v also first decreases and then increases to values similar to that in the AI condition. The complementary HH STEM-EDS data in Figure 7.2.2 also show slight MNSP coarsening at 52 weeks. Note, not surprisingly, the r values measured by STEM-EDS are systematically larger and N lower than observed in the APT studies. The $\bar{r}$, N and f_v trends are expected and are well-predicted by a cluster dynamics and KLMC annealing models [121,136][(v)]. In the initially AI solute depleted matrix, the critical radius (r_c) is very large at 425°C. But as the MNSPs dissolve, and solutes reenter the matrix, r_c decreases. MNSPs with r that are greater than r_c then grow. A simple analysis of r_c is discussed next.

The MNSP compositions are generally consistent with the Γ_2 phase, with the exception of the AI HH condition, which is compositionally closer to the G phase. Note, the HH tips contained a larger Ni and lower Mn than average, respectively. The Γ_2 phase is formed by the

reaction: $3Ni(s) + 2Mn(s) + 1Si(s) \Leftrightarrow Ni_3Mn_2Si$ (nominal), where subscript s denotes dissolved solutes. At equilibrium, $\{[X_{Ni}]^3[X_{Mn}]^2[X_{Si}]\}^{1/6} = K(T)$, where X_i are the dissolved solutes mole fractions and K(T) is the temperature dependent reaction constant, incorporating the activity coefficients of the dissolved solutes and the formation free energy of the Γ_2 phase. Ke used CALPHAD to determine K(T), which is ≈ 0.008 at 425°C [22]. The solute supersaturation is $S = [X_{ni}]^3[X_{mn}]^2[X_{si}]\}^{1/6}/K(425°C)$ and the corresponding free precipitation energy change is $\Delta G_v = -[RT/V_m]\ln[S]$, where R is the gas constant and V_m is the Fe molar volume. The critical radius is $r_c = -2\gamma_{pm}/\Delta G_v$, where the interface energy is $\gamma_{pm} = 0.175$ J/m^2. The corresponding HH r_c for the matrix compositions in Table 2 are 2.07 nm (22 weeks) and 2.53 nm (52 weeks). For the G phase, nominally $Ni_{16}Mn_6Si_7$, r_c=2.5nm (22 weeks) and 3.49 nm (52 weeks).

These r_c estimates are very consistent with the observed HH MNSP stability. Figure 7.2.3a shows the calculated Ni phase boundary solvus line (X_{Nis}) as a function of temperature for stoichiometric G and Γ_2 phases [68]. Notably the X_{Nis} is ≈ 3.5 times lower at 290°C versus 425°C. The filled circles are the measured matrix X_{Nim} in the AI (400°C) and HH 52-week PIA (425°C) conditions, which are consistent with the computed X_{Nis}. However, the Gibbs Thomson effect, $X_{Nis} = X_{Nim}\exp(-2\gamma_{pm}V_m/rRT)$, would suggest that the actual equilibrium X_{Nis} is lower, as shown as the blue squares. The adjusted X_{Nis} agreement with the predicted solvus is not as good, but it is still reasonable. Figure 7.2.3b shows a semitransparent EDS map of the MNSPs (Ni-red) overlaying a dark field TEM micrograph of the dislocation structure in the LH 52 week condition. The arrows show that most of the MNSPs are associated with dislocations, consistent with previous observations of 425°C PIA after a high dpa neutron irradiation [121].

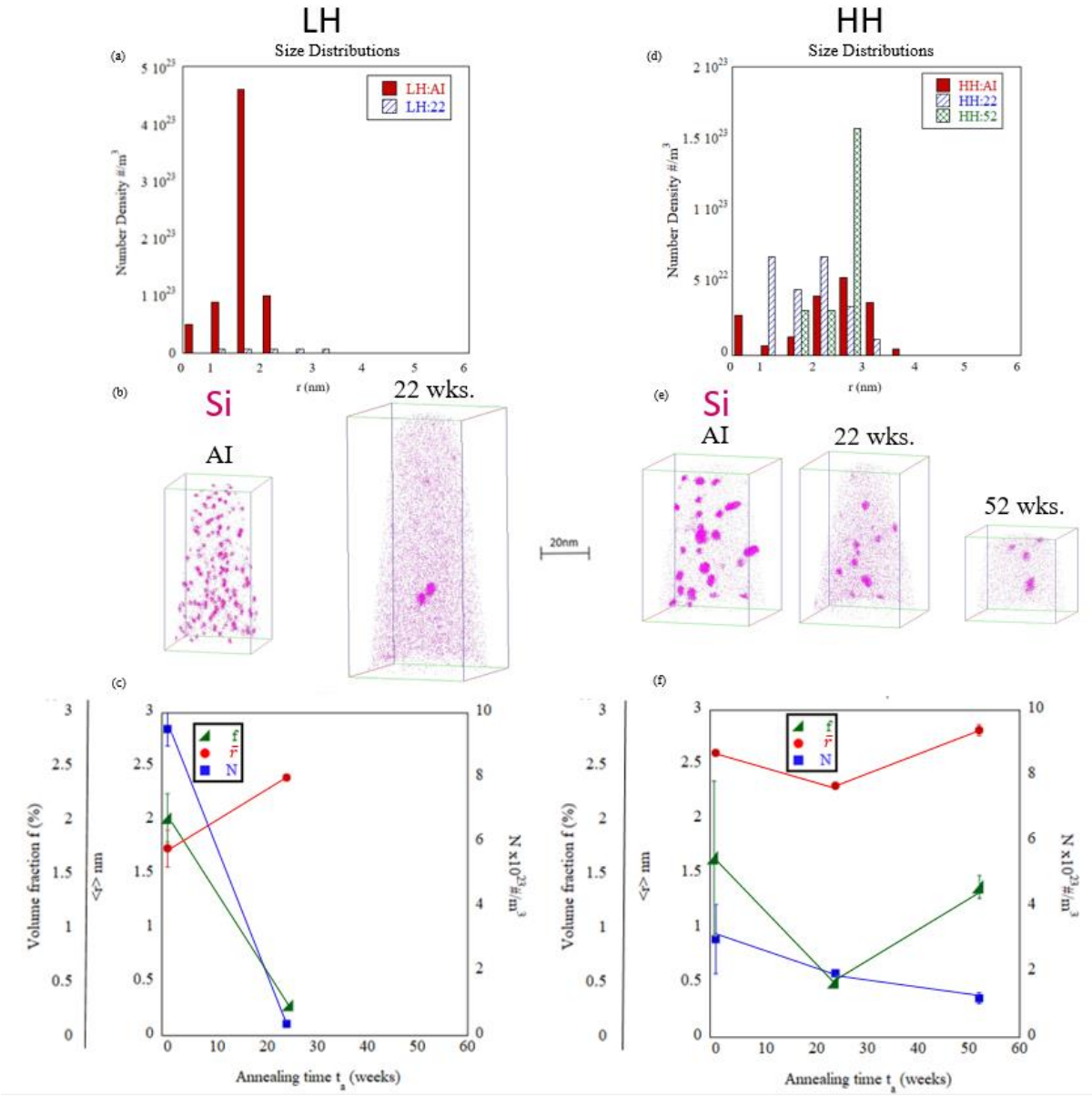

Figure 7.2.1. a) and d) APT N(r) for the LH and HH conditions, respectively; b) and e) examples of APT reconstruction for the LH and HH conditions, respectively; and, c) and f) N, $\bar{r}$ and f_v for the LH and HH conditions, respectively[(i)].

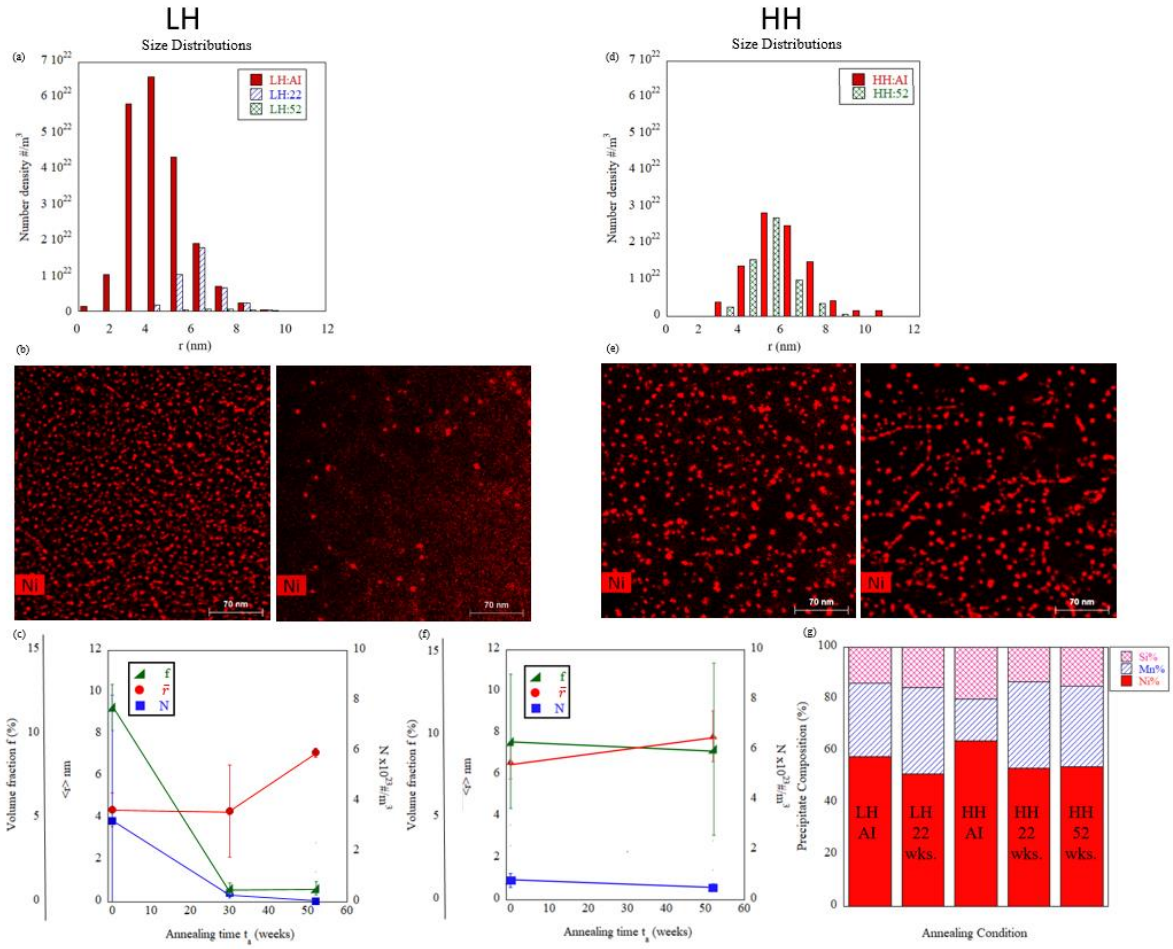

Figure 7.2.2. a) and d) STEM-EDS N(r) for the LH and HH conditions, respectively; b) and e) STEM-EDS micrographs of Ni in the Mn-Ni-Si precipitates for the LH and HH conditions, respectively; and, c) and f) and f) N, $\bar{r}$ and f_v for the LH and HH conditions, respectively; and g) bar graphs comparing the Ni, Mn, and Si precipitate compositions for various conditions[iv].

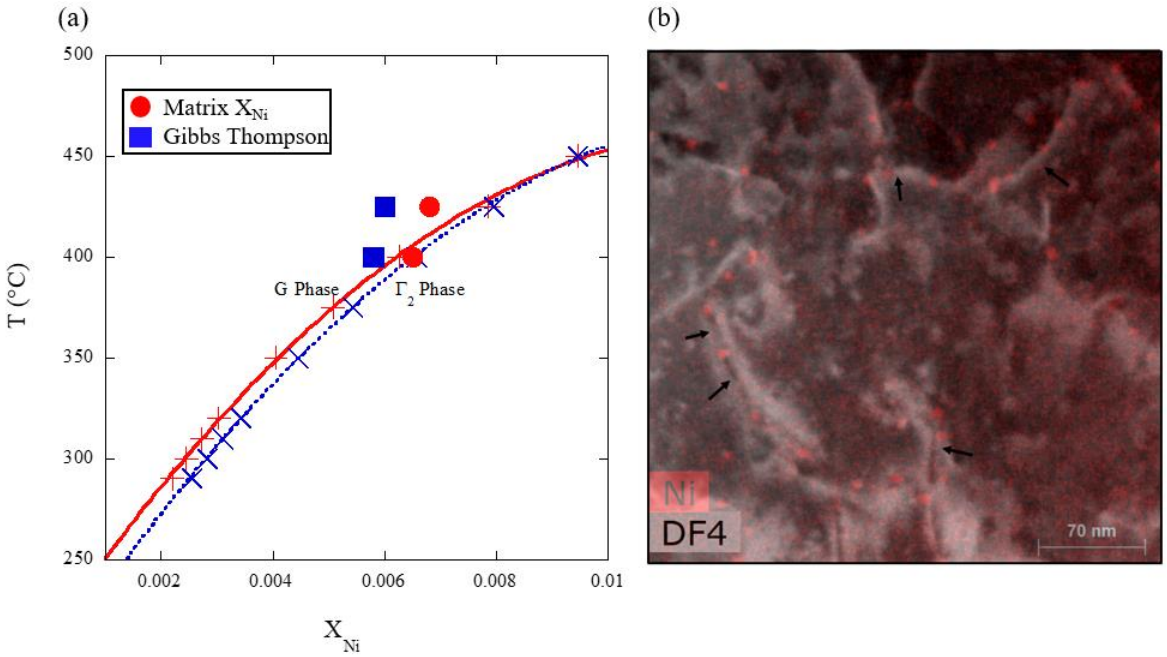

Figure 7.2.3. a) Calculated Ni Phase boundary solvus lines (X_{Nis}) as a function of temperature for G and Γ_2 phases along with the measured matrix Ni compositions, X_{Nim} (filled red circles), in the HH AI and 52 week PIA conditions, as well as the Gibbs Thompson adjusted X_{Nis} (blue filled squares) based on the matrix X_{Nim}; and, b) dark field micrograph of the dislocations overlaid with a partially transparent image of the Ni EDS signal (red spots) for the associated MNSPs LH 52 week PIA condition[iv,v].

7.2.3 Summary and Conclusions

In summary, ion irradiations and long term annealing at 425ºC successfully probed the thermal stability of MNSPs larger (irradiated at 400°C) and smaller (irradiated at 330°C and 400°C) than r_c. Analysis of the data generated by these complementary techniques leads to the following conclusions:

– MNSPs that are both larger and smaller than r_c were generated in high Ni (~1.6%) RPV steel CM6 by varying the ion irradiation temperature sequence.

- The smaller precipitates in LH condition, with $r < r_c$, largely dissolve after annealing at 425°C for long times.
- The larger precipitates in the HH condition, with $r > r_c$, are stable.
- Thus it must be concluded that the MNSPs are thermodynamically stable, and are likely the Γ_2 phase in most cases.
- The MNSPs would be even more thermodynamically stable at much lower neutron irradiation RPV service temperatures around 290°C
- The MNSPs in the HH 52 week condition are largely associated with network dislocations.

Acknowledgements

(i) Dr. Takuya Yamamoto conducted the CPI at the Dual Beam Facility for Energy Science and Technology (DuET) at Kyoto University in Japan with the support of Dr. Kiyohiro Yabuuchi, Akihiko Kimura, and Mr. O. Hashitomi.
(ii) Dr. Peter Wells designed the annealing experiment, collected part of the APT data and produced comprehensive interpretations of results.
(iii) Dr. Peter Wells and Dave Gragg supported the isothermal PIA.
(iv) Drs. Philip Edmondson, Peter Wells and Soupitak Pal performed the S/TEM-EDS characterization at ORNL and UCSB CNSI.
(v) Drs. Huibin Ke, Mahmood Mamivand, Shipeng Shu and Professor Dane Morgan at the University of Wisconsin provided all the CD and CALPHAD modeling cited in this paper. They were the source of many helpful discussions and much insight.

Chapter 8: Developing a Low ϕ-High ϕt ΔT Prediction Model

Introduction

The overriding objective of this dissertation is to contribute to accurate modeling for predicting ΔT for low ϕ, high ϕt extended life conditions in RPV steels. Due to there being little surveillance data in this regime, this dissertation's focus was to create and analyze the high ϕt intermediate ϕ ATR-2 database on both $\Delta\sigma_y$ and microstructural changes in a large number of irradiated alloys. Thus, ATR-2 results were integrated by Dr. Peter Wells and Nathan Almirall with a variety of other comprehensive databases (IVAR, ATR-1, BR2, US surveillance data and other databases). The international surveillance database was also updated beyond what was tabulated in the ASTM Plotter package. This integrated embrittlement database was used to refine the empirical relationship between the $\Delta\sigma_y$ and $\sqrt{f_v}$ and derive a composition dependent chemistry factor (CF = $\Delta\sigma_y$ (Cu, Ni, Mn, Si, P)) for the ATR-2 irradiation. Special emphasis is on the $\Delta\sigma_y$ contributions of MNSPs, which are observed in a wide range of RPV steels at high ϕt. Existing model predictions of ΔT at high ϕt are compared to the Odette, Wells, Almirall, Yamamoto (OWAY) model.

8.1 Integrated UCSB Embrittlement Database

There are a total of ≈ 190 alloys with over 1500 alloy/conditions in the integrated UCSB embrittlement database. This database includes macros which generate single variable plots and sort data by irradiation conditions, composition factor and by characterization technique[(i)]. The data contains the UCSB irradiation experiments, US surveillance and the US Power Reactor Data Base (PREDB), compiled by Mark Kirk as part of a 2013 activity, which led to the adoption of the ASTM E900 [139]. Figure 8.1 compares the PREDB compositions to the compositions of the ATR-2 alloys analyzed in this thesis. The axes are for Cu (x) and Ni (y), while the x error bars are the alloy Si divided by 5 and the y error bars are the P.

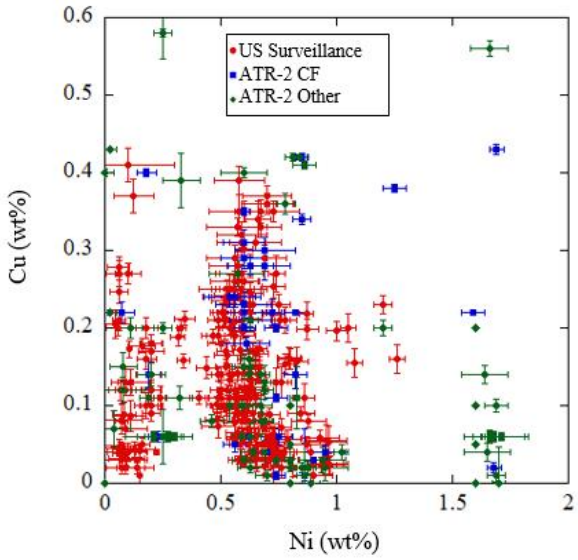

Figure 8.1. A map of the Cu and Ni contents of the ATR-2 and the 272 US power reactor surveillance database alloys.

Figure 8.2 shows a simple empirical tensile $\Delta\sigma_y$-$\sqrt{f_v}$ correlation using 299 alloy-conditions has SD ≈ 32 MPa. The scatter sources are not yet analyzed but are not surprising since f_v was characterized by various methods with similar uncertainties.

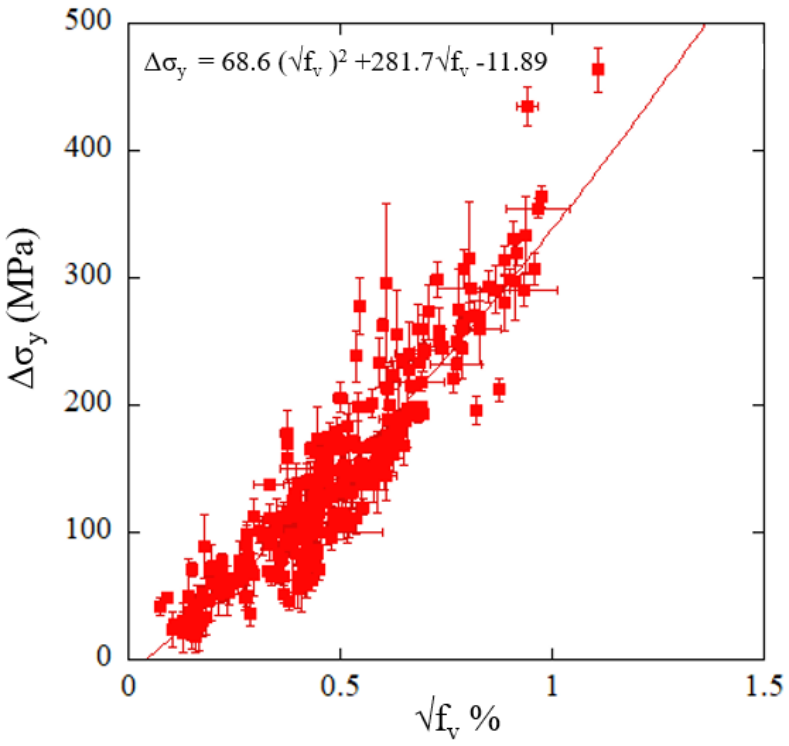

Figure 8.2. A simple empirical tensile $\Delta\sigma_y$-$\sqrt{f_v}$ correlation for 299 alloy/conditions has SD ≈ 32 MPa.

The data from surveillance programs has been archived by the US Nuclear Regulatory Commission (USNRC), which subsequently have been compiled by the Reactor Embrittlement Archive Project (REAP) sponsored by the USNRC at ORNL [140,141]. Figure 8.3 shows the hardening from REAP and ATR-2 as a function of ϕt plotted for 9 surveillance steels with low (0.07%) and higher bulk nominal (>0.07%) Cu. The ATR-2 data points at highest plotted fluence were the result of mechanical property measurements of the irradiation hardening via microhardness. APT demonstrates the growing f_v of MNSPs and CRPs with fluence are predominantly responsible for this hardening, see Chapter 5. For the lowest Cu alloy, starting from lowest ϕt there is virtually zero hardening, which manifests as negative hardening within the acceptable bounds of measurement technique error. The low Cu steels exhibit a delayed hardening response, followed by gradually increasing $\Delta\sigma_y$ to the ATR-2 condition. In Figure

8.3b at lower ϕt four of the five higher Cu (>0.14%) steels show 100-200MPa of hardening as a result of CRPs. The lower levels of bulk Cu and Ni of the 0.14Cu 0.19Ni steel resulted in a large reductions of hardening and volume fraction in ATR-2 (0.25%). The Cu-driven hardening is responsible for the rapid $\Delta\sigma_y$ increase at low ϕt followed by slightly accelerated increase to high ϕt in ATR-2. Again this is expected and well-understood to be due to supersaturated Cu rapidly precipitating out of solution [8,31]. Figure 8.4 converts the measured ATR-2 (black) $\Delta\sigma_y$ to ΔT using established correlations and compares to REAP (purple) and current embrittlement models (lines). The three surveillance steels contain 0.05% Cu, 1.3-1.4% Mn and show a strong Ni effect.

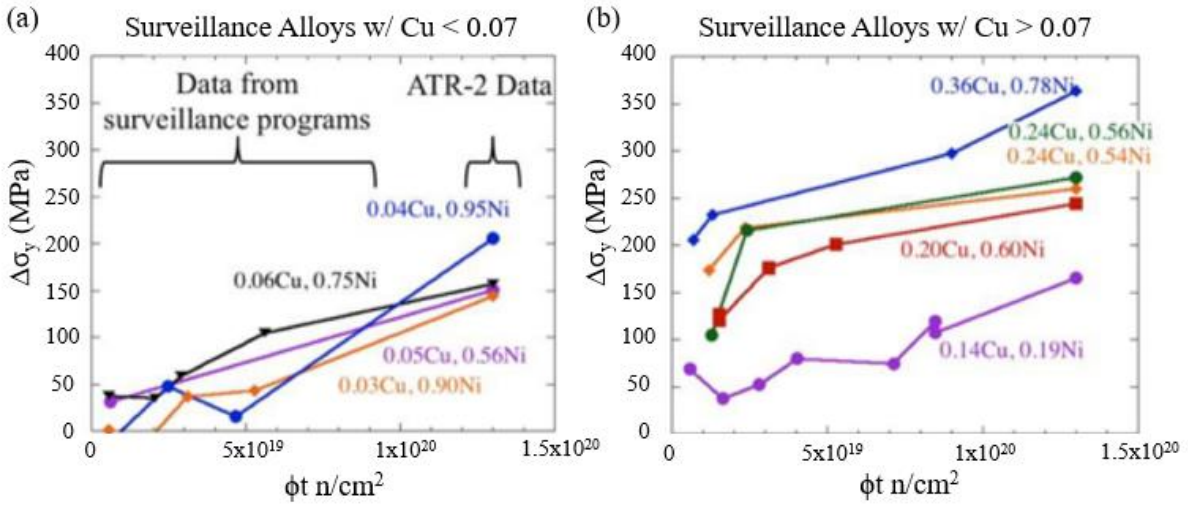

Figure 8.3. Hardening vs neutron fluence for 9 surveillance steels with a) low <0.07at% Cu and b) higher >0.07at% Cu surveillance steels.

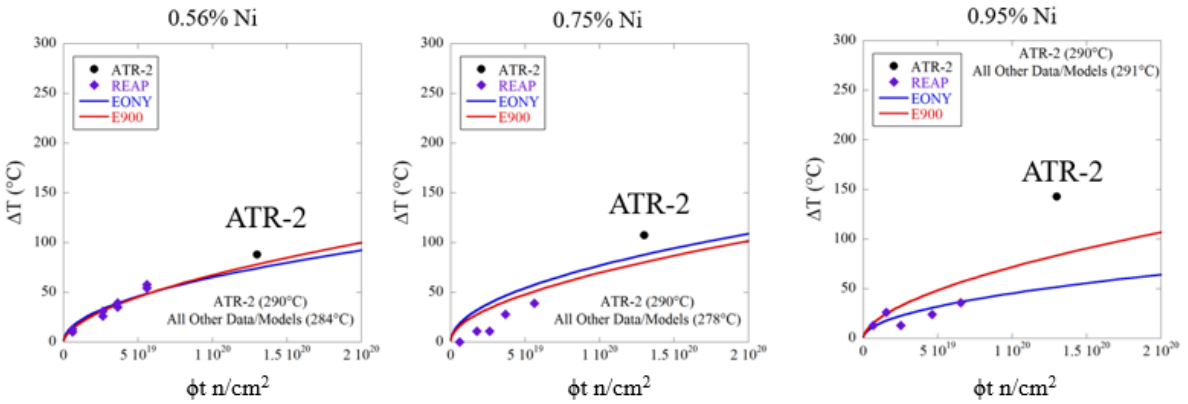

Figure 8.4. Conversions of measured ATR-2 (black) $\Delta\sigma_y$ to ΔT using established correlations and comparisons with REAP (purple) and current embrittlement models (lines). The three surveillance steels contain 0.05% Cu, 1.3-1.4% Mn and show an unaccounted strong Ni effect [141][(ii)].

8.2 ATR-2 Hardening for Surveillance Steels

Figure 8.5 shows the shows measured surveillance-program $\Delta\sigma_y$ from ATR-2 cup 7 along with predictions from existing ΔT surveillance database based Eason-Odette-Nanstad-Yamamoto (EONY) and ASTM E900 models, as well as a $\Delta\sigma_y$ model derived from the UCSB Irradiation Variables (IVAR) database[(ii)]. In the case of both EONY and E900 the ΔT predictions have been converted to $\Delta\sigma_y$ using established correlations [55]. With few exceptions, all of these the models under-predict the high fluence ATR-2 data. The under-predictions are as much as 129 MPa, averaging 62 and 54 MPa for EONY and E900, respectively. The under-predictions for the IVAR model are generally slightly less, averaging 45 MPa. Again these comparisons do not account for potential flux effects.

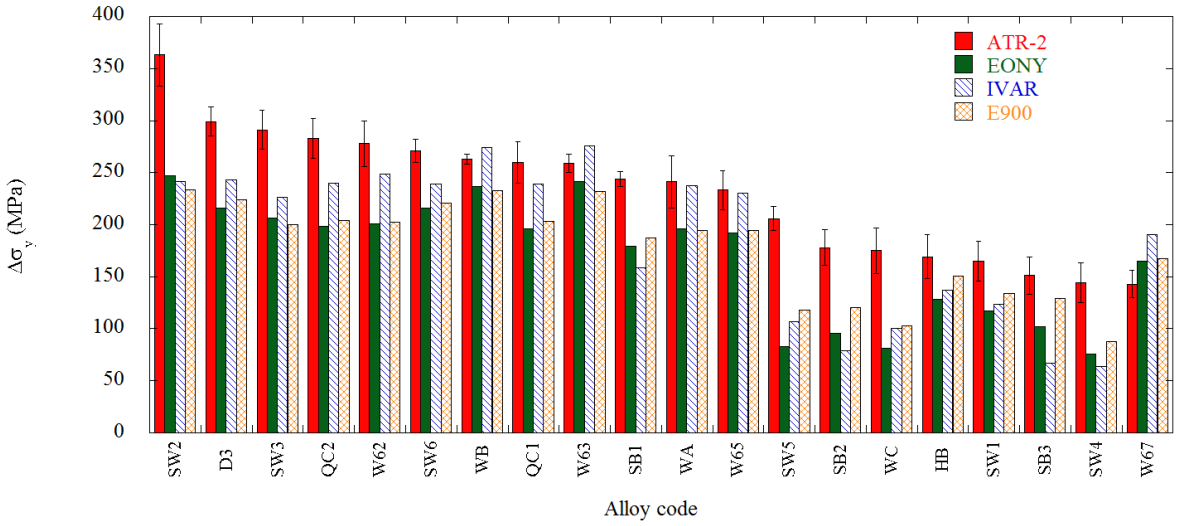

Figure 8.5. ATR-2 cup 7 hardening for various surveillance alloys along with predictions from existing models[ii].

Figure 8.6 shows a similar comparison for the UCSB L and CM-series SMS and the program alloys that have been previously irradiated but not in surveillance programs. Here only the EONY and E900 predictions are compared with the ATR-2 data. In this case, both models generally under-predict, but E900 gives 4 very large over-predictions for alloys CM20, CM17, CM7 and CM6, which all have high Ni from 1.59 to 1.70%. The average error for the EONY model is a 78 MPa under-prediction, though the E900 model has an average 24 MPa over-prediction, due to the very large over-predictions in the high Ni steels.

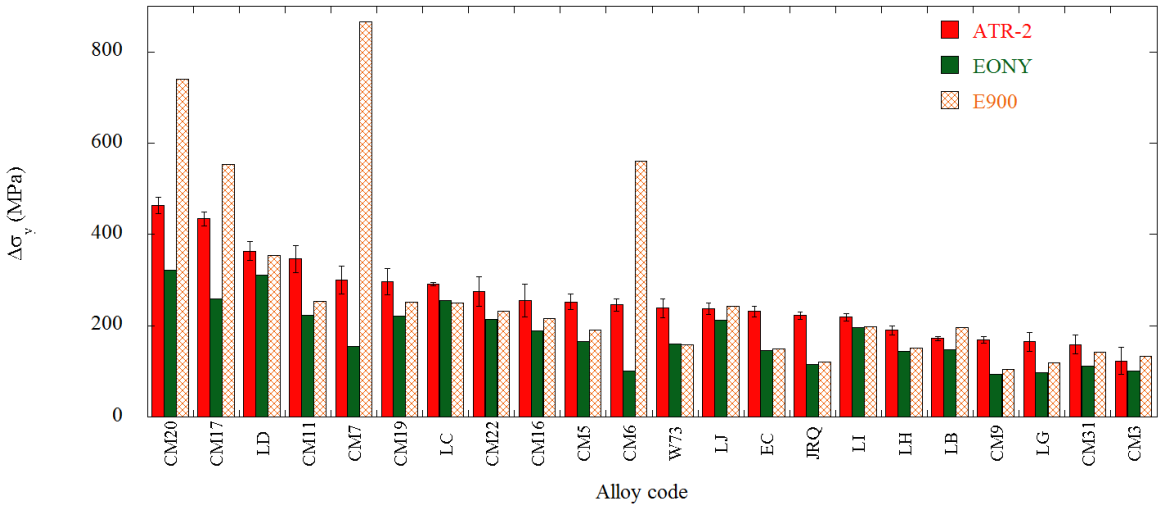

Figure 8.6. ATR-2 cup 7 hardening for the UCSB SMS and program alloys along with predictions from existing models[ii].

8.3 Composition Effects

The section focuses on a preliminary analysis of the composition dependence of the increase in tensile yield strength ($\Delta\sigma_y$) for ATR-2 irradiation conditions in terms of a chemistry factor (CF) that accounts for the individual and combined effects of Cu, Ni, Mn and P. The UCSB SMS have systematic variations in Cu, Ni, Mn and P thus they provide a basis to directly assess alloy composition effects on precipitation and hardening. 8.7-8.10 compare data from ATR-2 cup 7 to two conditions from the IVAR experiment, T6 (ϕ = 1x10^{12} n/cm^2-s, ϕt = 3.4 x10^{19}) and T16 (ϕ = 3x10^{11} n/cm^2-s, ϕt = 1.6x10^{19} n/cm^2).

Figure 8.6 shows the effect of Cu for both ≈ 0.8% Ni (left) and ≈ 1.6% Ni (right). Note the highest bulk Cu is ≈ 0.4%, but the data are plotted based on the estimated initial Cu in solution of ≈ 0.25%. The effect of Cu is generally similar, but somewhat weaker at the higher ATR-2 fluence.

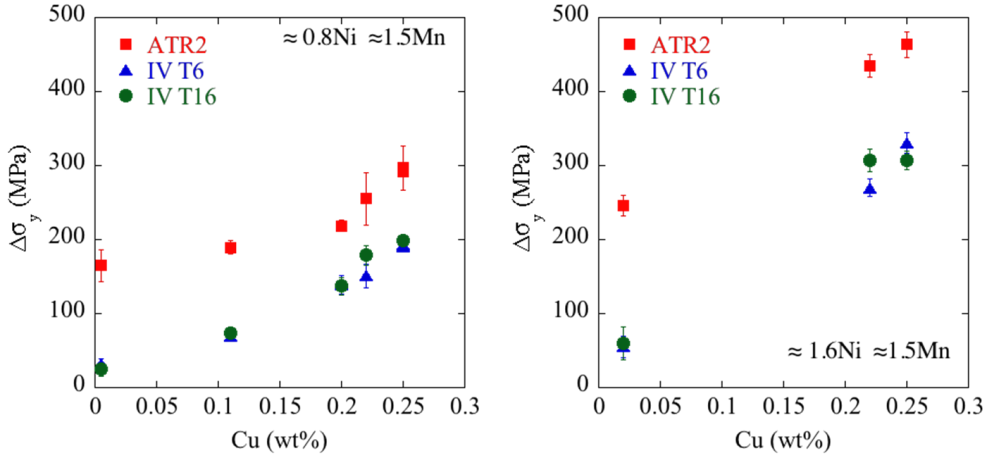

Figure 8.7. The effect of Ni at both ≈ 0.0%Cu (left) and ≈ 0.4% bulk Cu (right). The effect of Ni is generally similar, but stronger at the higher ATR-2 fluence.

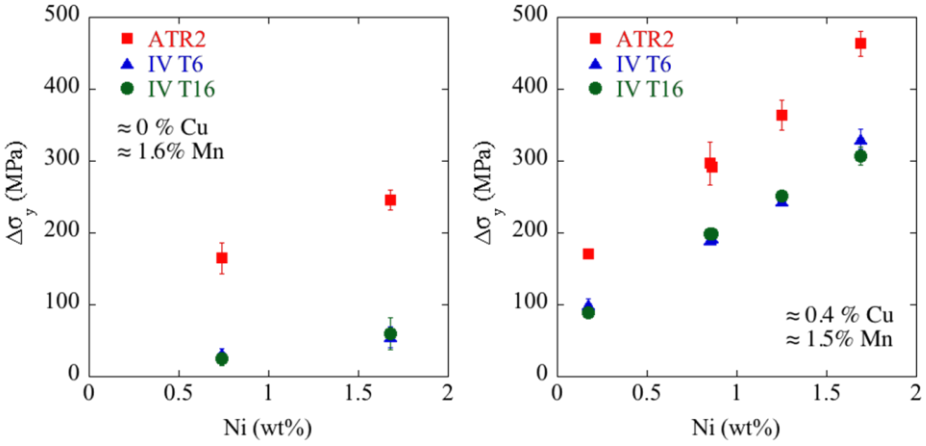

Figure 8.8. $\Delta\sigma_y$ versus Ni content at either 0.0%Cu (left) or 0.4%Ni (right) for two different conditions from the IVAR experiment (T6 and T16) and cup 7 from the ATR-2 experiment.

Figure 8.9 shows the effect of Mn at 0.0%Cu (left) and 0.4% bulk Cu (right) at 0.8%Ni. The effects of Mn are weak in all cases.

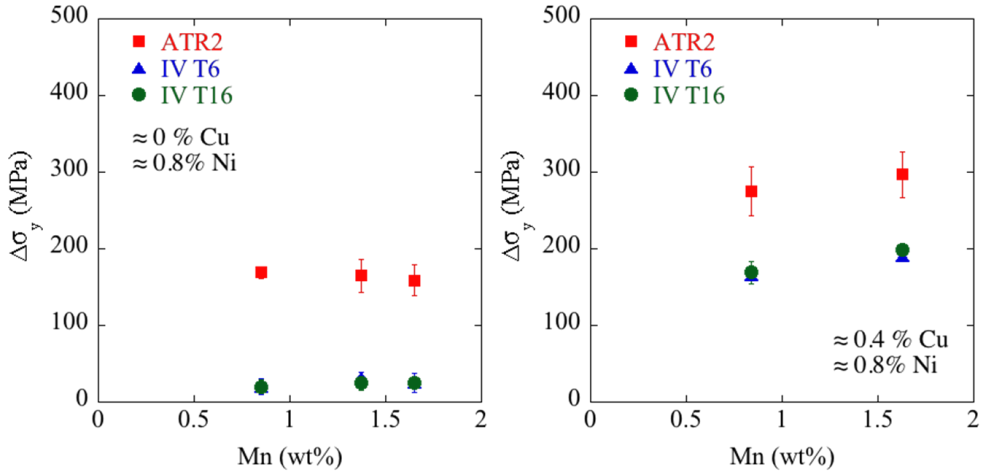

Figure 8.9. $\Delta\sigma_y$ versus Mn content at either 0.0%Cu (left) or 0.4%Cu (right) for two different conditions from the IVAR experiment (T6 and T16) and cup 7 from the ATR-2 experiment.

Figure 8.10 shows the effect of P at 0.0%Cu, 1.6%Mn and either 0.8%Ni (left) or 1.6%Ni (right). The effect of P is generally moderate, but is stronger for lower Ni and at higher ATR-1 fluence.

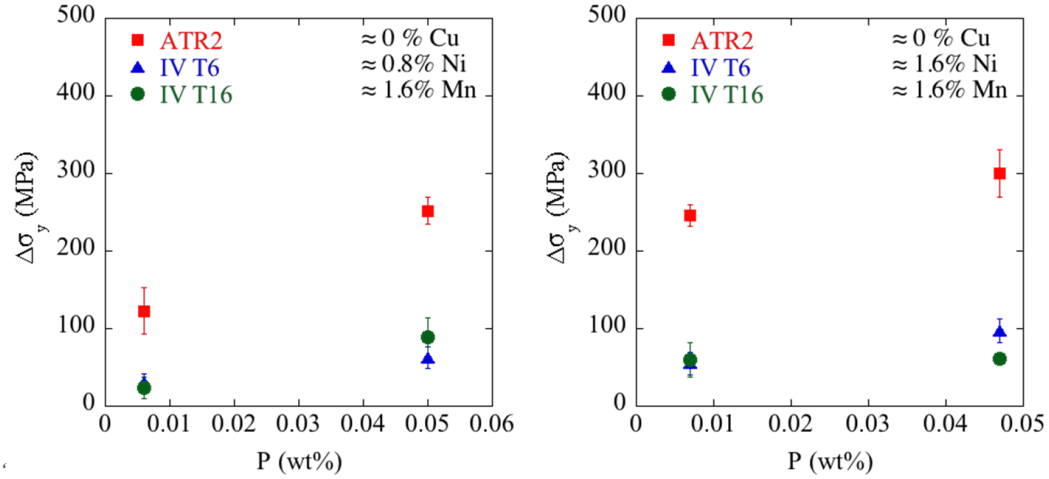

Figure 8.10. $\Delta\sigma_y$ versus P content at 0%Cu, 1.6%Mn and either 0.8%Ni (left) or 1.6%Ni (right) for two different conditions from the IVAR experiment (T6 and T16) and cup 7 from the ATR-2 experiment.

8.4 Odette Wells Almirall Yamamoto (OWAY) ΔT Model

The derivation of the ATR-2 chemistry factor, intermediate to high fluence dependence modeling and power law modeling was carried out by Professor G.R. Odette and Dr. Takuya Yamamoto. This procedure to predict ΔT was called the Odette, Wells, Almirall, Yamamoto (OWAY) model. Derivation of the ATR-2 CF was based on the 49 tensile $\Delta\sigma_y$ test data points, confidential data is not shown here. Various CF fitting functions were tried. The best fit was provided by a simple equation with Cu and Mn dependent terms, and an interactive Ni-Cu term applied to the low P tensile $\Delta\sigma_y$ data. A P-Cu term that was separately determined. The results show that Cu and Ni dominate irradiation hardening. Figure 8.11 shows the predicted versus $\Delta\sigma_y$ plot for the ATR-2 tensile data. The CF was then used to predict the $\Delta\sigma_y$ in for 272 alloys in the power reactor surveillance database, as tabulated in the ASTM Plotter compilation available through the ASTM E10 Committee [142]. Details of this fitting procedure and the OWAY model is described elsewhere [26].

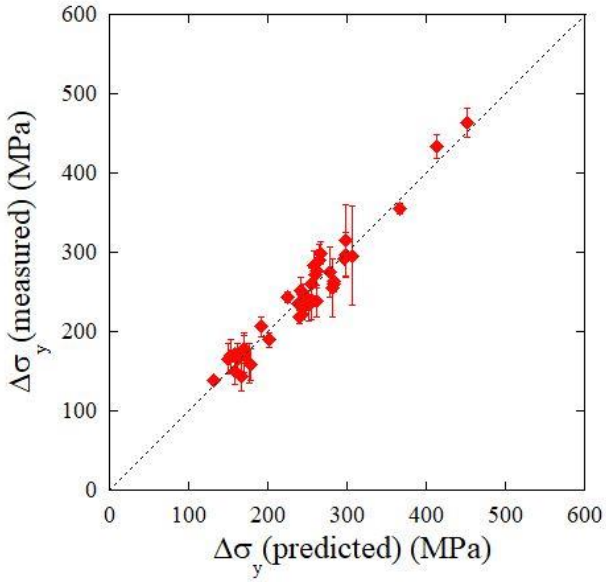

Figure 8.11. The predicted versus measured $\Delta\sigma_y$ plot for the ATR-2 tensile data[(ii)].

Figure 8.12 compares the OWAY ATR-2 CF with other embrittlement correlation model transition temperature shift (ΔT) predictions at the ATR-2 $\phi t = 1.37 \times 10^{20}$ n/cm^2. Here the $\Delta\sigma_y$ predictions have been converted to ΔT values, using previously derived conversion equations.

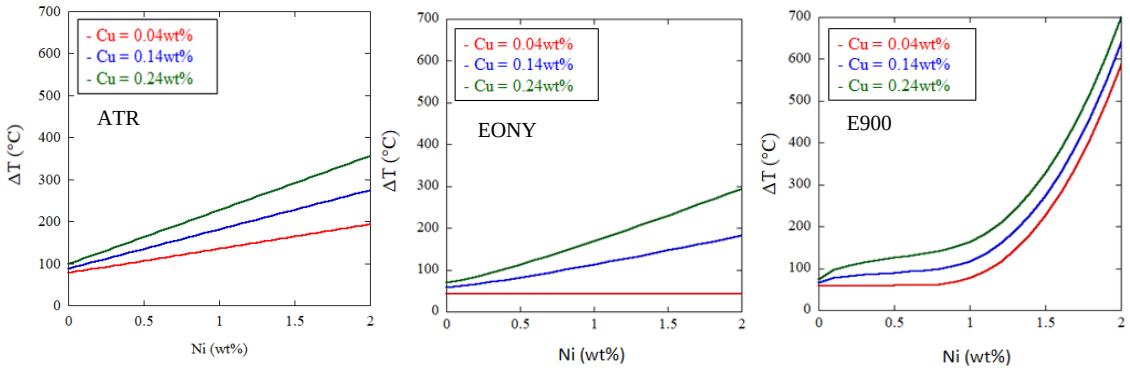

Figure 8.12. The predicted ΔT versus Ni at different Cu contents for various embrittlement models[(ii)].

To create the OWAY model, the composition dependent CF based ΔT for the ATR-2 condition, at $\phi t_e = 1.25 \times 10^{20}$ n/cm^2, coupled with corresponding intermediate low flux $\phi t = \phi t_e$ estimates, was used to linearly interpolate to estimate ΔT down to 4×10^{-2} n/cm^2 [143]. The corresponding intermediate ϕt ΔT can be determined either directly from surveillance data as available, as in the OWAY model, or as predicted by EONY or other ΔT models, see Figure 8.13a-b. Figure 8.13a-b, through comparisons in surveillance steels of the OWAY model with these other models, shows systematic underpredictions of embrittlement in the EONY and E900 models. Figure 8.13c-d shows the unirradiated and irradiated, T_u and T_i, for the US RPV fleet at 1 (right) and 1.25×10^{20} n/cm^2 (left) based on the EONY prediction at $\phi t = 4 \times 10^{19}$ n/cm^2. The estimated maximum T_i is about 150°C.

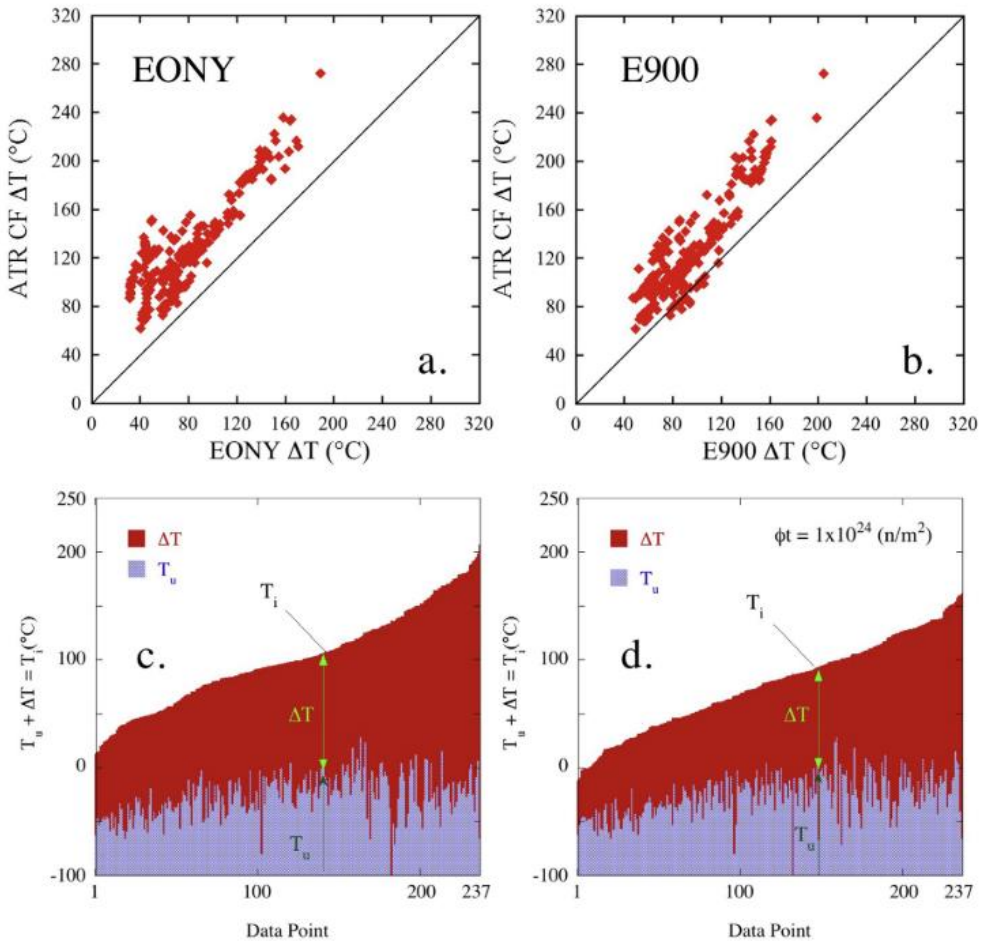

Figure 8.13. a), b) Comparisons of OWAY model predictions of ΔT for steel compositions in the US surveillance data base with a) EONY and b) E900 predictions: and predictions of in-service surveillance T_i at the c) estimated ATR $\phi t_e \approx 1.25x10^{24}$ n/m^2 and d) 10^{24} n/m^2 (d) based on a linear interpolations, where T_u is the unirradiated 41-J Charpy transition temperature [26] [(iii)].

Acknowledgements

(i) Dr. Peter Wells collected part of the data and wrote the macros in the Master Database.

(ii) Dr. Peter Wells, Doug Klingensmith, David Gragg and Kirk Fields carried out tensile testing, microhardness and shear punch testing that fed Master Database and the EONY model.

(iii) Dr. Takuya Yamamoto plotted the unirradiated and irradiated, T_u and T_i, for the US RPV fleet

Chapter 9: Conclusions and Future Work

This work succeeded in advancing understanding of embrittlement in Reactor Pressure Vessel (RPV) steels as it pertains to 80-year life extension of fission reactors. This post irradiation examination campaign bridged a flux-fluence gap in the UCSB databases, which is needed to better understand extended life embrittlement. These efforts utilized APT, EDS, PIA and mechanical test experiments to characterize over 100 alloy/conditions from the large scale ATR-2 irradiation experiment. Ultimately this feeds into a worldwide embrittlement database and UCSB model development.

Precipitation and Hardening

NI and CPI were leveraged here to characterize precipitation for a matrix of advanced alloys with compositions that extend beyond the typical range the current RPV steels. The focus was on developing so-called super-clean steels, with very high Ni contents (> 3%), that have superior unirradiated properties [53,99–103]. However, significant volume fractions of MNSPs form in all of the high Ni steels at the high ATR-2 fluence, leading to enormous irradiation hardening and embrittlement in RPV steels with typical Mn and Si contents, see Chapters 5.1 and 6 [53]. . However, the NI and CPI studies reported here demonstrated that the f_v decreases approximately linearly with the alloy Mn content, and is found to vary as $f_v \approx 0.13 + 0.3Ni^{1.6}Mn^{0.8}$. Thus precipitation hardening is much lower in high ≈ 3.5% Ni < 0.3% Mn steels due to Mn starvation.

On the use of CPI to characterize precipitation

This work explored the potential of convenient CPI to study microstructural evolutions, with emphasis on the nanoscale precipitates. Heavy ion CPI do not produce radioactive byproducts, thus samples can be handled without any special safety procedures. While they do not simulate neutron embrittlement, CPI provide a rapid and cost effective way to gain insight into precipitation mechanisms. Limited comparisons of steels containing the same Cu, Ni, Mn and Si show that CPI result in precipitate volume fractions (f) and compositions that are similar to those formed in neutron irradiations (NI). These trends are similar to those in the same steels at lower dpa [52]. Chapter 6 show the <d>, N and f_v all increase with Ni, in a way that is similar for both the NI and CPI conditions. Clearly, NI and CPI produce similar precipitate microstructures. In a given alloy, the major differences are lower N and f_v and slightly larger <d> (at high dpa) in the CPI condition. It should be emphasized that these conclusions are for modest dpa and dpa rate CPI irradiations. This degree of NI and CPI similitude may not be the case for much higher CPI dpa and dpa rates used in studies of phenomena like void swelling and irradiation effects in Fe-Cr steels for advanced reactor applications. Ultimately the CPI study builds a strong case for allowing CPI scoping studies of the embrittlement sensitivity of new RPV alloys.

Nature of MNSPs

CPI and long-term PIA at 425ºC successfully probed the thermal stability of MNSPs larger (irradiated at 400°C) and smaller (irradiated at 330°C and 400°C) than r_c. MNSPs that are both larger and smaller than r_c were generated in high Ni (~1.6%) RPV steel CM6 by varying the ion irradiation temperature sequence. The smaller precipitates, with $r < r_c$, largely dissolve after annealing at 425°C for long times. The larger precipitates, with $r > r_c$, are stable

and largely associated with network dislocations. Thus, it must be concluded that the MNSPs are thermodynamically stable, and are likely the Γ_2 phase in most cases. Further, the MNSPs would be even more thermodynamically stable at much lower neutron irradiation RPV service temperatures around 290°C. Notably, these conclusions are consistent with both CALPHAD thermodynamic predictions and XRD measurements at very high fluence [19,106].

9.1 Key Insights

Here, is a summary of the key insights found.

- Significant volume fractions (f) of MNSPs form in all of the high Ni (>3%) steels at the high fluence $1.4x10^{20}n/cm^2$ at 290°C in the Advanced Test Reactor.
- Modest volume fractions (f) of CRPs and MNSPs form in all of the Cu bearing and Cu free steels surveillance at the high fluence $1.4x10^{20}n/cm^2$ at 290°C in the Advanced Test Reactor.
- In Cu bearing steels, at high fluence in ATR-2, the CRPs first grow rapidly to a saturated plateau f_v, at dissolved matrix Cu depletion, followed by growth of MNSPs at higher fluence. The precipitates first grow with a CRP core Mn-Ni-Si shell structure, but the MNSPs later transform to discrete ordered intermetallic appendages at higher fluence. This confirms observations of irradiated RPV steel microstructures at higher fluence [52].
- At typical Mn and Si levels and low <0.07%Cu steels, both N and f_v increase roughly linearly with increasing Ni. For the high >0.2%Cu steels <d> and f_v linearly increases with Cu.
- While Ni generally plays the strongest role in the formation of MNSPs, f_v and $\Delta\sigma_y$ increase synergistically and systematically with Mn, especially at higher Ni.

- In the absence of sufficient Cu and low to intermediate Ni, the MNS precipitates have difficulty nucleating homogeneously in a defect free matrix, and microstructural features such as network dislocations and irradiation induced interstitial loops act as heterogeneous nucleation sites.
- The wide range of compositions in the ASM alloys results in very different precipitate compositions - for example, near G ($Mn_6Ni_{16}Si_7$) or Γ_2 (Mn_2Ni_3Si) phases in alloys with 0.75% to 1.62% Ni with ≥ 0.8% Mn, versus Ni-silicide type compositions in alloys with very low ≤ 0.24 Mn and high ≈ 1.6 to 3.4% Ni. When Ni is low, a MnSi phase field type composition, which still contains ≈ 28-38% Ni, is observed. High Ni and Mn alloys with lower Si form Ni_3Mn type precipitates alloyed with small amounts of Si (10-12%).Note that the G and Γ_2 phases have been identified at high fluence at typical RPV compositions, the specific phase structures not yet confirmed identified in this work.
- The Mn and Si in the precipitates roughly trade off depending on the alloy Mn content.
- At normal levels of > 1% Mn, very large MNS precipitate f_v form in 3.5% Ni advanced steels at high fluence.
- However, f_v decreases approximately linearly with the alloy Mn content, and is found to vary as $f_v \approx 0.13 + 0.3Ni^{1.6}Mn^{0.8}$.
- The surveillance and ASM steels studies show f_v is relatively insensitive to variations in Si and P
- The CPI also demonstrates that reductions in Mn do indeed reduce the precipitate f_v, but only to a limited extent. Thus precipitation hardening is much lower in high ≈ 3.5% Ni < 0.3% Mn steels due to Mn starvation.

- ASM steels with very low Mn and high Ni and Si, $Ni_{2-3}Si$ silicide type compositions are selected rather than those for the G or Γ_2 type phases; and when Ni is low, a MnSi phase field type composition, which still contains ≈ 28-38% Ni, is observed. High Ni and Mn alloys with lower Si form Ni_3Mn type precipitates alloyed with small amounts of Si (10-12%).
- The CPI and NI for similar bulk steel solute contents yield nearly the same precipitate compositions, albeit with some differences in their N, <r>, f_v, and dose dependence. This allows CPI scoping studies of the embrittlement sensitivity of new RPV alloys.
- CPI produces fewer and larger precipitates. Further, higher dpa are needed to form the same precipitate f_v for CPI versus NI conditions. The MNSP grow slowly, but eventually reach large f_v at high dpa.
- The $\Delta\sigma_y$ is well correlated with the $\sqrt{f_v}$ and can be understood based on dispersed barrier hardening models.
- The tensile, shear and microhardness results ($\Delta\sigma_y$) also suggested that Ni-Si dominated precipitates may be weaker dislocation obstacles than the G and Γ_2 type MNSPs.
- Post irradiation annealing (PIA) provided significant insight into the thermal stability of MNSPs. These studies show that the MNSPs are equilibrium phases but ones that can dissolved below a critical radius r_c in a solute depleted matrix.
- Annealing at 425°C for long times, resulted in complete precipitate dissolution in a NI medium Ni (0.69%) steel after only 7 weeks, consistent with thermodynamic predictions [52,121].

- For a NI high Ni steels (1.6%) APT and TEM-EDS clearly showed stable precipitates in grains with sufficient Ni and Mn, even after annealing at 425°C for 57 weeks, again strongly supporting the conclusion that MNSPs are a thermodynamically stable phase.
- MNSPs that are both larger and smaller than r_c were generated in high Ni (~1.6%) RPV steel CM6 by varying the ion irradiation temperature sequence.
- The smaller precipitates in CPI condition, with $r < r_c$, largely dissolve after annealing at 425°C for long times.
- The larger precipitates in the CPI condition, with $r > r_c$, were stable and even slightly coarsened.
- In NI and CPI APT and TEM-EDS showed evidence of heterogeneous nucleation on loops, line dislocations and grain boundaries, especially at lower alloy solute contents and or higher irradiation temperatures. Indeed, RIS likely plays a role in solute cluster formation, widely identified as a generic G-phase, in highly sub saturated alloys [95,97,109,124,135].
- Since ΔG_v is of order 4 times larger, and r_c is 4 times smaller, at 290°C compared to 425°C, there can be no question that MNSPs a stable thermodynamics phase at such service relevant temperatures. Notably, these conclusions are consistent with both CALPHAD thermodynamic predictions and XRD measurements [19,106].
- ATR-2 hardening and embrittlement were underpredicted by regulatory models. EONY systematically underpredicts the ATR-2 results by an average of -57°C, as does E900, but by less, with an average of -41°C [55,139]. The French FIS equation (not shown) both underpredicts and over predicts with an average over prediction of +31.6°C [144].

– A new composition dependent chemistry factor (CF = $\Delta\sigma_{y\,(Cu,Ni,Mn,Si)}$) was derived for the ATR-2 condition This CF was based on the 49 tensile $\Delta\sigma_y$ test data points shown in Table 8.3.

9.2 Future Work

The work reported here is still in need of progress. ATR-2 contained a total of 13 Cups irradiated over a range of ϕt, ϕ and T_i, see Appendix B. To date PIE has been carried out on two 290°C high ϕt Cups 7 and 8, with a small amount of PIE on a lower 255°C cup 5. So the T_i dependence of ΔT at high ϕt has not been characterized. Further there has been no testing on lower ϕt Cups that are necessary to further verify the model. Another important step is to compare the proposed procedure to ΔT in the international database, aggregated in the ASTM E900 Plotter package

A second critical issue is to develop a microstructural basis for modeling the decrease in the effect of ϕ at high ϕt; and to further quantify and verify the ϕt_e for ATR-2 conditions. This would require additional TEM studies of dislocation evolution (loop and network) under irradiation and additional experiments of the sink and defect trapping efficiency of the CRPs and MNSPs. Dislocation characterization in the unirradiated and irradiated conditions is also critical to understanding and modeling start of life and product form effects; and more generally the variability of ΔT in steels with similar chemistries. Further quantitative analysis of linear complexions, defined as structurally and chemically discrete phases, precipitation and segregation to dislocations is currently underway. A detailed discussion of dislocation structures and the character, as well as the causes and consequences of the corresponding solute

segregation, are being addressed in detail as part of ongoing work[7]. This information is also needed for developing better irradiation hardening and constitutive laws.

[7] G.R. Odette, N. Almirall, P.B. Wells, T. Yamamoto, Dislocation Complexion in Irradiated Multi Constituent Reactor Pressure Vessel Steels, (2021) Under Review in Acta Materialia.

References

[1] Climate Change and Nuclear Power 2018, International Atomic Energy Agency. Vienna (2018).

[2] D.O.E. Office, N. Energy, Light Water Reactor Sustainability Research and Development Program Plan Fiscal Year 2009 – 2013, (2013).

[3] G.R. Odette, B.D. Wirth, D.J. Bacon, N.M. Ghoniem, Multiscale-Multiphysics Modeling of Materials : Embrittlement of Pressure-Vessel Steels, MRS Bull. 26 (2001) 176–181. doi:10.1557/mrs2001.39.

[4] G.R. Odette, G.E. Lucas, Embrittlement of nuclear reactor pressure vessels, JOM. 53 (2001) 18–22. doi:10.1007/s11837-001-0081-0.

[5] G.R. Odette, R.K. Nanstad, Predictive reactor pressure vessel steel irradiation embrittlement models: Issues and opportunities, JOM. 61 (2009) 17–23. doi:10.1007/s11837-009-0097-4.

[6] C. English, J. Hyde, Radiation damage of reactor pressure vessel steels, Elsevier, 2012. doi:10.1016/B978-0-08-056033-5.00087-2.

[7] G.R. Odette, On the dominant mechanism of irradiation embrittlement of reactor pressure vessel steels, Scr. Metall. 17 (1983) 1183–1188. doi:10.1016/0036-9748(83)90280-6.

[8] G.R. Odette, G.E. Lucas, Recent progress in understanding reactor pressure vessel steel embrittlement, Radiat. Eff. Defects Solids. 144 (1998) 189–231. doi:10.1080/10420159808229676.

[9] R.E. Stoller, G.R. Odette, B.D. Wirth, Primary damage formation in bcc iron, J. Nucl. Mater. 251 (1997) 49–60. doi:10.1016/S0022-3115(97)00256-0.

[10] E. Meslin, B. Radiguet, P. Pareige, C. Toffolon, a. Barbu, Irradiation-Induced Solute Clustering in a Low Nickel FeMnNi Ferritic Alloy, Exp. Mech. 51 (2011) 1453–1458. doi:10.1007/s11340-011-9476-1.

[11] E. Meslin, A. Barbu, L. Boulanger, B. Radiguet, P. Pareige, K. Arakawa, C.C. Fu, Cluster-dynamics modelling of defects in a-iron under cascade damage conditions, J. Nucl. Mater. 382 (2008) 190–196. doi:10.1016/j.jnucmat.2008.08.010.

[12] E. Meslin, B. Radiguet, M. Loyer-Prost, Radiation-induced precipitation in a ferritic model alloy: An experimental and theoretical study, Acta Mater. 61 (2013) 6246–6254. doi:10.1016/j.actamat.2013.07.008.

[13] R. Ngayam-Happy, C.S.S. Becquart, C. Domain, L. Malerba, Formation and evolution of MnNi clusters in neutron irradiated dilute Fe alloys modelled by a first principle-based AKMC method, J. Nucl. Mater. 426 (2012) 198–207. doi:10.1016/j.jnucmat.2012.03.033.

[14] P. Auger, P. Pareige, S. Welzel, J.C. Van Duysen, Synthesis of atom probe experiments on irradiation-induced solute segregation in French ferritic pressure vessel steels, J. Nucl. Mater. 280 (2000) 331–344. doi:10.1016/S0022-3115(00)00056-8.

[15] J.T. Buswell, W.J. Phythian, R.J. McElroy, S. Dumbill, P.H.N. Ray, J. Mace, R.N. Sinclair, Irradiation-induced microstructural changes , and hardening, 225 (1995) 196–214. doi:10.1016/0022-3115(95)00026-7.

[16] M.K. Miller, K.F. Russell, Embrittlement of RPV steels: An atom probe tomography perspective, J. Nucl. Mater. 371 (2007) 145–160. doi:10.1016/j.jnucmat.2007.05.003.

[17] G.R. Odette, On the ductile to brittle transition in martensitic stainless steels — Mechanisms, models and structural implications, J. Nucl. Mater. 212–215 (1994) 45–51. doi:10.1016/0022-3115(94)90032-9.

[18] D.A. Curry, J.. Knot, Effect of Microstructure on Cleavage Fracture Toughness in Mild Steel, Met. Sci. 13 (1979) 341–345. doi:10.1179/msc.1979.13.6.341.

[19] H. Ke, P. Wells, P.D. Edmondson, N. Almirall, L. Barnard, G.R. Odette, D. Morgan, Thermodynamic and kinetic modeling of Mn-Ni-Si precipitates in low-Cu reactor pressure vessel steels, Acta Mater. 138 (2017) 10–26. doi:10.1016/j.actamat.2017.07.021.

[20] E.D. Eason, G.R. Odette, R.K. Nanstad, T. Yamamoto, A Physically Based Correlation of Irradiation-Induced Transition Temperature Shifts for RPV Steels, (2006). http://www.info.ornl.gov/sites/publications/files/Pub2592.pdf.

[21] G.R. Odette, T. Yamamoto, Advanced Models of LWR Pressure Vessel Embrittlement for Low Flux-HighFluence Conditions, Rep. to US DOE Nucl. Energy Univ. Progr. (2013). doi:10.2172/1084639.

[22] G.R. Odette, P. Wells, T. Yamamoto, Y. Wu, N. Cunningham, On the Evolution of Late Blooming Phases in RPV Steels : Theoretical Foundations , Experimental Observations and Recent Insights, in TMS San Antonio, TX (2013).

[23] G.R. Odette, T. Yamamoto, Advanced Models of LWR Pressure Vessel Embrittlement for Extended Life Conditions, DOE NEUP Project 09-196 Final report (2012).

[24] J.T. Busby, Light Water Reactor Sustainability Materials Aging and Degradation Pathway Technical Program Plan ORNL/LTR-2012/327, (2012).

[25] Expanded Materials Degradation Assessment (EDMA): Aging of Reactor Pressure Vessels NUREG/CR-7153 V3, (2013).

[26] G.R. Odette, T. Yamamoto, T.J. Williams, R.K. Nanstad, C.A. English, On the history and status of reactor pressure vessel steel ductile to brittle transition temperature shift prediction models, J. Nucl. Mater. 526 (2019) 151863. doi:10.1016/j.jnucmat.2019.151863.

[27] G.R. Odette, Neutron Irradiation Effects in Reactor Pressure Vessel Steels and Weldments, International Atomic Energy Agency, Vienna, IAEA IWG-LMNPP-98/3, 1998, p. 438. https://inis.iaea.org/collection/NCLCollectionStore/_Public/30/013/30013700.pdf.

[28] B.D. Wirth, G.R. Odette, Kinetic lattice Monte Carlo simulations of cascade aging in iron and dilute iron-copper alloys in Microstructural Processes in Irradiated Materials, Ed. by S. J. Zinkle, G.E. Lucas, R.C. Ewing, J.S. Williams, Mater. Res. Soc. Symp. Proc. 540 (1999) 754.

[29] M. Otaka, T. Osaki, Reduction of Upper Shelf Energy of Highly Irradiated RPV Steels, 30th MPA-Seminar-Japan Nucl. Energy Saf. Organ. (2004).

[30] A. E1921-97, Standard Test Method for Determination of Reference Temperature To for Ferritic Steels in the Transition Range, Annu. B. ASTM Stand. (1998) 1068–1084.

[31] G.R. Odette, Radiation induced microstructural evolution in reactor pressure vessel steels, in: Mater. Res. Soc. Symp. - Proc., Materials Research Society, 1995: pp. 137–148. doi:10.1557/PROC-373-137.

[32] P.B. Wells, T. Yamamoto, B. Miller, T. Milot, J. Cole, Y. Wu, G.R. Odette, Evolution of manganese–nickel–silicon-dominated phases in highly irradiated reactor pressure vessel steels, Acta Mater. 80 (2014) 205–219. doi:10.1016/j.actamat.2014.07.040.

[33] T. Yamamoto, T. Toyama, P. Wells, Y. Nagai, G.R. Odette, Microstructural Characterization of Test Reactor Irradiated RPV Steels by Post- Irradiation Annealing and State-of-the-Art Characterization Tools, (2013).

[34] W.J. Phythian, C. a English, Microstructural evolution in reactor pressure vessel steels, J. Nucl. Mater. 205 (1993) 162–177. doi:10.1016/0022-3115(93)90079-E.

[35] P. Pareige, M.K. Miller, Characterization of neutron-induced copper-enriched clusters in pressure vessel steel weld: an APFIM study, Appl. Surf. Sci. 94–95 (1996) 370–377. doi:10.1016/0169-4332(95)00399-1.

[36] A. Kuramoto, T. Toyama, T. Takeuchi, Y. Nagai, M. Hasegawa, T. Yoshiie, Y. Nishiyama, Post-irradiation annealing behavior of microstructure and hardening of a reactor pressure vessel steel studied by positron annihilation and atom probe tomography, J. Nucl. Mater. 425 (2012) 65–70. doi:10.1016/j.jnucmat.2011.10.019.

[37] E. Meslin, B. Radiguet, P. Pareige, a. Barbu, Kinetic of solute clustering in neutron irradiated ferritic model alloys and a French pressure vessel steel investigated by atom probe tomography, J. Nucl. Mater. 399 (2010) 137–145. doi:10.1016/j.jnucmat.2009.11.012.

[38] E. Mader, Kinetics of irradiation embrittlement and the post-irradiation annealing of nuclear reactor pressure vessel steels, University of California, Santa Barbara, 1995.

[39] P.D. Styman, J.M. Hyde, K. Wilford, a. Morley, G.D.W. Smith, Precipitation in long term thermally aged high copper, high nickel model RPV steel welds, Prog. Nucl. Energy. 57 (2012) 86–92. doi:10.1016/j.pnucene.2011.10.010.

[40] R.G. Carter, N. Soneda, K. Dohi, J.M. Hyde, C. a. English, W.L. Server, Microstructural characterization of irradiation-induced Cu-enriched clusters in reactor pressure vessel steels, J. Nucl. Mater. 298 (2001) 211–224. doi:10.1016/S0022-3115(01)00659-6.

[41] G.R. Odette, Radiation Induced Microstructural Evolution In Reactor Pressure Vessel Steels, 373 (1995) 7–16. doi:10.1557/PROC-373-137.

[42] M.K. Miller, K.A. Powers, R.K. Nanstad, P. Efsing, Atom probe tomography characterizations of high nickel, low copper surveillance RPV welds irradiated to high fluences, J. Nucl. Mater. 437 (2013) 107–115. doi:10.1016/j.jnucmat.2013.01.312.

[43] J.M. Hyde, M.G. Burke, R.M. Boothby, C. a English, Characterisation of the early stages of solute clustering in 1Ni-1.3Mn welds containing Cu., Ultramicroscopy. 109 (2009) 510–7. doi:10.1016/j.ultramic.2008.10.018.

[44] M.. Miller, K.. Russell, J. Kocik, E. Keilova, Embrittlement of low copper VVER 440 surveillance samples neutron-irradiated to high fluences, J. Nucl. Mater. 282 (2000) 83–88. doi:10.1016/S0022-3115(00)00240-3.

[45] M.K. Miller, K.F. Russell, J. Kocik, E. Keilova, Atom probe tomography of 15Kh2MFA Cr–Mo–V steel surveillance specimens, Micron. 32 (2001) 749–755. doi:10.1016/S0968-4328(00)00082-2.

[46] M.K. Miller, K.F. Russell, M. a. Sokolov, R.K. Nanstad, APT characterization of irradiated high nickel RPV steels, J. Nucl. Mater. 361 (2007) 248–261. doi:10.1016/j.jnucmat.2006.12.015.

[47] P. Auger, P. Pareige, M. Akamatsu, D. Blavette, APFIM Investigation of Clustering in Neutron-Irradiated Fe-Cu Alloys and Pressure Vessel Steels, J. Nucl. Mater. 225 (1995) 225–230. doi:10.1016/0022-3115(94)00522-2.

[48] M.K. Miller, A.A. Chernobaeva, Y.I. Shtrombakh, K.F. Russell, R.K. Nanstad, D.Y. Erak, O.O. Zabusov, Evolution of the nanostructure of VVER-1000 RPV materials under neutron irradiation and post irradiation annealing, J. Nucl. Mater. 385 (2009) 615–622. doi:10.1016/j.jnucmat.2009.01.299.

[49] P. Pareige, R.E. Stoller, K.F. Russell, M.K. Miller, Atom probe characterization of the microstructure of nuclear pressure vessel surveillance materials after neutron irradiation and after annealing treatments, J. Nucl. Mater. 249 (1997) 165–174. doi:10.1016/S0022-3115(97)00215-8.

[50] K.C. Russell, L.M. Brown, A dispersion strengthening model based on differing elastic moduli applied to the iron-copper system, Acta Metall. 20 (1972) 969–974. doi:10.1016/0001-6160(72)90091-0.

[51] D. Bhattacharyya, T. Yamamoto, P. Wells, E. Marquis, M. Bachhav, Y. Wu, J. Davis, A. Xu, G.R. Odette, Microstructural changes and their effect on hardening in neutron irradiated Fe-Cr alloys, J. Nucl. Mater. 519 (2019) 274–286. doi:https://doi.org/10.1016/j.jnucmat.2019.03.022.

[52] P.B. Wells, The Character and Stability of Mn-Ni-Si Precipitates in Reactor Pressure Vessel Steels [PhD Thesis], Univ. Calif. St. Barbar. (2015).

[53] N. Almirall, P.B. Wells, T. Yamamoto, K. Wilford, T. Williams, N. Riddle, G.R. Odette, Precipitation and Hardening in Irradiated Low Alloy Steels with a Wide Range of Ni and Mn Compositions, Acta Mater. 179 (2019) 119–128. doi:10.1016/j.actamat.2019.08.027.

[54] E.D. Eason, G.R. Odette, R.K. Nanstad, T. Yamamoto, A physically-based correlation of irradiation-induced transition temperature shifts for RPV steels, J. Nucl. Mater. 433 (2013) 240–254. doi:10.1016/j.jnucmat.2012.09.012.

[55] E.D. Eason, G.R. Odette, R.K. Nanstad, T. Yamamoto, A physically based correlation of irradiation-induced transition temperature shifts for RPV steels Ch2., Oak Ridge National Lab, 2007. https://info.ornl.gov/sites/publications/files/Pub2592.pdf.

[56] G.R. Odette, T. Yamamoto, E.D. Eason, R.K. Nanstad, On the metallurgical and irradiation variable dependence of the embrittlement of RPV steels, Proc. Int. Symp. Res. Aging Manag. Light Water React. (2007) 279–306.

[57] M. Erickson, Kirk, "A Review of ΔT30 Data for Reactor Pressure Vessel Steels Obtained at High Fluences," J. ASTM Intl. (West Conshohocken, PA: ASTM Intl., 2009), JAI102000-8.

[58] A. N. Kolmogorov, Statistical theory of crystallization of metals. (in Russian). Izvestia Akademia Nauk SSSR Ser. Mathematica (Izv. Akad. Nauk SSSR, Ser. Mat; Bull. Acad. Sci. USSR. Ser. Math)., 1, 1937, S. 355–359.

[59] W. A. Johnson, R. F. Mehl, Reaction kinetics in processes of nucleation and growth, Transactions of American Institute of Mining and Metallurgical Engineers (Trans. Am. Inst. Min. Metall. Eng.), 135, 1939, S. 416–458.

[60] M. Avrami, Kinetics of phase change. III: Granulation, Phase Change and Microstructure, Journal of Chemical Physics (J. Chem. Phys.), 9, 1941, S. 177–184.

[61] As-Run Thermal Analysis of the UCSB-2 Experiment in the ATR, 2016.

[62] J.W. Nielsen, As-Run Physics Analysis for the UCSB-1 Experiment in the Advanced Test Reactor, 2015.

[63] G.S. Was, Fundamentals of Radiation Materials Science, Springer, 2007.

[64] G. Was, Challenges to the use of ion irradiation for emulating reactor irradiation, J. Mater. Res. 30 (2015) 1158–1182. doi:10.1557/jmr.2015.73.

[65] B. Heidrich, S.M. Pimblott, G.S. Was, S. Zinkle, Roadmap for the application of ion beam technologies to the challenges of nuclear energy technologies, Nucl. Instruments Methods Phys. Res. Sect. B Beam Interact. with Mater. Atoms. 441 (2019) 41–45. doi:10.1016/J.NIMB.2018.12.022.

[66] M.Y. He, G.R. Odette, T. Yamamoto, D. Klingensmith, A universal relationship between indentation hardness and flow stress, J. Nucl. Mater. 367–370 (2007) 556–560. doi:10.1016/j.jnucmat.2007.03.044.

[67] W.R. McKenzie, E.A. Marquis, P.R. Munroe, Focused Ion Beam Sample Preparation for Atom Probe Tomography, Microsc. Sci. Technol. Appl. Educ. 3 (2010) 1800–1810. http://www.formatex.info/microscopy4/1800-1810.pdf.

[68] N. Almirall, P.B. Wells, T. Yamamoto, K. Yabuuchi, A. Kimura, G.R. Odette, On the use of charged particles to characterize precipitation in irradiated reactor pressure vessel steels with a wide range of compositions, J. Nucl. Mater. 536 (2020) 152173. doi:10.1016/j.jnucmat.2020.152173.

[69] T. Williams and D. Ellis, A Mechanistically-Based Model of Irradiation Damage in Low Alloy Steel Submerged Arc Welds, Eff. Radiat. Mater. 20th Int. Symp. Ed. S. Rosinski, M. Grossbeck, T. Allen, A. Kumar (West Conshohocken, PA ASTM Int. 2001). (2001) 8–27. doi:10.1520/STP10522S.

[70] N.J. Cunningham, Study of the Structure, Composition, and Stability of Y-Ti-O nm-Scale Features, University of California, Santa Barbara, 2012.

[71] B.D. Wirth, On the Character of the Nano-Scale Features in Reactor Pressure Vessel Steels, University of California, Santa Barbara, 1998.

[72] M.J. Alinger, On the Formation and Stability of Nanometer Scale Precipitates in Ferritic Alloys during Processing and High Temperature Service, University of California, Santa Barbara, 2004.

[73] M.J. Alinger, G.R. Odette, D.T. Hoelzer, On the role of alloy composition and processing parameters in nanocluster formation and dispersion strengthening in nanostuctured ferritic alloys, Acta Mater. 57 (2009) 392–406. doi:10.1016/j.actamat.2008.09.025.

[74] S.P. Gault, B., Moody, M.P., Cairney, J.M., Ringer, Atom Probe Microscopy, 2012.

[75] M.K. Miller, Atom Probe Tomography, Kluwer Academic/Plenum Publishers, 2000.

[76] E.A. Marquis, Atom probe tomography applied to the analysis of irradiated microstructures, J. Mater. Res. 30 (2015) 1–9. doi:10.1557/jmr.2014.398.

[77] B. Gault, F. De Geuser, L.T. Stephenson, M.P. Moody, B.C. Muddle, S.P. Ringer, Microscopy Microanalysis Estimation of the Reconstruction Parameters for Atom Probe Tomography, Microsc. Microanal. 14 (2008) 296–305. doi:10.1017/S1431927608080690.

[78] E.A. Marquis, J.M. Hyde, Applications of atom-probe tomography to the characterisation of solute behaviours, Mater. Sci. Eng. R Reports. 69 (2010) 37–62. doi:10.1016/j.mser.2010.05.001.

[79] K. Lindgren, K. Stiller, P. Efsing, M. Thuvander, On the Analysis of Clustering in an Irradiated Low Alloy Reactor Pressure Vessel Steel Weld, Microsc. Microanal. 23 (2017) 376–384. doi:10.1017/S1431927617000162.

[80] K. Lindgren, M. Boåsen, K. Stiller, P. Efsing, M. Thuvander, Evolution of precipitation in reactor pressure vessel steel welds under neutron irradiation, J. Nucl. Mater. 488 (2017) 222–230. doi:10.1016/j.jnucmat.2017.03.019.

[81] S. Shu, P.B. Wells, N. Almirall, G.R. Odette, D.D. Morgan, Acta Materialia Thermodynamics and kinetics of core-shell versus appendage co- precipitation morphologies : An example in the Fe-Cu-Mn-Ni-Si system, Acta Mater. 157 (2018) 298–306. doi:10.1016/j.actamat.2018.07.037.

[82] D.J. Larson, B. Gault, B.P. Geiser, F. De Geuser, F. Vurpillot, Atom probe tomography spatial reconstruction: Status and directions, Curr. Opin. Solid State Mater. Sci. 17 (2013) 236–247. doi:10.1016/j.cossms.2013.09.002.

[83] M.K. Miller, M.G. Hetherington, Local magnification effects in the atom probe, Surf. Sci. 246 (1991) 442–449. doi:10.1016/0039-6028(91)90449-3.

[84] C. Oberdorfer, G. Schmitz, On the Field Evaporation Behavior of Dielectric Materials in Three-Dimensional Atom Probe: A Numeric Simulation, Microsc. Microanal. 17 (2010) 15–25. doi:10.1017/S1431927610093888.

[85] D. Beinke, C. Oberdorfer, G. Schmitz, Towards an accurate volume reconstruction in atom probe tomography, Ultramicroscopy. 165 (2016) 34–41. doi:10.1016/j.ultramic.2016.03.008.

[86] A. Morley, G. Sha, S. Hirosawa, A. Cerezo, G.D.W. Smith, Determining the composition of small features in atom probe: bcc Cu-rich precipitates in an Fe-rich matrix, Ultramicroscopy. 109 (2009) 535–540. doi:10.1016/j.ultramic.2008.09.010.

[87] P.D. Edmondson, C.M. Parish, R.K. Nanstad, Using complimentary microscopy methods to examine Ni-Mn-Si-precipitates in highly-irradiated reactor pressure vessel steels, Acta Mater. 134 (2017) 31–39. doi:10.1016/j.actamat.2017.05.043.

[88] S. Shu, B.D. Wirth, P.B. Wells, D.D. Morgan, G.R. Odette, Multi-technique characterization of the precipitates in thermally aged and neutron irradiated Fe-Cu and Fe-Cu-Mn model alloys: Atom probe tomography reconstruction implications, Acta Mater. 146 (2017) 237–252. doi:10.1016/j.actamat.2017.12.006.

[89] J.M. Hyde, C.A. English, An Analysis of the Structure of Irradiation induced Cu-enriched Clusters in Low and High Nickel Welds, MRS Proc. 650 (2000) R6.6. doi:10.1557/PROC-650-R6.6.

[90] L.T. Stephenson, M.P. Moody, P. V. Liddicoat, S.P. Ringer, New Techniques for the Analysis of Fine-Scaled Clustering Phenomena within Atom Probe Tomography (APT) Data, Microsc. Microanal. 13 (2007) 448–463. doi:10.1017/S1431927607070900.

[91] J.M. Hyde, E.A. Marquis, K.B. Wilford, T.J. Williams, A sensitivity analysis of the maximum separation method for the characterisation of solute clusters., Ultramicroscopy. 111 (2011) 440–447. doi:10.1016/j.ultramic.2010.12.015.

[92] N.J. Cunningham, Study of the Structure, Composition, and Stability of Y-Ti-O nm-Scale Features in Nano-Structured Ferritic Alloys [PhD Thesis], Univ. Calif. St. Barbar. (2012).

[93] E.D. Eason, J. E. Wright and G. R. Odette, An Improved Embrittlement Correlation for Reactor Pressure Vessel Steels, Proc. Sixth Int. Symp. Environ. Degrad. Mater. Nucl. React.-Water React. TMS. (1998). https://www.nrc.gov/docs/ML1401/ML14010A095.pdf.

[94] B. Zhang, F. Xue, S. Li, X. Wang, N. Liang, Y.H. Zhao, G. Sha, Non-uniform phase separation in ferrite of a duplex stainless steel, Acta Mater. 140 (2017) 388–397. doi:10.1016/j.actamat.2017.08.044.

[95] Y. Matsukawa, T. Takeuchi, Y. Kakubo, T. Suzudo, H. Watanabe, H. Abe, T. Toyama, Y. Nagai, The two-step nucleation of G-phase in ferrite, Acta Mater. 116 (2016) 104–113. doi:10.1016/j.actamat.2016.06.013.

[96] H. Leitner R. Schnitzer M. Schober et al, Precipitate modification in PH13-8 Mo type maraging steel, Acta Mater. 59 (2011) 5012–5022. doi:10.1016/j.actamat.2011.04.053.

[97] W.W. Sun, R.K.W. Marceau, M.J. Styles, D. Barbier, C.R. Hutchinson, G phase precipitation and strengthening in ultra-high strength ferritic steels: Towards lean 'maraging' metallurgy, Acta Mater. 130 (2017) 28–46. doi:10.1016/j.actamat.2017.03.032.

[98] W. Martin, Micromechanisms in Particle-Hardened Alloys, Cambridge University Press, 1980.

[99] M.G. Burke, R.J. Stofanak, J.M. Hyde, C.A. English, W.L. Server, Microstructural aspects of irradiation damage in A508 Gr 4N forging steel: Composition and flux effects, J. ASTM Int. 1 (2002) 1–14. doi:10.1520/JAI11773.

[100] G. Wire, W. Beggs, T. Leax, Evaluation of irradiation embrittlement of A508 Gr 4N and comparison to other low-alloy steels, in: 21st Int. Symp. Eff. Radiat. Mater., 2002: pp. 179–193. doi:10.1520/STP11227S.

[101] T. Leax, Temperature dependence and variability of fracture toughness in the transition regime for A508 grade 4N pressure vessel steel, 5th Int. ASTM/ESIS Symp. Fatigue Fract. 3 (2005) 1–20. doi:10.1520/JAI13230.

[102] S. Wu, H. Jin, Y. Sun, E. Al., Critical cleavage fracture stress characterization of A508 nuclear pressure vessel steels, Int. J. Press. Vessel. Pip. 123 (2014) 92–98. doi:10.1016/j.ijpvp.2014.08.003.

[103] M. Kim, S. Park, B. Lee, K. Lee, Comparison of Fracture Properties in SA508 Gr.3, Gr.4N high strength low alloy steels for advanced pressure vessel materials, Int. J. Press. Vessel. Pip. 131 (2015) 60–66. doi:10.1016/j.ijpvp.2015.04.010.

[104] G. Bonny, D. Terentyev, E.E. Zhurkin, L. Malerba, Monte Carlo study of decorated dislocation loops in FeNiMnCu model alloys, J. Nucl. Mater. 452 (2014) 486–492. doi:10.1016/j.jnucmat.2014.05.051.

[105] W. Xiong, H. Ke, P.B. Wells, L. Barnard, R. Krishnamurthy, G.R. Odette, D. Morgan, Thermodynamic models of low temperature Mn-Ni-Si precipitation in reactor pressure vessel steels, Mater. Res. Soc. Commun. 4 (2014) 101–105. doi:10.1557/mrc.2014.21.

[106] D.J. Sprouster, J. Sinsheimer, E. Dooryhee, S.K. Ghose, P. Wells, T. Stan, N. Almirall, G.R. Odette, L.E. Ecker, Structural characterization of nanoscale intermetallic precipitates in highly neutron irradiated reactor pressure vessel steels, Scr. Mater. 113 (2016) 18–22. doi:10.1016/j.scriptamat.2015.10.019.

[107] G.S. Was, M. Hash, G.R. Odette, Hardening and microstructure evolution in proton-irradiated model and commercial pressure-vessel steels, Phi. 85 (2005) 703–722. doi:10.1080/14786430412331319974.

[108] S. Shu, N. Almirall, P.B. Wells, T. Yamamoto, G.R. Odette, D.D. Morgan, Precipitation in Fe-Cu and Fe-Cu-Mn model alloys under irradiation: Dose rate effects, Acta Mater. 157 (2018) 72–82. doi:10.1016/j.actamat.2018.07.017.

[109] J.H. Ke, H. Ke, G.R. Odette, D. Morgan, Cluster dynamics modeling of Mn-Ni-Si precipitates in ferritic-martensitic steel under irradiation, J. Nucl. Mater. 498 (2018) 83–88. doi:10.1016/j.jnucmat.2017.10.008.

[110] G.R. Odette, T. Yamamoto, B.D. Wirth, Late Blooming phases and Dose Rate Effects in RPV Steels: Integrated Experiments and Models, Proceeding of the Second International Conference on Multiscale Modeling, October 11-15, 2004, Los Angeles, CA (2004) pp. 10.

[111] H. Ke, P. Wells, P.D. Edmondson, N. Almirall, L. Barnard, G.R. Odette, D. Morgan, Thermodynamic and kinetic modeling of Mn-Ni-Si precipitates in low-Cu reactor pressure vessel steels, Acta Mater. 138 (2017) 10–26. doi:10.1016/j.actamat.2017.07.021.

[112] M. Mamivand, P. Wells, H. Ke, S. Shu, G. R. Odette, D. Morgan, CuMnNiSi precipitate evolution in irradiated reactor pressure vessel steels: integrated cluster dynamics and experiments, Acta Mater. 180 (2019) 199-217. doi:10.1016/j.actamat.2019.09.016.

[113] J.H. Ke, E.R. Reese, E.A. Marquis, G.R. Odette, D. Morgan, Flux effects in precipitation under irradiation – Simulation of Fe-Cr alloys, Acta Mater. 164 (2019) 586–601. doi:10.1016/J.ACTAMAT.2018.10.063.

[114] A.M. Monterrosa, D. Woodley, Z.J. Jiao, G. Was, The influence of carbon on cavity evolution in ion-irradiated ferritic-martensitic steels, J. Nucl. Mater. 509 (2019) 722-735. doi:10.1016/j.jnucmat.2018.05.012.

[115] M.P. Short, D.R. Gaston, M. Jin, L. Shao, F.A. Garner, Modeling injected interstitial effects on void swelling in self-ion irradiation experiments, J. Nucl. Mater. 471 (2016) 200–207. doi:10.1016/j.jnucmat.2015.10.002.

[116] Malerba, L. (2008). Personal Communication.

[117] ECAR-2982, As-Run Thermal Analysis for the UCSB-1 Experiment in the Advanced Test Reactor, S.M. Wilson, November 2015.

[118] ASTM E521, Standard Practice for Neutron Radiation Damage Simulation by Charged Particle Irradiation, Annual Book of ASTM Standards, ASTM International, West Conshohocken, PA, Vol. 12.02.

[119] K. Thompson, D. Lawrence, D.J. Larson, J.D. Olson, T.F. Kelly, B. Gorman, In situ site-specific specimen preparation for atom probe tomography, Ultramicroscopy. 107 (2007) 131–139. doi:10.1016/j.ultramic.2006.06.008.

[120] S. Shu, P.B. Wells, N. Almirall, G.R. Odette, D.D. Morgan, Thermodynamics and kinetics of core-shell versus appendage co-precipitation morphologies: An example in the Fe-Cu-Mn-Ni-Si system, Acta Mater. 157 (2018) 298–306. doi:10.1016/j.actamat.2018.07.037.

[121] N. Almirall, P.B. Wells, H. Ke, P. Edmondson, D. Morgan, T. Yamamoto, G.R. Odette, On the elevated temperature thermal stability of nanoscale Mn-Ni-Si precipitates formed at lower temperature in highly irradiated reactor pressure vessel steels, Sci. Rep. 9 (2019). doi:10.1038/s41598-019-45944-z.

[122] R. Ngayam-Happy, C.S. Becquart, C. Domain, First principle-based AKMC modelling of the formation and medium-term evolution of point defect and solute-rich clusters in a neutron irradiated complex Fe-CuMnNiSiP alloy representative of reactor pressure vessel steels, J. Nucl. Mater. 440 (2013) 143–152. doi:10.1016/j.jnucmat.2013.04.081.

[123] G. Bonny, D. Terentyev, A. Bakaev, E.E. Zhurkin, M. Hou, D. Van Neck, L. Malerba, On the thermal stability of late blooming phases in reactor pressure vessel steels: An atomistic study, J. Nucl. Mater. 442 (2013) 282–291. doi:10.1016/j.jnucmat.2013.08.018.

[124] P.B. Wells, T. Yamamoto, B. Miller, T. Milot, J. Cole, Y. Wu, G.R. Odette, Evolution of manganese–nickel–silicon-dominated phases in highly irradiated reactor pressure vessel steels, Acta Mater. 80 (2014) 205–219. doi:10.1016/j.actamat.2014.07.040.

[125] M.K. Miller, A. A. Chernobaeva, Y.I. Shtrombakh, K.F. Russell, R.K. Nanstad, D.Y. Erak, O.O. Zabusov, Evolution of the nanostructure of VVER-1000 RPV materials under neutron irradiation and post irradiation annealing, J. Nucl. Mater. 385 (2009) 615–622. doi:10.1016/j.jnucmat.2009.01.299.

[126] P.D. Styman, J.M. Hyde, D. Parfitt, K. Wilford, M.G. Burke, C. a. English, P. Efsing, Post-irradiation annealing of Ni–Mn–Si-enriched clusters in a neutron-irradiated RPV steel weld using Atom Probe Tomography, J. Nucl. Mater. 459 (2015) 127–134. doi:10.1016/j.jnucmat.2015.01.027.

[127] G.R. Odette, B.D. Wirth, A computational microscopy study of nanostructural evolution in irradiated pressure vessel steels, J. Nucl. Mater. 251 (1997) 157–171. doi:10.1016/S0022-3115(97)00267-5.

[128] G.R. Odette, T. Yamamoto, D. Klingensmith, On the effect of dose rate on irradiation hardening of RPV steels, Philos. Mag. 85 (2005) 779–797. doi:10.1080/14786430412331319910.

[129] J.O. Andersson, T. Helander, L. Höglund, P. Shi, B. Sundman, THERMO-CALC & DICTRA, Computational Tools For Materials Science, 26 (2002) 273–312.

[130] Thermo-Calc Software TCAL2 / Aluminum database version 2.

[131] Y.R. Wen, A. Hirata, Z.W. Zhang, T. Fujita, C.T. Liu, J.H. Jiang, Microstructure characterization of Cu-rich nanoprecipitates in a Fe – 2 . 5, Acta Mater. 61 (2013) 2133–2147. doi:10.1016/j.actamat.2012.12.034.

[132] K. Hirano, M. Cohen, B.L. Averbach, Diffusion of nickel into iron, Acta Metall. 9 (1961) 440–445. doi:10.1016/0001-6160(61)90138-9.

[133] A.J. Ardell, On the coarsening of grain boundary precipitates, Acta Metall. 20 (1972) 601–609. doi:10.1016/0001-6160(72)90015-6.

[134] N. Almirall, P. Wells, T. Yamamoto, K. Wilford, T. Williams, N. Riddle, G.R. Odette, Precipitation and Hardening in Irradiated Low Alloy Steels with a Wide Range of Ni and Mn Compositions, Acta Mater. Manuscript (2018).

[135] W.Y. Chen, M. Li, X. Zhang, M.A. Kirk, P.M. Baldo, T. Lian, In situ TEM study of G-phase precipitates under heavy ion irradiation in CF8 cast austenitic stainless steel, J. Nucl. Mater. 464 (2015) 185–192. doi:10.1016/j.jnucmat.2015.04.042.

[136] S. Shu, P.B. Wells, G.R. Odette, D. Morgan, A kinetic lattice Monte Carlo study of post-irradiation annealing of model reactor pressure vessel steels, J. Nucl. Mater. 524 (2019) 312–322. doi:10.1016/J.JNUCMAT.2019.07.018.

[137] M. I. Pascuet, G. Monnet, G. Bonny, E. Martinez, J. J. H. Lim, M.G. Burke, L. Malerba, Solute precipitation on a screw dislocation and its effects on dislocation mobility in bcc Fe, J. Nucl. Mater. 519 (2019) 265-273. doi:10.1016/j.jnucmat.2019.04.007.

[138] R.E. Stoller, M.B. Toloczko, G.S. Was, A.G. Certain, S. Dwaraknath, F.A. Garner, On the use of SRIM for computing radiation damage exposure, Nucl. Instruments Methods Phys. Res. Sect. B Beam Interact. with Mater. Atoms. 310 (2013) 75–80. doi:10.1016/j.nimb.2013.05.008.

[139] ASTM Subcommittee E10.02, Adjunct for ASTM E900-15: Technical Basis for the Equation used to Predict Radiation-Induced Transition Temperature shift in Reactor Vessel Materials, ASTM International, West Conshohocken, PA, 2015.

[140] R.K. Nanstad, G.R. Odette, N. Almirall, J.P. Robertson, L. Server, T. Yamamoto, Effects of ATR-2 Irradiation to High Fluence on Nine RPV Surveillance Materials, 2017.

[141] H.B. Klasky, B.R. Bass, P.T. Williams, R.D. Phillips, M. Erickson, M.T. Kirk, G.L. Stevens. *Radiation Embrittlement Archive Project*. United States: 2013. https://www.ornl.gov/sites/default/files/SMiRT-22_REAP_Paper.pdf.

[142] Users' Manual & ETC Assessment Guidelines, International Standards Worldwide, E10.02 PLOTTER Tool Version 2013-10-04(R6); 2013.

[143] G.R. Odette, P.B. Wells, N. Almirall, T. Yamamoto, K. Fields, D. Gragg, R. K. Nanstad, M. A. Sokolov, J. P. Robertson, Update on the Advanced Test Reactor 2 Reactor Pressure Vessel Steel High Fluence Irradiation Project, Light Water React. Sustain. Program (2016).

[144] C. Brillaud , F. Hedin and B. Houssin , A comparison between French surveillance program results and predictions of irradiation embrittlement, Effects of Radiation on Materials: 13th International Symposium , ASTM STP 956, ed. F.A. Garner, C.H. Henager Jr., and N. Igata, American Society for Testing and Materials, 1987, pp. 420-447.

[145] R.K. Nanstad, G.R. Odette, Reactor Pressure Vessel Task of Light Water Reactor Sustainability Program : Milestone M2LW-13OR0402013 , Progress Report on Status of Advanced Test Reactor-2 Reactor Pressure Vessel Materials Irradiation Project, (2013).

[146] B. Gault ; M.P. Moody; J.M. Cairney; S.P. Ringer, Atom Probe Microscopy, Springer, 2012.

[147] J.M. Hyde, M.G. Burke, B. Gault, D.W. Saxey, P. Styman, K.B. Wilford, T.J. Williams, Atom probe tomography of reactor pressure vessel steels: an analysis of data integrity., Ultramicroscopy. 111 (2011) 676–82. doi:10.1016/j.ultramic.2010.12.033.

[148] J.M. Hyde, A. Cerezo, R.P. Setna, P.J. Warren, G.D.W. Smith, Lateral and depth scale calibration of the position sensitive atom probe, Appl. Surf. Sci. 76–77 (1994) 382–391. doi:10.1016/0169-4332(94)90371-9.

[149] C. A. Williams, D. Haley, E.A. Marquis, G.D.W. Smith, M.P. Moody, Defining clusters in APT reconstructions of ODS steels., Ultramicroscopy. 132 (2013) 271–8. doi:10.1016/j.ultramic.2012.12.011.

[150] F. Vurpillot, A. Bostel, D. Blavette, Trajectory overlaps and local magnification in three-dimensional atom probe, Appl. Phys. Lett. 76 (2000) 3127–3129. doi:10.1063/1.126545.

[151] K.P. Gupta, The Mn-Ni-Si (Manganese-Nickel-Silicon) System, J. Phase Equiilibria Diffus. 27 (2006) 529–534. doi:10.1361/154770306X136520.

Appendix A: Small Angle Neutron Scattering

The focus of this section is describing the ongoing research into SANS, APT and Small Angle X-ray Scattering (SAXS), where the latter adds a third electron density contrast factor (CF = the scattering length density difference squared) to magnetic and nuclear SANS. [6] One challenge with the interpretation of SANS results is that the scattering contrast of the precipitates must be known a priori [6]. Historically, the magnetic contrast has assumed that the precipitates are non-magnetic holes in a saturated magnetic Fe matrix. This assumption is valid if the precipitates are predominantly nonmagnetic Cu. But at higher fluences, other solutes, most notably Ni, are enriched in MNSPs thus they may be partially magnetic. Recent comparisons between SANS and atom probe tomography (APT), shown in Figure 2, support our hypothesis where lower fluence conditions, or alloys with high Cu and lower Ni, show very reasonable agreement between SANS and APT precipitate volume fractions (f), while higher fluence conditions, with MNSPs, show that SANS consistently measures smaller f_v than APT. In collaboration with BNL at NSLS-II we found good agreement between XRD, SAXS and APT when the composition of the alloys results in the precipitation of known G or Γ_2 phases [7]. However, the SAXS CF is not known for alloys with a wide range of other compositions that result in a variety of intermetallic precipitates. Thus we sought to inform and train the SAXS analysis with the results of APT and SANS. It is very important to emphasize that resolution of these issues, and the new methodologies that will be created, will have far broader impact on solid matter scattering science than the immediate problem at hand, which in itself will have enormous scientific and technological impact.

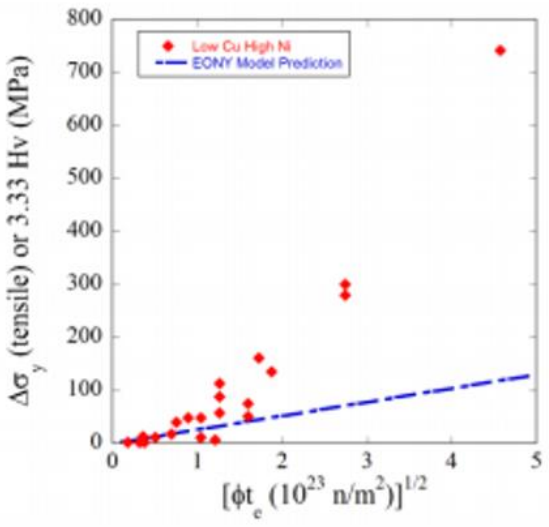

Figure A1. Measured irradiation hardening as a function of flux-adjusted neutron fluence for a low-Cu and high-Ni (0.02Cu 1.60Ni wt.%) irradiated steel compared to the EONY prediction.

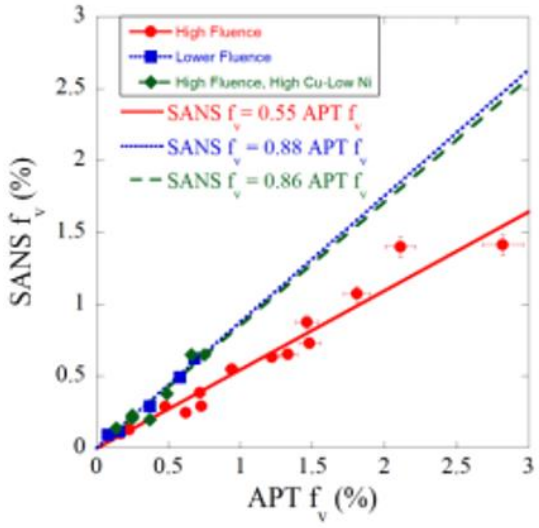

Figure A2. Comparison showing high Ni results with lower measured f_v in SANS versus APT.

UCSB collaborated on a large number of SAXS/XRD experiments at BNL, and has carried out decades of studies SANS at NIST, while the APT was primarily at UCSB. About 50 SAXS and XRD patterns for ~50 irradiated RPV alloys have been collected. However, SAXS data interpretation is difficult because the electron CFs are not known a priori. The

unique combination of independent measurements (SAXS, SANS, and APT) will take advantage of the differences in the CF for neutron magnetic and nuclear interactions versus the electron CF for x-rays, to more uniquely determine the atomic density and composition of the Mn-Ni-Si-Cu precipitates. Figure A3a shows SAXS and SANS scattering intensity as a function of q^2 for a Cu-free very high 3.5% Ni steel. APT provides the precipitate f_v (and number density and size distribution) along with 3D elemental maps of their compositions. Figure A3b shows example of an atom map, demonstrating that MNSPs form even in the absence of a significant amount of Cu at high fluence, especially at high Ni. However, these APT reconstructions are limited to small sample volumes, and APT requires time consuming and costly specimen preparation, greatly limiting the number of measurements.

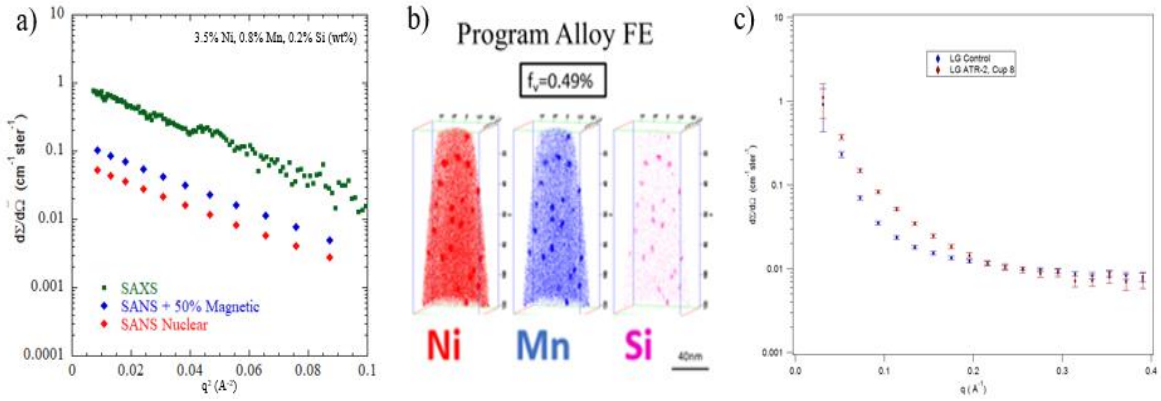

Figure A3. a) SAXS, SANS nuclear scattering and SANS nuclear + 50% magnetic scattering for RPV steel with 3.5% Ni, 0.8% Mn and 0.2% Si; b) APT solute maps for with 0.01% Cu, 1.70% Ni, 1.30% Mn, 0.20% Si surveillance steel. The alloys are from ATR-2 irradiated to peak fluence≈ $1.4x10^{20}$ n/cm^2 at 290°C; and c) a typical set of irradiated and control SANS curves we obtained at NIST.

To further explain the examples shown above, the nm-scale precipitate scattering results in the bulge in the irradiated condition in the example in Fig. A3c (red symbols), which is plotted along with the precipitate free control (blue symbols). After subtraction (example

Fig. A3a), this high quality data is readily fitted derive the precipitate size distribution, <d>, f_v and N by assuming that they are not magnetic, thus have a known CF. However, the magnetization of the precipitate is not always well known.

Results

Small angle neutron scattering has been completed on 8 UCSB alloys, 9 surveillance alloys and 20 ASM alloys. These results are shown below. There are compared with measured APT data in Chapter 5 and show qualitatively similar results.

UCSB Alloys

Figure A4 shows scattering curves for the baseline and irradiated samples for two UCSB alloys, LG (low Cu, medium Ni) on the left and LD (high Cu, high Ni) on the right. Note that the high Cu, high Ni steel has much more scattering from the precipitates, consistent with APT data.

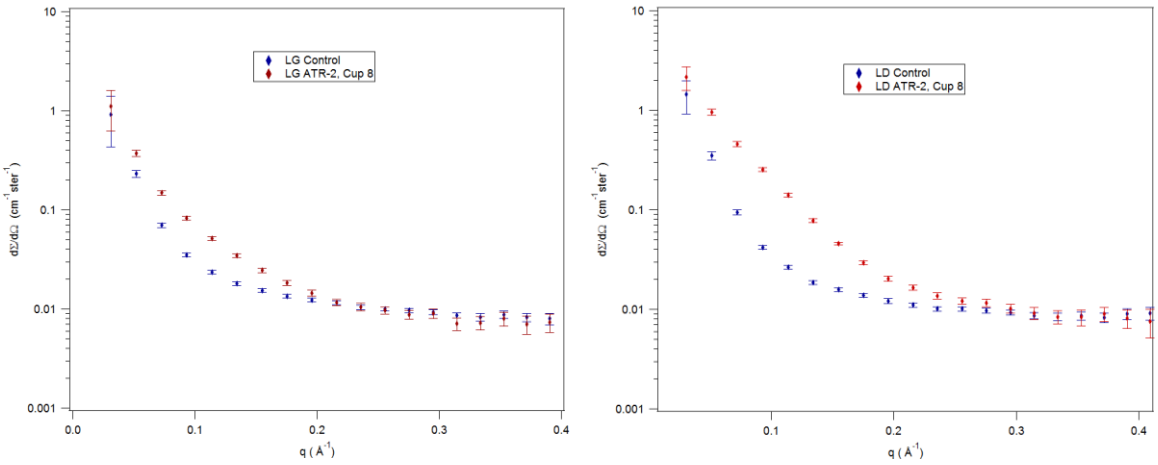

Figure A4. SANS 45° scattering curves from an angle on the detector that are higher at intermediate q due to the precipitates. Note that there is less scattering in the irradiated low Cu, medium Ni steel (LG: left) compared to the high Cu, high Ni steel (LD: right).

Table A1 shows the SANS measured precipitate <d>, N, f_v and magnetic-to-nuclear scattering ratios (M/N). The general trends of the effects of Cu and Ni are consistent the APT data. The M/N reflect the composition and atomic density of the precipitates. For example, the measured M/N vary from 1.41 to 2.32 in the UCSB steel matrix. APT shows that the precipitates do not have exact stoichiometric compositions compared to the Γ_2 and G phases. Assuming the APT measured MNSP compositions for LD, the M/N are estimated to be 2.32 and 2.50 for the Γ_2 and G-phases, respectively. These results are preliminary, and the analysis is ongoing. Future work will expand the analysis to the rest of the alloys, and use complementary SAXS data to help to further constrain the compositions and structures precipitates phases.

Table A1. Small Angle Neutron Scattering precipitate <d>, N, f_v, and M/N for the measured UCSB alloys from cup 8.

Alloy	<d> (nm)	+/- (nm)	N (10^{23} m^{-3})	+/- (10^{23} m^{-3})	f_v (%)	+/- (%)	M/N
C7	2.52	0.13	4.50	1.13	0.37	0.06	1.66
C9	2.96	0.15	1.02	0.26	0.14	0.02	2.35
C13	3.54	0.18	1.00	0.25	0.22	0.03	1.41
C16	4.04	0.20	1.18	0.30	0.40	0.06	2.07
C17	3.64	0.18	3.39	0.85	0.84	0.13	1.60
LD	3.90	0.20	1.79	0.45	0.55	0.08	2.32
LG	3.56	0.18	0.56	0.41	0.13	0.02	2.17
LI	4.20	0.21	0.75	0.19	0.29	0.04	2.27

Surveillance Alloys

Table A2 shows SANS data for 9 surveillance alloys. Note that the surveillance M/N are very consistent with the UCSB alloys except in the case of KP, which has the lowest Mn content in both. This is consistent with the high M/N ratio.

Table A2. Small Angle Neutron Scattering precipitate <d>, N, f_v, and M/N for the measured surveillance alloys from cup 8.

Alloy	<d> (nm)	+/- (nm)	N (10^{23} m^{-3})	+/- (10^{23} m^{-3})	f_v (%)	+/- (%)	M/N
QC1	3.06	0.15	2.81	0.70	0.42	0.06	2.22
D3	2.98	0.15	3.52	0.88	0.49	0.07	2.55
SW1	2.92	0.15	1.79	0.45	0.23	0.03	1.59
SB1	2.88	0.14	3.05	0.76	0.38	0.06	2.13
SB2	2.64	0.13	1.46	0.37	0.14	0.02	14.75
SW2	3.24	0.16	3.66	0.91	0.65	0.10	2.17
SW3	3.48	0.17	2.96	0.74	0.65	0.10	2.58
SW4	2.62	0.13	2.11	0.53	0.2	0.03	2.1
SW5	2.64	0.13	2.17	0.54	0.21	0.03	2.68

Advanced Steel Matrix

Table A3 shows the SANS measured precipitate <d>, N, f_v and M/N for 20 ASM alloys. The ASM alloys show very large ranges of M/N, and a number of them have M/N > 10 or < 1.5. This is very different than the UCSB and surveillance matrices where most M/N fell between 1.5 and 2.5.

Table A3. Small Angle Neutron Scattering precipitate <d>, N, f_v, and M/N for the measured ASM alloys from Cup 8.

Alloy	<d> (nm)	+/-	N (m^{-3})	+/-	f_v (%)	+/-	M/N
A1	3.84	0.19	1.20E+22	3.00E+21	0.04	0.01	9.96
A4	4.64	0.23	7.58E+21	1.90E+21	0.04	0.01	10.87
A10	2.24	0.11	3.00E+24	7.50E+23	1.77	0.27	1.78
A14	3.86	0.19	4.50E+23	1.13E+23	1.35	0.20	1.17
A17	2.28	0.11	2.90E+24	7.25E+23	1.82	0.27	1.69
A18	2.70	0.14	2.25E+24	5.63E+23	2.31	0.35	1.93
A20	2.28	0.11	3.00E+23	7.50E+22	0.19	0.03	10.68
A21	2.92	0.15	1.10E+23	2.75E+22	0.15	0.02	15.22
A22	2.22	0.11	9.40E+23	2.35E+23	0.54	0.08	1.54
A26	2.26	0.11	6.30E+23	1.58E+23	0.39	0.06	19.3
A28	2.52	0.13	6.30E+23	1.58E+23	0.53	0.08	22.9
A32	1.49	0.07	1.25E+24	3.13E+23	1.72	0.26	1.31
A33	2.20	0.11	5.70E+23	1.43E+23	0.32	0.05	13.6
A34	3.04	0.15	9.10E+22	2.28E+22	0.13	0.02	> 100
A35	2.22	0.11	1.21E+23	3.03E+22	0.09	0.01	0.98
A37	2.50	0.13	7.70E+22	1.93E+22	0.06	0.01	1.36
A39	2.58	0.13	1.39E+23	3.48E+22	0.13	0.02	1.65
A42	1.74	0.09	1.74E+24	4.35E+23	0.49	0.07	3
A47	1.78	0.09	1.10E+24	2.75E+23	0.32	0.05	3.44
A48	2.16	0.11	1.50E+24	3.75E+23	0.81	0.12	2.8

The large variation of M/N ratios is due to the wide range of compositions in the ASM, hence, corresponding differences in precipitate compositions and phases (see Chapter 5.2). For example, as noted previously, the precipitates in A34 and A26 have compositions of approximately Ni_3Si, while in SANS they have M/N of 19.3 and > 100, respectively. The scattering length of the Ni_3Si precipitates similar to that of the Fe matrix, so the corresponding scattering contrast is small, leading to very large M/N assuming these features are not magnetic. The two unknowns are the actual phase and corresponding atomic density and the magnetization of the precipitate, if any.

Figure A5. Additional SANS Curves for the Surveillance Alloys at 45° with respect to the magnetic field.

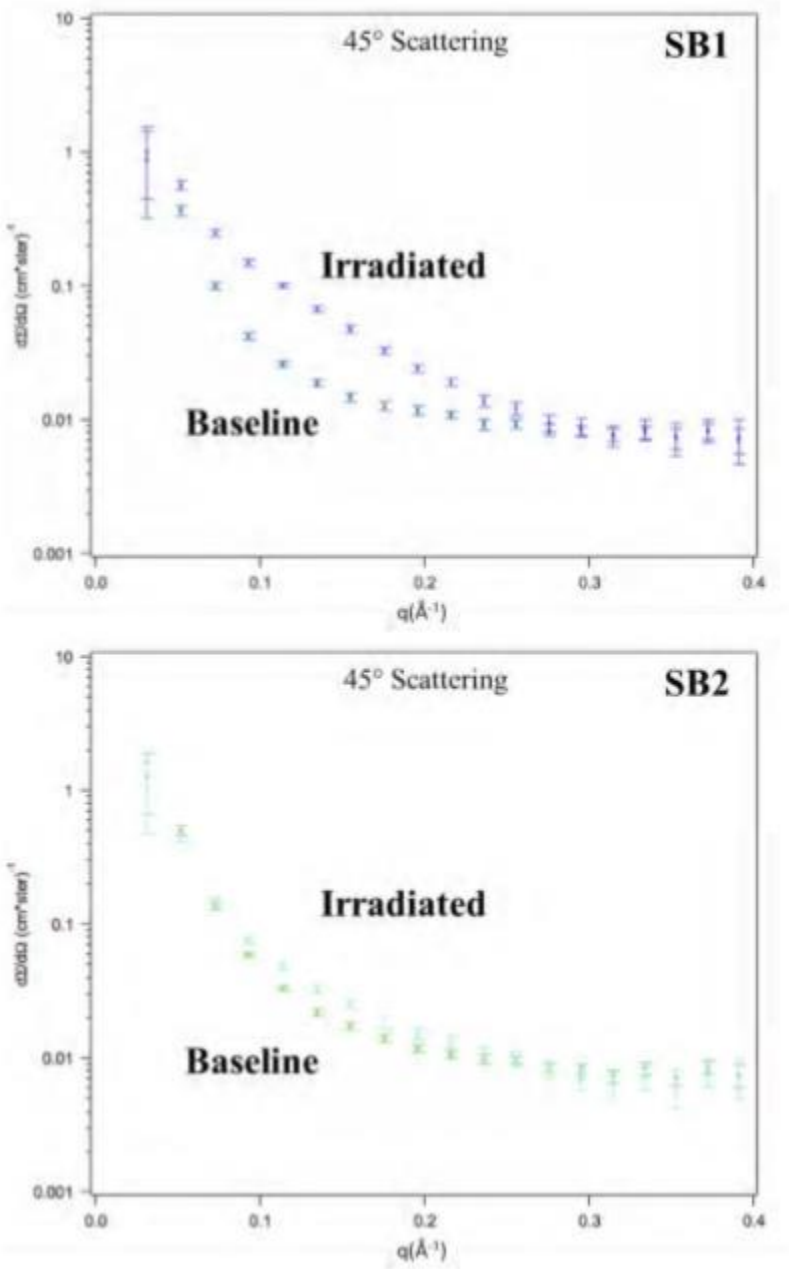

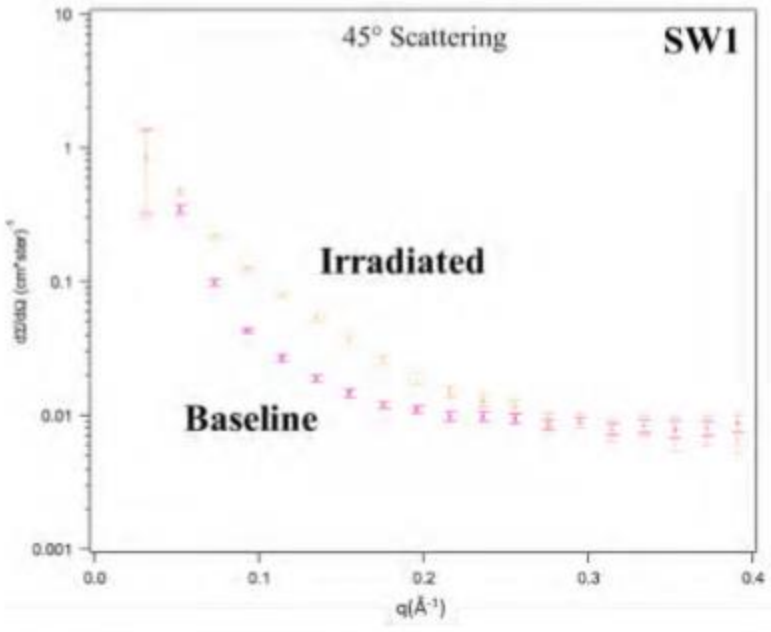
45° Scattering
SW1
Irradiated
Baseline
10
1
0.1
0.01
0.001
0.0
0.1
0.2
0.3
0.4
q(Å⁻¹)

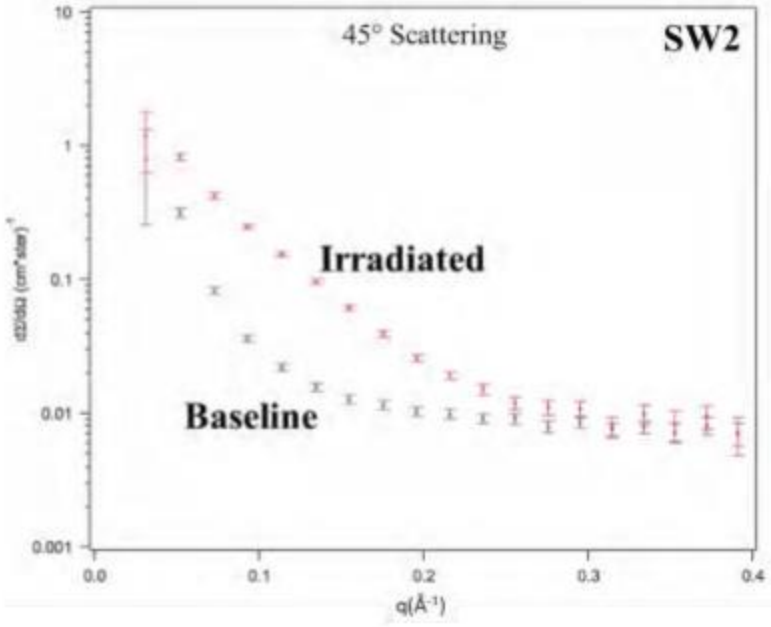
45° Scattering
SW2
Irradiated
Baseline
10
1
0.1
0.01
0.001
0.0
0.1
0.2
0.3
0.4
q(Å⁻¹)

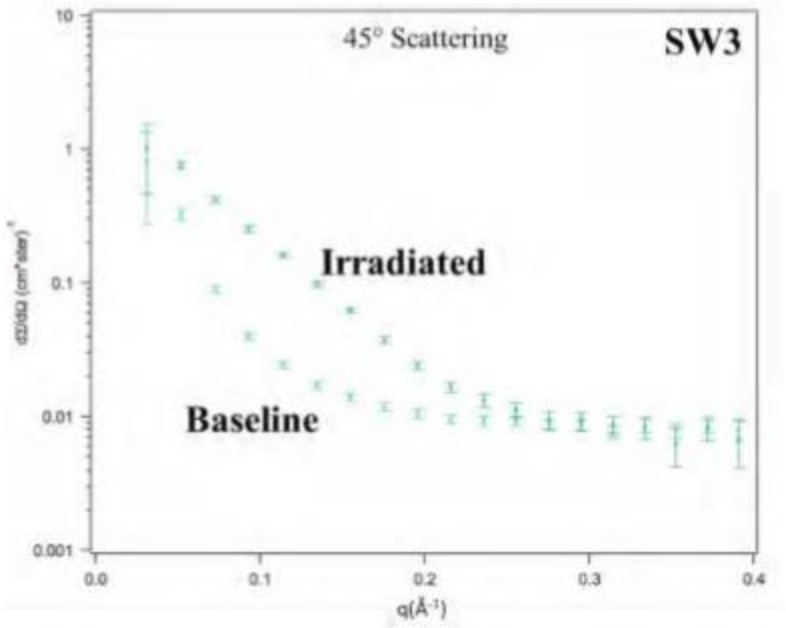
45° Scattering
SW3
Irradiated
Baseline
10
1
0.1
0.01
0.001
0.0
0.1
0.2
0.3
0.4
q(Å⁻¹)

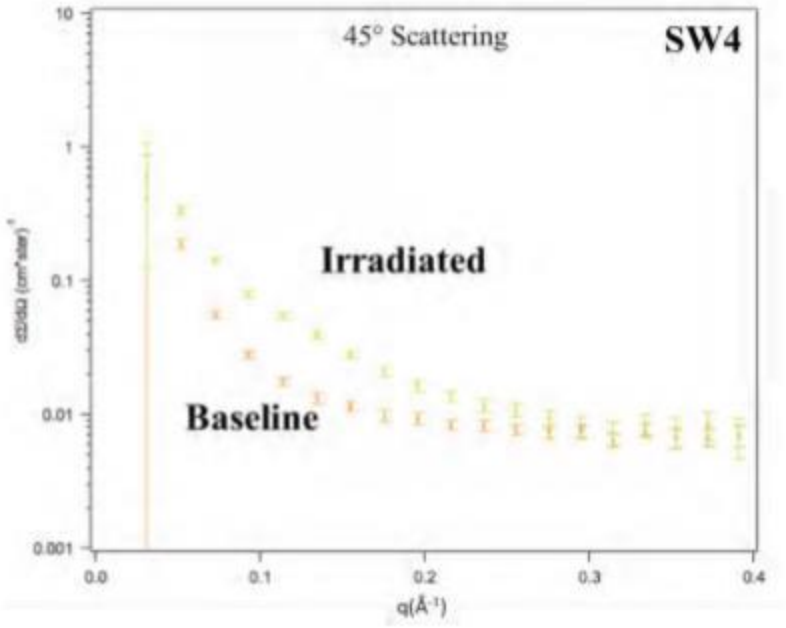
45° Scattering
SW4
Irradiated
Baseline
10
1
0.1
0.01
0.001
0.0
0.1
0.2
0.3
0.4
q(Å⁻¹)

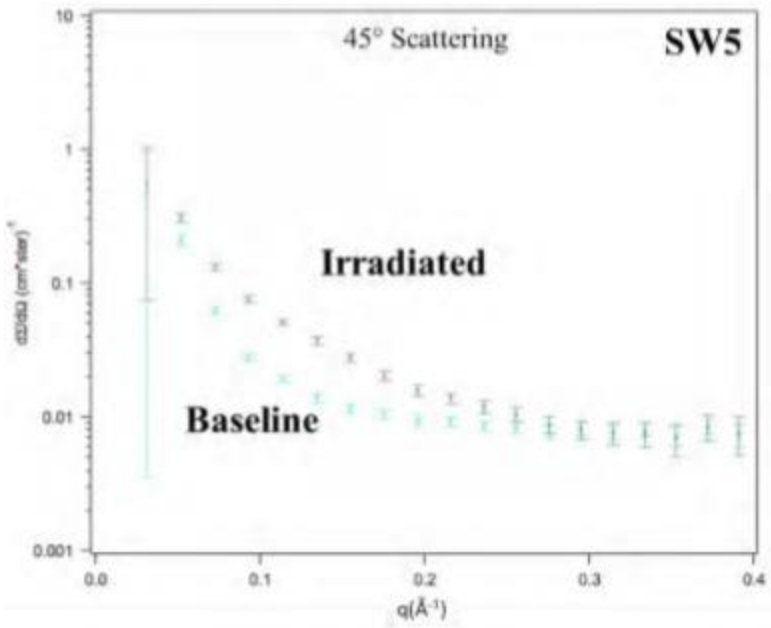
45° Scattering
SW5
Irradiated
Baseline
10
1
0.1
0.01
0.001
0.0
0.1
0.2
0.3
0.4
q(Å⁻¹)

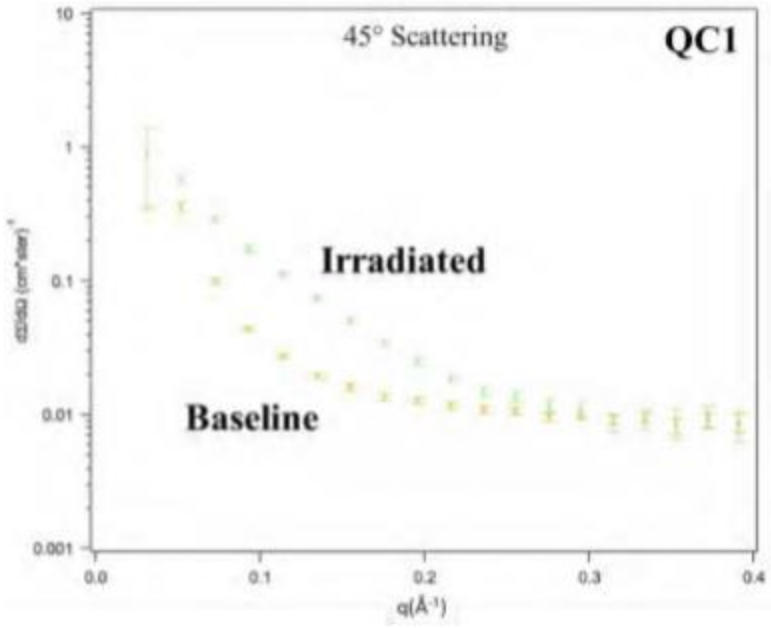
45° Scattering
QC1
Irradiated
Baseline
10
1
0.1
0.01
0.001
0.0
0.1
0.2
0.3
0.4
q(Å⁻¹)

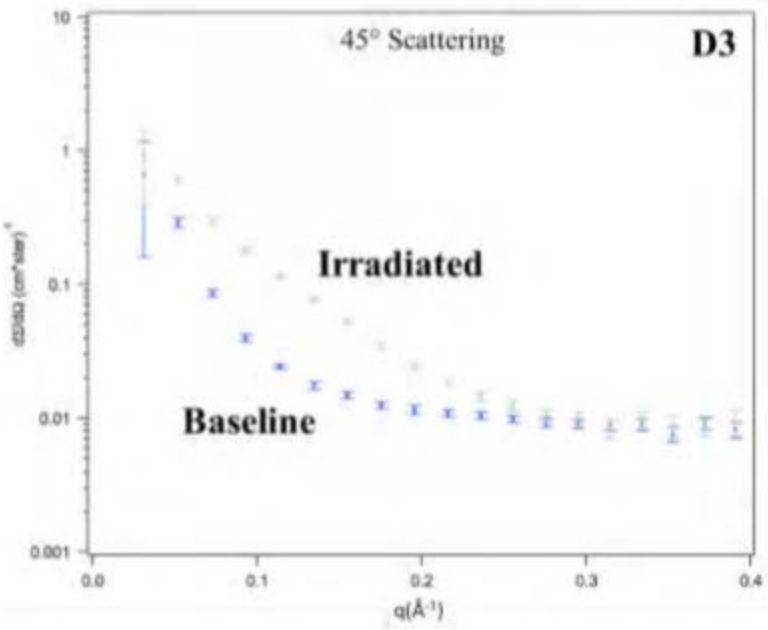
45° Scattering
D3
Irradiated
Baseline
10
1
0.1
0.01
0.001
0.0
0.1
0.2
0.3
0.4
q(Å⁻¹)

Appendix B: ATR-2 Additional Information

ATR-2 flux is ≈ 80x the in-service vessel flux that will reach 10^{20} n/cm^2 in 80 years of operation. The UCSB ATR-2 experiment reached a peak $\phi t \approx 1.38 \times 10^{20}$ n/cm^2, which is about 40% larger than what some RPVs will reach at an 80 year extended life. In addition, four capsules reached a peak ϕt ranging from 5.1×10^{19} to 9.1×10^{19} n/cm^2. These capsules were to be used to directly compare data from this experiment to the lower fluence data available in surveillance programs. The specimens were irradiated at four nominal T_i: 250, 270, 290 and 310°C. The ≈ 109 cm long test train consisted of an assembly of concentric tubes, with an inner tube containing 13 thin-walled (0.125 mm) specimen cups. Temperatures were monitored by 28 thermocouples on the outside of an engineered gas gap tube. Finite element heat transfer models were used to design the gas gaps and calculate the predicted specimen temperatures. The gas gap provided active temperature control by adjusting a flowing He-Ar gas mixture based on temperature readings from the 28 thermocouples. Gas was provided to three separate compartments of the test train. One of the most remarkable features of the ATR-2 irradiation was that the entire test train was successfully removed and re-inserted to avoid a PALM cycle when the ATR lobe containing the test train (the I-22 position) ran at high power. Finally, a gadolinium shield was included in the test train to reduce the thermal neutron flux on the specimens, hence minimizing their activities. Overall the UCSB irradiation was a resounding success, primarily due to the extraordinary and creative contributions of the INL engineering team that designed and conducted the irradiation.

Table B1. Summary of ATR-2 specimen matrices sorted by alloy groups and sample geometry [21,145]

	Lg Disc		Sm Disc		Tens		DCT		Any Type	
Total # alloy/irrad cond	Alloy	Spc.	Alloy	Spc.	Alloy	Spc.	Alloy	Spc.	Alloy	Spc.
Total # spc	144	1028	40	224	55	367	3	45	173	1664
DCT matrix	3	14			3	54	3	45	3	113
CM alloys	21	231			13	92			21	323
Laval alloys	10	72			8	48			10	120
UCSB Commercial alloys	13	107	1	4	9	53			13	164
EPRI alloys	20	141			6	21			20	162
ORNL alloys	5	64	5	41	8	51			9	156
RR alloys	57	356	11	80	8	48			68	484
Bettis alloys	5	25							5	25
CRIEPI alloys			13	65					13	65
OV model alloys	9	15	10	34					10	49
Diffusion Multiples	1	3							1	3

UCSB/ORNL	290°C high flux disc coupons	290°C high flux tensiles	290°C med flux disc coupons	290°C med flux tensiles	290°C low flux disc coupons	290°C low flux tensiles	250°C disc coupons	270°C disc coupons	310°C disc coupons
31split melt commercial model alloys	78	69	72	71	68		7	36	42
10 simple model alloys	30				9		4	3	3
16 RPV plates/forgings	34	12	35	13	35		3	10	9
26 RPV welds	71	57	61	41	50	2	5	23	21

Rolls Royce	290°C high flux disc coupons	290°C high flux tensiles	290°C med flux disc coupons	290°C med flux tensiles	290°C low flux disc coupons	290°C low flux tensiles	250°C disc coupons	270°C disc coupons	310°C disc coupons
56 RR model alloys & H.T. variations	56	17	106	16	115	15	56	9	10
12 RR archival crossover welds & plates	25		25		22		12		

Other participants	290°C high flux disc coupons	290°C med flux disc coupons	290°C low flux disc coupons	250°C disc coupons	270°C disc coupons	310°C disc coupons
5 Bettis plate & weld alloys	5			10	5	5
13 CRIEPI alloys	13	13	13		13	13

Figure B1. ATR-2 Coupon and tensile summary for each participant [1-4].

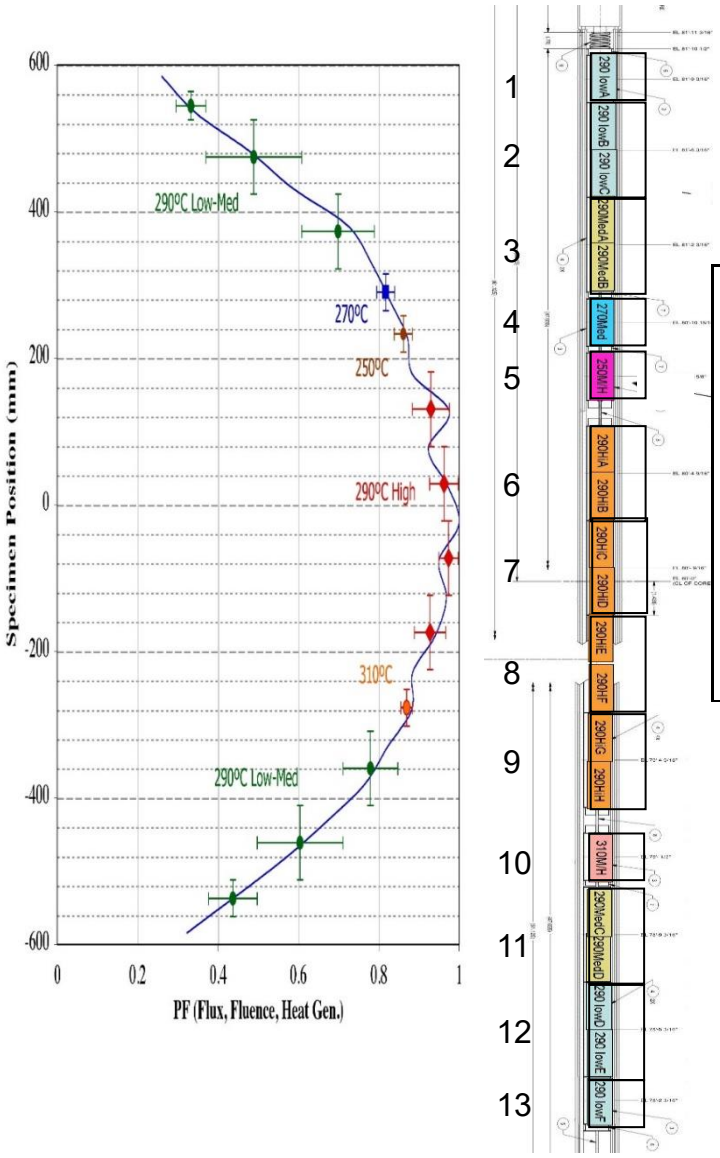

Capsule ID	Materials	Target Temp.	Nominal Target ft ($x10^{19}$n/cm^2)
UCSB-1	coupon/tensile	290 ºC	low 4.2
UCSB-2	coupon/tensile	290 ºC	low 6.2
UCSB-3	coupon/tensile	290 ºC	med 8.8
UCSB-4	coupon/tensile	270 ºC	med 10.3
UCSB-5	coupon/tensile	250 ºC	med/hi 10.9
UCSB-6	DCT	290 ºC	hi 11.7
UCSB-7	coupon/tensile	290 ºC	hi 12.2
UCSB-8	coupon/tensile	290 ºC	hi 12.3
UCSB-9	DCT	290 ºC	hi 11.7
UCSB-10	coupon/tensile	310 ºC	med/hi 11.0
UCSB-11	coupon/tensile	290 ºC	med 9.8
UCSB-12	DCT	290 ºC	low 7.6
UCSB-13	coupon/tensile	290 ºC	low 5.5

Figure B2. ATR-2 capsule summary and layout ≈ 180 materials, ≈ 1600 specimens, 7 dosimeter packets, T_{irr}: 250-310ºC, ϕt: 4-9x10^{19} n/cm^2 [1-4].

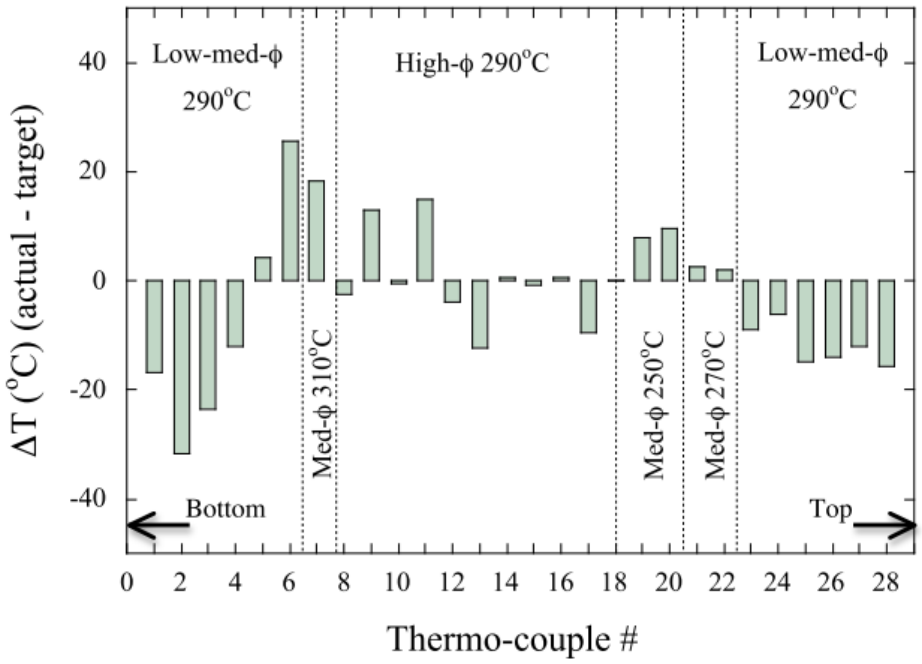

Figure B3. ATR-2 Temperature differences from target values recorded during irradiation [1-3].

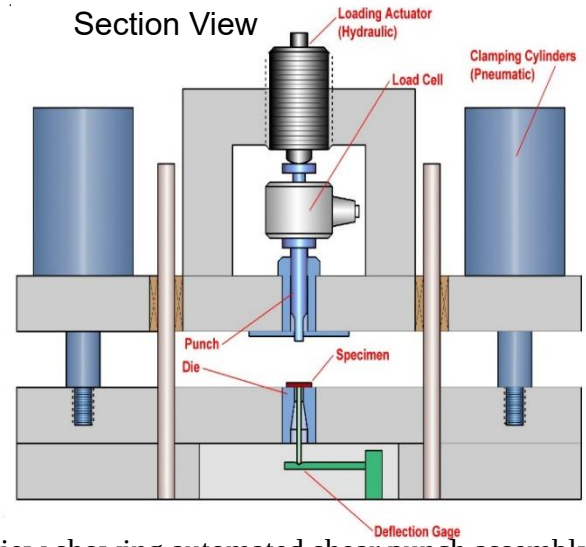

Figure B4. Section view showing automated shear punch assembly [1-4].

Appendix C: Materials and Methods

Chapter 5

Alloys and Irradiations

The UCSB ATR-2 experiment was designed to investigate embrittlement at extended life fluences at intermediate flux of 3.6×10^{12} n/cm^2-s for T_i from 250 to 310°C. The peak ATR-2 flux is ≈ 90 times than that experienced by an in-service vessel. The ATR-2 alloy matrix includes ≈ 172 RPV alloys, in several sample geometries, yielding a total of ≈ 1600 specimens. The ASM, supplied by Rolls Royce, is comprised of fifty-five new split-melt advanced steels, spanning 50 compositions and an additional 5 heat treatments on selected alloys. All the alloys were irradiated in ATR-2 in the form of 20 mm diameter, 0.5 mm thick disc multipurpose coupons, along with 62 alloys in the form of subsized SS-J2 16 x 4 x 0.5 mm tensile specimens. The primary focus of this chapter is on the APT characterization of 9 ASM steels neutron irradiated to ≈ 1.4×10^{20} n/cm^2 at ≈ 290°C. The bulk alloy compositions are given in Table 5.1.1 (in at.%), along with the baseline heat treatment.

Table 5.1 Nominal steel compositions (%)

Alloy	Bulk at%								
	Cu	Ni	Mn	Si	Cr	Mo	P	C	Fe
A1	0.05	0.28	0.26	0.41	0.11	0.28	0.009	0.97	Bal.
A17	0.05	3.26	1.52	0.39	0.11	0.29	0.005	1.06	Bal.
A19	0.05	1.57	0.26	0.39	0.14	0.30	0.014	1.06	Bal.
A22	0.05	1.58	1.51	0.41	0.11	0.30	0.011	1.34	Bal.
A26	0.04	3.29	0.25	0.37	0.11	0.30	0.016	1.20	Bal.
A34	0.06	3.25	0.08	0.38	0.10	0.30	0.011	1.02	Bal.
A35	0.05	0.22	1.51	0.41	0.12	0.28	0.012	1.24	Bal.
A39	0.03	0.66	1.47	0.41	0.12	0.28	0.007	0.97	Bal.
A48	0.06	3.29	0.77	0.41	0.11	0.29	0.005	1.29	Bal.

Austenitized at 920°C for 1 h followed by an air cool, then tempered at 600°C for 5 h followed by an air cool.

Chapter 6

Atom Probe Tomography (APT) was used to characterize the volume fraction (f), diameter (d), average diameter (<d>), number density (N), and precipitate composition [32,75,78,146,147]. The high dpa NI specimens were examined using a Cameca LEAP 4000X HR at the Idaho Center for Advanced Energy Studies (CAES) while the ion irradiated specimens were run in a CAMECA LEAP 3000X HR at the University of California, Santa Barbara (UCSB). The specimens were run in voltage mode, which utilized identical systems within the LEAP 3000-4000 X HR, at a target evaporation rate of 0.50%, a pulse repetition rate of 200 kHz with a 20% pulse fraction and a specimen temperature of $\leq$ 50K.

The reconstructions were performed with the CAMECA Integrated Visualization and Analysis Software (IVAS v3.6.12). Planes within low index poles were used to depth scale the reconstruction [148]. The cluster analysis was performed using the core-linkage algorithm, an extension of the maximum separation method, in the IVAS reconstruction package, as

described elsewhere [82,91,149]. Based on a sensitivity analysis the following parameters were consistently used: order = 5; d_{max}=0.50-0.65 nm, N_{min}=15-65 and maximum separation envelope of additional elements (L) = erosion distance of matrix elements (d_{er}) < = d_{max}. Further information on and improvements made to selection of cluster parameters can be found elsewhere and in Chapter 4 [77].

Chapter 7.1

Atom Probe Tomography

Atom probe tomography (APT) was used to measure the MNSP composition, size distribution and average radius (<*r*>), number density (*N*) and mole fraction (*f*) in the AI condition and following each anneal for all times but the longest annealing time of 57 weeks. The APT was carried out at the Center for Advanced Energy Studies (CAES) located in Idaho Falls, ID, with support from the Idaho National Laboratory managed Nuclear Science User Facilities. APT tips were fabricated using a FEI Quanta 3D FEG Focused Ion Beam, using 5kV and 2kV cleanup steps to reduce Ga damage. The tips were examined in a CAMECA LEAP 4000X HR in voltage mode, at a 20% pulse fraction and 50K. Note one tip of the high Ni steel (CM6), annealed for 29 weeks, was run in laser mode with a pulse energy of 75 pJ, a repetition rate of 250 kHz and a temperature of 40K, in anticipation that only a very low number density of MNSPs would remain in this condition, so a larger sample volume was required to increase the probability of observing them. However, an MNSP with similar size and composition was also seen in a shorter voltage mode run as well. A full description of the APT analysis procedures can be found in [124].

APT reconstructions and analysis were performed using the CAMECA Integrated Visualization and Analysis Software (IVAS). The clusters were defined using the cluster analysis tool in the IVAS software with order = 5, d_{max} = 0.6 nm, N_{min} = 20-30 and envelope =

erosion = 0.6 nm. A constant d_{max} was used for all conditions. Decreases in d_{max} in a given tip results in a lower measured f and $<r>$. Thus, measuring changes in f and $<r>$ using a different d_{max} for each annealing interval could introduce artificial biases. The main consequence of choosing a d_{max} that is too large is that random solute density variations in the matrix might be misidentified as clusters. Note in the AI condition, the solutes are highly depleted from the matrix; hence, the probability of identifying random fluctuations as clusters is negligible. However, significant precipitate dissolution occurs after long-term annealing at 425°C, resulting in a much higher matrix solute contents. In these cases, all measured precipitates had $N >> N_{min}$, so no random solute density fluctuations were incorrectly identified as precipitates. The MNSP f was defined as the number of solute atoms in the clusters divided by the total number of atoms in the analyzed volume. The precipitate mole fraction varies slightly from volume fraction if the atomic densities of the precipitate and matrix phases differ. Thus, all model data shown for comparisons is also mole fraction. For further information regarding this difference see Appendix E.

Chapter 7.2

Atom Probe Tomography

Atom probe tomography (APT) was used to measure the MNSP composition, size distribution and average radius (<*r*>), number density (*N*) and mole fraction (*f*) in the AI condition and following each anneal for all times but the longest annealing time of 57 weeks. The APT was carried out at the Center for Advanced Energy Studies (CAES) located in Idaho Falls, ID, with support from the Idaho National Laboratory managed Nuclear Science User Facilities. APT tips were fabricated using a FEI Quanta 3D FEG Focused Ion Beam, using 5kV and 2kV cleanup steps to reduce Ga damage. The tips were examined in a CAMECA LEAP 4000X HR in voltage mode, at a 20% pulse fraction and 50K. Note one tip of the high Ni steel (CM6), annealed for 29 weeks, was run in laser mode with a pulse energy of 75 pJ, a repetition rate of 250 kHz and a temperature of 40K, in anticipation that only a very low number density of MNSPs would remain in this condition, so a larger sample volume was required to increase the probability of observing them. However, an MNSP with similar size and composition was also seen in a shorter voltage mode run as well. A full description of the APT analysis procedures can be found in [124].

APT reconstructions and analysis were performed using the CAMECA Integrated Visualization and Analysis Software (IVAS). The clusters were defined using the cluster analysis tool in the IVAS software with order = 5, d_{max} = 0.6 nm, N_{min} = 20-30 and envelope = erosion = 0.6 nm. A constant d_{max} was used for all conditions. Decreases in d_{max} in a given tip results in a lower measured *f* and <*r*>. Thus, measuring changes in *f* and <*r*> using a different d_{max} for each annealing interval could introduce artificial biases. The main consequence of choosing a d_{max} that is too large is that random solute density variations in the matrix might be

misidentified as clusters. Note in the AI condition, the solutes are highly depleted from the matrix; hence, the probability of identifying random fluctuations as clusters is negligible. However, significant precipitate dissolution occurs after long-term annealing at 425°C, resulting in a much higher matrix solute contents. In these cases, all measured precipitates had $N >> N_{min}$, so no random solute density fluctuations were incorrectly identified as precipitates. The MNSP f was defined as the number of solute atoms in the clusters divided by the total number of atoms in the analyzed volume. The precipitate mole fraction varies slightly from volume fraction if the atomic densities of the precipitate and matrix phases differ. Thus, all model data shown for comparisons is also mole fraction. For further information regarding this difference see the supplemental information.

Appendix D: Acknowledgements

This section provides a detailed accounting of the many invaluable contributions of institutions and researchers. Professor Odette and the Materials Reliability and Performance Group have been working on measuring, modeling and managing irradiation effects, including hardening and embrittlement, for more than 40 years. The work reported in this thesis is built on this broad and deep foundation. As is normally the case for an advisor, Professor Odette has been deeply involved in all aspects of this work, with the exception of conduct of the hands-on experiments and measurements. His involvement includes conceptualization; fund raising; design, construction and implementation of a series of UCSB irradiation experiments; directing the corresponding PIE; analysis of the results; multiscale-multiphysics modeling; writing papers and reports; and, developing predictive models of embrittlement used by regulatory agencies. This involvement applies to the preceding chapters and will not be repeated each time. I acknowledge funding from Rolls-Royce and the U.S. Department of Energy (DOE) via a Light Water Reactor Sustainability (LWRS) program subcontract from Oak Ridge National Laboratory (ORNL). The Nuclear Science User Facilities (NSUF) program, at the Idaho National Laboratory (INL), sponsored the UCSB ATR-2 irradiation, which was carried out by an outstanding team led by Dr. Mitch Meyer and with the assistance of Colin Knight. The NSUF also funded FIB and APT LEAP access at the Center for Advanced Energy Studies (CAES) in Idaho Falls, as well as a DOE Nuclear University Program fellowship. I express gratitude for the assistance given by the support staff at CNSI and CAES, and also thank Professor Peter Hosemann for providing FIB access for active specimens at UC Berkeley. I thank Dr. Soupitak Pal for completing the sample preparation, EPMA measurements and data analysis at UCSB. I thank Keith Wilford, Tim Williams and Nick Riddle at Rolls Royce for

their excellent expertise, advice and funding. I also thank Drs. Randy Nanstad, Janet Robertson and Keith Leonard at ORNL for their advice, encouragement and technical support.

All the APT studies were conducted at ORNL, the CAES facility, or the UCSB California Nano Science Institute (CNSI), which is supported by the National Science Foundation. Peter Wells provided crucial mentorship and hands on training in APT data collection and analysis. The CPI was carried out at the Dual Beam Facility for Energy Science and Technology (DuET) at Kyoto University in Japan by Dr. Takuya Yamamoto with the support of Dr. Kiyohiro Yabuuchi, Akihiko Kimura, and Mr. O. Hashitomi. The design and assembly of a custom sample holder and sample preparation was due to a joint effort of Peter Wells and myself.

G.R. Odette and Peter Wells designed the annealing experiment and produced comprehensive interpretations of results. Peter Wells assisted in the APT data collection, analysis and the long term anneals. The STEM-EDS studies were conducted by Philip Edmondson, Peter Wells and Soupitak Pal at CNSI and ORNL LAMDA facility using instrumentation provided by the Department of Energy, Office of Nuclear Energy, Fuel Cycle R&D Program and the NSUF program. I am also grateful for our modeling collaboration with Professor Dane Morgan's group at the University of Wisconsin, and especially the work of Drs. Huibin Ke and Mahmood Mamivand. In particular, I note the helpful advice Dr. Ke provided regarding the solute products and critical radii used in the simplified thermodynamic modeling section.

G.R. Odette and Takuya Yamamoto completed the intermediate to high fluence dependence modeling and plotting. I am extremely grateful to these two for derivation of the ATR-2 CF and modeling expertise. Their direct efforts and guidance made possible the

development of a predictive embrittlement model. The power law modeling was carried out by Takuya Yamamoto. The work reported here is small part of a comprehensive RPV embrittlement research program supported previously by the DOE Nuclear Energy University Program and more recently by the Light Water Reactor Sustainability Program though ORNL subcontracts., this work was truly made possible by our UCSB colleagues David Gragg and Kirk Fields, though their central and critical role in all aspects of the irradiation experiment and post irradiation mechanical testing.

Appendix E: Supplemental Data

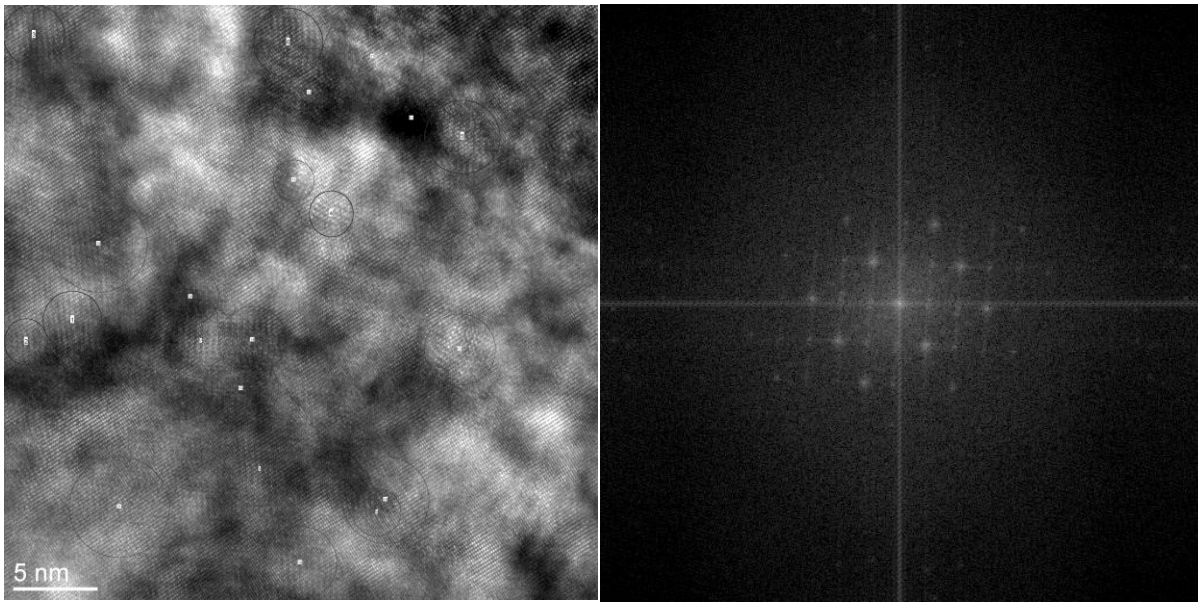

Figure E1. High resolution TEM image and a corresponding FFT image of one MNSP from alloy A28 (3.69% Ni 0.29% Mn 1.31%). This power spectra suggests that the MNSP structure is consistent with Ni_2Si[8].

Precipitate volume fraction vs mole fraction

The low evaporation potential of Mn-Ni-Si precipitates in an Fe matrix results in changes in local magnification and resulting in a focusing of matrix atoms into the precipitate region on the detector and is signaled by higher than physical atom densities in the reconstructed dataset [16,78]. These artifacts also result in the distortions of the compositions, shape, and size of precipitates, and most specifically their apparent Fe content, which actually comes from the adjoining matrix and contributes to the higher than physical atom density in the precipitate itself [70,150]. Using the number of solute atoms to define the cluster size minimizes these field evaporation distortions. For example, the MNSP mole fraction (*f*) was

[8] Dr. Yuan Wu conducted TEM from alloy A28 at UCSB CNSI.

defined as the number of solute atoms in the clusters divided by the total number of atoms in the analyzed volume. Mole fraction (*f*) can be converted to volume fraction (f_v) if the density of the precipitate phase is known, but since there are two likely potential phases for the precipitates in the as-irradiated condition, and the MNSPs may possibly transform to a different phase under annealing, the mole fraction is given in this chapter. Though a range of lattice constants for these phases are reporting in literature, using lattice constants of 1.1158 nm and 0.6687 for the G and Γ_2 phases [151], respectively, gives mole fractions are only ≈ 2% or ≈ 5% higher than for Fe.

Chapter 7.1 Atom Probe Tomography Data

Atom probe tomography (APT) data showed that there are large variations in solute content from region to region. These local solute contents directly influenced the precipitate stability, with higher solute content regions showing stable precipitates, while lower solute content regions showed completed dissolution. The tables below give the measured bulk, matrix and precipitate compositions for each individual atom probe tip along with the measured precipitate values for those tips where precipitates were observed.

Table E1. APT bulk and matrix compositions for all measured CM6 tips. Note that tips without any precipitation have dashes in the matrix composition as they were the same as the bulk composition[9].

Run Number	Condition	Bulk Composition (%)						Matrix Composition (%)					
		Fe	Ni	Mn	Si	C	Mo	Fe	Ni	Mn	Si	C	Mo
2179	AI	96.04	1.62	1.34	0.38	0.23	0.25	98.96	0.15	0.28	0.04	0.21	0.26
2180	AI	95.63	1.76	1.42	0.44	0.31	0.22	98.66	0.20	0.30	0.06	0.28	0.22
2185	AI	95.70	1.90	1.37	0.43	0.22	0.31	98.82	0.27	0.30	0.05	0.21	0.28
2186	AI	96.47	1.42	1.19	0.32	0.26	0.22	98.98	0.16	0.25	0.04	0.23	0.22
2493	AI	95.82	1.74	1.43	0.39	0.32	0.24	98.98	0.16	0.29	0.04	0.28	0.22
2495	AI	95.99	1.71	1.37	0.40	0.20	0.26	98.96	0.20	0.31	0.04	0.17	0.23
2496	AI	95.90	1.73	1.52	0.38	0.17	0.24	99.03	0.15	0.32	0.04	0.16	0.24
2497	AI	96.15	1.57	1.40	0.38	0.16	0.25	99.00	0.15	0.34	0.04	0.14	0.25
2498	AI	96.02	1.69	1.50	0.40	0.08	0.27	99.06	0.18	0.35	0.04	0.07	0.27
3246	425°C/1 Wk	96.41	1.59	1.15	0.38	0.22	0.20	97.11	1.21	0.93	0.31	0.20	0.20
3252	425°C/1 Wk	96.34	1.49	1.30	0.37	0.21	0.25	98.72	0.26	0.42	0.09	0.20	0.25
3270	425°C/1 Wk	96.78	1.37	1.16	0.33	0.08	0.23	98.54	0.45	0.54	0.15	0.06	0.23
3272	425°C/1 Wk	96.68	1.38	1.19	0.34	0.09	0.24	98.53	0.41	0.52	0.14	0.08	0.23
3273	425°C/1 Wk	96.71	1.39	1.10	0.35	0.14	0.22	98.01	0.69	0.66	0.22	0.12	0.22
3274	425°C/1 Wk	96.76	1.38	1.17	0.33	0.07	0.23	98.80	0.32	0.43	0.11	0.07	0.23
3742	425°C/7 Wks	96.16	1.64	1.41	0.36	0.13	0.26	96.52	1.49	1.28	0.34	0.11	0.23
3745	425°C/7 Wks	96.30	1.63	1.37	0.37	0.07	0.25	96.62	1.45	1.25	0.34	0.06	0.25
3766	425°C/7 Wks	96.29	1.64	1.37	0.36	0.05	0.25	96.72	1.40	1.22	0.33	0.05	0.25
3920	425°C/17 Wks	96.36	1.63	1.38	0.34	0.05	0.23	96.46	1.58	1.34	0.33	0.04	0.22
3923	425°C/17 Wks	96.96	1.49	1.01	0.34	0.02	0.17	-	-	-	-	-	-
3929	425°C/17 Wks	96.67	1.71	0.72	0.45	0.18	0.26	-	-	-	-	-	-
3930	425°C/17 Wks	96.38	1.66	1.27	0.36	0.07	0.21	-	-	-	-	-	-
4275	425°C/29 Wks	96.54	1.53	1.27	0.36	0.09	0.20	96.68	1.48	1.21	0.34	0.08	0.20
4328	425°C/29 Wks	96.16	1.66	1.34	0.38	0.16	0.25	96.35	1.58	1.25	0.36	0.13	0.28
4276	425°C/29 Wks	96.77	1.44	1.30	0.33	0.06	0.08	-	-	-	-	-	-
4277	425°C/29 Wks	97.03	1.33	1.10	0.30	0.08	0.15	-	-	-	-	-	-

**Trace amounts of P and Cr also present, but not listed.*

[9] Dr. Peter Wells conducted the APT data collection and analysis.

Table E2. APT Precipitate composition and <r>, N and f_v for all measured CM6 tips. Note that any tips with dashes did not have any measured precipitation[10].

Run Number	Condition	Precipitate Composition (%)						Precipitate <r>, N, f_v		
		Fe	Ni	Mn	Si	C	Mo	<r> (nm)	N (10^{23} m^{-3})	f_v(%)
2179	AI	60.58	20.33	13.95	4.50	0.24	0.23	1.53	19.02	2.77
2180	AI	56.66	22.49	15.06	5.26	0.25	0.12	1.43	22.99	2.92
2185	AI	61.21	21.28	11.87	4.97	0.23	0.26	1.43	21.17	2.82
2186	AI	57.96	21.72	14.68	4.96	0.29	0.25	1.50	16.56	2.31
2493	AI	58.02	21.80	14.46	4.88	0.44	0.27	1.54	20.09	2.86
2495	AI	60.53	20.59	13.55	4.70	0.24	0.25	1.50	20.30	2.81
2496	AI	57.35	21.87	15.58	4.68	0.20	0.21	1.61	17.44	2.97
2497	AI	59.76	20.67	14.27	4.81	0.17	0.20	1.51	19.46	2.68
2498	AI	57.52	21.62	15.50	4.94	0.11	0.22	1.54	19.50	2.89
3246	425°C/1 Wk	57.88	22.86	13.70	4.65	0.33	0.26	1.26	7.05	0.60
3252	425°C/1 Wk	64.20	18.86	12.47	3.82	0.20	0.27	1.53	14.25	2.12
3270	425°C/1 Wk	61.72	20.28	13.65	3.75	0.13	0.28	1.46	11.51	1.50
3272	425°C/1 Wk	62.09	20.04	13.53	3.76	0.10	0.26	1.43	12.96	1.59
3273	425°C/1 Wk	61.51	20.57	13.47	3.72	0.15	0.28	1.34	12.05	1.19
3274	425°C/1 Wk	62.02	20.03	13.63	3.81	0.07	0.26	1.45	14.41	1.79
3742	425°C/7 Wks	52.66	22.66	19.71	3.33	0.41	0.89	2.06	1.04	0.31
3745	425°C/7 Wks	55.45	23.52	16.76	3.64	0.16	0.32	1.56	1.98	0.33
3766	425°C/7 Wks	59.72	21.76	15.02	3.07	0.05	0.28	1.57	2.70	0.43
3920	425°C/17 Wks	55.84	23.21	16.59	3.12	0.38	0.70	2.12	0.30	0.12
3923	425°C/17 Wks	-	-	-	-	-	-	-	-	-
3929	425°C/17 Wks	-	-	-	-	-	-	-	-	-
3930	425°C/17 Wks	-	-	-	-	-	-	-	-	-
4275	425°C/29 Wks	35.72	22.72	22.85	9.04	3.25	5.82	2.78	0.10	0.09
4328	425°C/29 Wks	40.93	21.48	20.53	8.65	3.04	4.72	2.64	0.25	0.14
4276	425°C/29 Wks	-	-	-	-	-	-	-	-	-
4277	425°C/29 Wks	-	-	-	-	-	-	-	-	-

**Trace amounts of P and Cr also present, but not listed.*

[10] Dr. Peter Wells conducted the APT data collection and analysis.

EDS Line Scan

While the TALOS provided very high resolution elemental maps showing MNSPs remaining in the high Ni steel (CM6) at an annealing time of 57 weeks, the quantitative analysis was not consistent with APT as all maps had measured Mn contents of > 3.5%, which is significantly higher than any region seen in APT (or expected based on the known composition of the alloy, CM6). While future work will focus on better calibrating the TALOS for more quantitative measurement, in the short term, the FEI Titan at UCSB was used to perform a line scan and determine the local solute content of the grain containing very large precipitates and compare this with the neighboring grains, which did not contain and precipitates.

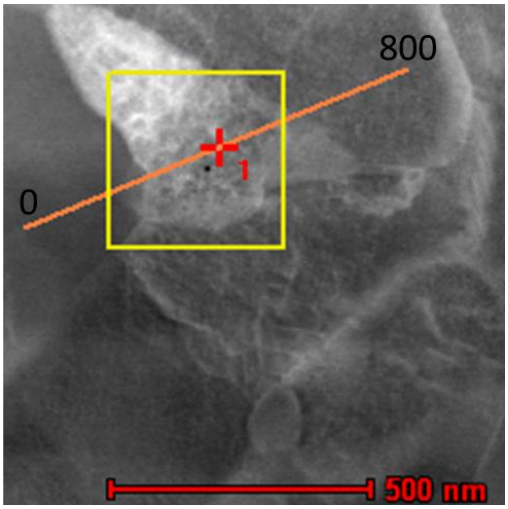

Figure E2. Location of line scan taken in the FEI Titan at UCSB where the region centered in the box contained a high density of large MNSPs as measured by the TALOS at ORNL (Figure 7.1.2, in the text)[11].

[11] Drs. Tiberiu Stan and Soupitak Pal assisted in completing the EDS line scans on the FEI Titan at UCSB CNSI.